Universidad Autónoma de Madrid

Departamento de Física Teórica de la Materia Condensada

ELECTROMAGNETIC PHENOMENA BASED ON SURFACE MODES AND THEIR TRANSFER TO ATOM OPTICS

Memoria de la tesis presentada por

Antonio I. Fernández Domínguez

para optar al grado de Doctor en Ciencias Físicas

Directores:

Francisco José García Vidal

Luis Martín Moreno

Madrid, Mayo de 2009

Contents

List of Figures

Abstract

English

This thesis is devoted to the study of the electromagnetic phenomena assisted by surface modes bound to metal structures. In order to treat the interaction of light with these complex systems, we have developed a theoretical formalism based on the modal expansion of the electromagnetic fields. Within this framework, metals are modelled as perfect conductors, which prevents the penetration of electromagnetic fields into them. This approximation provides accurate results at low frequency domains (microwave and terahertz regimes) and still has semi-quantitative value at visible and optical frequencies.

We analyze the formation of geometrically induced electromagnetic modes in different metallic structures. The dependence of the modal characteristics on the various structure parameters is thoroughly studied. Based on this analysis, we develop different guiding and focusing schemes featuring subwavelength confinement of electromagnetic fields. Our models are designed so that they operate in the terahertz regime, which is being currently explored due to its high technological potential. The agreement between our theoretical results and experiments realized in this frequency range is excellent.

Our theoretical formalism enables us to treat the scattering properties of perforated metallic films. In this context, we study the role of order in the extraordinary transmission phenomenon. Considering periodic and quasiperiodic systems, we identify the leaky modes supported by these structures as the main actors in the transmission process.

Finally, the transfer of extraordinary transmission and beaming effects to matter waves is studied. We show that, as in the electromagnetic case, surface modes are the fundamental ingredient for the appearance of these phenomena in cold atoms.

Español

Esta tesis se ocupa del estudio de fenómenos electromagnéticos basados en modos superficiales de estructuras metálicas. Para tratar la interacción de la luz con estos complejos sistemas, hemos desarrollado un formalismo teórico basado en la expansión modal de los campos electromagnéticos. En este marco teórico, consideramos que los metales se comportan como conductores perfectos, lo que impide la penetración de los campos electromagnéticos dentro de ellos. Esta aproximación proporciona resultados precisos a bajas frecuencias (microondas y terahercios) y tiene una validez semicuantitativa en los rangos visible y óptico.

Hemos analizado la formación de modos electromagnéticos en diferentes estructuras metálicas demostrando su origen geométrico, y hemos estudiado la dependencia de sus características con los diferentes parámetros de la estructura. Basándonos en estos resultados, desarrollamos diferentes diseños que permiten el guiado y focalización de campos electromagnéticos confinados en regiones menores que la longitud de onda. Nuestros modelos están diseñados para trabajar en el régimen de terahercios, que actualmente está despertando un gran interés tecnológico. La comparación de nuestros resultados teóricos con experimentos realizados en este rango es excelente.

Nuestro formalismo teórico nos permite también tratar las propiedades de scattering de láminas metálicas perforadas. En este contexto, estudiamos el papel que juega el orden en la aparición del fenómeno de transmisión extraordinaria. Analizando sistemas periódicos y quasiperiódicos, hemos identificado a los modos radiativos en estas estructuras como los actores principales en el proceso de transmisión.

Finalmente, hemos estudiado la transferencia de los fenómenos de transmisión extraordinaria y colimación a ondas de materia, mostrando que el ingrediente fundamental para la aparición de estos fenómenos es, como en el caso electromagnético, la presencia de ondas de superficie en estos sistemas.

List of acronyms

This is a list of the acronyms used in the text:

- **CPPs** Channel plasmon polaritons
- **EM** Electromagnetic
- **EOT** Extraordinary optical transmission
- **FDTD** Finite difference time domain
- **FIT** Finite integration technique
- **ME** Modal expansion
- **PEC** Perfect electric conducting
- **SIBCs** Surface impedance boundary conditions
- **SMWs** Surface matter waves
- **SPPs** Surface plasmon polaritons
- **TE** Transverse electric
- **TM** Transverse magnetic
- **TMM** Transfer matrix method
- **THz** Terahertz
- **WPPs** Wedge plasmon polaritons

Throughout this thesis, the Gaussian system of electromagnetic units is used, unless otherwise indicated.

1. General introduction

The enormous development of telecommunications technology during the last century has led to a growing interest in electromagnetic (EM) surface waves among the scientific community. Already around 1900, Sommerfeld [1] and Zenneck [2] published their pioneering works accomplishing the mathematical description of the propagation of radio waves along conductors of finite conductivity. Since then and during the whole 20^{th} century, surface EM waves have been rediscovered in a variety of different contexts. Soon after the publication of the Sommerfeld's work, Wood [3] reported the appearance of anomalous intensity drops in the spectra produced when visible light reflects at metallic gratings. Only five years later, Lord Rayleigh [4] devised his theoretical description of the scattering of scalar waves by periodic surfaces. However, it was not until the early 40's when Fano [5] connected the Wood's findings with the former theoretical works. In the late 50's, based on experiments studying the diffraction of electron beams by thin metal films, Ritchie [6] predicted that fast moving charged particles could excite surface waves in metals, and considered such modes as elementary excitations in solids. Ten years later, this was confirmed by experiments [7], which demonstrated the close link between these surface waves and the reflection anomalies observed by Wood more than fifty years before. By that time, the excitation of Sommerfeld's waves with visible light using prism coupling was also realized [8], and an unified description of all these phenomena in the form of surface plasmon polaritons (SPPs) was finally established.

SPPs are guided EM waves confined at the interface between a metal and a dielectric. Their origin resides in the interaction between light and the conduction electrons in the metal surface [9]. SPPs arise in metals because of the quasi-free character of conduction electrons, which allows them to respond collectively to external EM fields. This fact provides SPPs a mixed electromagnetic-wave and surface-charge nature. Such hybrid character is illustrated in the left panel of Fig. 1.1, which depicts the interaction between surface charges and EM fields associated with SPPs. This interaction binds SPPs to the metal surface and makes EM fields decay exponentially into both the metal and dielectric media. The dispersion relation (dependence of the mode frequency, ω, on the parallel wave vector, k) that Maxwell equations yields for such surface waves is sketched in the right panel of Fig. 1.1. At low frequencies, SPPs lie close to the light line ($\omega = ck$) and are pre-

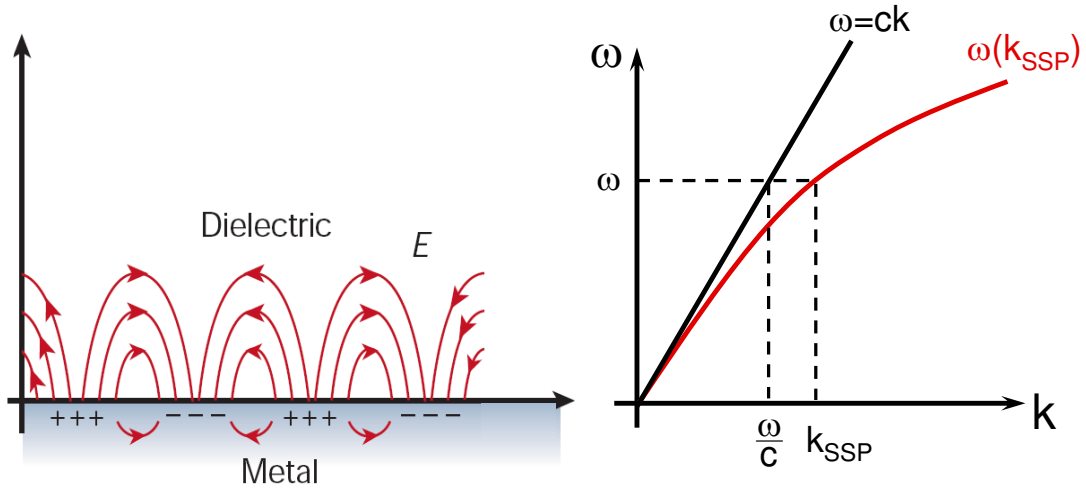

Figure 1.1.: Left panel: Electric field and charge distribution associated with SPPs travelling within a metal-dielectric interface. Right panel: Dispersion relation for SPPs. Note that the SPP wave vector is always larger than that corresponding to freely propagating waves, $k_{SPP} > \omega/c$.

dominantly light-like. For larger frequencies, the dispersion relation deviates from this linear dependence and the wave vector becomes much larger than for freely propagating waves. For most metals, this increase in k takes place in the telecom and visible regimes, which correspond to wavelengths of the order of hundreds of nanometers up to a few microns ($300\,\text{nm} \lesssim \lambda \lesssim 1\,\mu\text{m}$). There are another two parameters which characterize SPP modes: the decay length and the propagation length. The first one is related to the normal component of the SPP wave vector into the dielectric and reflects the binding of the EM fields to the metal surface. The second one, which is given by the imaginary part of k, provides the distance that SPPs can travel before they attenuate due to the damping of the electronic oscillations inside the metal. These two magnitudes are closely related. Large decay lengths imply that SPPs are weakly bound to the metal surface, which reduces energy losses inside the metal and enlarges the propagation lengths. This occurs at low frequencies, where the SPP band approaches the light line. At higher frequencies, SPPs become confined and the absorption at the metal surface increases rapidly, which makes both decay and propagation lengths decrease. This is the well-known trade-off between SPPs confinement and propagation [9].

Traditionally, the use of metals in optical components has been reduced to the areas of mirrors and highly absorbing media. The reason for this is the presence of SPPs deco-

rating their surfaces. As we have shown above, the localization of EM fields linked to SPPs, if uncontrolled, represents an energy sink. However, the scientific and technological developments in the last decade has changed this perception drastically. In particular, modern nanofabrication and characterization techniques have made possible to structure metal surfaces in order to control the flow of SPPs and to map the associated fields with unprecedented detail. Although absorption remains a very important issue which prevents the use of metals for long distance communications, SPPs have opened the way to the use of metallic surfaces for miniaturized optical and optoelectronic devices. Up to the emergence of SPPs, dielectric-based optical components were constrained by the so-called diffraction limit [10], according to which light can not be squeezed into volumes smaller than the wavelength. This meant a crucial drawback for the development of photonic compact devices, whose sizes could not be smaller than those of electronic components. Note that the dimensions of current microelectronic circuits are below 100 nm, several times smaller than optical wavelengths.

There are several features which make SPPs so promising from the technological point of view. On the one hand, as we have mentioned above, they present a unique ability for concentrating EM energy in subwavelength volumes. Moreover, they can propagate EM fields along distances up to hundreds of wavelengths. Finally, they allow combining electromagnetic and electronic phenomena in the same material platform. Therefore, it is clear that the challenge consists in achieving compact SPP-based photonic elements with specific functionalities. Such devices would allow overcoming the limitations of current microelectronic technology, which are mainly related to the lost of efficiency as the size of the chips is reduced. These photonic circuits would operate as follows: first, free radiation would be converted into SPPs, which would then propagate and be processed by logic elements, before being transformed back into light. The building of photonic devices requires the development of a broad variety of active and passive components such as couplers, filters or switchers [11].

In the last decade, many research efforts have been devoted to the design and realization of structures with SPP functionalities. This has converted SPP-based photonics, also termed *plasmonics* [12, 13], in a well established research field. One of the main factors behind the fast development of plasmonics is the excellent agreement between experiments and theory, which is highly non-trivial. From the experimental side, small imperfections in sample fabrication can ruin the flow of SPPs either by increasing of absorption or by coupling to radiation out of the structure. From the theoretical point of view, although the equations that govern EM phenomena are well known (Maxwell equations plus the constitutive relations describing the material properties), solving them is a very difficult task due to the very different length scales explored by SPPs: the wavelength, the

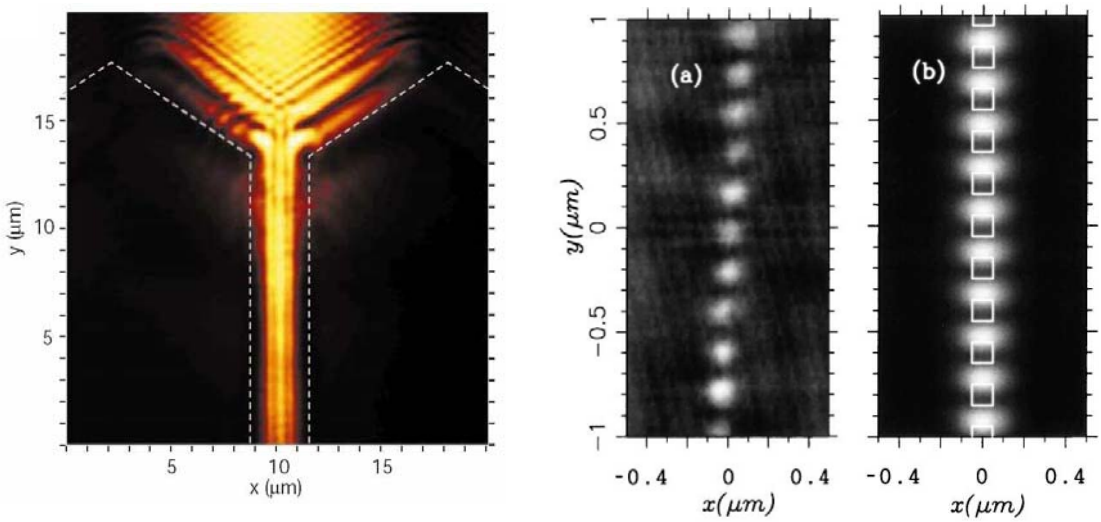

Figure 1.2.: Plasmonic waveguiding schemes. Left panel: Near field map of the SPPs propagation along a metal strip. Right panel: Comparison between experimental (a) and theoretical (b) fields distribution in a periodic chain of square gold nanoparticles.

propagation length, the decay length, and the metal skin depth. The good comparison with experiments means that theoretical results have predictive value, which is crucial for understanding and discovering new fundamental phenomena as well as guiding the optimization of structures.

Among the great amount of plasmonic designs with different functionalities proposed in the last years, undoubtedly, waveguides have been one of the most thoroughly explored. These could be used to interconnect the various elements within a photonic device as well as different components comprising a more complex circuit. The hybrid nature of SPPs enable them to carry both optical signals and electric current, making plasmonic waveguides also useful as interconnections of microelectronic elements. The latter offers the potential to combine the technical advantages of photonics and electronics in the same chip [14]. Depending on the characteristics required, SPP waveguides can be configured using various geometries. In what follows, some of the most relevant proposals are briefly described.

The most straightforward SPP guiding scheme consists in a two-dimensional flat metal surface. By creating defects on it, the pathway of the surface waves can be modified, allowing the direct implementation of functional elements such as mirrors or splitters [15]. Another simple routing system is made up of a metallic strip of width comparable to λ. It has been shown that lateral confined surface EM waves are efficiently excited on

these waveguides by SPPs launched in 2D homogeneous surfaces [16]. A near field map of the SPPs propagation along a metal strip waveguide is shown in Fig. 1.2. Modulated surfaces can also be used for routing purposes. By structuring periodically a metal surface, a photonic band gap arises in the SPP dispersion relation [17]. In these systems, SPP waveguides correspond to line defects created in the surface lattice [18].

Thin metallic films embedded in dielectric media have been also used as plasmonic waveguides [19]. This geometry offers long propagation lengths but large modal sizes. Considering thin strips instead of homogeneous 2D films [20, 21] allows reducing the modal size in these waveguides. Metal nanowires have been also tested as routing devices [22]. They display subwavelength confinement in the transverse plane but the losses associated with resistive heating limit the propagation of light in these structures. A completely different approach consists of nanoparticle arrays. These guides feature subwavelength transverse confinement of EM fields but, again, the high localization of EM energy increases the absorption effects in these systems [23, 24]. The fields distribution (experiment and theory) in an SPP waveguide composed of square nanoparticles is shown in Fig. 1.2.

The examples above indicate that the main difficulty in the design of plasmonic waveguides is finding structures that support EM fields with small modal sizes and large propagation lengths. In the last years, two different guiding schemes have been proposed satisfying these requirements. The first of these designs consists in V-shaped grooves carved in a flat metal surface. The EM modes supported by such structure, termed channel plasmon polaritons (CPPs), were studied within the electrostatic approximation two decades ago [25]. Subsequently, several theoretical works analyzing CPPs in realistic geometries were published [26–28]. Recently, CPPs have been experimentally investigated at telecom frequencies [29, 30], displaying strong confinement, low damping, and robustness against channel bending. Thank to these properties, prototypes of basic devices such as splitters, interferometers or resonators have been demonstrated [31].

The potential of V-grooves in the context of SPP waveguiding has given rise to comprehensive theoretical studies on the modal characteristics of CPPs [32]. Importantly, these works have shown that a strong field enhancement occurs in the CPPs modal shape at the groove edges. This fact indicates that for relatively shallow grooves, CPPs are hybridized with EM modes travelling along the channel corners. These are the so-called wedge plasmon polaritons (WPPs). EM modes sustained by metal wedges were theoretically suggested more than 30 years ago [33]. However, the guiding capabilities of WPPs have not been demonstrated until very recently [34–36]. These papers have shown that WPPs, while having propagation lengths similar to CPPs, exhibit smaller modal sizes. Apart from their advantageous guiding properties, CPP and WPP based plasmonic wa-

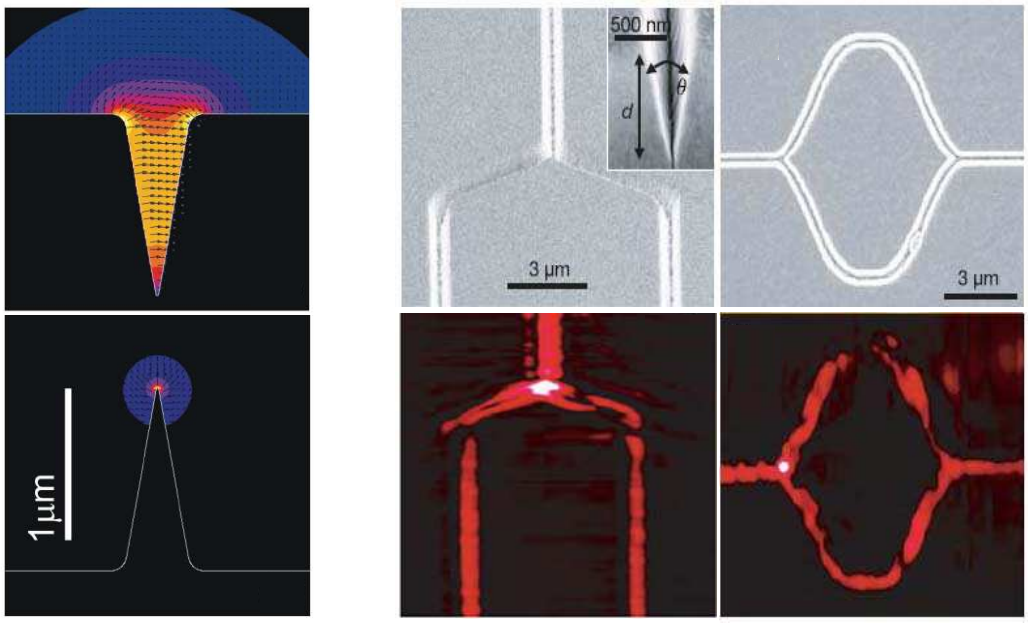

Figure 1.3.: Left panel: Theoretical transverse electric field of CPP (up) and WPP (bottom) modes sustained by structures of the same dimensions. Right panel: CPP based Y-splitter (left) and Mach-Zehnder interferometer (right) operating at telecom frequencies. SEM (up) and near field optical SNOM (bottom) images are shown.

veguides can be easily combined with planar metal structures, which is very convenient for technological purposes. It is also remarkable that edges and corners appear whenever a surface is folded. In this sense, CPPs and WPPs constitute building blocks present in other kinds of plasmonic guides. In the left panel of Fig. 1.3, the modal shape for the CPP and WPP modes supported by structures of the same dimensions are depicted [36]. The right panel shows the experimental realization of a CPP-based Y-splitter and a Mach-Zender interferometer operating at telecom frequencies [31].

The emerging field of plasmonics is not only limited to to the propagation and processing of EM signals. SPPs have been identified as key actors in many other EM phenomena [12, 14]. Due to both fundamental and technological reasons, one of the most relevant is the so-called extraordinary optical transmission (EOT) through perforated metallic films. The diffraction of light by an aperture drilled in a metal film is an old problem. It was firstly treated using a full vectorial approach by Bethe [37] in 1944. Bethe's theory established that the transmission of the EM energy through a circular aperture pierced in

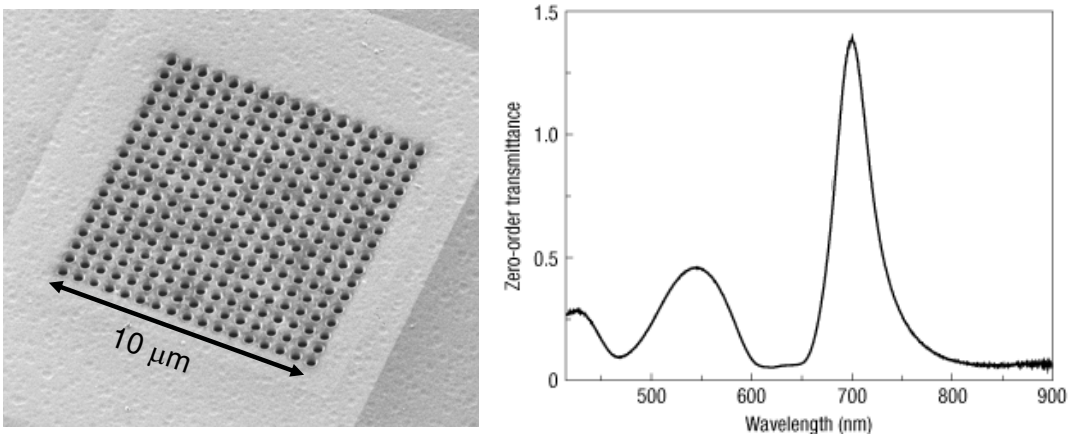

Figure 1.4.: Left panel: SEM image of an Au film perforated with a periodic array of 17×17 holes. Right panel: Experimental zero-order transmittance through a 31×31 hole array of period 600 nm.

an infinitely thin metallic film is proportional to $(a/\lambda)^4$ (where a is the aperture radius). Thus, in the limit of aperture sizes much smaller than the incoming wavelength ($a << \lambda$), only a negligible fraction of the incident EM flux is transmitted. More than 40 years later, Roberts [38] revisited the problem. By means of numerical calculations, he demonstrated that the transmissivity of the aperture was even lower when the finite thickness of the film was taken into account.

It was thought that Bethe's theory described correctly the scattering of light by apertures much smaller than the wavelength. However, in 1998, Ebbesen and co-workers [39] found accidentally, while analyzing the optical properties of cylindrical cavities in metallic films, that the transmittance of visible light through a periodic array of nanometric holes was several orders of magnitude larger than expected. They observed that, surprisingly, at certain wavelengths, the transmission efficiency (normalized to the total area of the holes) exceeded unity. In other words, for these wavelengths a periodic array of subwavelength holes transmits more light than a large, macroscopic hole of the same area as the sum of all the holes. This finding indicated that the metal film was not merely a screen, which blocks the light, but rather an active participant in the transmission process, and that a collective response of the periodic array of holes should occur in order to give rise to such enhancement in the transmissivity. The term *extraordinary optical transmission* was coined in the seminal paper [39] where the phenomenon was reported for the first time. Left panel of Figure 1.4 shows the type of structures considered in the

experiments [40]: a periodic hole lattice pierced in a metal film. The right panel displays the transmittance spectrum measured from an array of holes of radius $a = 135$ nm. A transmission peak occurs at wavelengths much larger than the hole radius, where the Bethe's theory predicts that the transmissivity should decrease smoothly with increasing wavelength.

The discovery of EOT gave rise to an exhaustive research to clarify the physical mechanisms behind the effective response of the apertures observed in the experiments. Due to its simplicity, first theoretical analysis considered the one-dimensional analog of the experimental structure: a periodic array of slits [41–43]. As a result, it was shown that EOT also takes place in these systems, pointing out that the phenomenon was more general than expected. In 2001, the first complete theoretical treatments of EOT in hole arrays where published [44–46]. These works provided the explanation of the phenomenon which is generally accepted today. According to it, the light impinging on the apertures is collected by the SPPs supported by the input side of the film. These explore the film surface and tunnel the EM energy through the holes. At the output side of the film, SPPs scatter again with the aperture openings and emit the EM energy out of the structure. This resonant transmission process is strongly dependent on the incoming wavelength, as it controls the coupling between light and SPPs at both film surfaces and the transport of EM energy through the holes. Since these first studies, a great amount of experimental and theoretical works have been devoted to further investigate the fundamental aspects of the phenomenon. Remarkably, EOT has also found applications in a broad range of areas such as sensing or optoelectronics [47].

Four years after the publication of the first experiments, the appearance of EOT in single apertures was demonstrated experimentally [48]. It was shown that an aperture much smaller than the incident wavelength can exhibit transmission resonances if it is surrounded by periodic indentations located at the input side of the film. Moreover, the light exiting from this system can be collimated into a very narrow beam if the output surface of the film is also corrugated. This phenomenon was addressed theoretically only one year later [49, 50]. These works demonstrated that transmission resonances and beaming effects are almost independent, and that they are due to the presence of SPPs at the input and output sides of the film, respectively. In Figure 1.5, the structures studied in [48] are depicted. The angular distribution of the beam emerging from the bull's eye geometry (upper image) is rendered. Light is directionally transmitted by the structure with an angular divergence of a few degrees.

Up to this point, we have focused our attention on the appearance of extraordinary transmission in the optical regime. However, already in 2001 [45], it was shown that EOT occurs even in perforated perfect electric conducting (PEC) films. A perfect conductor

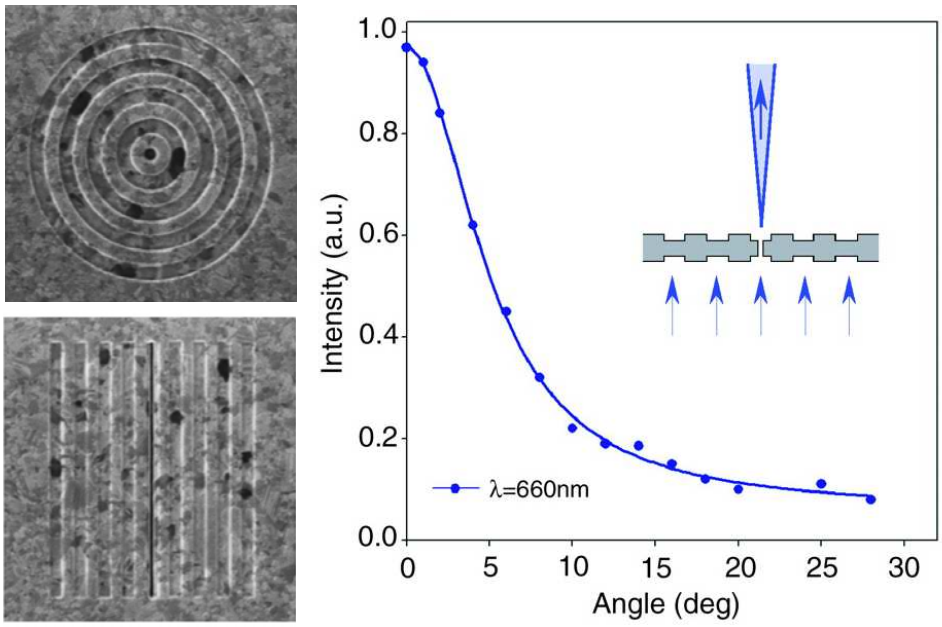

Figure 1.5.: Left panels: FIB micrograph image of a bull's eye structure (up) and its 1D analog (bottom). Experimental angular transmission-intensity distribution at resonance emerging from the bull's eye geometry.

is a theoretical idealization which models the dielectric response of metals by taking $\epsilon_M = -\infty$ (where ϵ_M stands for the metal permittivity). This makes the conduction electrons completely free and able to respond immediately to any EM disturbance. Therefore, PEC materials are impenetrable to EM fields, which prevents the presence of SPPs decorating their surfaces. The discovery of EOT in PEC structures led to the study of the transmission properties of drilled films at frequencies below the optical regime, where PEC models are quasi-exact and SPPs are not confined to metal-dielectric interfaces. In the following years, extraordinary transmission was experimentally reported at terahertz (THz) [51–53] and microwave [54, 55] frequencies.

The formation of transmission resonances in structures which do not support tightly bound SPPs reopened the problem of the fundamental physics behind EOT. The issue was clarified by two theoretical papers published in 2004 and 2005 [56, 57] demonstrated that the texturing of a flat PEC surface makes it behave as an effective metal whose dielectric response is controlled by geometry. These works also showed that such structures sustain EM modes whose characteristics resemble those of SPPs. For this reason,

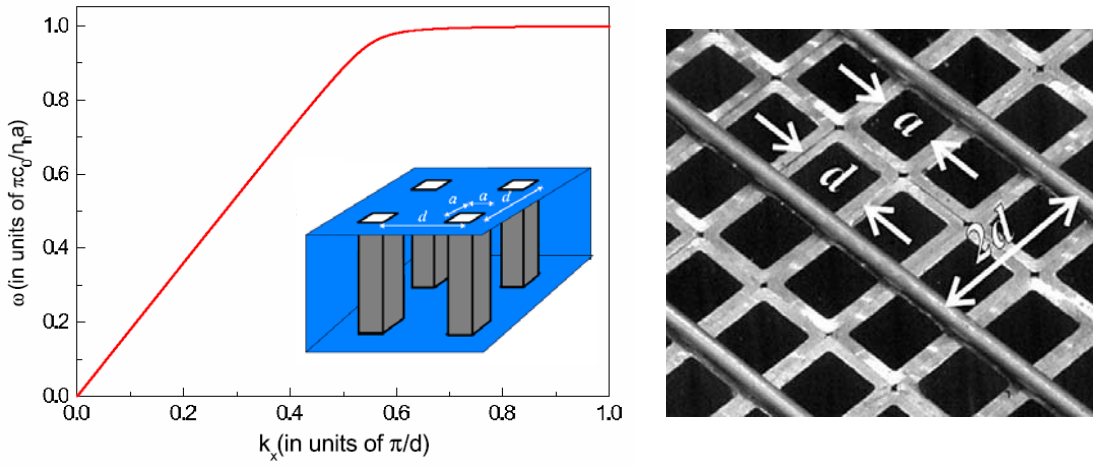

Figure 1.6.: Left panel: Dispersion relation of the spoof SPPs supported by periodic holes filled with a dielectric. Right panel: Photograph of the experimental sample supporting SPPs at GHz frequencies.

these surface waves were termed *spoof* SPPs. The physical origin of these EM modes is completely different from conventional SPPs, whose attributes are dictated by the metal composition. The dispersion relation of spoof SPPs is governed by the geometry of the structured PEC surface supporting them. The left panel of Fig. 1.6 renders $\omega(k)$ for the spoof SPPs propagating along a periodic array of holes [57]. Note that the behavior of the mode frequency with increasing k is similar to that of conventional SPPs (see Fig. 1.1).

Bound EM modes in periodic metal structures have been studied for decades in the context of radio waves [58–60]. However, the emergence of the spoof SPP concept has renewed the interest on the fundamental and applied aspects of these EM modes. As a result, in the last years, the first spoof SPP models have been corrected [61, 62] and extended to different geometries [63]. Moreover, spoof SPPs have been recently verified experimentally in the microwave [64, 65] and THz [66] regimes. The right panel of Fig. 1.6 shows a photograph of the sample in which leaky spoof SPPs at microwave frequencies were observed for the first time [64].

Although the origin of spoof SPPs is linked to the EOT phenomenon, it was soon realized that these EM modes can be used to guide radiation in the same way as conventional SPPs [57]. The behavior of conventional SPPs is imposed by the electronic properties of metals. However, the characteristics of spoof SPPs can be tailored in order to control

the flow of light just by playing with the geometry of the indentations disposed at the metal surface. This geometric character of spoof SPPs has allowed considering textured metallic surfaces as *plasmonic metamaterials*, since they gain their properties from their structure rather than their composition.

The application of the spoof SPP concept in the optical regime allows combining intrinsic plasmonic and geometric effects. Moreover, plasmonic metamaterials also make possible to transfer the routing and confinement capabilities of conventional SPPs to lower frequency domains. Specifically, spoof SPPs are expected to play a key role in the development of the emergent THz technology [67]. THz radiation is situated between the infrared and microwave parts of the EM spectrum. During the last decades, this frequency range has remained unexplored because of its resistance to the techniques commonly employed in these well established neighbor bands. This situation has changed in the last decade. Advances in material science have led to the development of new routes for generation [68] and detection [69] of THz waves and the potential of this radiation for advanced physics research has been demonstrated. Moreover, current THz technology is an extremely attractive field, with applications in areas such as time-domain spectroscopy [70], biosensing [71] or security [72] and biomedical [73] imaging. Thus, an intense scientific activity is currently devoted to exploit the opportunities that spoof SPPs provide in the context THz photonics.

Analogies has played a prominent role in the current development of plasmonics. They constitute a basic research strategy which allows the transfer of notions and concepts from one field to another, yielding deeper physical insights in both fields. Following this approach, and taking advantage of the broad perspective that spoof SPPs have provided on the extraordinary transmission phenomenon, in the last years, many research efforts have been dedicated to analyze the transferability of EOT to other physical domains. As a result, enhanced transmission and associated beaming effects have been reported in photonic crystals [74–76]. Subsequently, the EOT process have been also applied to other undulatory entities. Thus, transmission resonances have been predicted theoretically for non-interacting cold atoms [77] and Dirac electrons in graphene [78]. Moreover, the acoustic equivalent of EOT has received much attention recently due to its numerous technological possibilities [79–83]. In these systems, the fundamental ingredient needed for the appearance of extraordinary transmission is the presence of localized waves playing the same role as SPPs in the original version of the phenomenon.

Structure of the thesis

Once we have outlined the research frame within which our theoretical investigation has been carried out, in the last part of this chapter, the contents of this thesis are briefly summarized:

In Chapter 2, the theoretical tools employed in our research are presented. First, the fundamentals of our modal expansion formalism are detailed. We demonstrate the suitability of this approach for analyzing the scattering properties of perforated metallic films and for studying the electromagnetic modes sustained by structured metals. We show how both infinitely periodic and finite systems can be treated within this framework. Additionally, the reciprocal-space version of our formalism is developed. In the last sections of the chapter, three different numerical schemes employed in our investigation, the transfer matrix method, the finite difference time domain method, and the finite integration technique, are briefly described.

In Chapter 3, we study the formation of spoof surface plasmon polaritons in different geometries. First, the electromagnetic modes bound to planar structures are considered. We analyze the modal characteristics in both single surfaces and films. Moreover, the comparison of our theoretical results with experiments performed in the terahertz regime is shown. Secondly, we treat the spoof surface polariton modes sustained by cylindrical structures. We analyze the dependence of the mode characteristics on the geometrical parameters for the case of milled wires. Based on these results, we propose a conical design for achieving subwavelength focusing of light. Our theoretical predictions are verified by experiments performed on helical grooved wires at terahertz frequencies. Finally, two distinct routing schemes featuring subwavelength confinement in the transverse plane are presented. They combine the spoof plasmon concept with channel and wedge plasmon polaritons. The dimensions of the designs are chosen so that the optimal frequencies for guiding lie in the terahertz range of the electromagnetic spectrum.

Chapter 4 studies the transmission properties of finite arrays of apertures perforated in metallic films. We consider periodic as well as quasiperiodic arrangements of both slits and holes. By means of our modal expansion formalism, we obtain the transmittance and the distribution of electromagnetic fields in such structures. In its reciprocal version, our theoretical framework enables us to link the transmission resonances in these systems with their structure factor. Finally, we identify the leaky electromagnetic modes supported by perforated films as the main actors in the transmission process.

In Chapter 5, the appearance of extraordinary transmission and beaming for non-interacting cold atoms in various geometries is demonstrated theoretically. We show that the resonant excitation of surface matter waves, the analog of surface plasmon polaritons

in the electromagnetic case, leads to the formation of efficient transmission channels in these systems. In contrast to their electromagnetic counterpart, surface matter waves require an attractive potential close to a solid surface in order to be supported. In our research, we consider simple models based on square well potentials which nevertheless contain all the physical mechanisms behind both phenomena. The issue of a feasible scenario for the implementation of these ideas is also addressed. We propose an experimental setup in which extraordinary transmission of matter waves takes place. In this system, the realistic attractive potential sustaining surface matter waves results from the combination of the van der Waals interaction between a neutral atom and a dielectric surface and an external repulsive optical potential.

Finally, in Chapter 6 a short overview of the main results and the general conclusions of this thesis is presented.

2. Theoretical methods

2.1. Introduction

In this chapter we describe in detail the different theoretical approaches used throughout this thesis. First, we present our quasi-analytical formalism based on the modal expansion technique. It is illustrated through the analysis of the scattering properties of arrays of one and two-dimensional apertures perforated in metallic films. We treat both infinitely periodic and finite systems, and develop the reciprocal-space version of the formalism. Moreover, we show how the theoretical framework presented allows the study of the geometrically induced bound electromagnetic modes supported by corrugated metallic surfaces. Finally, the incorporation in an approximate way of the dielectric properties of real metals into the formalism is also described.

In our research, we have also used three different numerical schemes: the transfer matrix method, the finite difference time domain method, and the finite integration technique. In the second part of this chapter, the fundamentals of these computational approaches are detailed. Additionally, the characteristics of the three methods are compared in terms of efficiency, versatility and numerical stability.

2.2. Modal expansion formalism

The Modal Expansion (ME) technique is a very general method for solving linear differential equations describing physical systems of very different nature. It is a very useful tool in current research in a broad range of fields such as acoustics, quantum mechanics or electromagnetics. In this section, we present a theoretical formalism for solving Maxwell equations in complex metallic structures based on this technique.

Due to its suitability for analyzing electromagnetic (EM) processes occurring at textured metallic surfaces, first ME methods were already used by engineers in the early 50's and 60's for the design and analysis of antennas, transmission lines and filtering devices operating in the microwave regime [84]. ME approaches were also a useful tool [85–87] for the study of the Surface Enhanced Raman Scattering [88], discovered in the 70's. Finally, in the last decade ME has become a very fruitful framework for theoretical

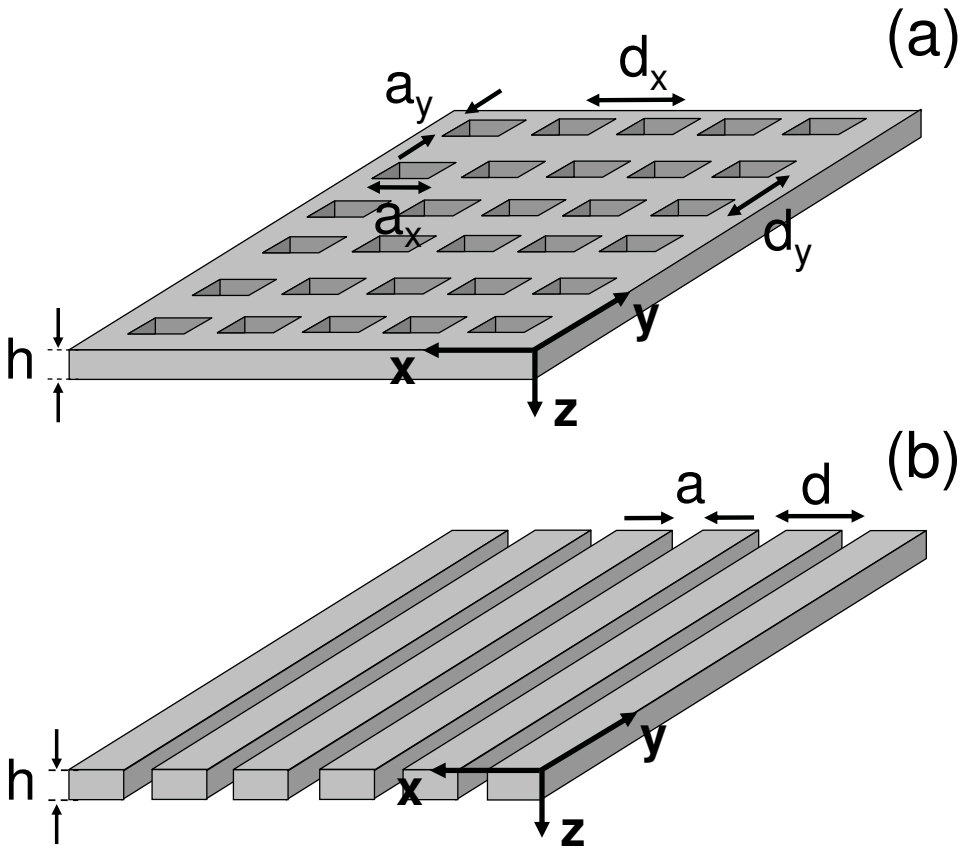

Figure 2.1.: View of the periodic structures under study. The geometrical parameters defining the arrangement of holes are the array periods, d_x and d_y, and holes sides, a_x and a_y. The array of slits is characterized by the periodicity d and the slits width a. In both cases, the film thickness is denoted by h.

research in nanophotonics, being applied in various fields such as extraordinary optical transmission (EOT) [43, 49, 50] or metamaterials science [56, 89].

The ME technique is based on the decomposition of the EM fields into eigenmodes of the Maxwell equations within the various regions comprising the complex structure under study. Therefore, by imposing the appropriate continuity conditions [90] at the region boundaries, Maxwell equations can be solved in all the space. We have developed a ME framework which has enabled us to model and analyze very different physical systems. Throughout this thesis, our formalism will be presented and all the modifications performed on it for each problem will be shown. However, the fundamental aspects of the ME technique are illustrated in the following sections through the study of two

simple problems: the scattering of light by metallic films perforated with periodic arrangements of subwavelength apertures and the formation of geometrically induced EM modes in these structures. In order to give a general view of the method, two different geometries are considered, two-dimensional (2D) arrangements of rectangular holes and one-dimensional (1D) arrays of slits (see Figure 2.1).

The only approximation involved in our model consists in treating the metal as perfect electric conducting (PEC) [10], i.e., the metal permittivity $\epsilon_M = -\infty$. This involves neglecting the penetration of the fields into the metal, which enables us to express EM fields in the apertures in terms of waveguide modes, which are analytically known for both geometries (holes and slits). Additionally, the use of PEC boundary conditions make all lengths involved in the system scalable, which allows transferring the results obtained in one frequency range to another ones. However, since the PEC approximation prevents the penetration of EM fields into metallic media, it works properly at microwave and far infrared frequencies, whereas it is less accurate in the optical and telecom ranges of the EM spectrum. In Section 2.2.5, we discuss briefly how this limitation of the model can be overcome by incorporating surface impedance boundary conditions (SIBCs) [91, 92] in our ME formalism.

2.2.1. Periodic systems

Hole arrays

Panel (a) of Figure 2.1 shows a schematic picture of the most general structure under study, a periodic 2D arrangement of rectangular holes. The geometrical parameters defining the system are the film thickness, h, the array periods, d_x and d_y, and the holes sides, a_x and a_y. Slit geometries, shown in panel (b), can be considered as a limiting case of rectangular holes with $d_y, a_y \to \infty$. Here, we present our theoretical framework based on the ME method through its application to the problem of the scattering properties of periodic 2D structures. The modifications performed in the formalism in order to deal with 1D apertures are also detailed.

The ME technique allows writing EM fields in a very compact representation. In principle, the full EM field comprises six components, three for the electric field, $\mathbf{E}$, and three for the magnetic field, $\mathbf{H}$. However, in our approach, EM fields are expanded in terms of eigenmodes having a well defined propagation constant along z-direction (see Fig. 2.1). This enables us to keep track of only the transverse components, $\mathbf{E}_t$ and $\mathbf{H}_t$ (parallel to xy plane). The longitudinal components, E_z and H_z, can be straightforwardly obtained from the transverse ones through the divergence Maxwell equations, $\nabla \cdot \mathbf{H} = 0$ and $\nabla \cdot \mathbf{E} = 0$. Thus, we can describe the EM fields through only two bivectors, that using

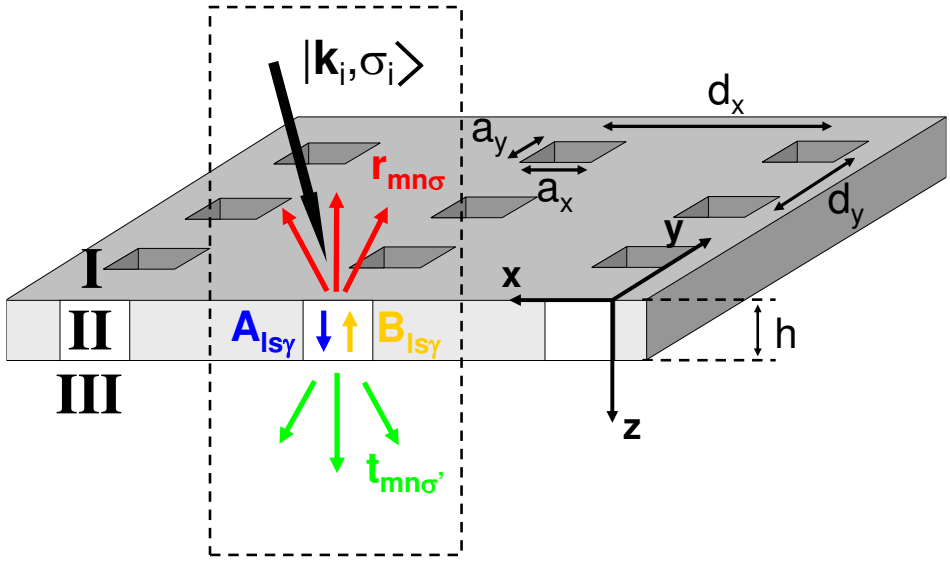

Figure 2.2.: Sketch of the modal expansion procedure for the case of hole arrays. The space is divided into three regions. In region I, EM fields are expressed as a sum of the impinging plane wave (black arrow) plus reflected waves (red arrows). In region II, the basis is comprised by waveguide modes propagating (blue) and counterpropagating (orange) along z-direction. Finally, EM fields in region III are expanded as a sum of diffracted waves (green arrows).

Dirac's notation can be written as $|\mathbf{E}_t\rangle$ and $|\mathbf{H}_t\rangle$.

By introducing the index σ, our ME method incorporates the classification of EM fields according to the polarization. Thus, fields with $E_z = 0$, which correspond to s-polarized light or transverse electric (TE) modes, are labelled with $\sigma = 1$, whereas $\sigma = 2$ is associated with fields with $H_z = 0$, p-polarized light or transverse magnetic (TM) modes.

The expansion of EM fields in TE and TM modes with a well defined propagation constant enables us to link magnetic and electric fields associated with free space and waveguide eigenmodes by means of modal admittances Y_{mode}, having $-\mathbf{u}_z \times |\mathbf{H}_t\rangle = Y_{\text{mode}}|\mathbf{E}_t\rangle$. The modal admittances are defined through the application of the curl Maxwell equations in the frequency domain, $\nabla \times \mathbf{E} = i\frac{\omega}{c}\mathbf{H}$, and $\nabla \times \mathbf{H} = -i\epsilon\frac{\omega}{c}\mathbf{E}$. Note that we assume a $e^{-i\omega t}$ temporal dependence of the EM fields.

Figure 2.2 shows a schematic view of the fields expansion procedure. The system is divided into three regions along the z-direction. Taking advantage of the periodic character of the structure within the xy plane, we can apply Bloch's theorem and solve Maxwell

equations only inside a unit cell of area $d_x \times d_y$, which contains only one rectangular hole (represented by the black dashed line in Fig. 2.2). Before describing in detail the expansion procedure, we provide analytical expressions for the eigenmodes associated with the different regions comprising the structure.

In regions I ($z < 0$) and III ($z > h$), EM fields can be expressed in terms of Bloch waves labelled with index σ, which indicates the polarization, and two integers, m and n, defining the transverse wave vector

$$\mathbf{k}_{mn} = \mathbf{k}_\mathrm{i} + m\frac{2\pi}{d_x}\mathbf{u}_x + n\frac{2\pi}{d_y}\mathbf{u}_y, \tag{2.1}$$

where $\mathbf{k}_\mathrm{i}$ is the transverse wave vector of the plane wave impinging from the top on the film (represented by a black arrow in Fig. 2.2). It is convenient to define the components along x and y-directions, $k_x^{(m)} = \mathbf{k}_\mathrm{i}\cdot\mathbf{u}_x + m\frac{2\pi}{d_x}$ and $k_y^{(n)} = \mathbf{k}_\mathrm{i}\cdot\mathbf{u}_y + n\frac{2\pi}{d_y}$, respectively. Therefore, the bivectors associated with s-polarized ($\sigma = 1$) Bloch waves in real space, $\mathbf{r} = x\mathbf{u}_x + y\mathbf{u}_y = (x\,y)$, can be written as

$$\langle \mathbf{r}|\mathbf{k}_{mn}, \sigma = 1\rangle = \frac{e^{i\mathbf{k}_{mn}\mathbf{r}}}{|\mathbf{k}_{mn}|\sqrt{d_x d_y}}\begin{pmatrix} -k_y^{(n)} \\ k_x^{(m)} \end{pmatrix}, \tag{2.2}$$

whereas for p-polarized ($\sigma = 2$) waves, we have

$$\langle \mathbf{r}|\mathbf{k}_{mn}, \sigma = 2\rangle = \frac{e^{i\mathbf{k}_{mn}\mathbf{r}}}{|\mathbf{k}_{mn}|\sqrt{d_x d_y}}\begin{pmatrix} k_x^{(m)} \\ k_y^{(n)} \end{pmatrix}. \tag{2.3}$$

Note that these Bloch waves are, by definition, orthonormal, i.e., they satisfy

$$\langle \mathbf{k}_{mn}, \sigma|\mathbf{k}_{m'n'}, \sigma'\rangle = \int d\mathbf{r}\langle \mathbf{k}_{mn}, \sigma|\mathbf{r}\rangle\langle \mathbf{r}|\mathbf{k}_{m'n'}, \sigma'\rangle = \delta_{mm'}\delta_{nn'}\delta_{\sigma\sigma'}, \tag{2.4}$$

where the integral ranges the unit cell area $d_x \times d_y$, and δ denotes the Kronecker's delta function.

Region II ($0 \leq z \leq h$) corresponds to the perforated metallic film. PEC approximation makes EM fields vanish within this region except inside the rectangular holes, where they can be expressed in terms of hole waveguide modes $|\mathbf{q}_{ls}, \gamma\rangle$. As Bloch waves, these modes are labelled with three indexes: the polarization γ, and l and s, which characterize the transverse wave vector

$$\mathbf{q}_{ls} = l\frac{\pi}{a_x}\mathbf{u}_x + s\frac{\pi}{a_y}\mathbf{u}_y. \tag{2.5}$$

The bivectors for TE modes ($\gamma = 1$) are given by

$$\langle \mathbf{r}|\mathbf{q}_{ls}, \gamma = 1\rangle = \begin{pmatrix} \frac{s\pi}{a_y|\mathbf{q}_{ls}|}\sqrt{\frac{2(2-\delta_{l0})}{a_x a_y}}\cos\frac{l\pi}{a_x}\left(x+\frac{a_x}{2}\right)\sin\frac{s\pi}{a_y}\left(y+\frac{a_y}{2}\right) \\ -\frac{l\pi}{a_x|\mathbf{q}_{ls}|}\sqrt{\frac{2(2-\delta_{s0})}{a_x a_y}}\sin\frac{l\pi}{a_x}\left(x+\frac{a_x}{2}\right)\cos\frac{s\pi}{a_y}\left(y+\frac{a_y}{2}\right) \end{pmatrix}, \tag{2.6}$$

and for TM ($\gamma = 2$) modes

$$\langle \mathbf{r}|\mathbf{q}_{ls}, \gamma = 2\rangle = \begin{pmatrix} \frac{l\pi}{a_x|\mathbf{q}_{ls}|}\sqrt{\frac{2(2-\delta_{l0})}{a_x a_y}}\cos\frac{l\pi}{a_x}\left(x+\frac{a_x}{2}\right)\sin\frac{s\pi}{a_y}\left(y+\frac{a_y}{2}\right) \\ \frac{s\pi}{a_y|\mathbf{q}_{ls}|}\sqrt{\frac{2(2-\delta_{s0})}{a_x a_y}}\sin\frac{l\pi}{a_x}\left(x+\frac{a_x}{2}\right)\cos\frac{s\pi}{a_y}\left(y+\frac{a_y}{2}\right) \end{pmatrix}. \tag{2.7}$$

These waveguide modes are also defined as orthonormal, having

$$\langle \mathbf{q}_{ls}, \gamma|\mathbf{q}_{l's'}, \gamma'\rangle = \int d\mathbf{r}\langle \mathbf{q}_{ls}, \gamma|\mathbf{r}\rangle\langle \mathbf{r}|\mathbf{q}_{l's'}, \gamma'\rangle = \delta_{ll'}\delta_{ss'}\delta_{\gamma\gamma'}, \tag{2.8}$$

where now the integral ranges only the hole area, $a_x \times a_y$. Wavefunctions for TE and TM waveguide modes for circular holes are provided in Appendix B.

Once we have defined a complete set of wavefunctions for the three regions forming the structure, we describe the mode matching procedure. EM fields in region I can be expressed as the incident plane wave $|\mathbf{k}_\mathrm{i}, \sigma_\mathrm{i}\rangle$ plus a sum of reflected Bloch waves $|\mathbf{k}_{mn}, \sigma\rangle$ (red arrows in Fig. 2.2) weighted with their corresponding reflection coefficients, $r_{mn\sigma}$,

$$|\mathbf{E}_\mathrm{t}\rangle = |\mathbf{k}_\mathrm{i}, \sigma_\mathrm{i}\rangle e^{ik_z^{(\mathrm{i})}z} + \sum_{m\,n\,\sigma} r_{mn\sigma}|\mathbf{k}_{mn}, \sigma\rangle e^{-ik_z^{(mn)}z}, \tag{2.9}$$

$$-\mathbf{u}_z \times |\mathbf{H}_\mathrm{t}\rangle = Y^I_{\mathbf{k}_\mathrm{i}\sigma_\mathrm{i}}|\mathbf{k}_\mathrm{i}, \sigma_\mathrm{i}\rangle e^{ik_z^{(\mathrm{i})}z} - \sum_{m\,n\,\sigma} Y^I_{\mathbf{k}_{mn}\sigma}\, r_{mn\sigma}|\mathbf{k}_{mn}, \sigma\rangle e^{-ik_z^{(mn)}z}. \tag{2.10}$$

The longitudinal component of the wave vector associated with the mn^{th} reflected Bloch wave is $k_z^{(mn)} = \sqrt{k_0^2 - |\mathbf{k}_{mn}|^2}$, where $k_0 = \frac{\omega}{c} = \frac{2\pi}{\lambda}$ denotes the wave vector modulus. Finally, the mode admittances are $Y^I_{\mathbf{k}_{mn}\sigma=1} = k_z^{(mn)}/k_0$ for TE modes, and $Y^I_{\mathbf{k}_{mn}\sigma=2} = k_0/k_z^{(mn)}$ for TM modes.

In region II, EM fields can be expanded into hole waveguide modes propagating and counterpropagating (blue and orange arrows in Fig. 2.2) along the z-direction

$$|\mathbf{E}_\mathrm{t}\rangle = \sum_{l\,s\,\gamma}[A_{ls\gamma}e^{iq_z^{(ls)}z} + B_{ls\gamma}e^{-iq_z^{(ls)}z}]|\mathbf{q}_{ls}, \gamma\rangle, \tag{2.11}$$

$$-\mathbf{u}_z \times |\mathbf{H}_\mathrm{t}\rangle = \sum_{l\,s\,\gamma} Y^{II}_{ls\gamma}[A_{ls\gamma}e^{iq_z^{(ls)}z} - B_{ls\gamma}e^{-iq_z^{(ls)}z}]|\mathbf{q}_{ls}, \gamma\rangle, \tag{2.12}$$

where $A_{ls\gamma}$ and $B_{ls\gamma}$ are the expansion coefficients. The wave vector component along z-direction is defined as $q_z^{(ls)} = \sqrt{k_0^2 - |\mathbf{q}_{ls}|}$, and $Y^{II}_{ls\gamma=1} = q_z^{(ls)}/k_0$ and $Y^{II}_{ls\gamma=2} = k_0/q_z^{(ls)}$ are the admittances for TE and TM modes, respectively.

In region III, EM fields are written as a linear combination of diffracted Bloch waves (green arrows in Fig. 2.2), with transmission coefficients $t_{mn\sigma}$. We have

$$|\mathbf{E}_\mathrm{t}\rangle = \sum_{m\,n\,\sigma} t_{mn\sigma}|\mathbf{k}_{mn}, \sigma\rangle e^{ik_z^{(mn)}z}, \tag{2.13}$$

$$-\mathbf{u}_z \times |\mathbf{H}_\mathrm{t}\rangle = \sum_{m\,n\,\sigma} Y^{III}_{\mathbf{k}_{mn}\sigma}\, t_{mn\sigma}|\mathbf{k}_{mn}, \sigma\rangle e^{ik_z^{(mn)}z}, \tag{2.14}$$

where $k_z^{(mn)}$ has the same form as in region I and $Y^{III}_{\mathbf{k}_{mn}\sigma} = Y^{I}_{\mathbf{k}_{mn}\sigma}$.

The unknown expansion coefficients $r_{mn\sigma}$, $A_{ls\gamma}$, $B_{ls\gamma}$ and $t_{mn\sigma'}$ are calculated by imposing the appropriate continuity conditions to the EM fields at the two interfaces of the system ($z = 0$ and $z = h$) [90]. The continuity equations for $|\mathbf{E}_t\rangle$ and $|\mathbf{H}_t\rangle$ at the interface between regions I and II ($z = 0$) read

$$|\mathbf{k}_i, \sigma_i\rangle + \sum_{m\,n\,\sigma} r_{mn\sigma}|\mathbf{k}_{mn}, \sigma\rangle = \sum_{l\,s\,\gamma}[A_{ls\gamma} + B_{ls\gamma}]|\mathbf{q}_{ls}, \gamma\rangle, \tag{2.15}$$

$$Y^{I}_{\mathbf{k}_i\sigma_i}|\mathbf{k}_i, \sigma_i\rangle - \sum_{m\,n\,\sigma} Y^{I}_{\mathbf{k}_{mn}\sigma}\, r_{mn\sigma}|\mathbf{k}_{mn}, \sigma\rangle = \sum_{l\,s\,\gamma} Y^{II}_{ls\gamma}[A_{ls\gamma} - B_{ls\gamma}]|\mathbf{q}_{ls}, \gamma\rangle, \tag{2.16}$$

whereas for the interface II-III ($z = h$), we have

$$\sum_{l\,s\,\gamma}[A_{ls\gamma}e^{iq_z^{(ls)}h} + B_{ls\gamma}e^{-iq_z^{(ls)}h}]|\mathbf{q}_{ls}, \gamma\rangle = \sum_{m\,n\,\sigma} t_{mn\sigma}|\mathbf{k}_{mn}, \sigma\rangle e^{ik_z^{(mn)}h}, \tag{2.17}$$

$$\sum_{l\,s\,\gamma} Y^{II}_{ls\gamma}[A_{ls\gamma}e^{iq_z^{(ls)}h} - B_{ls\gamma}e^{-iq_z^{(ls)}h}]|\mathbf{q}_{ls}, \gamma\rangle = \sum_{m\,n\,\sigma} Y^{I}_{\mathbf{k}_{mn}\sigma}\, t_{mn\sigma}|\mathbf{k}_{mn}, \sigma\rangle e^{ik_z^{(mn)}h}. \tag{2.18}$$

Equations (2.15) and (2.17) hold within the entire unit cell, as $\mathbf{E}_t$ is continuous in the whole space. However, Eqs. (2.16) and (2.18), which are linked to $\mathbf{H}_t$, are fulfilled only within the hole area. The use of PEC boundary conditions in our model leads to the appearance of discontinuities in the parallel components of the magnetic field at the structure interfaces (see Sec. 2.2.5). Their origin resides in the formation of induced surface charge densities and currents at the film sides. For fundamental and technical reasons, it is convenient to project the continuity equations associated with $\mathbf{E}_t$ over Bloch waves $\langle\mathbf{k}_{mn}, \sigma|$ (different from zero within the entire unit cell) and equations for $\mathbf{H}_t$ over hole waveguide modes $\langle\mathbf{q}_{ls}, \gamma|$ (which vanish outside the apertures). Hence, the matching equations at the interface between regions I and II now read

$$\delta_{m0}\,\delta_{n0}\,\delta_{\sigma\sigma_i} + r_{mn\sigma} = \sum_{l\,s\,\gamma}[A_{ls\gamma} + B_{ls\gamma}]S^{ls\gamma}_{mn\sigma}, \tag{2.19}$$

$$Y^{I}_{\mathbf{k}_i\sigma_i}(S^{ls\gamma}_{00\sigma_i})^* - \sum_{mn\sigma} Y^{I}_{\mathbf{k}_{mn}\sigma}\, r_{mn\sigma}(S^{ls\gamma}_{mn\sigma})^* = Y^{II}_{ls\gamma}[A_{ls\gamma} - B_{ls\gamma}], \tag{2.20}$$

where we have used orthonormality relations (2.4) and (2.8), and we have defined the overlapping integrals

$$S^{ls\gamma}_{mn\sigma} = \langle\mathbf{k}_{mn}, \sigma|\mathbf{q}_{ls}, \gamma\rangle = \int d\mathbf{r}\langle\mathbf{k}_{mn}, \sigma|\mathbf{r}\rangle\langle\mathbf{r}|\mathbf{q}_{ls}, \gamma\rangle. \tag{2.21}$$

In Appendix A, general expressions for these integrals are presented. Additionally, overlapping integrals between Bloch waves and circular hole waveguide modes are shown in Appendix B.

The continuity equations for the transverse EM fields at the interface II-III have the form

$$\sum_{l\,s\,\gamma}[A_{ls\gamma}e^{iq_z^{(ls)}h}+B_{ls\gamma}e^{-iq_z^{(ls)}h}]S_{mn\sigma}^{ls\gamma} = t_{mn\sigma}e^{ik_z^{(mn)}h}, \tag{2.22}$$

$$Y_{ls\gamma}^{II}[A_{ls\gamma}e^{iq_z^{(ls)}h}-B_{ls\gamma}e^{-iq_z^{(ls)}h}] = \sum_{m\,n\,\sigma}Y_{\mathbf{k}_{mn}\sigma}^{I}\,t_{mn\sigma}(S_{mn\sigma}^{ls\gamma})^*e^{ik_z^{(mn)}h}. \tag{2.23}$$

It is convenient to write continuity equations in a compact form. By combining Eqs. (2.19) and (2.20), we can write the continuity of EM fields at $z=0$ in terms of only the the waveguide mode coefficients, $A_{ls\gamma}$ and $B_{ls\gamma}$, as

$$2Y_{\mathbf{k}_i\sigma_i}^{I}(S_{00\sigma_i}^{ls\gamma})^*-\sum_{l'\,s'\,\gamma'}\Big[\sum_{m\,n\,\sigma}Y_{\mathbf{k}_{mn}\sigma}^{I}(S_{mn\sigma}^{ls\gamma})^*S_{mn\sigma}^{l's'\gamma'}\Big][A_{l's'\gamma'}+B_{l's'\gamma'}] = \\ = Y_{ls\gamma}^{II}[A_{ls\gamma}-B_{ls\gamma}]. \tag{2.24}$$

Similarly, from Eqs. (2.22) and (2.23), fields continuity at $z=h$ can be expressed as

$$\sum_{l'\,s'\,\gamma'}\Big[\sum_{m\,n\,\sigma}Y_{\mathbf{k}_{mn}\sigma}^{I}(S_{mn\sigma}^{ls\gamma})^*S_{mn\sigma}^{l's'\gamma'}\Big][A_{l's'\gamma'}e^{iq_z^{(l's')}h}+B_{l's'\gamma'}e^{-iq_z^{(l's')}h}] = \\ = Y_{ls\gamma}^{II}[A_{ls\gamma}e^{iq_z^{(ls)}h}-B_{ls\gamma}e^{-iq_z^{(ls)}h}]. \tag{2.25}$$

Note that for every $|\mathbf{q}_{ls},\gamma\rangle$ we have included in the expansion of the EM fields inside region II we have two continuity equations, one for each system interface. This is one of the most relevant characteristics of our formalism, that the number of linear equations to solve in order to know the expansion coefficients is equal to twice the number of waveguide modes considered inside the apertures. Below, we will see why this fact makes this theoretical framework very suitable for analyzing the transmission properties of apertures smaller than the wavelength.

We define the quantities

$$E_{ls\gamma} = A_{ls\gamma}+B_{ls\gamma}, \tag{2.26}$$

$$E'_{ls\gamma} = -[A_{ls\gamma}e^{iq_z^{(ls)}h}+B_{ls\gamma}e^{-iq_z^{(ls)}h}], \tag{2.27}$$

which are related to the amplitudes of the transverse electric field linked to the waveguide mode $|\mathbf{q}_{ls},\gamma\rangle$ at the input ($E_{ls\gamma}$) and output ($E'_{ls\gamma}$) sides of the holes. Thus, we can rewrite Eqs. (2.24) and (2.25) in their final form

$$\begin{aligned}(G_{ls\gamma}^{ls\gamma}-\epsilon_{ls\gamma})E_{ls\gamma}+\textstyle\sum_{(l's'\gamma')\neq(ls\gamma)}G_{ls\gamma}^{l's'\gamma'}E_{l's'\gamma'}-G_{ls\gamma}^{V}E'_{ls\gamma} &= I_{ls\gamma},\\ (G_{ls\gamma}^{ls\gamma}-\epsilon_{ls\gamma})E'_{ls\gamma}+\textstyle\sum_{(l's'\gamma')\neq(ls\gamma)}G_{ls\gamma}^{l's'\gamma'}E'_{l's'\gamma'}-G_{ls\gamma}^{V}E_{ls\gamma} &= 0.\end{aligned} \tag{2.28}$$

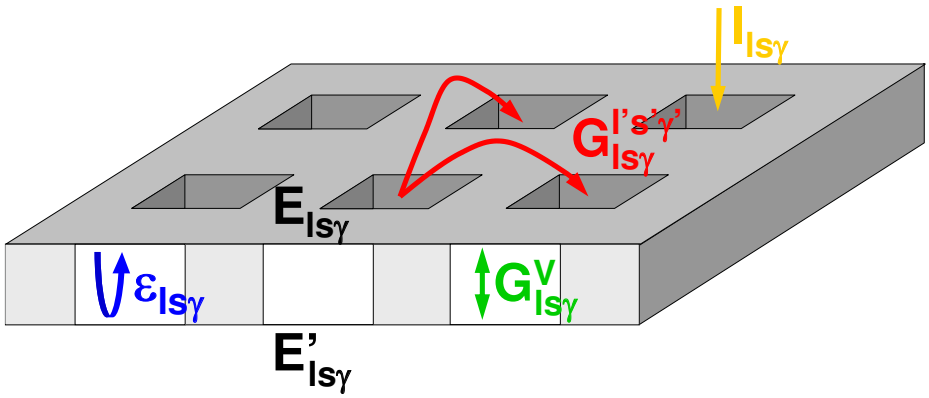

Figure 2.3.: Schematic representation of the terms in Eqs. (2.28).

This set of linear equations describes the behavior of the EM fields at the illuminated [upper equation in (2.28)] and non-illuminated [lower equation in (2.28)] sides of the perforated film. It will appear throughout this thesis when applying the ME technique to the study of different designs. Although the specific form of the various terms appearing in Eqs. (2.28) depends on the system under study, it is possible to give them a simple physical interpretation, valid for all cases. An schematic picture of the role played by all the terms in Eqs. (2.28) is shown in Figure 2.3.

The term $I_{ls\gamma}$ is only present in the upper equation of (2.28), which, as stated above, is linked to the input face of the film. It has the form

$$I_{ls\gamma} = 2iY^{I}_{\mathbf{k}_i\sigma_i}(S^{ls\gamma}_{00\sigma_i})^{*}. \tag{2.29}$$

Notice that it is proportional to the overlapping integral between the incident plane wave and the holes waveguide modes. Therefore, we can relate it to the direct initial illumination over the holes.

There are two terms involving only the waveguide mode $|\mathbf{q}_{ls}, \gamma\rangle$

$$\epsilon_{ls\gamma} = Y^{II}_{ls\gamma}\cot(q_z^{(ls)}h), \tag{2.30}$$

$$G^{V}_{ls\gamma} = Y^{II}_{ls\gamma}\frac{1}{\sin(q_z^{(ls)}h)}. \tag{2.31}$$

The difference between these two terms can be easily understood by looking at Eqs. (2.28). $\epsilon_{ls\gamma}$ describes how EM fields in the illuminated (non-illuminated) face of the film modify the electric field amplitudes at the input (output) side of the holes, $E_{ls\gamma}$ ($E'_{ls\gamma}$). On

the other hand, $G^V_{ls\gamma}$ takes into account the effect of EM fields at each surface of the film on the amplitudes at the other side of the holes. Thus, we can link $\epsilon_{ls\gamma}$ to the bouncing back and forth of the EM fields inside the apertures, and the term $G^V_{ls\gamma}$ to the coupling of EM fields at the two sides of the film through the holes.

Finally, the term

$$G^{l's'\gamma'}_{ls\gamma} = i \sum_{m\,n\,\sigma} Y^I_{\mathbf{k}_{mn}\sigma} (S^{ls\gamma}_{mn\sigma})^* S^{l's'\gamma'}_{mn\sigma}, \tag{2.32}$$

reflects the radiation that the waveguide mode $|\mathbf{q}_{l's'}, \gamma'\rangle$ emits into diffracted waves, $|\mathbf{k}_{mn}, \sigma\rangle$, which is finally collected by the mode $|\mathbf{q}_{ls}, \gamma\rangle$. Note that $G^{l's'\gamma'}_{ls\gamma}$ diverges whenever one of the diffraction modes in the sum in Eq. (2.32) becomes grazing. This occurs whenever $\mathbf{k_{mn}} = \mathbf{0}$ for any m and n, which makes $Y^I_{\mathbf{k}_{mn}\sigma=2}$ have a singularity. Therefore, the term $G^{l's'\gamma'}_{ls\gamma}$ governs the behavior of $E'_{ls\gamma}$ and $E'_{ls\gamma}$ when diffracted waves are tangent to the film surfaces. We will see in chapter 4, that this behavior of $G^{l's'\gamma'}_{ls\gamma}$ can be related to the appearance of surface EM modes on the sides of the perforated film.

Once Eqs. (2.28) are solved, the set of modal amplitudes $E_{ls\gamma}$, $E'_{ls\gamma}$ is known, and the EM fields in all the space can be constructed. Additionally, the transmissivity of the film (ratio between the transmitted and the incident EM power, $\wp_t/\wp_i$) can be also calculated. The EM energy carried by the incoming plane wave is given by the integral of the z component of the Poynting vector within the unit cell,

$$\begin{aligned} \wp_i &= \frac{1}{2}\int d\mathbf{r}\, \mathrm{Re}\{\langle \mathbf{r}|\mathbf{E}^{(i)}_t\rangle \times \langle \mathbf{r}|\mathbf{H}^{(i)}_t\rangle^*\} = \\ &= \frac{1}{2}\int d\mathbf{r}\, \mathrm{Re}\{\langle \mathbf{r}|\mathbf{E}^{(i)}_t\rangle \cdot (-\mathbf{u}_z \times \langle \mathbf{r}|\mathbf{H}^{(i)}_t\rangle)^*\} = \frac{1}{2}(Y^I_{\mathbf{k}_i\sigma_i})^*. \end{aligned} \tag{2.33}$$

The EM power transmitted through the structure can be obtained in two different ways:

1. Through the holes. By integrating the z-component of the Poynting vector associated to EM fields within region II (see Fig. 2.2), the EM energy flowing through the holes in the positive z-direction can be expressed as

$$\wp^{(1)}_t = \frac{1}{2}\mathrm{Re}\{\sum_{ls\gamma} Y^{II}_{ls\gamma}[|A_{ls\gamma}|^2 - |B_{ls\gamma}|^2]\} = \frac{1}{2}\mathrm{Im}\{\sum_{ls\gamma} G^V_{ls\gamma} E_{ls\gamma} E'^*_{ls\gamma}\}, \tag{2.34}$$

   where we have used relations (2.26) and (2.27). Note that real and imaginary part functions, Re and Im, ensure that only waveguide modes which are propagating along z-direction ($|\mathbf{q}_{ls}| < k_0$) contribute to the summation in Eq. (2.34).

2. In the far field. The total energy exiting from the structure can be written in terms of the transmission coefficients in region III as

$$\wp^{(2)}_t = \frac{1}{2}\mathrm{Re}\{\sum_{mn\sigma} Y^I_{\mathbf{k}_{mn}\sigma}|t_{mn\sigma}|^2\} = \frac{1}{2}\mathrm{Im}\{\sum_{ls\gamma\, l's'\gamma'} G^{l's'\gamma'}_{ls\gamma} E'_{ls\gamma} E'^*_{l's'\gamma'}\}, \tag{2.35}$$

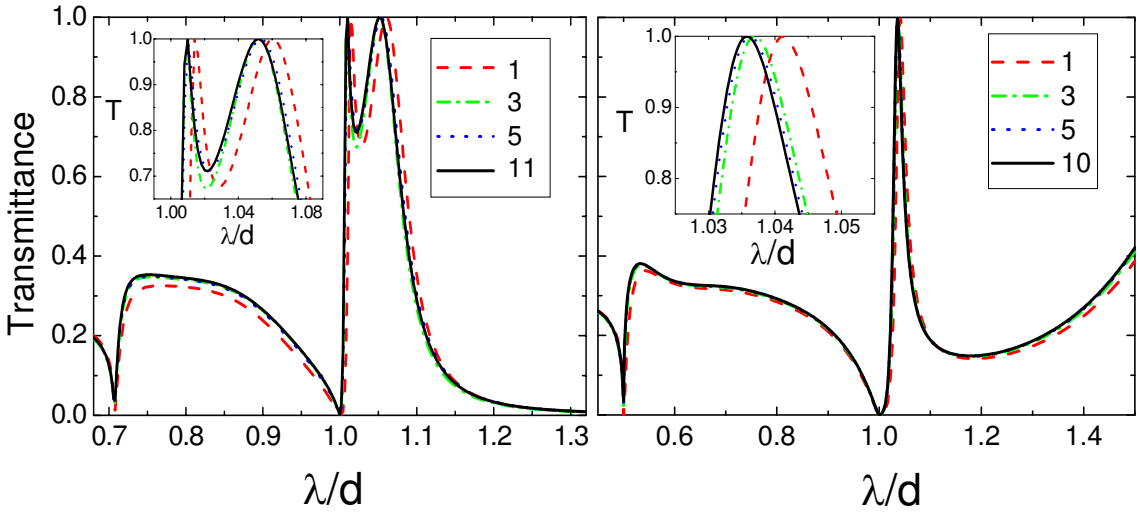

Figure 2.4.: Dependence of the transmittance on the number of waveguide modes involved in the expansion of EM fields inside the apertures. Left panel: square array ($d_x = d_y = d$) of square holes ($a_x = a_y = 0.5d$) perforated in a PEC film of width $h = 0.4d$. Right panel: slit array under p-polarization with $a = 0.3d$ and $h = 0.7d$. In both panels, the legend indicates the number of waveguide modes considered inside the apertures.

where the dependence of $t_{mn\sigma}$ with the modal amplitudes $E'_{ls\gamma}$ is given by Eq. (2.22).

The use of PEC approximation in our model translates into that the transmittances obtained from $\wp_t^{(1)}$ and $\wp_t^{(2)}$ are equal. However, when the dielectric properties of the metal film are taken into account (see Sec. 2.2.5), absorption effects arise in the model, and these two magnitudes become distinct. Therefore, in this case, only $\wp_t^{(2)}$ can be used to calculate the transmissivity of the structure in the far-field.

The ME technique presented above is a very suitable approach for analyzing the scattering of light with holes much smaller than the wavelength. In this geometric limit, the EM fields inside the film are accurately described by considering only the lowest waveguide modes in the summation of Eqs. (2.11) and (2.12), since they are the least evanescent modes and hence they control the flux of EM energy through the film. As we have shown above, the size of the set of continuity equations is equal to twice the number of waveguide modes considered. Therefore, for small enough holes, our ME formalism is quasi-analytic, which allows us to study the EM phenomena occurring in these complex structures with very low computational effort. The fast convergency of ME calculations with the number of modes inside the apertures is shown in Fig. 2.4. The left panel of the

figure renders the transmission spectrum for an square array ($d_x = d_y = d$) of square holes ($a_x = a_y = 0.5d$) perforated in a film of width $h = 0.4d$. The transmissivity of the structure displays the resonant features characteristic of the EOT phenomenon [39]. It is remarkable that the spectrum calculated considering only the two lowest waveguide modes (red dashed line) is already almost converged.

Slit arrays

Once we have presented our ME formalism for the general case of a periodic 2D hole array, we describe here how it can be modified to treat 1D slit arrangements [see schematic picture in Fig. 2.1 (b)]. These systems display translational symmetry along the direction parallel to the slits, which we have labelled arbitrarily as y-direction. If the illumination plane is normal to the slits i.e., $\mathbf{k}_{\rm i}$ belongs to the xz-plane, EM fields do not depend on y-coordinate, and the transverse wave vectors associated to the EM modes at the different regions of the structure must be parallel to the x-direction. Thus, the wave vector associated with diffracted Bloch waves in 1D systems have the form $\mathbf{k}_m = k_m \mathbf{u}_x = (k_i + m\frac{2\pi}{d})\mathbf{u}_x$, whereas for slit waveguide modes, they are $\mathbf{q}_l = q_l \mathbf{u}_x = l\frac{\pi}{a}\mathbf{u}_x$. Note that, for simplicity, we have done $d_x = d$ and $a_x = a$.

The Bloch waves in free space, into which EM fields are expanded above and below the film, read now

$$\langle x|k_m, \sigma = 1\rangle = \frac{e^{ik_m x}}{\sqrt{d}} \begin{pmatrix} 0 \\ 1 \end{pmatrix}, \langle x|k_m, \sigma = 2\rangle = \frac{e^{ik_m x}}{\sqrt{d}} \begin{pmatrix} 1 \\ 0 \end{pmatrix}, \tag{2.36}$$

and the slits waveguide modes are given by

$$\begin{aligned} \langle x|q_l, \gamma = 1\rangle &= \sqrt{\frac{2}{a}} \sin \frac{l\pi}{a}\left(x + \frac{a}{2}\right) \begin{pmatrix} 0 \\ 1 \end{pmatrix}, \\ \langle x|q_l, \gamma = 2\rangle &= \sqrt{\frac{2-\delta_{l0}}{a}} \cos \frac{l\pi}{a}\left(x + \frac{a}{2}\right) \begin{pmatrix} 1 \\ 0 \end{pmatrix}. \end{aligned} \tag{2.37}$$

In slit arrays, the overlap between Bloch waves with $\sigma = 1$ ($\sigma = 2$) and waveguide modes having $\gamma = 2$ ($\gamma = 1$) is zero. This reproduces a well-known property of EM fields which do not depend on one of the spatial coordinate, that the two light polarizations are decoupled. This fact translates into that in our ME formalism, s and p-polarized waves are treated independently. This means that only modes having the same polarization as the incoming light are involved in the fields expansion. Hence, as $\sigma_{\rm i} = \sigma = \gamma$, we can label the polarization of EM fields in all the space with only one index, γ. Following

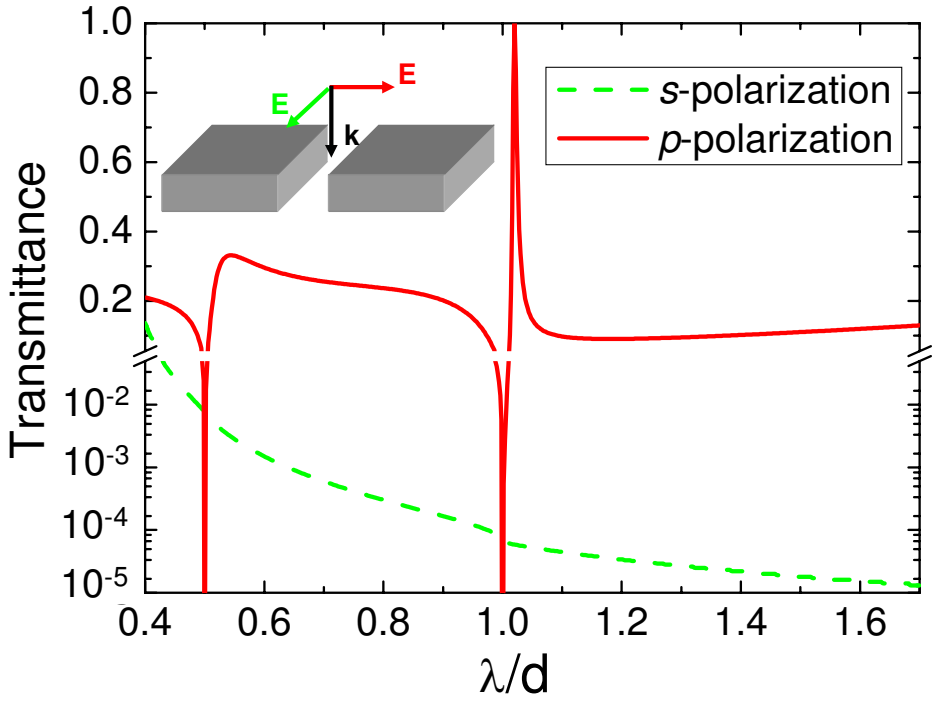

Figure 2.5.: Transmission spectra for a periodic array of slits under s (green line) and p-polarized (red line) illumination. The geometrical parameters of the structure are the slits width, $a = 0.2d$, and the film thickness, $h = 0.16d$.

the same matching procedure as for the 2D case, we end up with a set of continuity equations of the same form as Eqs. (2.28)

$$\begin{aligned}(G_{ll}^{\gamma} - \epsilon_l^{\gamma})E_l^{\gamma} + \textstyle\sum_{l'\neq l} G_{ll'}^{\gamma} E_{l'}^{\gamma} - G_l^{V\gamma} E_l^{\prime\gamma} = I_l^{\gamma},\\ (G_{ll}^{\gamma} - \epsilon_l^{\gamma})E_l^{\prime\gamma} + \textstyle\sum_{l'\neq l} G_{ll'}^{\gamma} E_{l'}^{\prime\gamma} - G_l^{V\gamma} E_l^{\gamma} = 0.\end{aligned} \tag{2.38}$$

All the terms in Eqs. (2.38) have the same form as their 2D counterparts by replacing the longitudinal wave vectors $k_z^{(mn)}$ and $q_z^{(ls)}$, by $k_z^{(m)} = \sqrt{k_0^2 - k_m^2}$ and $q_z^{(l)} = \sqrt{k_0^2 - q_l^2}$, respectively. Thus, we have

$$I_l^{\gamma} = 2iY_{k_i}^{I\gamma}(\sigma_{0l}^{\gamma})^*, \tag{2.39}$$

$$\epsilon_l^{\gamma} = Y_l^{II\gamma}\cot(q_z^{(l)}h), \tag{2.40}$$

$$G_l^{V\gamma} = Y_l^{II\gamma}\frac{1}{\sin(q_z^{(l)}h)}, \tag{2.41}$$

$$G_{ll'}^{\gamma} = i\sum_m Y_{k_m}^{I\gamma}(\sigma_{ml}^{\gamma})^*\sigma_{ml'}^{\gamma}, \tag{2.42}$$

where we have introduced the 1D overlapping integrals (see Appendix A)

$$\sigma_{ml}^{\gamma} = \langle k_m, \gamma | q_l, \gamma \rangle = \int dx \langle k_m, \gamma | x \rangle \langle x | q_l, \gamma \rangle = \langle q_l, \gamma | k_m, \gamma \rangle^*. \tag{2.43}$$

Although, formally, both light polarizations are described equally within our ME framework, the underlying physics is very different. This fact is reflected by the distinct behavior of the term $G_{ll'}^{\gamma}$. For s-polarized light, the inclusion of a grazing diffracted wave ($k_z^{(m)} = 0$) in the sum of Eq. (2.42) makes the corresponding admittance $Y_{k_m}^{I\gamma=1} = k_z^{(m)}/k_0$ vanish. However, for p-polarization, $Y_{k_m}^{I\gamma=2} = k_0/k_z^{(m)}$ diverges for diffracted waves tangent to the metallic film. We will see in chapter 4 that this singularity in $G_{ll'}^{\gamma}$ is a fingerprint of the appearance of bound modes in the system. The strong dependence of the transmission properties on the polarization of the incoming light is illustrated in Fig. 2.5, which shows the transmissivity of a periodic array of slits with $a = 0.20d$ and $h = 0.16d$. For p-polarization, the spectrum shows the resonant features characteristic of the extraordinary transmission phenomenon [39]. However, for s-polarized light, the transmittance is much lower and does not develop any resonance, decaying monotonously within the spectral range considered. In the right panel of Fig. 2.4, the dependence of the ME calculations with the number of slit waveguide modes is analyzed. The figure shows the transmission spectrum for an array of slits of width $a = 0.3d$ and depth $h = 0.7d$. Note that considering only the lowest waveguide mode inside the slits results in a very good approximation for slits much smaller than the array period. This fact makes our formalism very appropriate for the study of the transmission properties of these systems.

2.2.2. Finite systems

Up to this point, we have applied our ME formalism to the analysis of infinitely periodic arrays of apertures. In this section, we show how it can be modified in order to treat structures which are not infinite [93–95], such as finitely periodic, quasiperiodic or disordered aperture arrangements. In what follows, we describe the two steps in which our formalism is transformed, schematically depicted in Figure 2.6. We focus on the case of 2D holes and, at the end of the section, we provide details for the case of 1D apertures.

First, instead of expanding EM fields within a unit cell including only one hole, as shown in Fig. 2.2, we consider a supercell of area $L_x \times L_y$ containing the finite hole arrangement that we want to analyze. Thus, the structure that we are describing is comprised by a 2D periodic array of these supercells, as shown in panel (a) of Fig. 2.6. Above (region I) and below (region III) the perforated film, the expressions describing the EM fields have the same form as in Section 2.2.1, where now, the periods d_x and d_y must be replaced by the supercell dimensions L_x and L_y, respectively. However, inside the me-

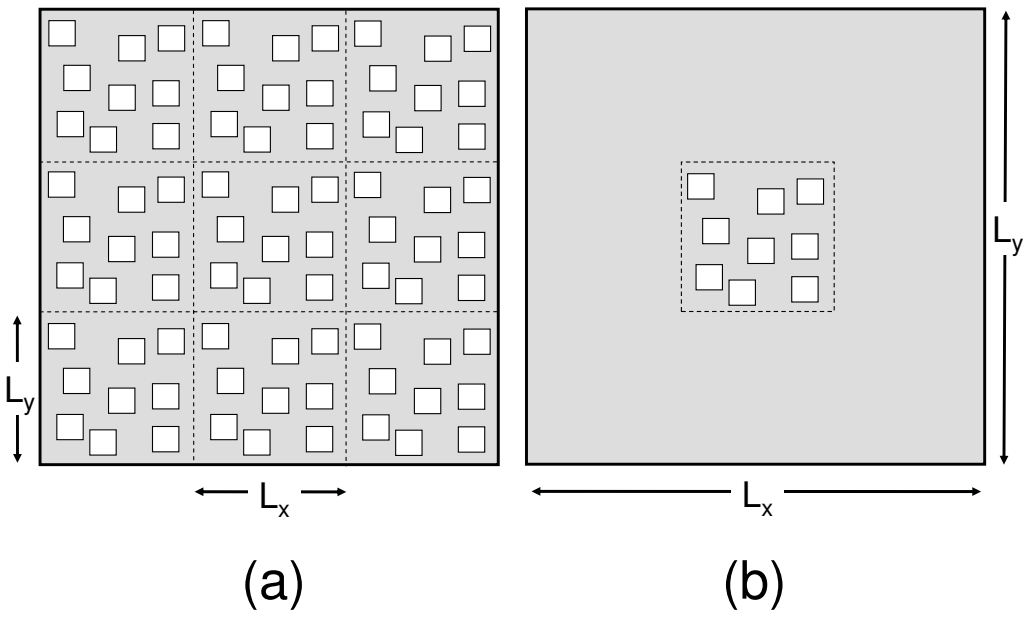

Figure 2.6.: Modifications performed in the ME formalism in order to treat finite systems. Panel (a): Definition of a supercell containing several apertures. Panel (b): Cell dimensions, L_x and L_y, are taken to infinity.

tallic film (region II), the EM fields are now written in terms of the waveguide modes corresponding to the different holes inside the supercell, having

$$|\mathbf{E}_t\rangle = \sum_{\alpha}[A_\alpha e^{iq_z^{(\alpha)}z} + B_\alpha e^{-iq_z^{(\alpha)}z}]|\alpha\rangle, \tag{2.44}$$

$$-\mathbf{u}_z \times |\mathbf{H}_t\rangle = \sum_{\alpha} Y_\alpha^{II}[A_\alpha e^{iq_z^{(\alpha)}z} - B_\alpha e^{-iq_z^{(\alpha)}z}]|\alpha\rangle, \tag{2.45}$$

where, in order to simplify the notation, we have introduced the compact index α, which characterizes not only the position of the holes inside the supercell but also the order and polarization of the waveguide modes inside each aperture.

As a result of the mode matching process at the system interfaces, we end up with a general version of the continuity equations in terms of compact indexes α and β, which reads

$$\begin{aligned}(G_{\alpha\alpha} - \epsilon_\alpha)E_\alpha + \textstyle\sum_{\beta\neq\alpha} G_{\alpha\beta}E_\beta - G_\beta^V E'_\alpha = I_\alpha,\\ (G_\alpha - \epsilon_\alpha)E'_\alpha + \textstyle\sum_{\beta\neq\alpha} G_{\alpha\beta}E'_\beta - G_\alpha^V E_\alpha = 0,\end{aligned} \tag{2.46}$$

where the definition of the different terms is the same as in the case of periodic arrangements. As we demonstrated in Section 2.2.1, all these terms refer to only one waveguide mode, except the G term, which takes into account the interaction of EM fields associated with different waveguide modes. As the supercell that we are considering now contains several apertures, $G_{\alpha\beta}$ in Eq. (2.46) reflects the EM coupling between waveguide modes which can belong to the same or different apertures. Using the definition of the overlapping integrals introduced in Eq. (2.21), this term can be written as

$$G_{\alpha\beta} = i \sum_{m\,n\,\sigma} Y^I_{\mathbf{k}_{mn}\sigma} \langle \alpha | \mathbf{k}_{mn}, \sigma \rangle \langle \mathbf{k}_{mn}, \sigma | \beta \rangle, \tag{2.47}$$

where now $\mathbf{k}_{mn} = \mathbf{k}_\mathrm{i} + m\frac{2\pi}{L_x}\mathbf{u}_x + n\frac{2\pi}{L_y}\mathbf{u}_y$. Hence, by writing $G_{\alpha\beta} = \langle \alpha | \hat{G} | \beta \rangle$, we can define the operator

$$\hat{G} = i \sum_{m\,n\,\sigma} Y^I_{\mathbf{k}_{mn}\sigma} |\mathbf{k}_{mn}, \sigma\rangle \langle \mathbf{k}_{mn}, \sigma|, \tag{2.48}$$

which couples EM fields corresponding to different waveguide modes, $|\alpha\rangle$, through all the Bloch waves, $|\mathbf{k}_{mn}, \sigma\rangle$.

The second step consists of taking the limit L_x, $L_y \to \infty$ in the continuity equations (2.46), keeping the holes positions inside the supercell. The geometric interpretation of this limit is sketched in panel (b) of Fig. 2.6. The supercell containing the holes has become artificial, as no periodicity is present in the structure. This modification does not affect all the terms in Eqs. (2.46) that refer to only one waveguide mode, whereas the transformation of the $G_{\alpha\beta}$ term occurs through the operator $\hat{G}$. Taking the limit L_x, $L_y \to \infty$ translates into that discrete diffraction orders cannot be defined and the spectrum of Bloch waves becomes continuous. Thus, the discrete sum in Eq. (2.48) transforms into an integral, resulting in a new formal expression for $\hat{G}$, which now reads

$$\hat{G} = \frac{i}{4\pi^2} \int\int d\mathbf{k} \sum_\sigma Y_\sigma(k)\, |\mathbf{k}, \sigma\rangle \langle \mathbf{k}, \sigma|, \tag{2.49}$$

where $\mathbf{k} = k_x \mathbf{u}_x + k_y \mathbf{u}_y$ is the transverse wave vector, $k = |\mathbf{k}|$, and the admittances are $Y_{\sigma=1}(k) = \sqrt{k_0^2 - k^2}/k_0$, for s-polarization, and $Y_{\sigma=2}(k) = k_0/\sqrt{k_0^2 - k^2}$, for p-polarization. Plane waves $|\mathbf{k}, \sigma\rangle$ are given by

$$\langle \mathbf{r} | \mathbf{k}, \sigma = 1 \rangle = \frac{e^{i\mathbf{k}\mathbf{r}}}{|\mathbf{k}|} \begin{pmatrix} -k_y \\ k_x \end{pmatrix}, \; \langle \mathbf{r} | \mathbf{k}, \sigma = 2 \rangle = \frac{e^{i\mathbf{k}\mathbf{r}}}{|\mathbf{k}|} \begin{pmatrix} k_x \\ k_y \end{pmatrix}. \tag{2.50}$$

Operator $\hat{G}$ can be projected into the position basis, $|\mathbf{r}\rangle$, having

$$\hat{G}(\mathbf{r}, \mathbf{r}') = \langle \mathbf{r} | \hat{G} | \mathbf{r}' \rangle = \frac{i}{4\pi^2} \int\int d\mathbf{k} e^{i\mathbf{k}(\mathbf{r}-\mathbf{r}')} \frac{1}{k_0^2 - k^2} \begin{pmatrix} k_0^2 - k_y^2 & k_x k_y \\ k_y k_y & k_0^2 - k_y^2 \end{pmatrix}. \tag{2.51}$$

Analytical expressions for the different entries of the tensor

$$\hat{G}(\mathbf{r},\mathbf{r}') = \begin{pmatrix} G_{xx}(\mathbf{r},\mathbf{r}') & G_{xy}(\mathbf{r},\mathbf{r}') \\ G_{yx}(\mathbf{r},\mathbf{r}') & G_{yy}(\mathbf{r},\mathbf{r}') \end{pmatrix}, \tag{2.52}$$

can be given by defining the normalized wave vector, $\mathbf{q} = \mathbf{k}/k_0 = (q_x, q_y)$, and relative position, $\mathbf{d}_0 = k_0(\mathbf{r} - \mathbf{r}') = (d_{0x}, d_{0y})$. If we make $q = |\mathbf{q}|$ and $d_0 = |\mathbf{d}_0|$, and using the relation [96]

$$\frac{i}{2\pi}\int d\mathbf{q}\frac{e^{i\mathbf{q}\mathbf{d}_0}}{\sqrt{1-q^2}} = \frac{1}{d_0}e^{id_0}, \tag{2.53}$$

which corresponds to the Green's function associated to the Helmholtz's equation in 3D, we find the dependence on the normalized distance, d_0, of each component of $\hat{G}(\mathbf{r}',\mathbf{r})$

$$G_{xx}(\mathbf{r},\mathbf{r}') = -ie^{id_0}\left[\frac{1}{d_0} + \frac{i}{d_0^2} - \frac{1}{d_0^3} - d_{0y}^2\left(\frac{1}{d_0^3} + \frac{3i}{d_0^4} - \frac{3}{d_0^5}\right)\right], \tag{2.54}$$

$$G_{xy}(\mathbf{r},\mathbf{r}') = ie^{id_0}d_{0x}d_{0y}\left[\frac{1}{d_0^3} + \frac{3i}{d_0^4} - \frac{3}{d_0^5}\right], \tag{2.55}$$

$$G_{yy}(\mathbf{r},\mathbf{r}') = -ie^{id_0}\left[\frac{1}{d_0} + \frac{i}{d_0^2} - \frac{1}{d_0^3} - d_{0x}^2\left(\frac{1}{d_0^3} + \frac{3i}{d_0^4} - \frac{3}{d_0^5}\right)\right], \tag{2.56}$$

$$G_{yx}(\mathbf{r},\mathbf{r}') = G_{xy}(\mathbf{r},\mathbf{r}'). \tag{2.57}$$

The scattering properties of finite arrangements of slits can also be described within our formalism by following the same approach we have developed for 2D hole arrays. Again, the starting point is a 1D supercell of length L containing the slit arrangement we want to study. Then, from the matching procedure, a set of continuity equations of the same form as Eqs. (2.46) can be built for both light polarizations. Therefore, two different 1D operators $\hat{G}_\gamma$ (where γ indicates the polarization) arise. In the limit $L \to \infty$, they have the form

$$\hat{G_\gamma} = \frac{i}{2\pi}\int dk\, Y_\gamma(k)\,|k\rangle\langle k|, \tag{2.58}$$

where k is the transverse wave vector parallel to x-direction and $Y_{\gamma=1}(k) = k_0/\sqrt{k_0^2 - k^2}$ and $Y_{\gamma=2}(k) = \sqrt{k_0^2 - k^2}/k_0$. In the position basis, $|x\rangle$, $\hat{G}_\gamma$ for s-polarization ($\gamma = 1$) reads

$$G_s(x,x') = \langle x|\hat{G}_s|x'\rangle = \frac{i}{2\pi}\int dk\,\frac{\sqrt{k_0^2 - k^2}}{k_0}\,e^{ik(x-x')}, \tag{2.59}$$

whereas for p-polarization ($\gamma = 2$), it is given by

$$G_p(x,x') = \langle x|\hat{G}_p|x'\rangle = \frac{i}{2\pi}\int dk\,\frac{k_0}{\sqrt{k_0^2 - k^2}}\,e^{ik(x-x')}. \tag{2.60}$$

Analytical expressions for both operators can be obtained from the 1D version of Eq. (2.53),

$$\frac{i}{2\pi}\int dq \frac{e^{iqd_0}}{\sqrt{1-q^2}} = \frac{1}{2}H_0^{(1)}(d_0), \tag{2.61}$$

where $H_0^{(1)}$ is the zero order Hankel function of the first kind. Eq. (2.51) corresponds to the Green's function for the Helmholtz's equation in 2D [96]. By making $d_0 = k_0|x-x'|$ and $q = k/k_0$, we have that, for s-polarization,

$$G_s(x,x') = \frac{ik_0}{4}[H_0^{(1)}(k_0|x-x'|) + H_2^{(1)}(k_0|x-x'|)], \tag{2.62}$$

where $H_2^{(2)}$ is the second order Hankel function of the first kind, whereas for p-polarized light,

$$G_p(x,x') = \frac{ik_0}{2}H_0^{(1)}(k_0|x-x'|). \tag{2.63}$$

2.2.3. Reciprocal space formalism

In order to relate the scattering properties of a perforated film to the structure factor [97] of the aperture array, it is convenient to transform our ME formalism into the reciprocal space. As we have seen in the previous sections, the real space version of our ME formalism allows constructing the EM fields in all the space from the electric field amplitudes at the input and output sides of the apertures. Therefore, these modal amplitudes control the transmission and reflection characteristics of the film. The set of continuity equations governing them can be rewritten as

$$\begin{aligned} -\epsilon_n E_n(\mathbf{R}) + \textstyle\sum_{\mathbf{R}'m} G_{nm}^{\mathbf{R}\mathbf{R}'} E_m(\mathbf{R}') - G_n^V E_n'(\mathbf{R}) = I_n(\mathbf{R}), \\ -\epsilon_n E_n'(\mathbf{R}) + \textstyle\sum_{\mathbf{R}'m} G_{nm}^{\mathbf{R}\mathbf{R}'} E_m'(\mathbf{R}') - G_n^V E_n(\mathbf{R}) = 0, \end{aligned} \tag{2.64}$$

where the definition of the different terms remains the same as in Eqs. (2.46) but index α (β) has been split into two different indexes: $\mathbf{R}$ ($\mathbf{R}'$), indicating the hole position, and n (m), which denotes the order of the waveguide mode. We can expect that the connection between the geometry of the arrangement and its transmission properties resides in the Fourier components of the electric field amplitudes, $E_n^{(\prime)}(\mathbf{k})$, defined as

$$E_n^{(\prime)}(\mathbf{k}) = \sum_{\mathbf{R}} E_n^{(\prime)}(\mathbf{R})e^{-i\mathbf{k}\mathbf{R}}, \tag{2.65}$$

where the sum ranges over all the apertures. These k-space amplitudes describe the dependence of EM fields at the sides of the perforated film on the parallel wave vector, $\mathbf{k}$.

The continuity equations for $E_n(\mathbf{k})$ and $E'_n(\mathbf{k})$ can be obtained from Eqs. (2.64) by multiplying each equation by $e^{-i\mathbf{kR}}$, and summing for all $\mathbf{R}$. Thus, for each $\mathbf{k}$, we find a system of integral equations in which the structure factor of the set of apertures, $S(\mathbf{k}) = \sum_{\mathbf{R}} e^{-i\mathbf{kR}}$, appears explicitly

$$\begin{aligned} -\epsilon_n E_n(\mathbf{k}) + \textstyle\sum_m \int d\mathbf{k}' G_{nm;\mathbf{k}'} S(\mathbf{k}-\mathbf{k}') E_m(\mathbf{k}') - G_n^V E'_n(\mathbf{k}) &= I_n(\mathbf{R}=\mathbf{0}) S(\mathbf{k}-\mathbf{k}_\mathrm{i}), \\ -\epsilon_n E'_n(\mathbf{k}) + \textstyle\sum_m \int d\mathbf{k}' G_{nm;\mathbf{q}} S(\mathbf{k}-\mathbf{k}') E'_m(\mathbf{k}') - G_n^V E_n(\mathbf{k}) &= 0. \end{aligned} \tag{2.66}$$

Note that the ϵ_n and G_n^V terms remain the same as in real space, as they do not link EM fields associated to different holes. The illumination term is now given by the product of the coupling between the incident light and the n^{th} waveguide mode at $\mathbf{R} = \mathbf{0}$, $I_n(\mathbf{R} = \mathbf{0})$, and the structure factor $S(\mathbf{k} - \mathbf{k}_\mathrm{i})$, where $\mathbf{k}_\mathrm{i}$ is the in-plane component of the incoming wave vector. The integral term $\sum_m \int d\mathbf{k}' G_{nm;\mathbf{k}'} S(\mathbf{k}-\mathbf{k}') E_m^{(\prime)}(\mathbf{k}')$ represents all the scattering processes that couples $E_n^{(\prime)}(\mathbf{k})$ to the continuum $E_n^{(\prime)}(\mathbf{k}')$. The crystal momentum needed for the coupling is provided by the structure through $S(\mathbf{k}-\mathbf{k}')$, and the amplitude of each scattering process is measured by

$$G_{mn;\mathbf{k}} = \frac{i}{4\pi^2} \sum_\sigma Y_{\mathbf{k}\sigma} \langle n|\mathbf{k},\sigma\rangle \langle \mathbf{k},\sigma|m\rangle \tag{2.67}$$

where $|\mathbf{k},\sigma\rangle$ are the plane waves defined by Eqs. (2.50), and $|n\rangle$ and $|m\rangle$ are waveguide modes evaluated at $\mathbf{R} = \mathbf{0}$. Note that $G_{mn;\mathbf{k}}$ diverges whenever a p-polarized diffraction wave goes glancing.

In what follows, we describe how this k-space framework enables us to reach a better understanding of the scattering of light by perforated films, although from a numerical point of view it is more convenient to work with our ME formalism in real space. We define the functions $\Sigma_n^{(\prime)}(\mathbf{k})$, which satisfy

$$\Sigma_n(\mathbf{k}) E_n^{(\prime)}(\mathbf{k}) = \sum_m \int d\mathbf{k}' G_{nm;\mathbf{k}'} S(\mathbf{k}-\mathbf{k}') E_m^{(\prime)}(\mathbf{q}). \tag{2.68}$$

As we showed in Section 2.2.1, for subwavelength apertures it is a very good approximation to consider only the least evanescent waveguide mode inside the holes (labelled as $n = 0$). Hence, for each $\mathbf{k}$, we can rewrite Eqs. (2.66) as a set of two linear equations

$$\begin{aligned} (\Sigma_0(\mathbf{k}) - \epsilon_0) E_0(\mathbf{k}) - G_0^V E'_0(\mathbf{k}) &= I_0(\mathbf{R}=\mathbf{0}) S(\mathbf{k}), \\ (\Sigma_0(\mathbf{k}) - \epsilon_0) E'_0(\mathbf{k}) - G_0^V E_0(\mathbf{k}) &= 0, \end{aligned} \tag{2.69}$$

where, for simplicity, we have restricted our analysis to normal illumination, i.e., $\mathbf{k}_\mathrm{i} = \mathbf{0}$.

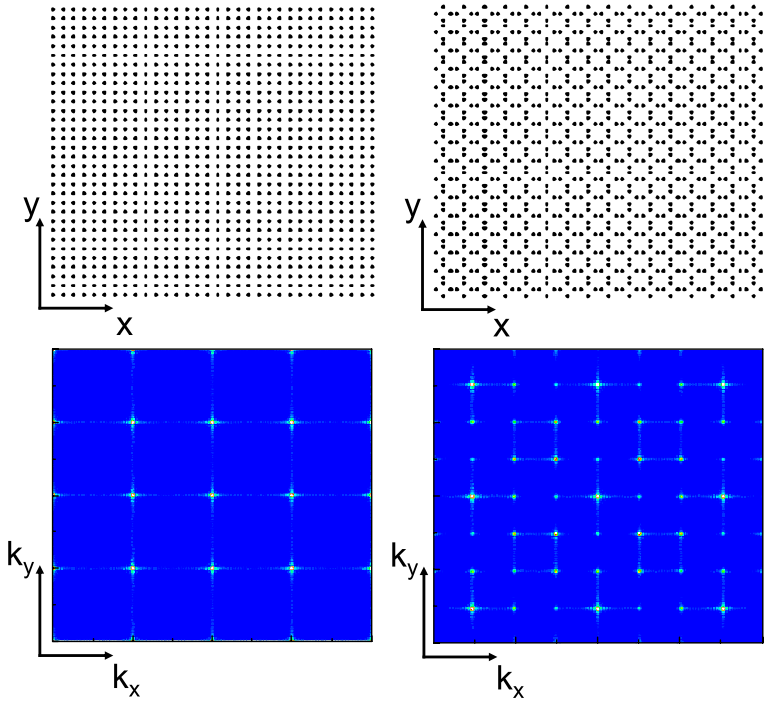

Figure 2.7.: Structure factor for two different periodic arrays of 1024 holes.

Let us consider firstly the case of an infinitely periodic array. Taking advantage of Bloch's theorem, we can write $E_0^{(\prime)}(\mathbf{k}+\mathbf{b}_l) = E_0^{(\prime)}(\mathbf{k})$ and $S(\mathbf{k}) = \frac{4\pi^2}{d_x d_y}\sum_{\mathbf{b}_l}\delta(\mathbf{k}-\mathbf{b}_l)$, where d_x and d_y are the array periods, $\mathbf{b}_l$ are the reciprocal lattice vectors, and $\delta(x)$ is the Dirac's delta function. Introducing these expressions in Eq. (2.68) we obtain $\Sigma_0^{(\prime)}(\mathbf{k}) = \frac{4\pi^2}{d_x d_y}\sum_{\mathbf{b}_l} G_{00;\mathbf{k}+\mathbf{b}_l}$. It is well known that, under normal incidence and for wavelengths larger than the array period, the transmissivity of periodic arrays is governed by the zero-order diffracted beam. Thus, the transmission features characteristic of such structures must be reflected in the two k-space linear equations for $\mathbf{k} = \mathbf{0}$

$$\begin{aligned}(\Sigma_0 - \epsilon_0)E_0(\mathbf{0}) - G_0^V E_0'(\mathbf{0}) &= I_0,\\ (\Sigma_0 - \epsilon_0)E_0'(\mathbf{0}) - G_0^V E_0(\mathbf{0}) &= 0,\end{aligned} \tag{2.70}$$

where we have done $\Sigma_0 = \Sigma_0(\mathbf{0}) = \frac{4\pi^2}{d_x d_y}\sum_{\mathbf{b}_l} G_{00;\mathbf{b}_l}$. Importantly, this Σ_0 function coincides with the real space G-term for periodic hole arrangements defined in Eq. (2.32) when only the lowest waveguide mode is considered. Thus, as ϵ_0, G_0^V and I_0 have the same form as their Fourier counterparts, we have found that real space (2.28) and reciprocal space (2.70) continuity equations are exactly the same for the case of perfectly periodic

aperture arrangements.

The arguments presented above can be applied to any finite distribution of apertures (periodic, quasiperiodic or disordered arrangements). Bloch's theorem cannot be applied to such structures and, in principle, Eqs. (2.66) must be solved for a continuum of states $\mathbf{k}$. However, we have found that for a finite array with a large number of holes, $\mathbf{k} = \mathbf{k}_{\rm i} = \mathbf{0}$ is the dominant transmission channel. Therefore, a good approximation can be obtained by only considering $E_0(\mathbf{0})$ and $E_0'(\mathbf{0})$. The equations for these magnitudes are written like Eqs. (2.70) where $\Sigma_0 = \Sigma_0^{(\prime)}(\mathbf{0})$ can be calculated numerically from $E_0^{(\prime)}(\mathbf{k})$ [see Eq. (2.68)]. Note that these last quantities can be easily obtained by a Fourier-transformation of the set of modal amplitudes in real space, $\{E_0(\mathbf{R}), E_0'(\mathbf{R})\}$. Then, within this approach we are able to relate transmission features with properties of just two equations, as in the case of an infinite periodic array.

Although here we have considered only the case of 2D hole arrangements, our framework can be easily extended to 1D slit apertures.

2.2.4. Bound modes

In the previous sections, we have applied our ME formalism to the analysis of the scattering properties of perforated films. Here, we show how the bound EM modes sustained by periodically structured PEC metals, the so-called spoof surface plasmon polaritons (spoof SPPs), can be also studied within our theoretical framework.

Our approach allows treating the bound modes in arrays of both 1D and 2D apertures. Our starting point are the continuity equations (2.28) and (2.38) associated to holes and slits, respectively. The EM modes supported by perforated films are characterized by having strong electric field at the film surfaces even for arbitrarily small illuminations. Therefore, they appear as solutions of the eigenvalue problem set by the ME continuity equations when the illumination term is removed. Hence, spoof SPP modes correspond to the non-vanishing solutions of the homogeneous version of Eqs. (2.28) and (2.38) which, using the compact notation introduced in Eq. (2.46), read

$$\begin{aligned} (G_{\alpha\alpha} - \epsilon_\alpha) E_\alpha + \textstyle\sum_{\beta\neq\alpha} G_{\alpha\beta} E_\beta - G_\beta^V E_\alpha' = 0, \\ (G_\alpha - \epsilon_\alpha) E_\alpha' + \textstyle\sum_{\beta\neq\alpha} G_{\alpha\beta} E_\beta' - G_\alpha^V E_\alpha = 0, \end{aligned} \tag{2.71}$$

where now index α corresponds to $\{l, s, \gamma\}$ for 2D holes, and to $\{l\}$ for 1D slits.

The bound modes sustained by single corrugated PEC surfaces can also be studied within our formalism. We showed in Section 2.2.1 that each equation in (2.71) can be related to one of the sides of the perforated film, and that the G^V term reflects the

coupling of the EM fields at the different film surfaces through the apertures. Thus, by removing this term, the film sides are disconnected, which enables us to treat the spoof SPP modes supported by single structured metallic surfaces. Thus, we find that the bound modes sustained by blind perforations (grooves and dimples) are described by

$$(G_{\alpha\alpha} - \epsilon_\alpha)E_\alpha + \sum_{\beta\neq\alpha} G_{\alpha\beta}E_\beta = 0. \tag{2.72}$$

where the $G_{\alpha\beta}$ and ϵ_α terms remain the same as in Eqs. (2.71).

The dispersion relation of the bound modes in such structures is calculated by finding the values of the parallel component and modulus of the wave vector (k and $k_0 = \omega/c$, respectively) for which the determinant associated with the continuity equations vanishes. Although, in general, this problem must be solved numerically, analytical expressions for the dispersion relation of spoof SPPs can be obtained by using two approximations:

- Only the fundamental waveguide mode is taken in the expansion of EM fields inside the aperture, which allows working with the single mode version of Eqs. (2.71) and (2.72).
- Only the p-polarized zero-order diffraction mode is considered in the G-term, which provides us simple expressions for this term governing the coupling between apertures.

The first approximation leads to accurate results for subwavelength apertures, failing when the size of the indentation is comparable to the array period. The second approximation, which is equivalent to consider the system as a metamaterial represented by the average EM fields, must be corrected close to the band edges, as it does not reflect the appearance of gaps due to diffraction effects. Additionally, it has been demonstrated that this approximation overestimates the binding of spoof SPP modes supported by 2D apertures [61]. In what follows, we describe how analytical expressions for the spoof SPP bands can be obtained. Importantly, despite of its approximate character, our analytical approach enables us to gain physical insight into the problem and to predict the dependence of the exact dispersion relations on the various geometrical parameters defining the structure (see Sec. 3.2.2).

First, we consider the case of blind apertures, i.e., those which do not pierce completely the metallic film. Two different periodic structures are analyzed, 1D arrays of grooves and 2D arrangements of dimples. The condition for the existence of bound modes in these systems reads

$$G - \epsilon = 0. \tag{2.73}$$

Neglecting diffraction effects, the G term in (2.73) is given by $G = i\frac{k_0}{\sqrt{k_0^2-k^2}}|S(k)|^2$, where $S(k)$ is the overlap between the p-polarized zero-order diffracted mode and the lowest waveguide mode inside the indentations. Moreover, for apertures much smaller than the wavelength, the dependence of the overlapping integral on the parallel wave vector can be neglected, having $S(k) \approx S$. Thus, the analytical spoof SPP bands for 1D and 2D blind apertures is given by

$$k = k_0\sqrt{1+\frac{|S|^4}{\epsilon^2}}. \tag{2.74}$$

Note that, as expected $k > k_0 = \omega/c$, which reflects the bound nature of EM modes.

For groove arrays, $\epsilon = \cot(k_0 h)$ [see Eq. (2.40)], where h is the depth of the indentation. The overlap can be calculated from Eq. (A-3), having $S = \sqrt{a/d}$ for small widths, a. Therefore, the dispersion relation of the bound modes supported by a periodic array of grooves reads

$$k = k_0\sqrt{1+\left(\frac{a}{d}\right)^2\tan^2(k_0 h)}. \tag{2.75}$$

On the other hand, for the case of dimple arrays in the subwavelength regime ($k_0 < \pi/a$), Eq. (2.30) yields

$$\epsilon = \frac{\sqrt{(\pi/a)^2-k_0^2}}{k_0}\coth\left(\sqrt{(\pi/a)^2-k_0^2}\,h\right). \tag{2.76}$$

The corresponding overlapping integral can be obtained from Eq. (A-7), having $S = \frac{2\sqrt{2}}{\pi}\frac{a}{d}$. Thus, the analytical spoof SPP band for 2D arrays of dimples is given by

$$k = k_0\sqrt{1+\left(\frac{2\sqrt{2}a}{\pi d}\right)^4\frac{k_0^2}{(\pi/a)^2-k_0^2}\tanh^2\left(\sqrt{(\pi/a)^2-k_0^2}\,h\right)}. \tag{2.77}$$

Note that, for simplicity, we are considering only the case of square arrays (of period d) of square dimples (of side a). Figure 2.8 plots the dispersion relation of the bound modes sustained by an array dimples of side $a = 0.6d$ and depth $h = d$. The convergence with the number of waveguide modes considered in Eq. (2.72) is shown. The number of diffraction orders considered in the calculations is sufficient to reach convergence. For comparison, the dispersion relation obtained from Eq. (2.77) is also shown.

We now focus on the bound modes sustained by PEC films fully perforated with periodic arrangements of slits and holes. The existence of bound modes in such structures requires the condition

$$(G-\epsilon) \pm G^V = 0 \tag{2.78}$$

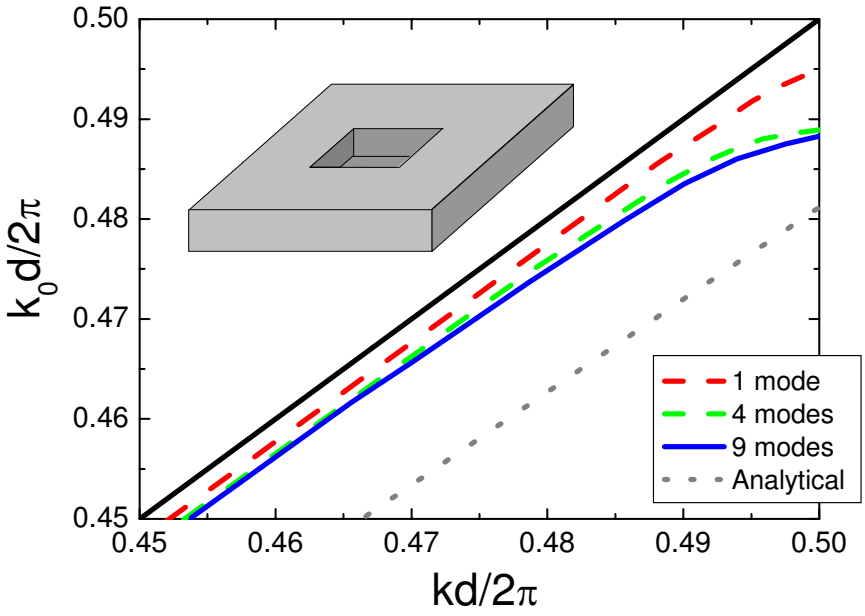

Figure 2.8.: Spoof SPP bands for a square array of square dimples of side $a = 0.6d$ and depth $h = d$. The convergence of the spoof SPP bands with the number of waveguide modes involved in the calculation is shown. In all cases, 25 diffraction orders are considered. Grey dotted line plots the analytical dispersion relation obtained with Eq. (2.77).

to be fulfilled, where the negative (positive) sign in Eq. (2.78) leads to symmetric (antisymmetric) modes with respect to the film center. Therefore, the analytical spoof SPP dispersion relation for fully perforated films read

$$k = k_0 \sqrt{1 + \frac{|S|^4}{(\epsilon \pm G^V)^2}}. \tag{2.79}$$

Note that, as in Eq. (2.74), $k > k_0$.

The terms S and the ϵ in Eq. (2.79) remain the same as in the case of blind apertures. For 1D perforations, the G^V term can be calculated from Eq. (2.41), having $G^V = 1/\sin(k_0 h)$. For 2D square holes, this term can be calculated from Eq. (2.31), having

$$G^V = \frac{\sqrt{(\pi/a)^2 - k_0^2}}{k_0} \frac{1}{\sinh\left(\sqrt{(\pi/a)^2 - k_0^2}\, h\right)}. \tag{2.80}$$

Introducing these two expressions in Eq. (2.79), we find the analytical dispersion relation of the bound modes supported by slit arrays,

$$k = k_0 \sqrt{1 + \left(\frac{a}{d}\right)^2 \frac{\sin^2(k_0 h)}{[\cos(k_0 h) \pm 1]^2}}, \tag{2.81}$$

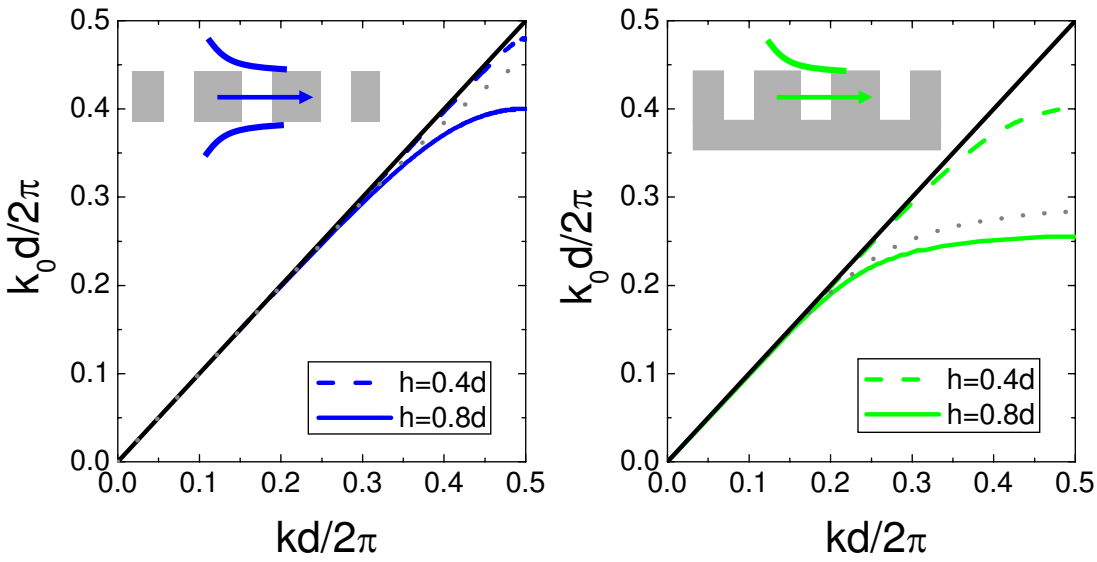

Figure 2.9.: Dispersion relation of the spoof SPPs supported by slit (left panel) and groove (right panel) arrays of the same geometry. The apertures width, a, is fixed to $0.2d$. Four waveguide modes and 21 diffracted waves are considered in the ME calculations. Grey dotted lines plot the analytical bands obtained from Eqs. (2.81) (left panel) and (2.75) for the case $h = 0.8d$.

and hole arrangements,

$$k = k_0 \sqrt{1 + \left(\frac{2\sqrt{2}a}{\pi d}\right)^4 \frac{k_0^2}{(\pi/a)^2 - k_0^2} \frac{\sinh^2\left(\sqrt{(\pi/a)^2 - k_0^2}\, h\right)}{(\cosh\left(\sqrt{(\pi/a)^2 - k_0^2}\, h\right) \pm 1)^2}}. \tag{2.82}$$

Figure 2.9 renders the dispersion relation of the spoof SPPs sustained by periodic arrays of 1D apertures of width $a = 0.2d$. Exact spoof SPP bands for slits (left panel) and grooves (right panel) are computed from equations (2.71) and (2.72), respectively. In the calculations, 4 waveguide modes and 21 diffracted orders were considered. Two different aperture depths, h, are considered. Grey dotted lines plot the analytical spoof SPP bands for $h = 0.8d$ obtained from equations (2.81), for slits, and (2.75), for the case of grooves. Within the frequency range shown in the figure, only a symmetric mode (positive sign in Eq. (2.79)) is supported by the slit arrays considered.

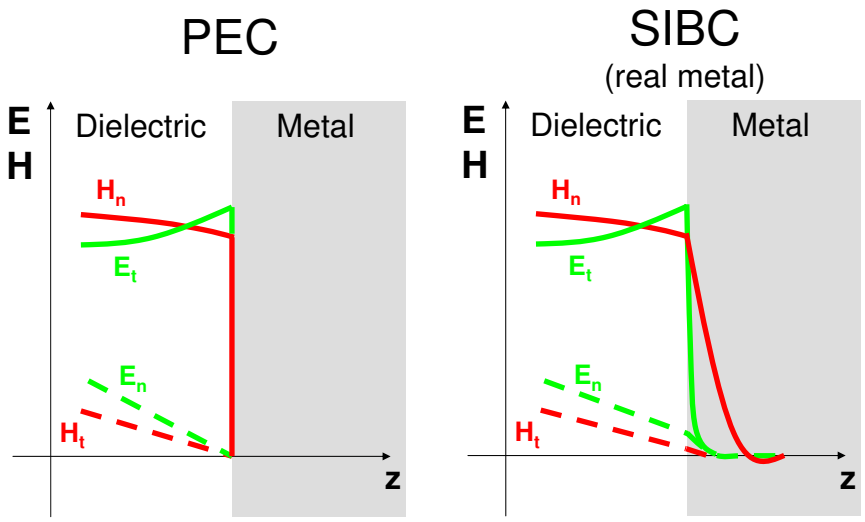

Figure 2.10.: Behavior of EM fields at a metal-dielectric interface within the perfect conductor and surface impedance approximations.

2.2.5. Surface impedance boundary conditions

Surface impedance boundary conditions (SIBCs) [91] allow the incorporation, in an approximate way, of the dielectric properties of real metals into our ME formalism. Before describing the basic ideas behind the SIBCs, we review briefly how EM fields behave at the interface between a PEC metal and a dielectric [10]. The main characteristic of PEC metals is that EM fields vanish inside them. Thus, just at the metal surface, tangential electric ($\mathbf{E}_t$) and normal magnetic ($\mathbf{H}_n$) fields are set equal to zero. However, this is not true for normal electric ($\mathbf{E}_n$) and tangential magnetic ($\mathbf{H}_t$) components of the EM fields. The appearance of screening charge densities and currents in the surface of PEC metals gives rise to discontinuities in these two last components of the EM fields. In the left panel of Figure 2.10 the behavior of EM fields in a PEC metal-dielectric interface are depicted schematically.

SIBCs allow exploring the changes suffered by EM fields close to a metallic surface with finite, rather than infinite, conductivity. However, as in PEC interfaces, Maxwell equations are not solved inside the metallic media. In the surface impedance approach, the effect of the fields penetration inside the metal is reflected in the EM fields just at the metallic surface. This is performed by defining a surface impedance Z_S that relates

tangential electric and magnetic fields just at the system interface.

The surface impedance approximation is based on the assumption that the spatial variation of the fields normal to the interface (z-direction in Fig. 2.10) is much more rapid than the variations parallel to it. This allows neglecting the parallel derivatives in the Maxwell-Faraday's equation, $\nabla \times \mathbf{H} = -i\epsilon k_0 \mathbf{E}$, when it is applied to the tangential EM fields close to the metal surface. Therefore, the tangential fields inside the metal and close to its surface satisfy $\mathbf{E}_t = \frac{1}{\epsilon_M k_0} \partial_z (\mathbf{n} \times \mathbf{H}_t)$, where ϵ_M is the metal permittivity and $\mathbf{n}$ is the vector normal to the interface directed outward from the metal. If parallel variations are much slower than normal ones, then k_x, $k_y << k_z$ and $k_z \simeq \sqrt{\epsilon_M} k_0$. Thus, we find that $\mathbf{E}_t$ and $\mathbf{H}_t$ just at the metal interface satisfy

$$\mathbf{E}_t|_S = -\frac{1}{\sqrt{\epsilon_M}} \mathbf{n} \times \mathbf{H}_t|_S = -Z_S \, \mathbf{n} \times \mathbf{H}_t|_S, \tag{2.83}$$

where we have defined the impedance of the metal surface $Z_S = \frac{1}{\sqrt{\epsilon_M}}$.

The surface impedance approach, differently from PEC approximation, allows the excitation of surface plasmon polaritons (SPPs) [6] on metal surfaces. Therefore, the validity of the approach [92] can be checked by calculating the dispersion relation of conventional SPPs on a flat surface with SIBCs and comparing it with the exact one. It can be obtained by combining Eq. (2.83) with the definition of the modal admittance presented in Sec. 2.2.1 ($-\mathbf{u}_z \times \mathbf{H}_t = Y_{\text{mode}} \mathbf{E}_t$) which provides us with the condition for the existence of SPPs under SIBCs, $(1 + Z_S) Y_{\text{mode}} = 0$. Introducing the admittance of p-polarized plane waves, $Y_{\text{mode}} = \frac{k_0}{\sqrt{k_0^2 - k^2}}$, we find the dispersion relation of SPPs within the SIBCs approximation

$$k = k_0 \sqrt{\frac{\epsilon_M - 1}{\epsilon_M}}. \tag{2.84}$$

For $|\epsilon_M| >> 1$, this expression coincides with the exact one, $k = k_0 \sqrt{\frac{\epsilon_M}{\epsilon_M + 1}}$ (see Sec. 3.2.1). Thus, we can expect that SIBCs provide accurate results for metals with large permittivities. This is true for most real metals in the terahertz and infrared regimes [98], where SIBCs are an excellent approximation . Furthermore, the surface impedance approach still leads to reasonable results in the telecom and optical ranges of the EM spectrum, where metal permittivities are lower [99, 100].

We illustrate the incorporation of SIBCs into our formalism by considering the case of an infinitely periodic array of holes. They are imposed at all the metal-dielectric interfaces except in those corresponding to the apertures walls, which are still treated as PEC. Thus, we avoid the application of SIBCs at corners [101], which would increase the complexity of our model. Moreover, considering the apertures walls as PEC enables us

to expand the EM fields inside them in terms of analytical wavefunctions. The effect of fields penetration at the apertures can be considered by enlarging the apertures area, so that the propagation constant of the approximated waveguide modes can be fitted to the real ones [102].

SIBCs modify the continuity conditions on EM fields at the interfaces of the structure. As for PEC boundaries, $\mathbf{H}_\mathrm{t}$ must be continuous only through the apertures. However, the continuity of $\mathbf{E}_\mathrm{t}$ is now replaced by Eq. (2.83), which must be satisfied over the entire unit cell. Therefore, it is convenient to define two effective transverse fields, $\mathbf{F}_{I-II} = \mathbf{E}_\mathrm{t} + Z_S\,\mathbf{u}_z \times \mathbf{H}_\mathrm{t}$ and $\mathbf{F}_{II-III} = \mathbf{E}_\mathrm{t} - Z_S\,\mathbf{u}_z \times \mathbf{H}_\mathrm{t}$, whose continuity is imposed at $z = 0$ and $z = h$, respectively (see Fig. 2.1). From these continuity conditions, a new set of linear equations of the same form as Eqs. (2.28) and (2.38) is obtained. However, the various terms appearing in this set of equations are now different from the PEC ones. For the general case of periodic 2D hole arrays, they read

$$I_{ls\gamma} = 2i\frac{Y^I_{\mathbf{k}_\mathrm{i}\sigma_\mathrm{i}}}{1+Z_S Y^I_{\mathbf{k}_\mathrm{i}\sigma_\mathrm{i}}}(S^{ls\gamma}_{00\sigma_\mathrm{i}})^*, \tag{2.85}$$

$$\epsilon_{ls\gamma} = iY^{II}_{ls\gamma}\frac{e^{iq_z^{(ls)}h}(1+Z_S Y^{II}_{ls\gamma}) + e^{-iq_z^{(ls)}h}(1-Z_S Y^{II}_{ls\gamma})}{e^{iq_z^{(ls)}h}(1+Z_S Y^{II}_{ls\gamma})^2 - e^{-iq_z^{(ls)}h}(1-Z_S Y^{II}_{ls\gamma})^2}, \tag{2.86}$$

$$G^V_{ls\gamma} = \frac{2iY^{II}_{ls\gamma}}{e^{iq_z^{(ls)}h}(1+Z_S Y^{II}_{ls\gamma})^2 - e^{-iq_z^{(ls)}h}(1-Z_S Y^{II}_{ls\gamma})^2} \tag{2.87}$$

$$G^{l's'\gamma'}_{ls\gamma} = i\sum_{mn\sigma}\frac{Y^I_{\mathbf{k}_{mn}\sigma}}{1+Z_S Y^I_{\mathbf{k}_{mn}\sigma}}(S^{ls\gamma}_{mn\sigma})^* S^{ls\gamma}_{mn\sigma}. \tag{2.88}$$

Similar expressions can be obtained for 1D periodic structures and 1D and 2D finite systems by applying the procedure described here to the corresponding continuity equations.

Notice how SIBCs modify the G-term (2.88) from its PEC version (2.32). As we stated in Section 2.2.1, under the PEC approximation, singularities in $Y^I_{\mathbf{k}_{nm}\sigma}$ make $G^{l's'\gamma'}_{ls\gamma}$ diverge. We associated those divergences with the formation of geometrically induced bound modes in the structure. Importantly, SIBCs shift that resonant condition and $G^{l's'\gamma'}_{ls\gamma}$ now explodes if $1 + Z_S Y^I_{\mathbf{k}_{mn}\sigma} = 0$. This equation coincides with the condition for the existence of conventional SPPs under the surface impedance approximation [see Eq. (2.84)]. Therefore, we have found that the divergences in the G-term (2.88) are related to the appearance of conventional SPPs in the system (described with SIBCs).

Figure 2.11 depicts the transmittance of a 200 nm thick Ag film perforated with a square array of square holes of side 250 nm and period 500 nm. The comparison of ME calculations and exact FDTD results is shown. The fundamentals of the FDTD method

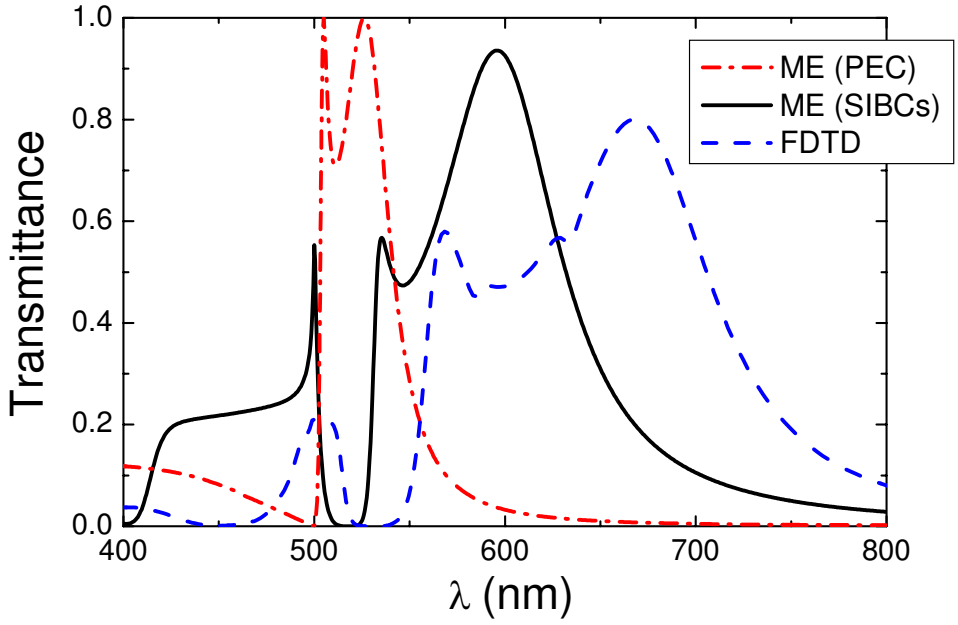

Figure 2.11.: Transmission spectrum for a 200 nm thick Ag film perforated with a square array of square holes. The array period is 500 nm and the holes side 250 nm. The number of hole waveguide modes and Bloch waves considered in the ME calculation are 4 and 121, respectively. The square mesh size used in the FDTD calculations is equal to 5 nm.

are detailed in Sec. 2.4. Red dotted dashed and black solid lines correspond to ME calculations under perfect conduction and surface impedance approximations, respectively. Blue dashed line plots the transmission obtained from FDTD simulations with a square mesh size of 5nm. The permittivity of Ag has been taken from the fitted Drude-Lorentz formula considered in [100]. The comparison of the ME calculations with exact FDTD results demonstrates the predictive value of our approach. It is remarkable that ME results reproduce, even with PEC boundaries, the main features appearing in the transmission spectrum of such structures even at optical wavelengths.

2.3. Transfer matrix method

In the early 90's the experimental realization by Yablonovitch and co-workers [103, 104] of photonic crystals featuring a full photonic band gap, grabbed the attention of solid state physicists who, at that time, were working on describing the properties of electrons moving in periodic structures. Theorists began trying to analyze the behavior of EM

fields in periodic dielectric media with the same tools that they used for calculating electronic band structures.

Very soon, they realized that the light could not be treated as a scalar quantity, similar to the electronic wavefunction, and that new approaches were needed for describing the full vector nature of EM fields. The transfer matrix method (TMM) [105] was then developed as a high efficient approach for solving Maxwell equations in complex media. In comparison with other proposed techniques, the TMM had several characteristics which made it very suitable for addressing the problems that the incipient field of nanophotonics was facing at that time. Some of these characteristics are:

- As a difference with other methods which provide the frequency, ω, associated with each real wave vector, k, TMM allows calculating photonic bands by finding all complex k's associated with a single ω, similarly to the experimental procedure.
- TMM works in real space, which allows avoiding the high computational efforts required to Fourier transform dielectric constants $\epsilon(\mathbf{r})$ displaying abrupt spatial variations.
- Within TMM, frequency dependent permittivities are treated straightforwardly, whereas in approaches working at a fixed k, the treatment of media having a dielectric constant $\epsilon(\omega)$ translates into that the dispersion relation, $\omega(k)$, must be obtained in a self-consistent manner.
- The fact that TMM works at a fixed frequency, enables the calculation of transmission and reflection coefficients of complex objects in a very efficient manner.

In this section, we describe the fundamentals of the TMM, focusing on the problem of the discretization of Maxwell equations, which lies at the core of this approach. Our starting point are the curl Maxwell equations which, in the reciprocal space $\{\mathbf{k}, \omega\}$, have the form

$$i\mathbf{k} \times \mathbf{E} = i\frac{\omega}{c_0}\mu(\mathbf{r})\mathbf{H}, \tag{2.89}$$

$$i\mathbf{k} \times \mathbf{H} = -i\frac{\omega}{c_0}\epsilon(\mathbf{r})\mathbf{E}. \tag{2.90}$$

Note that in this section, in order to avoid confusion with the unit vector that will be introduced below, the speed of light in vacuum is denoted as c_0.

Approximations crucial to the transfer matrix approach are now performed. In Eq. (2.89), we make

$$k_x \approx (e^{ik_x a} - 1)/ia, \;\; k_y \approx (e^{ik_y b} - 1)/ib, \;\; k_z \approx (e^{ik_z c} - 1)/ic, \tag{2.91}$$

where the unit vectors $\mathbf{a} = a\mathbf{u}_x$, $\mathbf{b} = b\mathbf{u}_y$, and $\mathbf{c} = c\mathbf{u}_z$ define the hexahedral mesh in which Maxwell equations are discretized. In Eq. (2.90), we make

$$k_x \approx -(e^{-ik_x a} - 1)/ia, \;\; k_y \approx -(e^{-ik_y b} - 1)/ib, \;\; k_z \approx -(e^{-ik_z c} - 1)/ic. \tag{2.92}$$

Fourier transforming back to real space the approximated version of Eq. (2.89), we have

$$\begin{aligned}
i\Big[\frac{E_z(\mathbf{r}+\mathbf{b}) - E_z(\mathbf{r})}{b} - \frac{E_y(\mathbf{r}+\mathbf{c}) - E_y(\mathbf{r})}{c}\Big] &= -\frac{\omega}{c_0}\mu(\mathbf{r})H_x(\mathbf{r}) \\
i\Big[\frac{E_x(\mathbf{r}+\mathbf{c}) - E_x(\mathbf{r})}{c} - \frac{E_z(\mathbf{r}+\mathbf{a}) - E_z(\mathbf{r})}{a}\Big] &= -\frac{\omega}{c_0}\mu(\mathbf{r})H_y(\mathbf{r}) \\
i\Big[\frac{E_y(\mathbf{r}+\mathbf{a}) - E_y(\mathbf{r})}{a} - \frac{E_x(\mathbf{r}+\mathbf{b}) - E_x(\mathbf{r})}{b}\Big] &= -\frac{\omega}{c_0}\mu(\mathbf{r})H_z(\mathbf{r})
\end{aligned} \tag{2.93}$$

and from Eq. (2.90), we obtain

$$\begin{aligned}
i\Big[\frac{H_z(\mathbf{r}-\mathbf{b}) - H_z(\mathbf{r})}{b} - \frac{H_y(\mathbf{r}-\mathbf{c}) - H_y(\mathbf{r})}{c}\Big] &= \frac{\omega}{c_0}\epsilon(\mathbf{r})E_x(\mathbf{r}) \\
i\Big[\frac{H_x(\mathbf{r}-\mathbf{c}) - H_x(\mathbf{r})}{c} - \frac{H_z(\mathbf{r}-\mathbf{a}) - H_z(\mathbf{r})}{a}\Big] &= \frac{\omega}{c_0}\epsilon(\mathbf{r})E_y(\mathbf{r}) \\
i\Big[\frac{H_y(\mathbf{r}-\mathbf{a}) - H_y(\mathbf{r})}{a} - \frac{H_x(\mathbf{r}-\mathbf{b}) - H_x(\mathbf{r})}{b}\Big] &= \frac{\omega}{c_0}\epsilon(\mathbf{r})E_z(\mathbf{r})
\end{aligned} \tag{2.94}$$

Introducing the z-component of Eqs. (2.93) into the x and y ones and defining $\mathbf{H}' = \frac{ic_0}{c\omega}\mathbf{H}$, we can write

$$\begin{aligned}
E_x(\mathbf{r}+\mathbf{c}) = E_x(\mathbf{r}) &+ \frac{c^2\omega^2}{c_0^2}\mu(\mathbf{r})H'_y(\mathbf{r}) \\
&+ \frac{c^2}{a\epsilon(\mathbf{r})}\begin{bmatrix} a^{-1}[H'_y(\mathbf{r}-\mathbf{a}) - H'_y(\mathbf{r})] \\ -b^{-1}[H'_x(\mathbf{r}-\mathbf{b}) - H'_x(\mathbf{r})] \end{bmatrix} \\
&- \frac{c^2}{a\epsilon(\mathbf{r}+\mathbf{a})}\begin{bmatrix} a^{-1}[H'_y(\mathbf{r}) - H'_y(\mathbf{r}+\mathbf{a})] \\ -b^{-1}[H'_x(\mathbf{r}+\mathbf{a}-\mathbf{b}) - H'_x(\mathbf{r}+\mathbf{a})] \end{bmatrix},
\end{aligned} \tag{2.95}$$

$$\begin{aligned}
E_y(\mathbf{r}+\mathbf{c}) = E_y(\mathbf{r}) &- \frac{c^2\omega^2}{c_0^2}\mu(\mathbf{r})H'_x(\mathbf{r}) \\
&+ \frac{c^2}{b\epsilon(\mathbf{r})}\begin{bmatrix} a^{-1}[H'_y(\mathbf{r}-\mathbf{a}) - H'_y(\mathbf{r})] \\ -b^{-1}[H'_x(\mathbf{r}-\mathbf{b}) - H'_x(\mathbf{r})] \end{bmatrix} \\
&- \frac{c^2}{b\epsilon(\mathbf{r}+\mathbf{b})}\begin{bmatrix} a^{-1}[H'_y(\mathbf{r}-\mathbf{a}+\mathbf{b}) - H'_y(\mathbf{r}+\mathbf{b})] \\ -b^{-1}[H'_x(\mathbf{r}) - H'_x(\mathbf{r}+\mathbf{b})] \end{bmatrix}.
\end{aligned} \tag{2.96}$$

The same procedure applied in Eqs. (2.94) yields

$$\begin{aligned} H'_x(\mathbf{r}+\mathbf{c}) &= H'_x(\mathbf{r}) + \epsilon(\mathbf{r}+\mathbf{c})E_y(\mathbf{r}+\mathbf{c}) \\ &- \frac{c_0^2}{a\omega^2\mu(\mathbf{r}-\mathbf{a}+\mathbf{c})}\begin{bmatrix} a^{-1}[E_y(\mathbf{r}+\mathbf{c}) - E_y(\mathbf{r}-\mathbf{a}+\mathbf{c})] \\ -b^{-1}[E_x(\mathbf{r}-\mathbf{a}+\mathbf{b}+\mathbf{c}) - E_x(\mathbf{r}-\mathbf{a}+\mathbf{c})] \end{bmatrix} \\ &+ \frac{c_0^2}{a\omega^2\mu(\mathbf{r}+\mathbf{c})}\begin{bmatrix} a^{-1}[E_y(\mathbf{r}+\mathbf{a}+\mathbf{c}) - E_y(\mathbf{r}+\mathbf{c})] \\ -b^{-1}[E_x(\mathbf{r}+\mathbf{b}+\mathbf{c}) - E_x(\mathbf{r}+\mathbf{c})] \end{bmatrix}, \end{aligned} \tag{2.97}$$

$$\begin{aligned} H'_y(\mathbf{r}+\mathbf{c}) &= H'_y(\mathbf{r}) - \epsilon(\mathbf{r}+\mathbf{c})E_x(\mathbf{r}+\mathbf{c}) \\ &- \frac{c_0^2}{b\omega^2\mu(\mathbf{r}-\mathbf{b}+\mathbf{c})}\begin{bmatrix} a^{-1}[E_y(\mathbf{r}+\mathbf{a}-\mathbf{b}+\mathbf{c}) - E_y(\mathbf{r}-\mathbf{b}+\mathbf{c})] \\ -b^{-1}[E_x(\mathbf{r}+\mathbf{c}) - E_x(\mathbf{r}-\mathbf{b}+\mathbf{c})] \end{bmatrix} \\ &+ \frac{c_0^2}{b\omega^2\mu(\mathbf{r}+\mathbf{c})}\begin{bmatrix} a^{-1}[E_y(\mathbf{r}+\mathbf{a}+\mathbf{c}) - E_y(\mathbf{r}+\mathbf{c})] \\ -b^{-1}[E_x(\mathbf{r}+\mathbf{b}+\mathbf{c}) - E_x(\mathbf{r}+\mathbf{c})] \end{bmatrix}. \end{aligned} \tag{2.98}$$

These equations express the transverse EM fields on a discrete mesh plane as a function of the fields on the previous plane. Therefore, given $\mathbf{E}_t$ and $\mathbf{H}_t$ at one end of the structure under study, Eqs. (2.95)-(2.98) allow integrating through the system to find the EM fields at the other end. The matrix relating the EM fields on one side of the structure to those in the other is termed as transfer matrix [105]. Eqs. (2.95)-(2.98) can be written in a more compact form as

$$\mathbf{F}(z+c) = \mathbf{T}(z)\mathbf{F}(z), \tag{2.99}$$

where we have defined the vector $\mathbf{F}(z)$ which has $4n_xn_y$ components, one for each transverse EM field at each point of the plane, and where $\mathbf{T}(z)$ denotes the $4n_xn_yn_xn_y$ transfer matrix [see panel (a) of Fig. 2.12]. If the structure analyzed is the unit cell of a more complex system, then the eigenvalues of $\mathbf{T}(z)$ give the band structure of the system.

In order to calculate transmission and reflection coefficients, we must express $\mathbf{T}(z)$ in the basis defined by the eigenvectors, $\mathbf{F}^{(0)}(z)$, of the transfer matrix in free space, $\mathbf{T}^0$. As, by definition, $\mathbf{T}^0$ does not depend on z, $\mathbf{F}^{(0)}(z)$ corresponds to plane waves with eigenvalues of the form e^{ikz}. If $\mathbf{S}(\mathbf{z})$ is the unitary transformation to this basis, we have

$$\hat{\mathbf{T}}(z) = \mathbf{S}^{-1}\mathbf{T}(z)\mathbf{S} = \begin{pmatrix} \hat{\mathbf{T}}^{++} & \hat{\mathbf{T}}^{+-} \\ \hat{\mathbf{T}}^{-+} & \hat{\mathbf{T}}^{--} \end{pmatrix}. \tag{2.100}$$

where $\hat{\mathbf{T}}(z)$ denotes the transfer matrix in the plane wave basis. It has been decomposed into four submatrices, which are related to the transmission and reflection matrices of

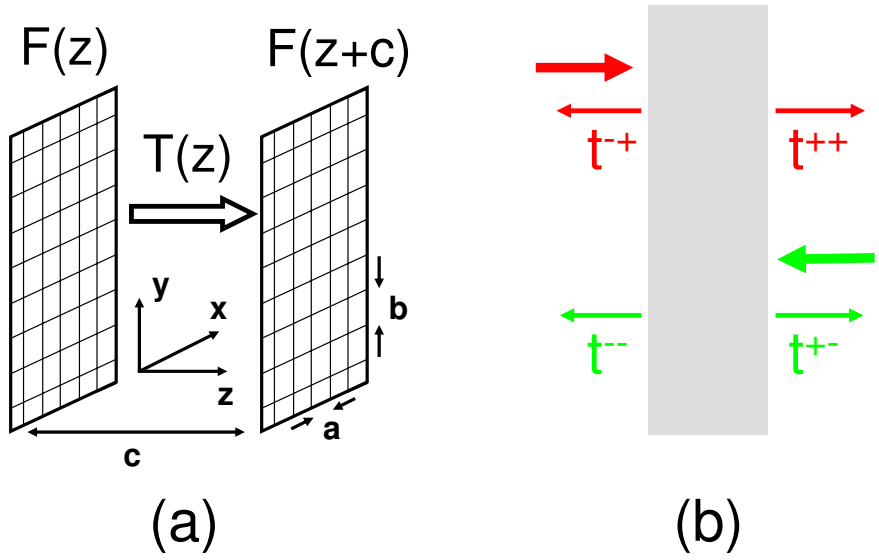

Figure 2.12.: Panel (a): Sketch of the TMM approach. The transfer matrix, $T(z)$, expresses transverse EM fields in a given plane, $\mathbf{F}(z+c)$, in terms of fields in the previous plane, $\mathbf{F}(z)$. Panel (b): Definition of the transmission and reflection coefficients for a system comprising a single discrete slice.

the layer by [106]

$$\mathbf{t}^{--} = (\hat{\mathbf{T}}^{--})^{-1}, \tag{2.101}$$

$$\mathbf{t}^{-+} = -(\hat{\mathbf{T}}^{--})^{-1}\hat{\mathbf{T}}^{-+}, \tag{2.102}$$

$$\mathbf{t}^{+-} = \hat{\mathbf{T}}^{+-}(\hat{\mathbf{T}}^{--})^{-1}, \tag{2.103}$$

$$\mathbf{t}^{++} = \hat{\mathbf{T}}^{++} - \hat{\mathbf{T}}^{+-}(\hat{\mathbf{T}}^{--})^{-1}\hat{\mathbf{T}}^{-+}. \tag{2.104}$$

The physical interpretation of the matrices $\mathbf{t}$ is depicted in the panel (b) of Fig. 2.12: $\mathbf{t}^{++}$ and $\mathbf{t}^{-+}$ are the reflection and transmission matrices on the left hand side of the slice and $\mathbf{t}^{--}$ and $\mathbf{t}^{+-}$ are the transmission and reflection matrices on the right.

In order to calculate the reflection and transmission coefficients of large structures transfer matrices for contiguous layers are multiplied. Then, the main drawback of the TMM arises, the appearance of numerical instabilities due to the eigenvalues of the form e^{ikz} (with imaginary k) which grow exponentially as z increases. However, this problem can be overcome by combining the TMM with the multiple scattering formalism [107].

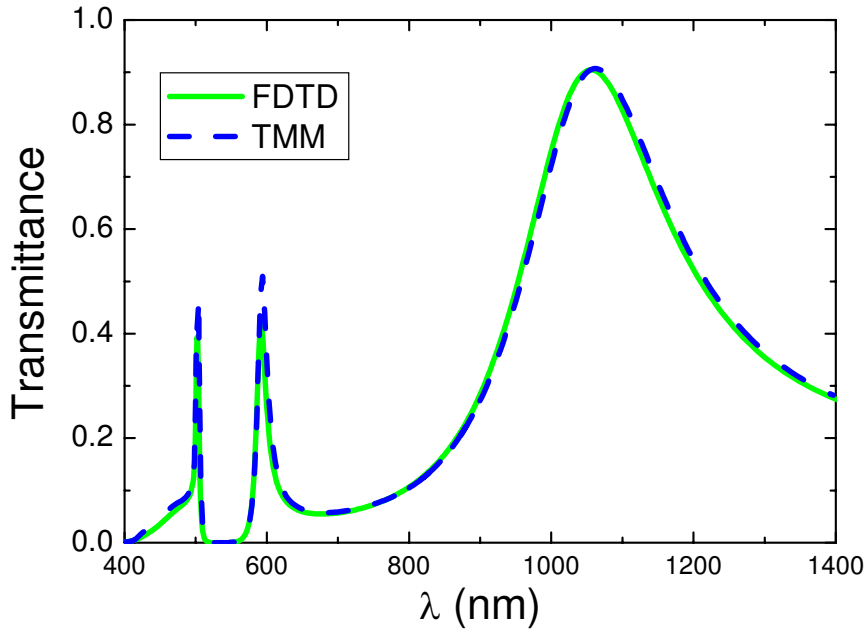

Figure 2.13.: TMM and FDTD transmission spectra for a 350 nm thick Ag film perforated with a periodic array of slits. The array period and slits width are equal to 500 nm and 100 nm, respectively. TMM and FDTD results are compared. Mesh sizes in both TMM and FDTD calculations are equal to 5nm.

Figure 2.13 shows the transmission versus wavelength for a periodic array of slits of width 100 nm and period 500 nm, drilled in a 350 nm thick Ag film. The dielectric constant of Ag has been taken from [100]. Numerical results obtained with TMM are compared with FDTD calculations. TMM allows performing simulations in 2D domains but the necessity of inverting transfer matrices every few discretized layers, makes the technique not suitable for treating 3D systems. Thus, although the scattering of light by 1D slits can be analyzed through the method, it is not possible to simulate accurately 2D apertures due to the high computational effort that TMM calculations require.

2.4. Finite difference time domain method

Differently from the ME and TMM approaches, which work in the frequency domain, the finite difference time domain (FDTD) method aims at solving the time-dependent Maxwell equations. The origin of the method can be linked to the limitations shown by frequency-domain techniques employed in defence and communications technologies in

the 70's and 80's. This led to the exploration of a novel alternative approach: direct time-domain solutions of curl Maxwell equations on spatial lattices. The FDTD method was the first technique of this class.

The fundamentals of the FDTD approach were established in 1966 by K. S. Yee [108], who designed the space grid and time-stepping algorithm which lie at the core of the method. However, it was not until 1980 when A. Taflove validated FDTD models of the interaction of EM fields with real metallic scatterers and coined the term "Finite difference time domain" for the method [109]. Since 1990, due to its versatility and modelling capabilities, the FDTD method has become one of the most extended tools for studying EM fields and their interaction with material structures, with applications ranging from ultralow-frequency geophysics to microwave communication devices or nano and biophotonics [110]. Some of the most relevant features of the method are the following:

- FDTD methodology avoids the difficulties with linear algebra that limit the size of the simulation domain in frequency-domain integral-equation and finite-element techniques.
- The time-domain character of the method allows obtaining the response of the system under study over a wide range of frequencies with a single simulation in which a broadband pulse is used as the source. This fact makes the FDTD method very useful in applications where the resonant frequencies are not known or broadband results are required.
- FDTD treats nonlinear effects naturally, which allows the analysis of a wide variety of EM phenomena arising in linear and nonlinear dielectric and magnetic structures.
- As a difference with other computational approaches where only some components of the EM fields are tracked, in the FDTD method the whole EM field is obtained directly. This fact provides high stability to the calculations and make the technique very useful in applications where all the components of the EM fields are relevant.
- Since EM fields are calculated in every point of the space as they evolve in time, FDTD method provides animated displays of the EM fields propagating through the system. These pictures can lead to a better understanding of the problem, and represent a way to check the numerical stability of the simulation.

The FDTD method is based on the volumetric sampling of the unknown electric and magnetic field vectors within the simulation domain and over a period of time. The

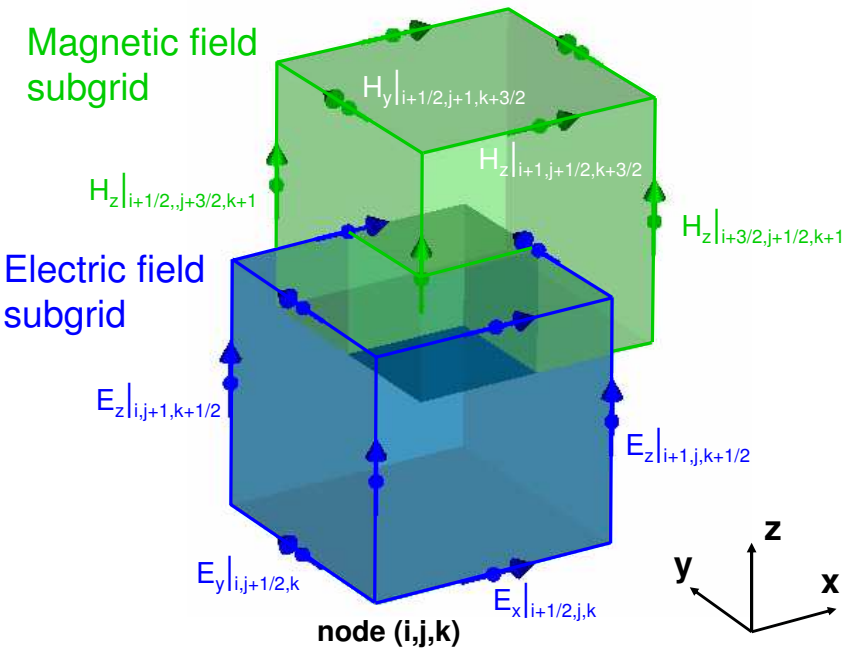

Figure 2.14.: Distribution of electric and magnetic field components in the Yee grid.

discretization in space provides the spatial resolution of the simulation whereas the sampling in time is related to convergence and numerical stability of the calculation. Both are linked through the Yee algorithm [108], which represents robustly the curl Maxwell equations.

Figure 2.14 shows how the components of the electric and magnetic field vectors are located in the Yee algorithm. They are placed in 3D space so that every component of **E** is surrounded by four circulating **H** components and vice versa. This gives rise to a filling of the space by interlinked contours of curl Maxwell equations. Moreover, this distribution of EM fields components enforces the Gauss-Maxwell relations. Thus, Yee grid is divergence free with respect to both **E** and **H** in absence of charges.

Yee algorithm also arranges **E** and **H** components in time, following the so-called leapfrog fashion. The electric field is calculated and stored at a given time using the magnetic field data obtained in the preceding time step. Then, new results for **H** components are obtained from the electric field just stored and the previous magnetic field. This cycle, depicted in Fig. 2.15 , is repeated until the loop in time finishes. The explicit character of this procedure avoids problems arising in other approaches due to simultaneous equations and matrix inversions.

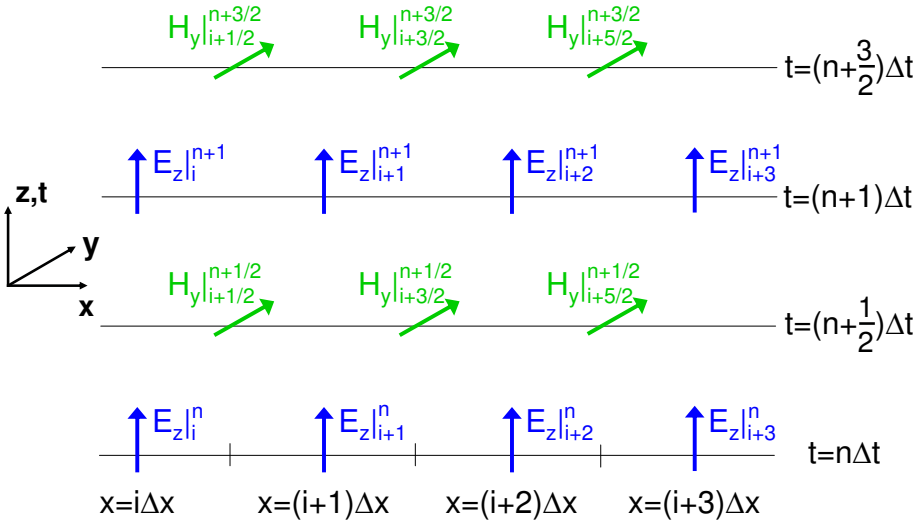

Figure 2.15.: Space-time sampling of the Yee algorithm showing the use of central differences for the spatial derivatives and leapfrog stepping for the time derivatives.

In order to show how the Yee algorithm is incorporated into the FDTD method, we build discretized expressions for the Faraday and Ampere-Maxwell equations

$$\nabla \times \mathbf{E} = -\frac{\mu(\mathbf{r})}{c}\partial_t \mathbf{H}, \tag{2.105}$$

$$\nabla \times \mathbf{H} = \frac{\epsilon(\mathbf{r})}{c}\partial_t \mathbf{E}. \tag{2.106}$$

We define Δx, Δy and Δz as the Yee mesh dimensions, and Δt as the time increment. Each node of the spatial grid is labelled with three integers, $\{i, j, k\}$ (see Fig. 2.14), and we associate index n with each time step (see Fig. 2.15). Thus, we can denote any function of space and time, u, evaluated at a discrete point in the spatial grid and at a discrete point in time as $u(i\Delta x, j\Delta y, k\Delta z, n\Delta t) = u|^n_{i,j,k}$.

The discrete version of the spatial derivatives of this function, evaluated at a fixed time, are

$$\begin{aligned}
\frac{\partial u}{\partial x}(i\Delta x, j\Delta y, k\Delta z, n\Delta t) &= \frac{u|^n_{i+1/2,j,k} - u|^n_{i-1/2,j,k}}{\Delta x} + O[(\Delta x)^2], \\
\frac{\partial u}{\partial y}(i\Delta x, j\Delta y, k\Delta z, n\Delta t) &= \frac{u|^n_{i,j+1/2,k} - u|^n_{i,j-1/2,k}}{\Delta y} + O[(\Delta y)^2], \\
\frac{\partial u}{\partial x}(i\Delta x, j\Delta y, k\Delta z, n\Delta t) &= \frac{u|^n_{i,j,k+1/2} - u|^n_{i,j,k-1/2}}{\Delta y} + O[(\Delta y)^2].
\end{aligned} \tag{2.107}$$

Similarly, the time derivative of u, evaluated at a fixed space point i, j, k, has the form

$$\frac{\partial u}{\partial t}(i\Delta x, j\Delta y, k\Delta z, n\Delta t) = \frac{u|_{i,j,k}^{n+1/2} - u|_{i,j,k}^{n-1/2}}{\Delta t} + O[(\Delta t)^2]. \tag{2.108}$$

Note that taking increments of the form $\pm 1/2\Delta$ is the most convenient choice in order to perform the interleave of electric and magnetic field components characteristic of the Yee algorithm. Thus, we can write the discrete version of Eqs. (2.105) and (2.106) in the grid shown in Fig. 2.14 as

$$\begin{aligned} E_x|_{i+1/2,j,k}^{n+1/2} &= E_x|_{i+1/2,j,k}^{n-1/2} \\ &+ \frac{c\Delta t}{\epsilon_{i+1/2,j,k}} \begin{bmatrix} (\Delta y)^{-1}[H_z|_{i+1/2,j+1/2,k}^{n} - H_z|_{i+1/2,j-1/2,k}^{n}] \\ -(\Delta z)^{-1}[H_y|_{i+1/2,j,k+1/2}^{n} - H_y|_{i+1/2,j,k-1/2}^{n}] \end{bmatrix}, \end{aligned} \tag{2.109}$$

$$\begin{aligned} E_y|_{i,j+1/2,k}^{n+1/2} &= E_x|_{i,j+1/2,k}^{n-1/2} \\ &+ \frac{c\Delta t}{\epsilon_{i,j+1/2,k}} \begin{bmatrix} (\Delta z)^{-1}[H_x|_{i,j+1/2,k+1/2}^{n} - H_x|_{i,j+1/2,k-1/2}^{n}] \\ -(\Delta x)^{-1}[H_z|_{i+1/2,j+1/2,k}^{n} - H_z|_{i-1/2,j+1/2,k}^{n}] \end{bmatrix}, \end{aligned} \tag{2.110}$$

$$\begin{aligned} E_z|_{i,j,k+1/2}^{n+1/2} &= E_x|_{i,j,k+1/2}^{n-1/2} \\ &+ \frac{c\Delta t}{\epsilon_{i,j,k+1/2}} \begin{bmatrix} (\Delta x)^{-1}[H_y|_{i+1/2,j,k+1/2}^{n} - H_x|_{i-1/2,j,k+1/2}^{n}] \\ -(\Delta y)^{-1}[H_x|_{i,j+1/2,k+1/2}^{n} - H_x|_{i,j-1/2,k+1/2}^{n}] \end{bmatrix}, \end{aligned} \tag{2.111}$$

$$\begin{aligned} H_x|_{i,j+1/2,k+1/2}^{n+1/2} &= H_x|_{i,j+1/2,k+1/2}^{n-1/2} \\ &+ \frac{c\Delta t}{\mu_{i,j+1/2,k+1/2}} \begin{bmatrix} (\Delta z)^{-1}[E_y|_{i,j+1/2,k+1}^{n} - E_y|_{i,j+1/2,k}^{n}] \\ -(\Delta y)^{-1}[E_z|_{i,j+1,k+1/2}^{n} - E_z|_{i,j,k+1/2}^{n}] \end{bmatrix}, \\ H_y|_{i+1/2,j,k+1/2}^{n+1/2} &= H_x|_{i+1/2,j,k+1/2}^{n-1/2} \\ &+ \frac{c\Delta t}{\mu_{i+1/2,j,k+1/2}} \begin{bmatrix} (\Delta x)^{-1}[E_z|_{i+1,j,k+1/2}^{n} - E_z|_{i,j,k+1/2}^{n}] \\ -(\Delta z)^{-1}[E_x|_{i+1/2,j,k+1}^{n} - E_x|_{i+1/2,j,k}^{n}] \end{bmatrix}, \end{aligned} \tag{2.112}$$

$$\begin{aligned} H_z|_{i+1/2,j+1/2,k}^{n+1/2} &= H_z|_{i+1/2,j+1/2,k}^{n-1/2} \\ &+ \frac{c\Delta t}{\epsilon_{i+1/2,j+1/2,k}} \begin{bmatrix} (\Delta y)^{-1}[E_x|_{i+1/2,j+1,k}^{n} - E_x|_{i+1/2,j,k}^{n}] \\ -(\Delta x)^{-1}[E_y|_{i+1,j+1/2,k}^{n} - E_y|_{i,j+1/2,k}^{n}] \end{bmatrix}, \end{aligned} \tag{2.113}$$

where $\epsilon_{i,j,k}$ and $\mu_{i,j,k}$ are the discrete version of the permittivity and permeability evaluated at the node $\{i, j, k\}$. Eqs. (2.109)-(2.113) illustrate the interspersed distribution of $\mathbf{E}$ and $\mathbf{H}$ in the Yee mesh and the performance of the leapfrog approach describing the evolution in time of the whole EM field.

Finally, we discuss briefly how the dispersive dielectric constant of real metals can be implemented in the FDTD approach. We consider a frequency-dependent Drude-like permittivity [97] of the form $\epsilon_M(\omega) = \epsilon_\infty - \frac{\omega_p^2}{\omega(\omega+i\gamma_p)}$. In time domain, the relation between the displacement field, $\mathbf{D}$, and the electric field, $\mathbf{E}$, is given by the convolution

$$\mathbf{D}(t) = \epsilon_\infty \mathbf{E}(t) + 4\pi \int_0^t \mathbf{E}(t-\tau)\chi(\tau)d\tau, \tag{2.114}$$

where $\chi(\tau) = -\frac{\omega_p^2}{\gamma_p}(1-e^{-\gamma_p t})U(t)$ is the time-domain susceptibility function, being $U(t)$ the unit step. This equation describes the causal relation between the displacement and electric fields, as only $\tau < t$ are involved in the convolution. Eq. (2.114) can be discretized following the recipes presented above, and using a linear approximation for $\mathbf{E}$ inside the integral, having

$$\mathbf{D}^n = \epsilon_\infty \mathbf{E}^n + 4\pi \sum_{m=0}^{n-1} \left[\mathbf{E}^{n-m}\chi^m + (\mathbf{E}^{n-m-1} - \mathbf{E}^{n-m})\xi^m\right], \tag{2.115}$$

where $\chi^m = \int_{m\Delta t}^{(m+1)\Delta t} \chi(\tau)d\tau$ and $\xi^m = \frac{1}{\Delta t}\int_{m\Delta t}^{(m+1)\Delta t}(\tau - m\Delta t)\chi(\tau)d\tau$.

The combination of Eq. (2.115) with the discretized Ampere's law, $\nabla \times \mathbf{H}^{n+1/2} = (c\Delta t)^{-1}[\mathbf{D}^{n+1} - \mathbf{D}^n]$, yields

$$\begin{aligned}\mathbf{E}^{n+1} = &\left[\frac{\epsilon_\infty - 4\pi\xi^0}{\epsilon_\infty - 4\pi(\xi^0 - \chi^0)}\right]\mathbf{E}^n \\ &+\left[\frac{c\Delta t}{\epsilon_\infty - 4\pi(\xi^0 - \chi^0)}\right]\nabla \times \mathbf{H}^{n+1/2} + \left[\frac{1}{\epsilon_\infty - 4\pi(\xi^0 - \chi^0)}\right]\mathbf{\Psi}^n.\end{aligned} \tag{2.116}$$

This vectorial equation allows the updating of the electric field inside a Drude metal. It replaces Eqs. (2.109)-(2.111) when solving Maxwell equations inside nondispersive media. In Eq. (2.116), we have introduced the artificial vector

$$\mathbf{\Psi}^n = \sum_{m=0}^{n-1}[\mathbf{E}^{n-m}(\chi^m - \chi^{m+1}) + (\mathbf{E}^{n-m-1} - \mathbf{E}^{n-m})(\xi^m - \xi^{m+1})], \tag{2.117}$$

which reflects the causal relation between $\mathbf{D}$ and $\mathbf{E}$ without the need to evaluate explicitly the convolution integral in Eq. (2.114). Thus, this approach, termed piecewise-linear recursive-convolution algorithm [111], allows the treatment of metallic media in a very efficient manner within the FDTD methodology, as vector $\mathbf{\Psi}^n$ can be calculated and updated recursively in time.

2.5. Finite integration technique

One decade after the publication of the seminal paper by Yee [108] establishing the foundations of the FDTD method, T. Weiland [112] introduced a different computational

approach for analyzing complex EM phenomena. Instead of starting from differential Maxwell equations, this novel method, termed finite integration technique (FIT), aimed at solving the Maxwell equations in integral form. It used all six vector components of the electric field strength and magnetic flux density on a dual grid system similar to the Yee mesh. In 1996, Weiland [113] reformulated the FIT in terms of quantities linked to space objects: electric and magnetic voltages assigned to grid contours, and electric and magnetic fluxes assigned to grid surfaces. This fact allows the matrix formulation of FIT, which made it also valid for irregular and non-orthogonal grids. For the case of leapfrog time-stepping schemes applied to cartesian meshes, the discrete equations coming out from FIT are identical to the FDTD ones. Therefore, FDTD method can be considered as a subset of the most general version of FIT [114].

In this section, we describe how the discrete integral Maxwell equations are constructed in FIT [115]. The first discretization step consists in the decomposition of the simulation domain into basic cells. In principle, these can have any geometry, while they fit exactly to each other, but for simplicity, here we consider the case of a uniform hexahedral computational grid, Γ. We label the positions of the grid nodes as (x_i, y_j, z_k), and the total number of nodes in Γ as $N_p = I \times J \times K$, where I, J and K stand for the number of nodes in the three spatial directions.

We restrict the finite integration procedure to the volume, V, of a single grid cell, shown in Fig. 2.16. First, we construct the discrete version of the integral Faraday's law

$$\oint_{\partial A} \mathbf{E}(\mathbf{r},t)\cdot d\mathbf{s} = -\frac{1}{c}\int\int_{A}\frac{\partial}{\partial t}\mathbf{B}(\mathbf{r},t)\cdot d\mathbf{A}, \tag{2.118}$$

where ∂A is the contour of the area A. For the face $A_z(i,j,k)$ of V [see panel (a) of Fig. 2.16], Eq. (2.118) can be written as

$$\widehat{\mathrm{e}}_x(i,j,k) + \widehat{\mathrm{e}}_y(i+1,j,k) - \widehat{\mathrm{e}}_x(i,j+1,k) - \widehat{\mathrm{e}}_y(i,j,k) = -\frac{1}{c}\frac{\partial}{\partial t}\widehat{\widehat{\mathrm{b}}}_z(i,j,k), \tag{2.119}$$

where we have defined $\widehat{\mathrm{e}}_x(i,j,k) = \int_{(x_i,y_j,z_k)}^{(x_i+1,y_j,z_k)} \mathbf{E}\cdot d\mathbf{s}$, which is the electric voltage along one edge of the surface $A_z(i,j,k)$. This scalar quantity represents the exact value of the integral of the electric field along this edge. We have also introduced the magnetic flux $\widehat{\widehat{\mathrm{b}}}_z(i,j,k) = \int\int_{A_z(i,j,k)} \mathbf{B}\cdot d\mathbf{A}$, given by the integral of the magnetic flux density through the cell surface $A_z(i,j,k)$.

The discrete version of the magnetic Gauss equation in integral form,

$$\int\int_{\partial V} \mathbf{B}(\mathbf{r},t)\cdot d\mathbf{A} = 0, \tag{2.120}$$

can be obtained following a similar procedure. Applied to the grid cell [see panel (b) of Fig. 2.16], the closed surface integral in Eq. (2.120) can be expressed in terms of the

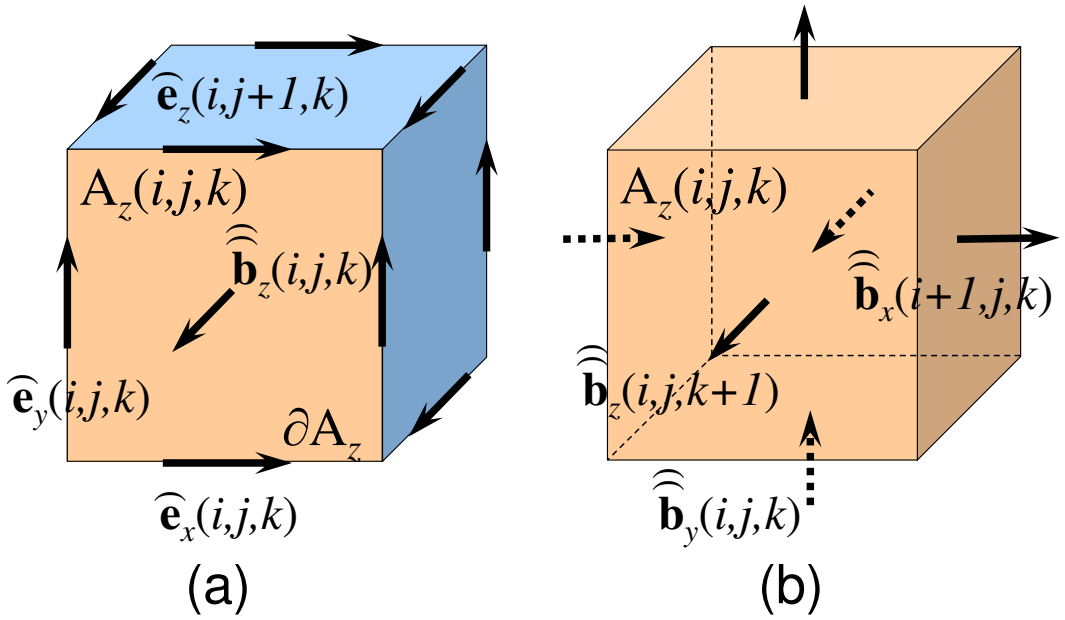

Figure 2.16.: Panel (a): FIT cell showing the electric voltages $\widehat{\mathrm{e}}$ on the edges of the face $A_z(i,j,k)$) and the magnetic fluxes $\widehat{\widehat{\mathrm{b}}}$ through this surface. Panel (b): Location of the six magnetic facet fluxes, $\widehat{\widehat{\mathrm{b}}}$, considered in the evaluation of the closed surface integral for the non-existence of magnetic charges within the cell.

magnetic fluxes through each of its faces as

$$\begin{aligned} -\widehat{\widehat{\mathrm{b}}}_x(i,j,k)+\widehat{\widehat{\mathrm{b}}}_x(i+1,j,k)-\widehat{\widehat{\mathrm{b}}}_y(i,j,k)+\widehat{\widehat{\mathrm{b}}}_y(i,j+1,k) & \\ -\widehat{\widehat{\mathrm{b}}}_z(i,j,k)+\widehat{\widehat{\mathrm{b}}}_z(i,j,k+1) &= 0 \end{aligned} \tag{2.121}$$

Up to this point, we have presented the integral formulation of Faraday and magnetic Gauss equations for a single cell. However, this discretization scheme can be extended to the whole simulation domain by introducing the $3N_p$-sized vectors

$$\widehat{\mathbf{e}} = (\widehat{\mathrm{e}}_{x,n}|\widehat{\mathrm{e}}_{y,n}|\widehat{\mathrm{e}}_{z,n})^T_{n=1,\ldots,N_p}, \tag{2.122}$$

$$\widehat{\widehat{\mathbf{b}}} = (\widehat{\widehat{\mathrm{b}}}_{x,n}|\widehat{\widehat{\mathrm{b}}}_{y,n}|\widehat{\widehat{\mathrm{b}}}_{z,n})^T_{i,j,k=1,\ldots,N_p}. \tag{2.123}$$

whose entries correspond to all the electric voltages and magnetic fluxes in Γ. Thus, the

equation (2.119) for all cell surfaces can be collected in matrix form as

$$\begin{pmatrix} & \cdots & \cdots & \cdots & \cdots & \\ \cdots & 1 & 1 & -1 & -1 & \cdots \\ & \cdots & \cdots & \cdots & \cdots & \end{pmatrix} \begin{pmatrix} \widehat{\mathrm{e}}_1 \\ \vdots \\ \widehat{\mathrm{e}}_{3N_p} \end{pmatrix} = -\frac{1}{c}\frac{\partial}{\partial t} \begin{pmatrix} \widehat{\widehat{\mathrm{b}}}_1 \\ \vdots \\ \widehat{\widehat{\mathrm{b}}}_{N_p} \end{pmatrix}, \tag{2.124}$$

which can be written as

$$\mathbf{C}\widehat{\mathbf{e}} = -\frac{1}{c}\frac{\partial}{\partial t}\widehat{\widehat{\mathbf{b}}} \tag{2.125}$$

where matrix $\mathbf{C}$ represents a discrete curl-operator on the grid Γ.

Similarly, Eq. (2.120) for a single cell can be expanded to the whole grid Γ as

$$\begin{pmatrix} & \cdots & \cdots & \cdots & \cdots & \cdots & \cdots & \\ \cdots & 1 & 1 & 1 & -1 & -1 & -1 & \cdots \\ & \cdots & \cdots & \cdots & \cdots & \cdots & \cdots & \end{pmatrix} \begin{pmatrix} \widehat{\widehat{\mathrm{b}}}_1 \\ \vdots \\ \widehat{\widehat{\mathrm{b}}}_{N_p} \end{pmatrix} = 0, \tag{2.126}$$

which enables us to define the discrete divergence matrix $\mathbf{S}$ and rewrite Eq. (2.126) as

$$\mathbf{S}\widehat{\widehat{\mathbf{b}}} = 0. \tag{2.127}$$

Note that both the curl, $\mathbf{C}$, and the divergence, $\mathbf{S}$, are discrete operators that only depend on the grid topology, and their entries satisfy C_{ij}, $S_{ij} \in \{1, 0, -1\}$.

The integral Ampere's law in absence of currents reads

$$\oint_{\partial \tilde{A}} \mathbf{H}(\mathbf{r}, t) \cdot d\mathbf{s} = -\frac{1}{c} \int \int_{\tilde{A}} \frac{\partial}{\partial t} \mathbf{D}(\mathbf{r}, t) \cdot d\mathbf{A}. \tag{2.128}$$

The Gauss' law in absence of charges has the form

$$\int \int_{\partial V} \mathbf{D}(\mathbf{r}, t) \cdot d\mathbf{A} = 0. \tag{2.129}$$

The discretization of these two remaining Maxwell equations requires the introduction of a second cell $\tilde{\Gamma}$ which is dual to the primary cell Γ. For the case of cartesian geometries, Γ and $\tilde{\Gamma}$ are equivalent to the electric and magnetic subgrids in the Yee mesh (see Fig. 2.14). Within the dual grid, we define the $3N_p$-sized vector of magneto motive forces $\widehat{\mathbf{h}}_n = \int_{\partial \tilde{A}_n} \mathbf{H} \cdot d\mathbf{s}$, which contains the integrals of the magnetic field along every edge $\partial \tilde{A}_n$ in $\tilde{\Gamma}$. Similarly, we introduce the $3N_p$-sized vector of displacement fluxes through all cells faces, $\tilde{A}_n$, $\widehat{\widehat{\mathrm{d}}}_n = \int \int_{\tilde{A}_n} \mathbf{D} \cdot d\mathbf{A}$. With these definitions, we are able to write the FIT expressions for Eqs. (2.128) and (2.129), having

$$\tilde{\mathbf{C}}\widehat{\mathbf{h}} = -\frac{1}{c}\frac{\partial}{\partial t}\widehat{\widehat{\mathbf{d}}}, \tag{2.130}$$

$$\tilde{\mathbf{S}}\widehat{\widehat{\mathbf{d}}} = 0, \tag{2.131}$$

where we have introduced the curl and divergence operators, $\tilde{\mathbf{C}}$ and $\tilde{\mathbf{S}}$, defined within $\tilde{\Gamma}$. Eqs. (2.125), (2.127), (2.130) and (2.131) define the complete set of the so-called Maxwell grid equations.

Up to here, we have focused on the spatial discretization of Maxwell equations but we have not considered the dependence on time of the EM fields within FIT. The algebraic properties of the FIT Maxwell grid equations allows proving charge and energy conservation within several time-stepping schemes. Some of the most extended time-stepping approaches are the leapfrog FDTD algorithm, certain second order implicit methods, and implicit time integration techniques [115]. The versatility and space-time stability featured by FIT distinguish it from many alternative methods whose range of application is much narrower and which may become unstable or inaccurate within long term calculations.

3. Geometrically induced surface electromagnetic modes

3.1. Introduction

The occurrence of transmission resonances in perforated perfect conducting films [45], which do not sustain surface plasmons, has led to a growing interest in these structures. Recently, it has been demonstrated that corrugations on the surface of a perfect conductor make it behave as an effective metal whose dielectric response is controlled by geometry [56, 57]. It has been also shown that the geometrically induced electromagnetic modes sustained by these systems, termed spoof surface plasmon polaritons, have characteristics resembling those of conventional surface plasmon polaritons in the optical regime.

At low frequencies, electromagnetic modes bound to metal-dielectric interfaces, the so-called Zenneck [2] or Sommerfeld [1] waves, are not suitable for guiding purposes due to their weak confinement to the metal surface. For this reason, surface modes in periodic metal designs have been thoroughly studied in the framework of telecommunication engineering [58–60]. In this context, spoof surface plasmon polaritons, despite of being theoretical idealizations, open the way to transfer the technological potential of plasmonics to low frequency domains, where perfect electric conducting metals are an excellent approximation. This has given rise to an intense scientific activity in the last years. Recently, theoretical corrections to the spoof plasmon concept have been introduced [61, 62], and its extension to new geometries has been proposed [63]. Moreover, geometrically induced surface modes have been experimentally verified in the microwave regime [64, 65].

In this chapter, we study the formation of spoof plasmon modes on planar and cylindrical structures and analyze the dependence of their characteristics on the different geometrical parameters. Additionally, we propose two distinct guiding schemes featuring subwavelength confinement in the transverse plane which borrow ideas from the spoof plasmon concept and channel and wedge plasmon polaritons in the visible range [31, 36]. In order to illustrate the technological capabilities of our work, we set the dimensions of our designs so that they operate at terahertz frequencies. Finally, we present the

comparison of our theoretical results with experiments realized in the terahertz regime.

3.2. Planar geometries

3.2.1. Surface Plasmon Polaritons on a flat metallic surface

We motivate our study of geometrically induced electromagnetic (EM) modes by briefly reviewing the properties of surface plasmon polaritons (SPPs) supported by flat metallic surfaces [7, 9]. These are p-polarized waves propagating at the interface between a metal and a dielectric, evanescently confined in the perpendicular direction (see sketch in the upper inset of Fig. 3.1). In our description, we characterize the metal response through a lossless Drude-like dielectric function of the form $\epsilon_M(\omega) = 1 - \omega_p^2/\omega^2$, where ω_p is the plasma frequency of the free electron gas modelling the metal. This quantity defines the frequency range involved in the system. For most metals, ω_p lies in the ultraviolet part of the EM spectrum ($\sim 10^{16}$ Hz). In the inset of Fig. 3.1, ϵ_M versus the normalized frequency, ω/ω_p, is shown.

The dispersion relation for the SPPs supported by a flat metallic surface is obtained by imposing fields continuity at the system interface, having:

$$k = k_0 \sqrt{\frac{\epsilon_M(\omega)}{\epsilon_M(\omega) + 1}}, \tag{3.1}$$

where k is the wave vector component parallel to the metal-dielectric interface, and $k_0 = \omega/c$. For simplicity, we have chosen $\epsilon = 1$ for the dielectric medium. According to Eq. 3.1, $k > k_0$ for $\omega \lesssim \omega_p$, which reveals the bound character of SPPs. However, in the limit $\omega << \omega_p$, Eq. (3.1) yields $k = k_0$, which indicates that no confined modes are sustained by flat perfect electric conducting (PEC) surfaces.

The lower panel of Fig. 3.1 renders the SPPs dispersion relation calculated from Eq. (3.1). The parallel wave vector deviates from the light line for increasing frequency until $\omega_p/\sqrt{2}$, where it diverges. This evolution of k with ω controls the normal component of the wave vector in vacuum, $k_\perp = \sqrt{k^2 - k_0^2}$. At low frequencies, $|\epsilon_M| >> 1$, EM fields are expelled out of the metal, and SPPs extend into vacuum. However, as ω approaches $\omega_p/\sqrt{2}$, $|\epsilon_M|$ is reduced (see the inset of Fig. 3.1) and the the binding of the mode increases, achieving subwavelength field localization in the direction normal to the metal-vacuum interface.

From our brief analysis, we conclude that SPPs present their most interesting properties at frequencies slightly below ω_p, which usually correspond to the visible range ($\sim 10^{15}$ Hz). At these frequencies, SPPs transport efficiently EM energy within the metal

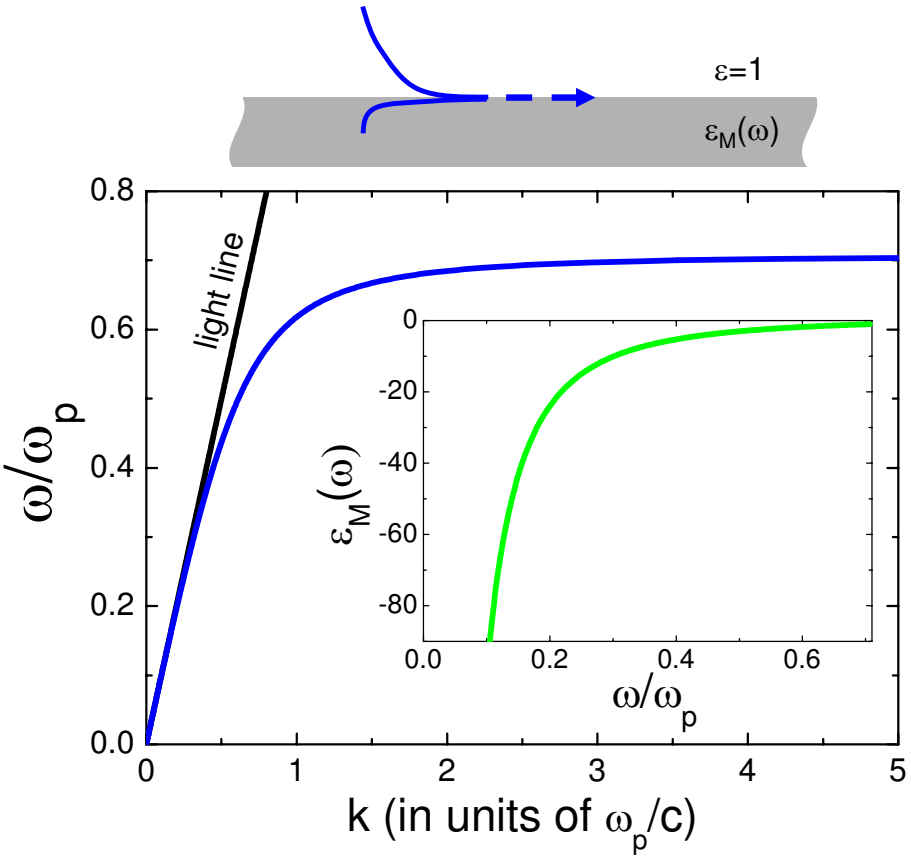

Figure 3.1.: Upper panel: Metal-vacuum interface supporting SPPs. Lower panel: Dispersion relation of SPPs supported by a flat lossless metal surface characterized by a Drude-like dielectric function. The inset plots the metal dielectric function versus frequency.

surface, featuring subwavelength fields confinement in the perpendicular direction. We have also shown that at frequencies much lower than ω_p, $k \simeq k_0$, EM fields spread into vacuum and SPPs lose their capabilities.

In the following sections, we describe how the limitations of conventional SPPs at frequencies much lower than ω_p can be overcome through the structuring of the metal surface. We will show that surface texturing creates surface EM modes even in the case of perfect conductivity (spoof SPPs). As length and frequency scales are not defined in PEC metals, this result allows transferring the properties of SPPs from the visible to lower frequency ranges. We will demonstrate that the characteristics of spoof SPPs are controlled by the geometry of the surface structure and compare our theoretical results with experiments performed at terahertz frequencies ($\lesssim 10^{14}$ Hz).

3.2.2. Spoof surface plasmon polaritons: groove and dimple arrays

We begin our analysis of the EM modes bound to textured PEC surfaces by considering the two geometries in which the concept of spoof SPPs was firstly developed: 1D arrays of grooves and 2D arrays of dimples. In Section 2.2.4, we introduced these two systems and discussed the suitability of our ME formalism for analyzing the characteristics of the EM modes bound to them. We showed that the spoof SPP dispersion relation in these two geometries is given by the non-vanishing solutions of the ME equations describing the fields continuity at the metal-vacuum interface (2.72)

$$(G_{\alpha\alpha} - \epsilon_\alpha)E_\alpha + \sum_{\beta\neq\alpha} G_{\alpha\beta}E_\beta = 0. \tag{3.2}$$

where α and β label the waveguide modes inside the indentations. The unknowns, E_α, correspond to the modal amplitudes of the electric field at the input side of the indentations. The term ϵ_α reflects the bouncing of the EM fields inside the indentations. It is given by Eqs. (2.40) and (2.30), for grooves and dimples, respectively. Finally, the term $G_{\alpha\beta}$ describes the interaction between EM fields linked to waveguide modes α and β through diffracted waves. Expressions for $G_{\alpha\beta}$ in the two systems considered are provided in Eqs. (2.42) (grooves) and (2.32) (dimples).

In Section 2.2.4, we demonstrated that it is possible to obtain analytical expressions for the spoof SPP dispersion relation in these two systems by introducing two approximations in our formalism. The first approximation consists in considering only the lowest waveguide mode inside the indentations, which leads to accurate results only for apertures much smaller than the wavelength. The second approximation consists in neglecting diffraction effects, taking only the zero-order diffracted wave in the expansion of the EM fields outside the indentations. This approximation is only valid for array periods much smaller than the wavelength, and even in this limit, it overestimates the binding of the EM modes. All the results shown in this section have been obtained through calculations including a sufficiently large number of modes as necessary for reaching convergence. However, it is worth taking into account the analytical dispersion relations since they enable us to gain physical insight into our problem.

We consider first the case of groove arrays. The left inset of Fig. 3.2 shows the geometrical parameters of the structure: the array period, d, and the grooves width and depth, a and h, respectively. As all lengths are scalable in PEC metals, we can consider d as the reference length. The approximated spoof SPP bands reads (2.75)

$$k_x = k_0\sqrt{1 + \left(\frac{a}{d}\right)^2 \tan^2(k_0 h)}. \tag{3.3}$$

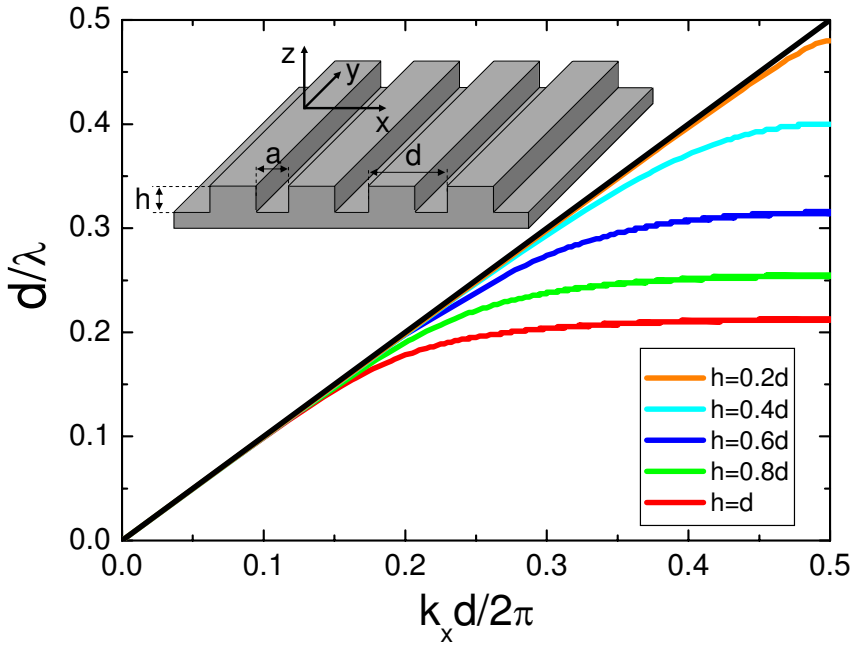

Figure 3.2.: Dispersion relation of the spoof SPPs sustained by arrays of grooves of width $a = 0.2d$. Five different grooves depth are represented ranging from $h = 0.2d$ to $h = d$. Black line corresponds to the light line. Left inset shows a schematic picture of the structure considered.

This analytical expression enables us to predict the behavior of the exact spoof SPP dispersion relation when the structure parameters are varied. Thus, according to Eq. (3.3), the spoof SPP bands deviate from the light line when the grooves depth, h, is enlarged. For $h = 0$, $k_x = k_0$ and, as expected, no bound mode is supported by the structure. However, when the PEC surface is milled with deeper grooves, the parallel wave vector increases having $k_x > k_0$.

Figure 3.2 displays the exact dispersion relation of the spoof SPPs supported by groove arrays of width $a = 0.2d$ and depth varying from $h = 0.2d$ to $h = d$. As predicted by Eq. (3.3), the spoof SPP bands shift to lower frequencies (d/λ) when the grooves depth is increased. This result can be understood in terms of groove cavity resonances. The lowest TM waveguide mode supported by 1D apertures is always propagating [see the lower equation in (2.37)]. Thus, the EM fields associated to spoof SPPs explore the whole groove depth, being very affected by changes in h. This fact provides the spoof SPP modes supported by 1D indentations a hybrid nature featuring characteristics of both surface and cavity EM modes.

In Fig. 3.3, the dispersion relation of the spoof SPPs sustained by periodic arrays of

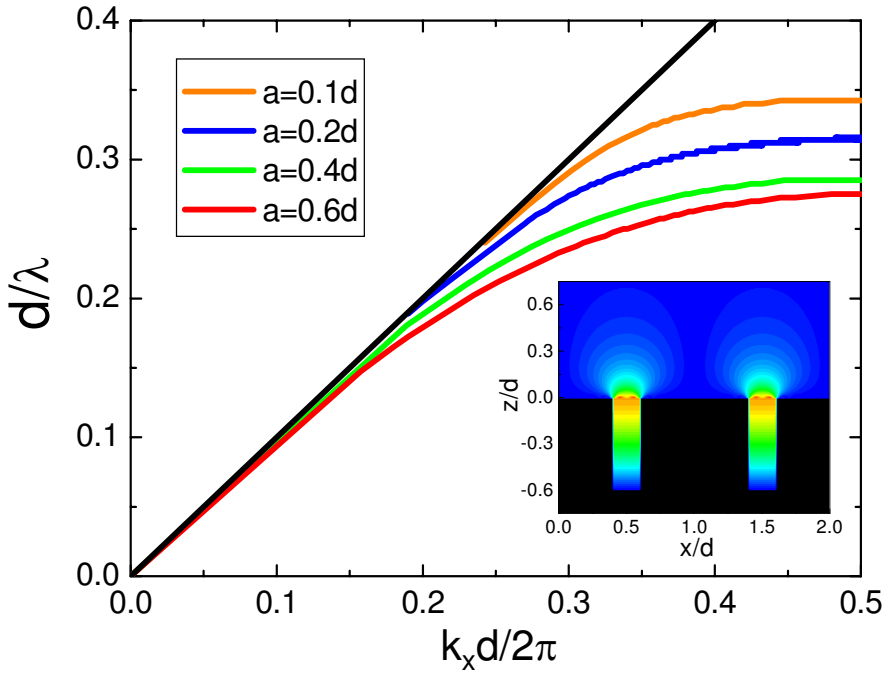

Figure 3.3.: Dispersion relation of the spoof SPPs supported by arrays of grooves of depth $h = 0.6d$. The grooves width is varied from $a = 0.1d$ to $a = 0.6d$. Black line shows the light line. Right inset: Electric field amplitude at the band edge for the case $a = 0.2d$.

grooves of depth $h = 0.6d$ is plotted. Four grooves widths between $a = 0.1d$ and $a = 0.6d$ are considered. The bands are lowered with larger a. This dependence on a is also predicted by Eq. (3.3), where k_x grows with increasing a. As we showed in 2.2.4, the ratio a/d governs the overlap between the zero-order diffracted wave and the first waveguide mode. Therefore, we can conclude that for wider indentations, the EM coupling at the system interface is larger, which increases the binding of the spoof SPP modes and shifts their dispersion relation to lower frequencies.

The right inset of Fig. 3.3 renders the electric field amplitude for the spoof SPPs on a groove array with $a = 0.2d$ and $h = 0.6d$. The electric field is evaluated at band edge ($k_x = \pi/d$), which corresponds to $d/\lambda = 0.31$ (blue line). Note that the electric field is enhanced inside the indentations at the system interface. The electric field decays more rapidly into the vacuum region than inside the grooves, which agrees with our interpretation of a spoof SPP as a hybrid between surface and groove cavity modes.

Now, we analyze the characteristics of the spoof SPPs on dimple arrays. In the inset of Fig. 3.4, the structure supporting geometrically induced bound modes is depicted. As in Section 2.2.4, we consider here only the case of square arrays of square dimples. The

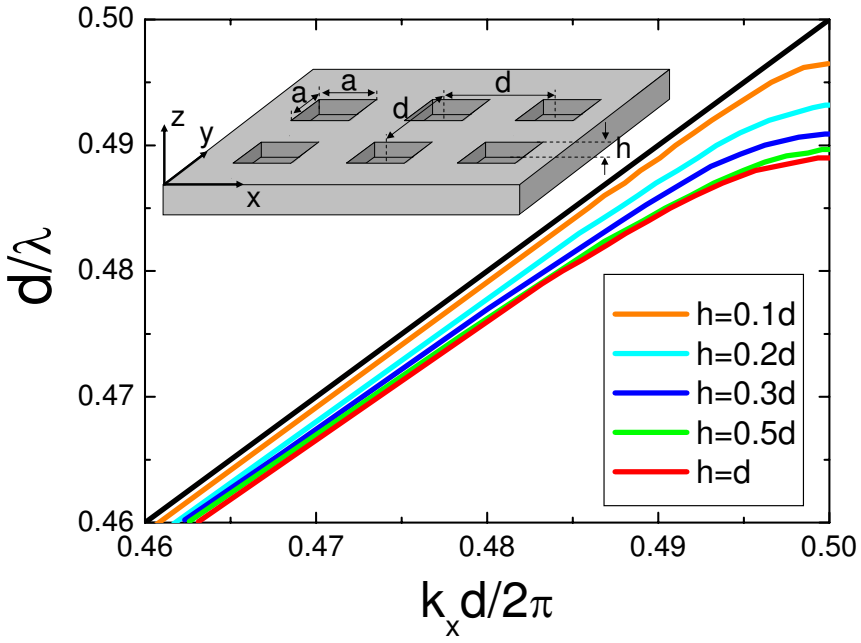

Figure 3.4.: Normalized frequency versus parallel wave vector for the spoof SPPs sustained by dimple arrays with $a = 0.6d$. Black line renders the light line. Bands corresponding to depths ranging from $h = 0.1d$ to $h = d$ are represented. Inset: sketch of the dimple array sustaining bound EM modes.

geometrical parameters of the system are now the 2D array period, d, taken as reference, and the dimples side and depth, a and h, respectively. The analytical expression for the dispersion relation of the corresponding spoof SPP modes has the form (2.77)

$$k_x = k_0 \sqrt{1 + \left(\frac{2\sqrt{2}a}{\pi d}\right)^4 \frac{k_0^2}{(\pi/a)^2 - k_0^2} \tanh^2\left(\sqrt{(\pi/a)^2 - k_0^2}\, h\right)}. \tag{3.4}$$

The main difference between Eqs. (3.3) and (3.4) resides in the different character of the lowest waveguide modes sustained by 1D and 2D indentations. As we showed above, this mode is always propagating inside 1D grooves. However, the lowest waveguide mode in 2D dimples, which corresponds to the TE mode with $l = 0$ and $s = 1$ in Eq. (2.7), is evanescent for $a < \lambda$ (which is the case we are analyzing). This fact leads to the tanh dependence on h that the analytical dispersion relation shows for dimple arrays. As we did for grooves, we can use Eq. (3.4) to predict the behavior of the exact spoof SPP bands when the geometrical parameters are modified.

Figure 3.4 plots the spoof SPP bands for dimples of side $a = 0.6d$. The depth of the indentations is varied from $h = 0.1d$ to $h = d$. Note that the dispersion relations are

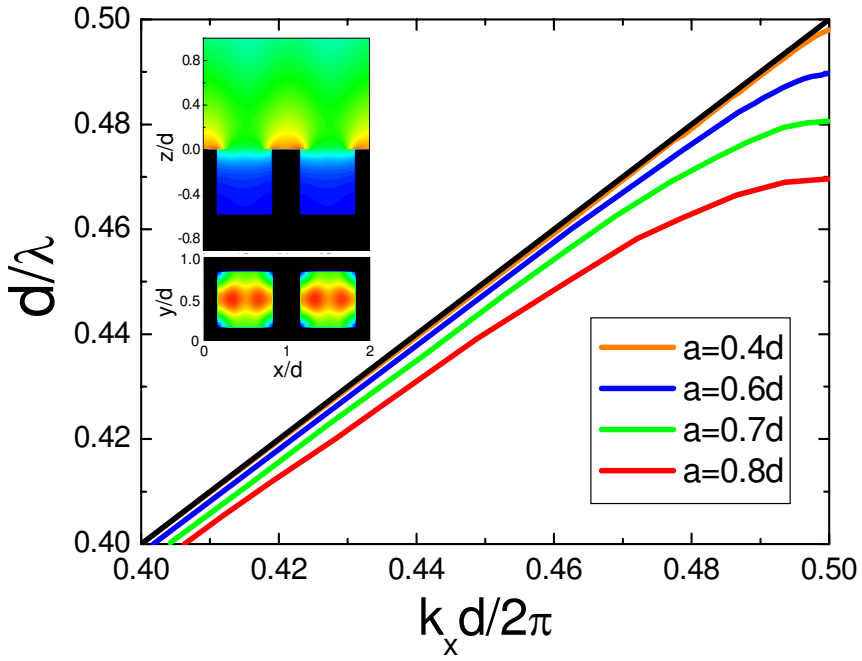

Figure 3.5.: Dispersion relation of the spoof SPPs on dimple arrays with $h = 0.6d$. The dimples width is varied from $a = 0.4d$ to $a = 0.8d$. Black line corresponds to the light line. Insets render the amplitude of the electric field at the band edge for the case with $a = 0.6d$. Two different cross-cuts are shown with different color scale: $y = 0.5d$ and $z = -0.2d$.

closer to the light line than in the case of 1D indentations. As in Fig. 3.2, the bands move to lower d/λ when the dimple depth is increased. However, this displacement is much smaller than in the case of grooves. This difference can be understood through Eq. (3.4). The tanh dependence on h in the analytical expression indicates that EM fields inside 2D indentations are evanescent. Thus, they decay before reaching the bottom of the dimples, making the spoof SPPs be less sensitive to variations in h.

In Figure 3.5, the dependence of the spoof SPP bands on the dimple area is analyzed. Dimples of depth $h = 0.6d$, and side between $a = 0.4d$ and $a = 0.8d$ are considered. As predicted by Eq. (3.4), the bands are bent at smaller d/λ as a is enlarged. Similarly to groove arrays, this effect can be interpreted as due to an increase in the EM coupling of diffracted and dimple waveguide modes, which in our analytical approach is proportional to $(a/d)^2$. The left insets render the electric field amplitude evaluated at the band edge for $a = 0.6d$ and $h = 0.5d$. The upper inset plots the electric field at $y = 0.5d$, whereas the lower one corresponds to the plane $z = -0.2d$. Note that the color scales in both cross-cuts are different. As we have predicted, the electric field is mostly located

at the system interface ($z = 0$) and decays along the z-direction inside the indentation ($z < 0$) and in vacuum ($z > 0$). This field distribution explains why the dispersion bands are closer to the light line than in groove arrays, as the binding of the modes to the surface texture is lower than in that case. Moreover, this result reinforces our view of the spoof SPPs supported by 2D indentations as surface EM modes.

We have analyzed the dependence of the dispersion relation of the spoof SPP modes supported by groove and dimple arrays on the depth, h, and width, a, of the indentations. Importantly, we have demonstrated that these two geometrical parameters govern the effective plasma frequency (see Sec. 3.2.1) for these EM modes, enabling the control of their propagation and confinement properties through the design of the surface structure. The emergence of this geometrically induced EM modes allows considering textured metallic surfaces as plasmonic metamaterials, as they gain their properties from their structure rather than their composition.

3.2.3. Spoof surface plasmon polaritons: slit and hole arrays

In this section, we study the spoof SPP modes supported by periodic arrays of 1D and 2D apertures drilled in PEC slabs of finite thickness and compare their characteristics with those of textured surfaces. In Section 2.2.4, we showed that, within our ME formalism, the geometrically induced modes in perforated films are given by the following set of linear equations describing the continuity of EM fields at both sides of the film (2.71)

$$\begin{aligned} (G_{\alpha\alpha} - \epsilon_\alpha)E_\alpha + \textstyle\sum_{\beta\neq\alpha} G_{\alpha\beta}E_\beta - G^V_\beta E'_\alpha = 0, \\ (G_\alpha - \epsilon_\alpha)E'_\alpha + \textstyle\sum_{\beta\neq\alpha} G_{\alpha\beta}E'_\beta - G^V_\alpha E_\alpha = 0. \end{aligned} \tag{3.5}$$

The unknowns in this system are E_α and E'_α, which are related to the electric field amplitudes at the aperture openings at both sides of the film. The definition of the $G_{\alpha\beta}$ and ϵ_α terms is the same as in Eq. (3.2). The G^V term links the electric field amplitudes at different sides of the film and takes into account the EM coupling through the perforations. Analytical expressions for G^V_α are provided in Eqs. (2.41) (slits) and Eq. (2.31) (holes).

As in the case of blind indentations, it possible to obtain analytical dispersion relations for spoof SPPs in perforated films. The approximations made in the model are the same as for grooves and dimples: considering only the first waveguide mode inside the apertures and the zero-order diffracted mode outside the film. For 1D arrays of slits, this approximate approach yields (2.81)

$$k_x = k_0\sqrt{1 + \left(\frac{a}{d}\right)^2 \frac{\sin^2(k_0 h)}{[\cos(k_0 h) \pm 1]^2}}, \tag{3.6}$$

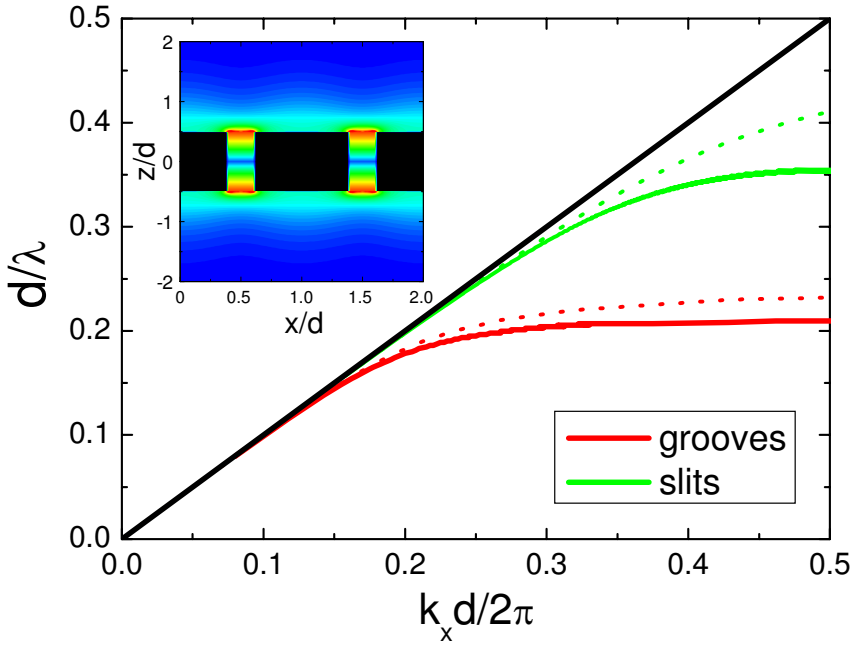

Figure 3.6.: Dispersion relation of the spoof SPPs supported by periodic arrays of 1D apertures (slits and grooves). In both cases, the apertures have the same width $a = 0.2d$ and depth $h = d$. Dotted lines render the analytical spoof SPP bands for both structures. Left inset depicts the amplitude of the electric field at the band edge for the slit array.

where the negative (positive) sign corresponds to spoof SPPs in which the electric field is symmetric (antisymmetric) with respect to the middle plane of the film.

Figure 3.6 renders the dispersion relation of the spoof SPPs supported by an array of slits and an array of grooves of the same dimensions. The width and depth of the apertures are $a = 0.2d$ and $h = d$, respectively. Note that in the case of slits, h corresponds to the thickness of the perforated film. For the geometrical parameters considered, both structures sustain only one bound mode. The dispersion relation for the array of slits is raised with respect to that of the groove array, which means that the spoof SPPs are less bounded to the structure. This can be understood by analyzing the behavior of EM fields inside the film. As we have already mentioned, the lowest TM waveguide mode in 1D apertures is always propagating, which translates into that EM fields bounce back and forth inside the perforations. Whereas the bottom of the grooves acts as a mirror, slit openings allow the coupling of waveguide modes with diffracted waves. This fact enables the spoof SPPs to extend out of the structure and shifts the spectral position of the cavity resonances (also termed Fabry-Perot resonances) inside slits to higher frequencies than in

the case of grooves. Dotted lines plot the bands obtained from our analytical approach. The approximated dispersion relation for the slit array has been calculated taking the positive sign in Eq. (3.6), which indicates that the spoof SPP mode is antisymmetric with respect to the middle plane of the structure.

The inset of Fig. 3.6 displays the electric field amplitude at the band edge for the slit array considered in the main panel. We can see that the electric field is enhanced at the slit openings, which demonstrates that the spoof SPPs are strongly influenced by diffraction effects at the slits ends. It can be also observed that the electric field vanishes at the center of the slits. This means that, as we have already predicted, the spoof SPPs have an odd parity with respect to the middle of the film.

Now, we consider the geometrically induced modes sustained by a PEC film pierced by an square arrangement of square holes. The analytical dispersion relation of these modes has the form (2.82)

$$k_x = k_0 \sqrt{1 + \left(\frac{2\sqrt{2}a}{\pi d}\right)^4 \frac{k_0^2}{(\pi/a)^2 - k_0^2} \frac{\sinh^2\left(\sqrt{(\pi/a)^2 - k_0^2}\, h\right)}{(\cosh\left(\sqrt{(\pi/a)^2 - k_0^2}\, h\right) \pm 1)^2}}. \tag{3.7}$$

As in the case of slits, the $\pm$ sign indicates the symmetry of the mode. Similarly to dimple arrays, the evanescent character of the EM fields inside the apertures is reflected through the hyperbolic functions in Eq. (3.7).

In Section 3.2.2 we demonstrated that the distinct character (propagating or evanescent) of the waveguide modes in grooves and dimples makes the characteristics of the spoof SPPs in such structures very different. This also occurs in the case of perforated films. We have seen that the main difference between spoof SPPs in slits and grooves resides in the modification of the cavity resonances inside the apertures. However, in the case of 2D perforations, the finite thickness of the PEC structure not only shifts the bands, but also gives rise to a splitting of the dispersion relation. This effect can be seen in Figure 3.7. It plots the spoof SPP bands for the case of a dimple array with $a = 0.6d$ and $h = 0.3d$. The dispersion relation corresponding to a periodic hole array of the same geometry is also shown. Note that as in 1D structures, h denotes now the thickness of the film. As we have anticipated, whereas the dimple array supports only one bound mode, two different spoof SPP bands appear for the hole array.

The origin of the two distinct spoof SPP modes in the hole array of Fig. 3.7 can be understood by looking at the field patterns in the upper insets of the figure. They show the electric field amplitude at $y = 0.5d$ (see insets of Fig. 3.5) corresponding to the two spoof SPP band edges. We can see that, in contrast to the modal shape displayed in Fig. 3.6, fields are not localized at the holes openings, but at the film surfaces. This agrees with

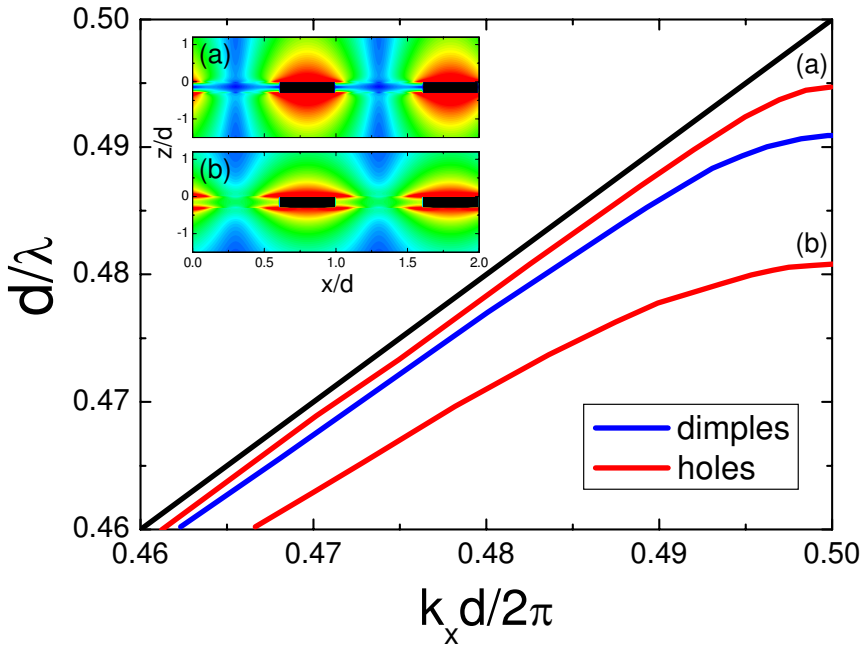

Figure 3.7.: Dispersion relation of the spoof SPPs sustained by periodic arrays of holes and dimples of the same dimensions. The side of the square apertures is $a = 0.6d$ and their depth is $h = 0.3d$. Insets show the electric field amplitude at the edge of the two spoof SPP bands for the hole array.

our interpretation of the spoof SPPs in 2D geometries as surface modes. According to this physical picture, the two spoof SPP modes in perforated films emerge from the interaction between the isolated surface modes at each side of the film. Thus, the lower band in Fig. 3.7 can be linked to the symmetric combination of both surface modes through the holes, whereas the higher band corresponds to the antisymmetric superposition of their evanescent tails. Note that the electric field in panel (a) vanishes inside the holes at the middle plane of the structure, while in panel (b) it shows a maximum at that position. This field pattern is similar to that corresponding to long range and short range SPPs in thin films [116].

Finally, notice that leaky spoof SPPs, whose dispersion relation lies above the light line, can be also treated with our formalism. These modes radiate while travelling within the system. Therefore, in the calculation of the dispersion relation for these modes, k must be considered as a complex quantity whose imaginary part describes the decay experienced by EM fields as they propagate along the PEC structure. Importantly, these leaky spoof SPPs play a crucial role in the reflection properties of corrugated surfaces, and in the transmission and reflection characteristics of perforated films.

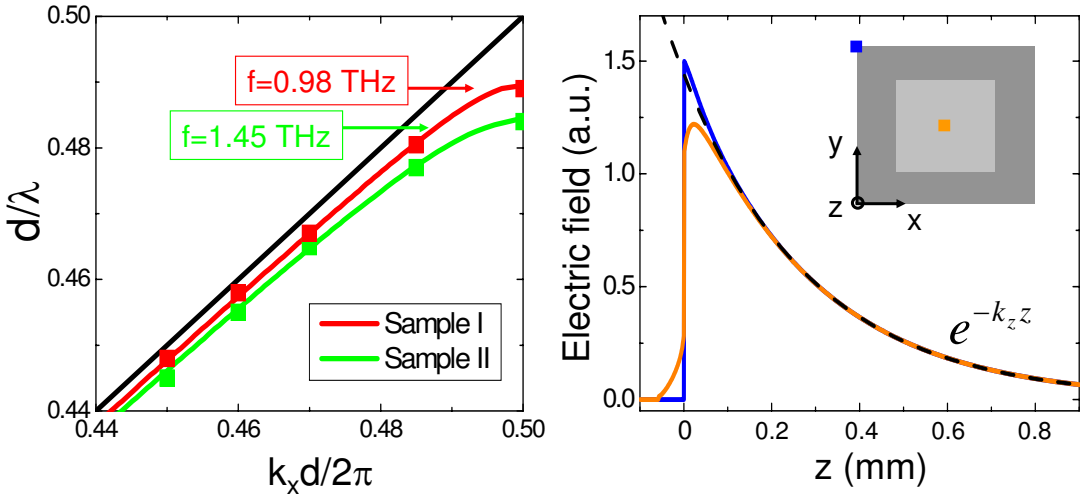

Figure 3.8.: Left panel: Dispersion relation of the spoof SPPs for the two experimental samples. Solid lines correspond to ME calculations and squares renders FDTD results. The frequencies at the band edge for both structures are indicated. Right panel: Electric field amplitude evaluated along the direction normal to the surface of sample I at two different positions within the dimple array unit cell.

3.2.4. Comparison with experiments in the terahertz regime

In this section, we present the comparison between the theoretical predictions obtained with our ME approach and the experiments carried out by the group of Prof. S. A. Maier and Dr. S. R. Andrews in the University of Bath on the propagation and confinement of spoof SPPs at THz frequencies. The measurements are performed on two planar copper surfaces (samples I and II) perforated by square arrays of square dimples (see insets of Fig. 3.9). The dimensions of the two samples are the following: the array period in sample I is $d = 150\,\mu$m, and the dimple side is $a = 91 \pm 5\,\mu$m, whereas sample II has $d = 100\,\mu$m and $a = 66 \pm 4\,\mu$m. The depth of the dimples in both samples is $h = 58 \pm 6\,\mu$m, and the thickness of the copper sheets is $0.5\,\mu$m. The samples are 40 mm long and 8 mm wide. Note that the uncertainties in the dimensions reflect systematic variations across the samples associated with the fabrication technique.

The left panel of Fig. 3.8 plots the theoretical dispersion relation of the spoof SPP modes supported by PEC dimple arrays with the same dimensions as the experimental samples. Solid lines correspond to the spoof SPP bands obtained through converged ME calculations and squares show FDTD results. The frequency at the band edge , f_{BE}, for both structures is also indicated: 0.98 THz (sample I) and 1.45 THz (sample II).

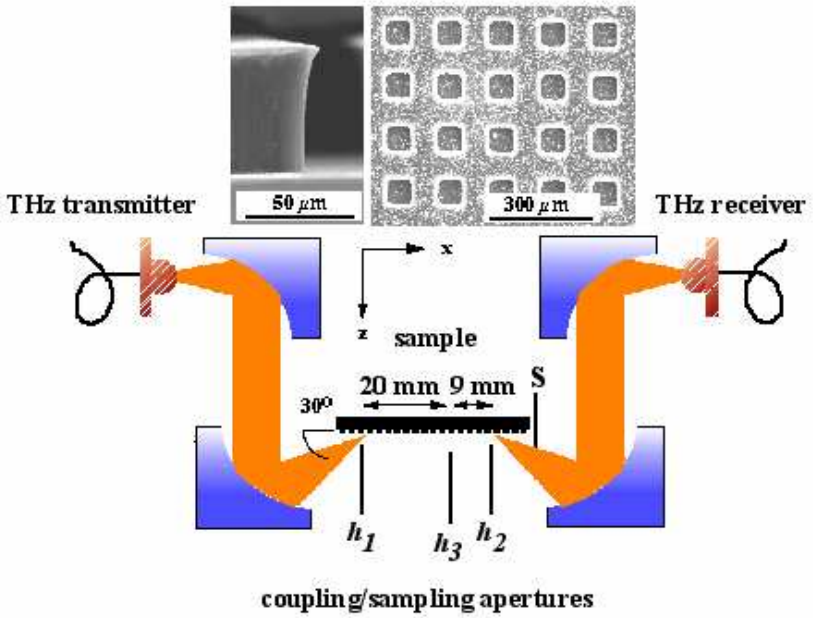

Figure 3.9.: Sketch of the experimental setup to study the propagation and confinement of spoof SPPs. Insets show electron micrographs of the top and cleaved edges of sample I.

The right panel of Fig. 3.8 displays the electric field amplitude at the band edge obtained through ME calculations for sample I. Electric field is evaluated along two lines perpendicular to the sample surface (z-direction), located at different positions within the structure unit cell (see inset). Black dashed line plots the fitting of the two field profiles to an exponential decay of the form $e^{-k_z z}$, where the normal wave vector, $k_z = \sqrt{k_x^2 - k_0^2}$, is calculated from the bands shown in the left panel of the figure. Note that 0.1 mm above the sample, the electric field decay is homogeneous within the dimple array unit cell.

The samples are studied experimentally using THz time-domain spectroscopy, in which the coherently detected signal current at a particular frequency is proportional to the electric field. Coupling of p-polarized free-space radiation to spoof SPPs is achieved using an aperture of wavelength-scale width, h_1, defined by a steel razor blade perpendicular to the sample surface (see Fig. 3.9). Diffraction at the aperture allows the phase matching to the spoof SPPs. An intermediate aperture, h_3, made from a 1.5 mm thick aluminum sheet is used to probe the extent of the spoof SPP field along the z-direction. Finally, diffraction at the final razor blade (with aperture h_2) is used to transform the spoof SPPs back into free-space radiation for detection. The propagation distance needed for the modal shape of the surface EM wave to be fully developed after its excitation is governed by the

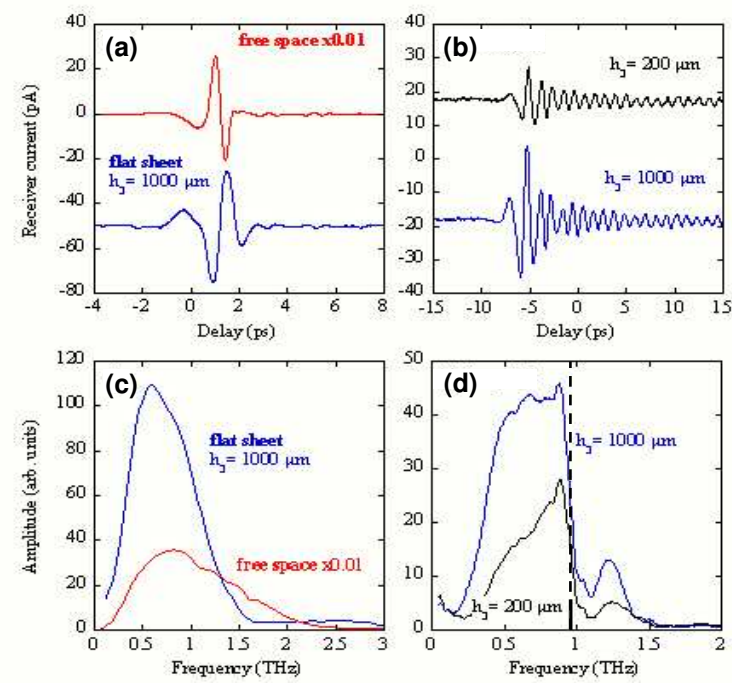

Figure 3.10.: Panels (a) and (c) show the time-domain signal and spectra corresponding to free-space coupling of the transmitter and receiver and to the propagation on a flat sheet. Panels (b) and (d) render the signals and spectra for sample I at two different intermediate apertures, h_3. Dash vertical line in panel (d) shows the theoretical f_{BE} for sample I.

perpendicular decay length, $l_z = 1/k_z$. This makes observations of SPPs on flat surfaces, the so-called Zenneck waves [2], difficult to measure as $l_z \simeq 10$ cm for copper at 1 THz [117]. In our case, l_z is of the order of few millimeters over a broad frequency range near the band edge, and therefore we can expect that spoof SPPs are fully developed in our setup.

Panels (b) and (d) of Fig. 3.10 render the time-domain signals and spectra after propagation along sample I. For comparison, data obtained by direct free-space coupling of the THz transmitter and receiver (that is, no sample) and for propagation on a perfectly flat copper surface are shown in panels (a) and (c). The time-domain trace of the unstructured surface is similar to that obtained with no sample. Because of the extremely low dispersion of Zenneck waves on flat surfaces, the small change in shape is mainly due to the effect of the apertures. In contrast, the signals from sample I show pronounced ringing, which persists for more than 10 ps, and the spectra exhibit sharp cut-offs at frequencies close to the theoretical f_{BE}, indicated by the vertical dashed line in panel (d).

If we suppose that the intermediate aperture simply passes part of the incident spoof

SPP without significantly altering its field distribution, then, to a first approximation, its effect is equivalent to integrate the Poynting vector parallel to the sample surface. As we have demonstrated in the right panel of Fig. 3.8, field profile for $z \gtrsim 0.1$ mm is homogeneous within the xy plane. This enables us to write the spoof SPPs electric field as $E(z,\omega) = A(\omega)e^{-k_z z}$. This approximated expression allows us to relate the electric field amplitudes at the input and output sides of the intermediate aperture, $A_1(\omega)$ and $A_2(\omega)$, respectively. Conservation of EM energy through h_3 requires that the ratio between the transmitted and incident field amplitudes is given by

$$A_2(\omega)/A_1(\omega) = \sqrt{1 - e^{-2k_z h_3}}. \tag{3.8}$$

The detected field after out-coupling, $E_D(\omega)$ is proportional to $A_2(\omega)$ if diffraction by the final razor blade can be neglected, so that k_z can, in principle, be determined from the variation of $E_D(\omega)$ with h_3.

In order to test the assumptions leading to Eq. (3.8) we perform numerical FIT simulations of the SPP propagation in the PEC approximation. Panels (a) to (c) of Fig. 3.11 render the distribution of the electric field evaluated within the xz plane of sample II for three different values of h_3. The aperture dimensions and positions are the same as in the experiments. The final razor blade is located at the right-hand edge of the structure and is not depicted in the figure. The frequency of the incident radiation (1.3 THz) is close to the band edge, where large confinement of the spoof SPP is expected. It is clear from Fig. 3.11 that the intermediate blade selectively passes the spoof SPP while blocking unwanted radiation diffracted at the input coupler. In panel (d), several z-cuts along the propagation direction showing the decay of the spoof SPP field in panel (b) ($h_3 = 0.5$ mm) are presented to allow comparison of the field confinement within and after the intermediate aperture. The field profile is maintained during the transmission process and the decay of the spoof SPP in the direction perpendicular to the surface closely corresponds to that calculated from the ME dispersion relation (see left panel of Fig. 3.8), as supposed in the derivation of Eq. (3.8).

We now verify that the dependence of the detected signal on h_3 carries information on the spatial confinement of the spoof SPPs propagating along the sample. In panel (e) of Fig. 3.11, the ratio A_2/A_1 obtained through FIT simulations (squares) is compared with that evaluated using Eq. (3.8) with k_z taken from the ME bands of Fig. 3.8. A_2/A_1 versus h_3 for sample II is shown at two different frequencies 0.7 THz (blue) and 1.3 THz (black). The good agreement obtained between FIT results, which include diffraction effects at the apertures, and the ME predictions, which neglect them, demonstrates the ability of the experimental technique to probe the confinement of the spoof SPP propagating at the samples, at least for $h_3 > \lambda$.

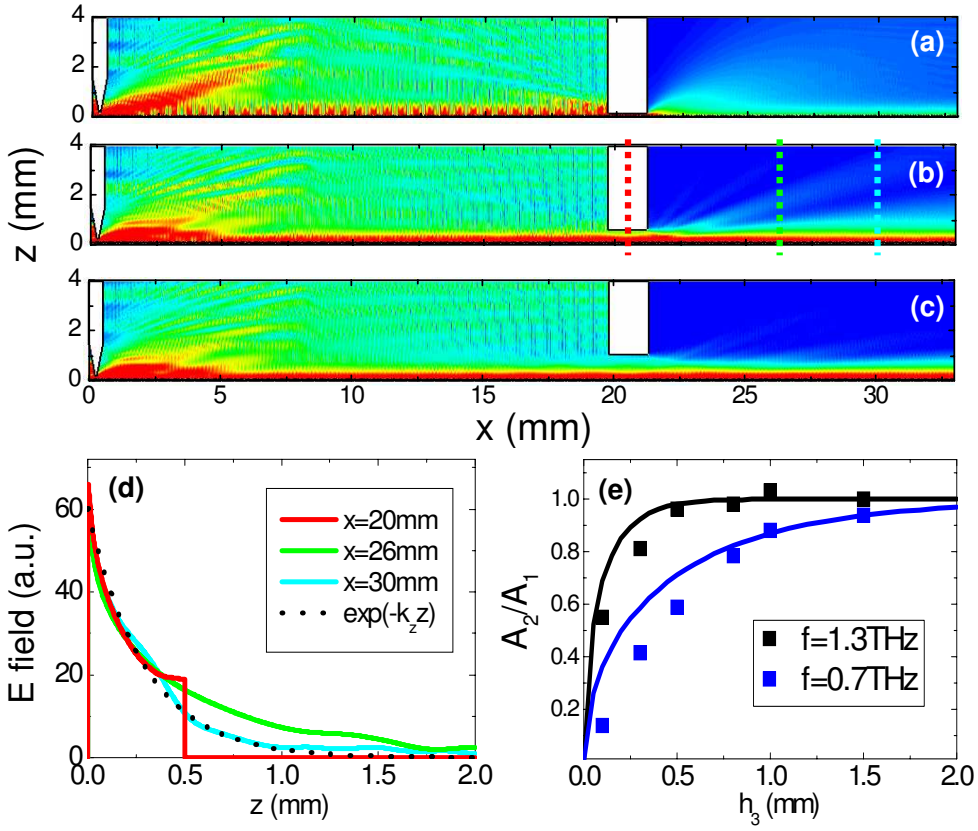

Figure 3.11.: Panels (a), (b) and (c) render FIT electric field amplitudes along sample II evaluated at 1.3 THz for $h_3 = 0.1$ mm, $h_3 = 0.5$ mm, and $h_3 = 1.0$ mm, respectively. Panel (d) shows the field profile along the z-direction at the positions indicated by dotted lines in panel (b). Panel (e) plots the ratio A_2/A_1 as a function of h_3 for two different frequencies: 1.3 THz (black line) and 0.7 THz (blue line). Squares correspond to values obtained from FIT simulations and solid lines are obtained using Eq. (3.8).

The experimental variation of $E_D(\omega)$ with h_3 for the two experimental samples is plotted in Fig. 3.12, which also plots theoretical predictions based on equation (3.8) (with k_z obtained from ME calculations) and scaled vertically to fit the data. The theoretical values for l_z are also shown in the figure. The agreement between theory and the measured amplitudes is very good, particularly for the higher frequencies where the confinement is strongest and diffraction effects are weakest, and for aperture heights of the order or greater than the wavelength, as anticipated from the above discussion. A fitting of the complete datasets (including the smallest aperture height) to Eq. (3.8) overestimates the decay length by a factor of the order of two for the reasons discussed above. A more

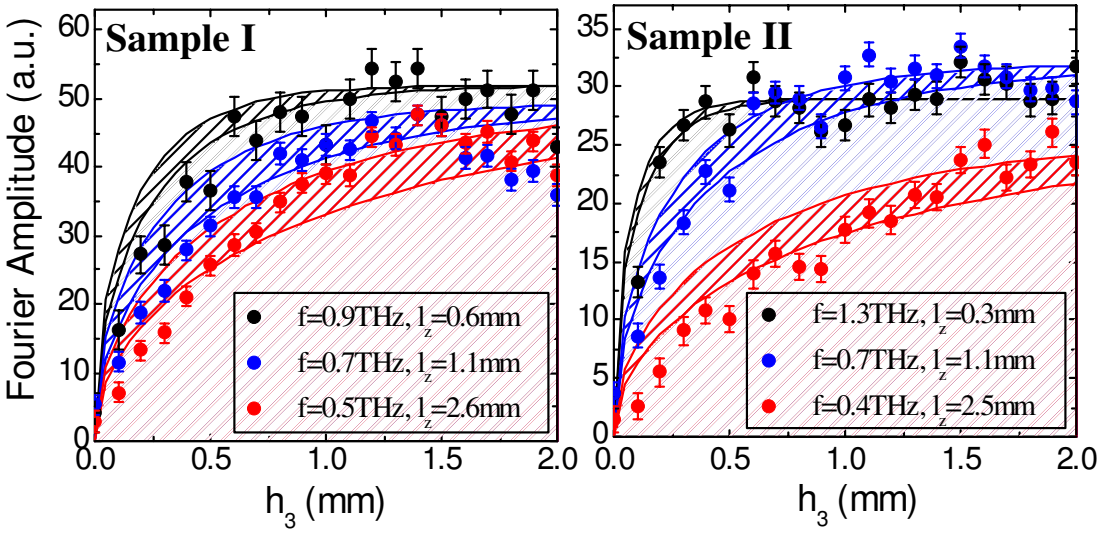

Figure 3.12.: Experimental (circles) and theoretical (shaded bands) electric field amplitudes as a function of the razor blade height, h_3. The error bars show the uncertainties in experimental measurements, and the theoretical curves are represented as bands in order to reflect the uncertainty in geometrical sample parameters. Theoretical results are evaluated from Eq. (3.8).

accurate experimental determination of l_z requires either a near-field probing scheme avoiding diffraction, or an analytical treatment that takes diffraction into account. However, it is clear that wavelength-scale energy confinement of the spoof SPPs over a wide frequency range near the band edge is experimentally observed, and that the degree of confinement is in close agreement with our theoretical predictions.

The measurements described in this section were the first experimental verification of the presence of bound spoof SPP modes decorating structured metal surfaces in the THz regime.

3.3. Cylindrical Geometries

3.3.1. Azimuthally independent surface plasmon polaritons

We introduce our study of geometrically induced EM modes on cylindrical structures by first analyzing the azimuthally independent SPPs propagating along the surface of real metal wires. We will focus on their behavior in the PEC limit, which will lead us to the application of the spoof SPP concept to wires. The rotational symmetry of the

system implies that the EM fields do not depend on θ (where θ is the azimuthal angle), leading to a decoupling of light polarizations (s and p). Since SPPs are TM modes, we restrict our study to the case of p-polarization, i.e., magnetic field normal to the wire axis (z-direction). In each region of the system, we write the relevant field components (E_z and H_θ) in terms of the corresponding solutions of Maxwell equations. As we are interested in EM modes propagating along the z-direction, we impose a $e^{ik_z z}$ behavior of EM fields. This allows us to consider only the radial dependence of E_z and H_θ which, in the vacuum region surrounding the wire, is given by

$$E_z^V(r) = E_V K_0(k_V r), \tag{3.9}$$

$$H_\theta^V(r) = Y_V(k_z) E_V K_1(k_V r), \tag{3.10}$$

where $k_V = \sqrt{k_z^2 - k_0^2}$ is the radial component of the wave vector and $Y_V(k_z) = ik_0/k_V$ is the mode admittance. The decaying behavior of the EM fields for increasing r is given by the modified Bessel functions of the second kind K_0 and K_1 [96].

Inside the metallic wire, EM fields must decay inwards with increasing distance from the wire surface (decreasing r). Their radial dependence can be expressed as

$$E_z^M(r) = E_M I_0(k_M r), \tag{3.11}$$

$$H_\theta^M(r) = Y_M(k_z) E_M I_1(k_M r), \tag{3.12}$$

where $k_M = \sqrt{k_z^2 - \epsilon_M(\omega) k_0^2}$ is the wave vector radial component into the wire, and $\epsilon_M(\omega)$ is the metallic dielectric function. The mode admittance inside the metal is defined as $Y_M(k_z) = -i\epsilon_M(\omega) k_0/k_V$. Finally, the radial dependence of the EM fields is now given by the modified Bessel functions of the first kind, I_0 and I_1 [96].

Imposing continuity of the EM fields at the cylindrical wire surface, we obtain the condition for the existence of nonzero solutions for the electric field amplitudes, E_V and E_M. This condition yields the dispersion relation of azimuthally independent SPP modes

$$k_V \frac{K_0(k_V R)}{K_1(k_V R)} = -\frac{k_M}{\epsilon_M(\omega)} \frac{I_0(k_M R)}{I_1(k_M R)}, \tag{3.13}$$

where R is the radius of the metallic wire.

In Figure 3.13, the dispersion relations of the azimuthally independent SPPs supported by lossless Au wires of different R calculated from Eq. (3.13) are plotted. The gold dielectric function considered in our calculations is taken from the experimentally fitted Drude-Lorentz-like formula of ref. [98]. We take only the real part of the complex Au permittivity, neglecting absorption effects inside the metallic wire. The wires radii (R) range from 0.02 μm (cyan short-dashed line) to 10 μm (green dashed line). It is worth commenting that the SPPs dispersion relation for the $R = 10\,\mu$m wire coincides (within

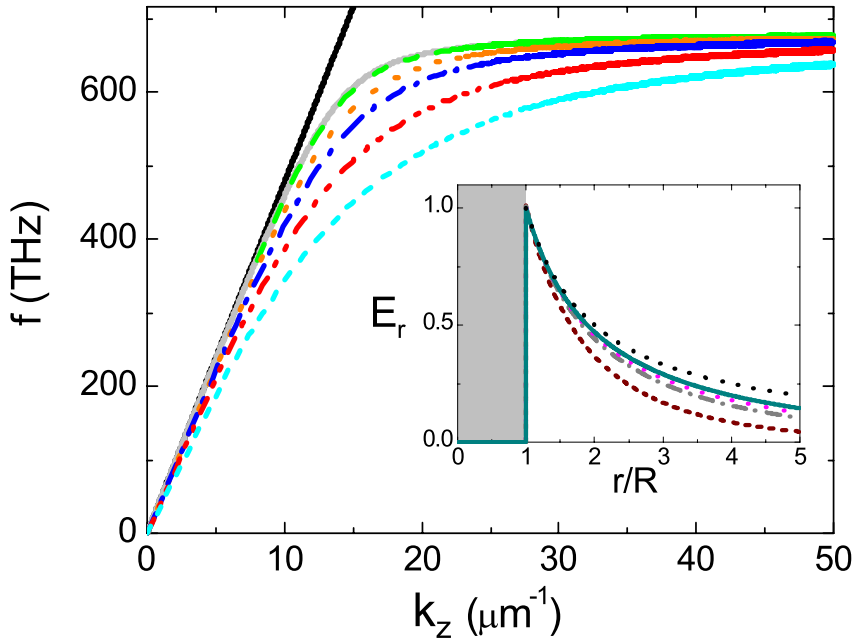

Figure 3.13.: Dispersion relation of SPPs on lossless Au wires of different radii (R): 10 μm (green dashed line), 3μm (orange dotted line), 0.2 μm (blue dotted-dashed line), 0.1 μm (red dashed-doubled-dotted line), and 0.05 μm (cyan short dashed line). Inset: Radial component of the electric field versus r for the SPPs supported by metallic wires ($R = 0.35\,\mu$m, $f = 330$ THz) with different dielectric constants: $\epsilon_M = -34$ (wine-colored short dashed line), $\epsilon_M = -200$ (grey dotted-dashed line), $\epsilon_M = -400$ (magenta dotted line) and $\epsilon_M = -1000$ (dark cyan solid line).

the precision of our calculations) with the SPPs supported by a lossless Au flat surface, whereas for narrower wires the frequency of the SPPs grows more slowly with increasing k_z, leading to stronger localization of EM fields to the wire.

The inset of Fig. 3.13 renders the radial dependence of $E_r^V = (k_z/k_0)H_\theta^V$ for the SPPs supported by metallic wires of radius $R = 0.35\,\mu$m at 330 THz. The wine-colored short dashed line shows the field decay for a lossless Au wire ($\epsilon_M = -34$ for gold at 330 THz). It can be observed how for increasing negative values of the metal permittivity E_r^V tends to the $1/r$ dependence (black dashed line) expected for a PEC wire [90]. Taking $\epsilon_M \to -\infty$, the SPP dispersion relation approaches the light line ($k_0 \to k_z$, $k_V \to 0$). As a result EM fields are expelled out from the wire, while in the vacuum region $E_r^V = H_r^V \propto K_1(k_V r) \to 1/r$ [96]. These asymptotic EM fields do not satisfy Gauss law in the absence of free charges. Thus, we can conclude that PEC wires, as flat surfaces, do not support surface EM modes [10].

3.3.2. Spoof surface plasmon polaritons on ring arrays

Once we have demonstrated that uncorrugated metallic wires do not support SPPs in the limit $\epsilon_M \to -\infty$, in this section we analyze in detail the formation of surface EM modes on periodically corrugated PEC wires [63], the cylindrical analog of the spoof SPPs on a flat PEC surface (see Sec. 3.2.2).

We develop a modal expansion formalism similar to that presented in chapter 2 for planar geometries in order to solve Maxwell equations for the system schematically depicted in Fig. 3.14: a PEC wire of radius R milled with a periodic array of subwavelength rings. We introduce the term metawire for the structure, as the emergence of spoof SPPs can be viewed in the context of metamaterials (see 3.2.2). We label the array period as d, and the rings width and depth as a and h, respectively. Taking advantage of the periodic character of the system, we can apply Bloch's theorem to the problem and solve Maxwell equations only inside a unit cell of length d (see Fig. 3.14). Within this unit cell, EM fields are nonzero only in the vacuum region surrounding the wire (region I), and inside the perforated rings (region II). As in the previous section, our analysis will be focused on azimuthally independent p-polarized surface modes. Under this constraint, EM fields in region I can be expressed as a sum over diffraction modes whose radial dependence is given by the modified Bessel functions of the second kind. Using Dirac's notation, we can write

$$|E_z^I\rangle = \sum_n C_n K_0(k_r^{(n)} r)|k_n\rangle, \tag{3.14}$$

$$|H_\theta^I\rangle = \sum_n Y_n^I C_n K_1(k_r^{(n)} r)|k_n\rangle, \tag{3.15}$$

where now, $k_n = k_z + n\frac{2\pi}{d}$ and $k_r^{(n)} = \sqrt{k_n^2 - k_0^2}$. The wavefunction for the Bloch waves is $\langle z|k_n\rangle = \frac{e^{ik_n z}}{\sqrt{d}}$, and $Y_n^I = ik_0/k_r^{(n)}$, the mode admittance.

Inside the rings, EM fields can be expanded as a sum over propagating and counter-propagating waveguide modes in the radial direction as:

$$|E_z^{II}\rangle = \sum_l D_l \Big(J_0(q_r^{(l)} r) - \alpha_l N_0(q_r^{(l)} r)\Big)|q_l\rangle, \tag{3.16}$$

$$|H_\theta^{II}\rangle = \sum_l Y_l^{II} D_l \Big(J_1(q_r^{(l)} r) - \alpha_l N_1(q_r^{(l)} r)\Big)|q_l\rangle, \tag{3.17}$$

where $q_r^{(l)} = \sqrt{k_0^2 - (l\pi/a)^2}$ and $Y_l^{II} = -ik_0/q_r^{(l)}$. The ring waveguide modes are given by $\langle z|q_l\rangle = \sqrt{(2-\delta_{l,0})/a}\cos\frac{l\pi}{a}(z + a/2)$ for $|z| < a/2$ (inside the rings) and $\langle z|q_l\rangle = 0$, otherwise. The radial dependence of these modes is described by Bessel and Neumann functions $J_{0,1}$ and $N_{0,1}$. The constant $\alpha_l = J_0[q_r^{(l)}(R-h)]/N_0[q_r^{(l)}(R-h)]$ is defined so that the electric field satisfies perfect conducting boundary conditions at the ring bottom.

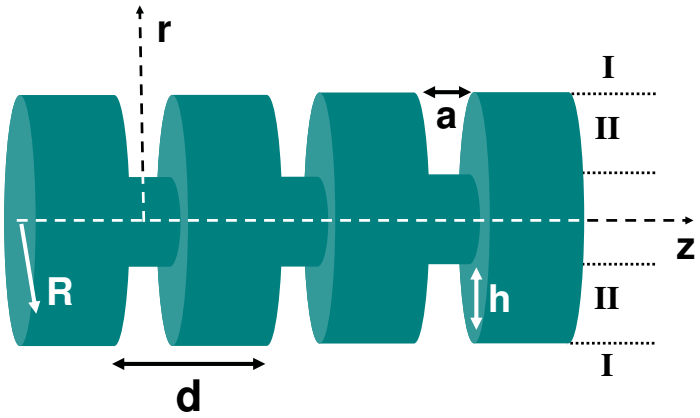

Figure 3.14.: Schematic picture of the structure supporting cylindrical spoof SPPs: a PEC wire drilled with a periodic array of rings.

The matching of the EM fields at the interface of the structure is performed similarly as in the case of planar geometries, explained in detail in Section 2.2.1. We impose continuity of the EM fields at the wire outer radius ($r = R$). The z-component of the electric field must be continuous everywhere on the interface, whereas the θ-component of the magnetic field is continuous only at the rings openings. Projecting the electric continuity equations over Bloch waves, and the equations linked to the magnetic field continuity over ring waveguide modes, we remove the dependence on z of the matching equations. Defining the quantities

$$E_l = D_l \Big(J_0(q_r^{(l)} R) - \alpha_l N_0(q_r^{(l)} R) \Big), \tag{3.18}$$

which are the modal amplitudes associated with the z-component of the electric field at the rings openings. The set of ME continuity equations has the form

$$(G_{ll} - \epsilon_l) E_l + \sum_{s \neq l} G_{ls} E_s = 0, \tag{3.19}$$

where l and s labels the ring waveguide mode order. Note that this system of equations is formally equal to that obtained for flat structures [Eqs. (3.2)]. Moreover, the various terms appearing in Eqs. (3.19) have the same physical interpretation as in dimple and groove arrays. Therefore, the term

$$\epsilon_l = Y_l^{II} \frac{J_1(q_r^{(l)} R) - \alpha_l N_1(q_r^{(l)} R)}{J_0(q_r^{(l)} R) - \alpha_l N_0(q_r^{(l)} R)} \tag{3.20}$$

describes all the bouncing processes experienced by the EM fields linked to mode l inside the rings, whereas

$$G_{ls} = \sum_n Y_n^I \frac{K_1(k_r^{(n)} R)}{K_0(k_r^{(n)} R)} \sigma_{nl}^* \sigma_{ns} \tag{3.21}$$

takes into account the EM radiation emitted by waveguide mode s into vacuum Bloch waves and collected by mode l. The overlapping integral, $\sigma_{nl} = \langle k_n | q_l \rangle$, provides the EM coupling between the n^{th} Bloch wave and the l^{th} waveguide mode. Analytical expressions for these overlapping integrals are given in Appendix A.

Once we have constructed the set of homogeneous matching equations (3.19), the dispersion relation of the spoof SPPs is given by the nonzero solutions of the modal amplitudes E_l. Here, we introduce a further approximation in our theoretical analysis by assuming that the wavelength is much larger than the rings width ($\lambda >> a$). In Section 2.2.1, we demonstrated that within this subwavelength regime it is a good approximation to consider only the lowest waveguide mode inside the indentations. Note that in this case, as in 1D slits, irrespective of the ratio between a and λ, the waveguide mode with $l = 0$ is always propagating. Under this approximation, the condition $(G_{00} - \epsilon_0) = 0$ gives the dispersion relation of the azimuthally independent spoof SPPs sustained by the metawire. It can be written as

$$\sum_n \frac{k_0}{k_r^{(n)}} \frac{K_1(k_r^{(n)} R)}{K_0(q_r^{(n)} R)} |\sigma_{n0}|^2 = -\frac{J_1(k_0 R) - \alpha_0 N_1(k_0 R)}{J_0(k_0 R) - \alpha_0 N_0(k_0 R)}, \tag{3.22}$$

where $\sigma_{n0} = \sqrt{\frac{a}{d}} \text{sinc}(k_n a/2)$.

In Figure 3.15, the spoof SPP bands for three different ring arrays are plotted. As PEC boundary conditions are considered, all lengths in the system are scalable and we can take d as the reference length. The wire radius is $R = 2d$, and the ring width $a = 0.2d$. The three ring depths are: $h = 1.6d$ (red solid line), $h = 0.8d$ (green dotted line) and $h = 0.4d$ (blue dashed line). We can observe how the spoof SPP dispersion relation deviates from the light line, resembling the behavior of SPPs propagating along metallic wires at optical frequencies (see Fig. 3.13).

At low frequencies ($\lambda >> d, a$), and for wires much thicker and rings much shallower than the array period ($R, R - h >> d$), we can obtain an analytical expression for the spoof SPP dispersion relation by introducing the asymptotic expansions of the different Bessel functions involved in Eq. (3.22), obtaining:

$$k_z = k_0 \sqrt{1 + \left(\frac{a}{d}\right)^2 \tan^2(k_0 h)}. \tag{3.23}$$

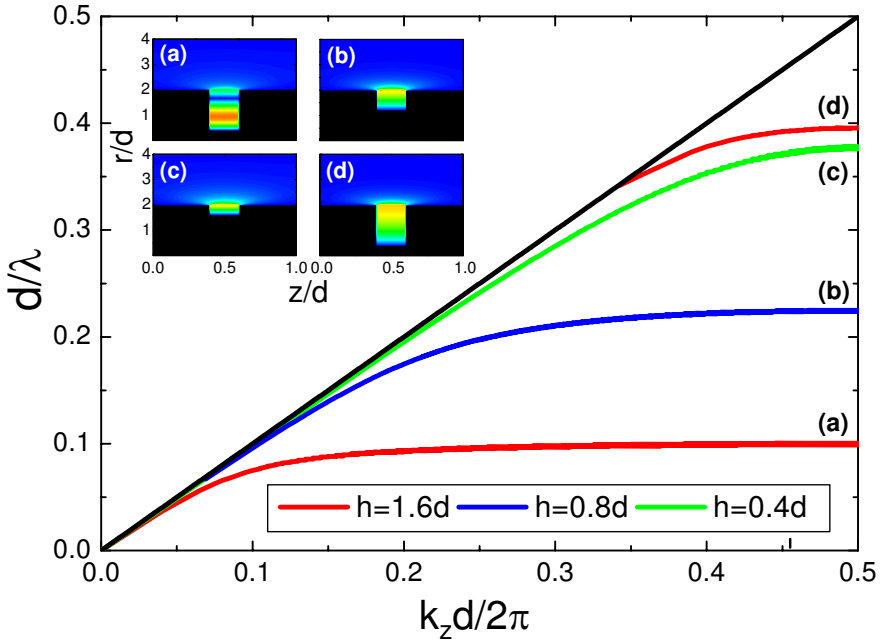

Figure 3.15.: Normalized frequency versus k_z for the θ-independent spoof SPPs supported by perforated wires of radius $R = 2d$ for three different ring depths. For all the structures, $a = 0.2d$. Inset: Electric field pattern at the band edge ($k_z = \pi/d$) for the four SPP bands shown in the main panel.

Notice Eq. 3.23 coincides with Eq. (3.3), which corresponds to spoof SPPs bands for a 1D array of grooves of width a and depth h. As in the planar case, the key parameter governing the surface EM mode confinement is the depth of the rings, h (see Fig. 3.15).

As we showed in Section 3.2.2, dispersion relation (3.23) allows us to analyze the dependence on the structure geometry of spoof SPPs on groove arrays. Here, we use it to define an asymptotic frequency ω_s playing the same role as $\omega_p/\sqrt{2}$ in conventional SPPs (see 3.2.1). According to Eq. (3.23), this asymptotic frequency is given by the condition $\tan(k_0 h) \to \infty$, which yields $\omega_s = \pi c/2h$. Note that the inversely proportional dependence of ω_s with h explains the lowering of the dispersion relation for increasing h observed in groove arrays (see Fig. 3.2). Fig. 3.15 renders the spoof SPP bands for ring arrays of different depths. We consider first the bands (b), (c) and (d). The electric field associated to these modes does not present any node in the radial direction (see the inset of Fig. 3.15). Moreover, as in 1D grooves, the flat region of the dispersion relations occurs at lower frequencies as h is enlarged. For $h = 1.6d$, another band linked to a spoof SPP mode presenting a radial node inside the ring (see inset (a)) appears at larger frequencies.

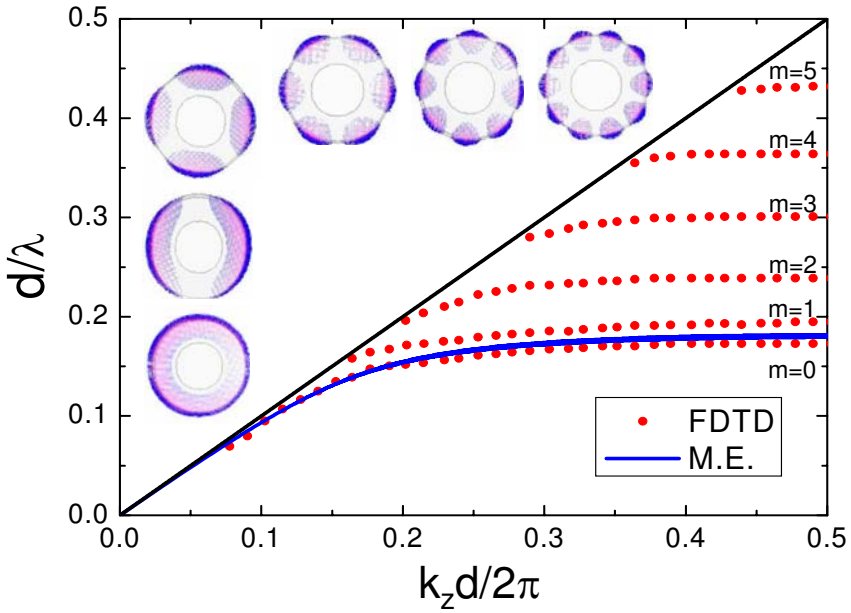

Figure 3.16.: Spoof SPP dispersion relation including higher azimuthal modes (labelled with m) for a PEC wire of radius $R = 2d$ drilled with rings of width $a = 0.2d$ and depth $h = 0.5d$. The insets show the electric field amplitude at the band edge associated to spoof SPPs with different m. They are ordered with increasing m from the left bottom corner to the right top corner of the figure.

Importantly, Eq. (3.23) also predicts the formation of this mode, which can be associated with another asymptotic frequency $\omega_s = 3(\pi c/2h)$ also satisfying $\tan(k_0 h) \to \infty$.

Figure 3.16 renders the dispersion relation of the spoof SPPs on a wire of radius $R = 2d$ perforated by periodic rings with $a = 0.2d$ and $h = d$. In this calculation, there is no restriction regarding the azimuthal dependence of the EM fields. The dispersion relation (red dots) has been obtained by means of a 3D FDTD numerical calculation. The number of mesh points considered in the calculation are $240 \times 240 \times 40$, with a mesh size equal to $0.08d$. The different bands (labelled with index m) correspond to different azimuthal symmetries of the electric field amplitude shown in the insets of the figure. For the structure considered, m ranges from $m = 0$ (θ-independent SPPs) to $m = 5$ (see insets from left bottom corner to right top corner of Fig. 3.16). The electric field associated to the m^{th} azimuthal mode presents $2m$ nodes and maxima in θ. Solid blue line shows the $m = 0$ band calculated from Eq. (3.22). We can see the very good agreement between the FDTD and ME results for the azimuthally independent spoof SPP band.

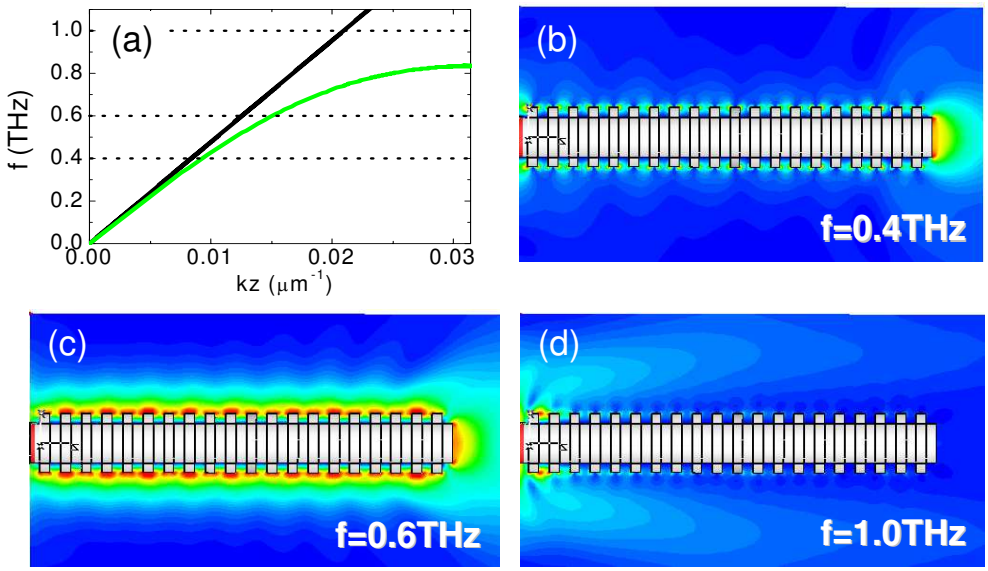

Figure 3.17.: Dispersion relation (a) and electric field plots (b)-(d) for THz spoof SPPs propagating along a metawire of radius $R = 150\,\mu$m perforated by an array of rings of period $d = 100\,\mu$m. The rings width and depth are $50\,\mu$m. Dotted lines show the three different frequencies (0.4, 0.6 and 1.0 THz) considered in the FIT simulations of the electric field amplitude in metawires of length $20 \times d$ illuminated from the left by a radially polarized plane wave.

3.3.3. Conical structures: guiding and focusing of light

One of the possible applications of cylindrical spoof SPPs is to guide EM radiation with frequencies lying within the microwave or THz ranges of the EM spectrum along a metallic wire. This functionality is illustrated in Figure 3.17.

In this case, the geometry of the ring array is chosen so that the optimal frequencies for guiding would be around $0.6 - 0.8$ THz. Panel (a) shows the dispersion relation of the spoof SPPs supported by the infinite structure calculated with Eq. (3.22) whereas panels (b), (c) and (d) depict electric field amplitude patterns (evaluated at three different frequencies) for a finite version of the structure (containing 20 periods), illuminated by a radially polarized broadband terahertz pulse. These pictures have been obtained through FIT simulations. As clearly seen in this figure, for the lowest frequency considered, $f = 0.4$ THz, as k_z is close to the light line, the guiding properties are poor in comparison with $f = 0.6$ THz for which the EM radiation is guided efficiently and strongly confined along the wire surface. At $f = 1.0$ THz, no spoof SPPs are supported by the system [see panel (d) of Fig. 3.17] and the incident radiation is scattered from the metawire.

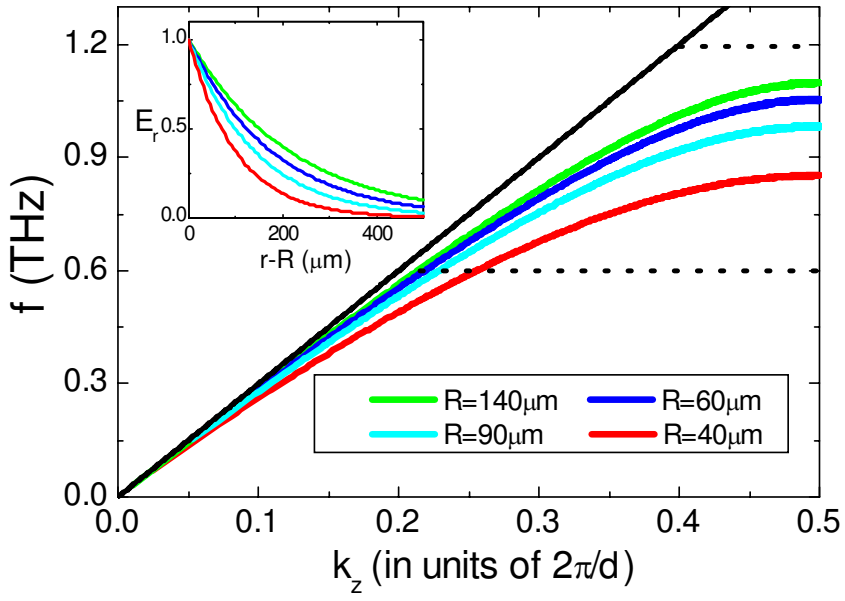

Figure 3.18.: Frequency versus parallel wave vector for spoof SPPs supported by metawires of different radii perforated with periodic ring arrays of period $d = 100\,\mu$m and ring dimensions $a = 50\,\mu$m and $h = 30\,\mu$m. Dotted lines indicate two different frequencies (0.6 and 1.2 THz). Inset: Electric field radial component versus $r - R$ at $f = 0.6$ THz for the four infinite metawires considered in the main panel.

By taking advantage of the dependence of the spoof SPP confinement on the geometry of the ring array, it is feasible to design a periodically corrugated wire able to concentrate EM energy at one of its ends [63]. Here, we present just one possible structure. It is a conical wire, in which the external radius is gradually decreased along the wire but the depth of the rings is fixed.

In Figure 3.18, we plot the dispersion relation of the spoof SPPs supported by corrugated wires in which the depth of the rings, $h = 30\,\mu$m, their width, $a = 50\,\mu$m, and the period of the array, $d = 100\,\mu$m, are fixed. The four curves correspond to the dispersion relations for four different values of R, ranging from $R = 140\,\mu$m to $R = 40\,\mu$m. As R is decreased, the spoof SPP bands deviate more and more from the light line. This implies that the confinement of the corresponding surface EM mode is increased as R is reduced, as can be seen in the inset of the figure, which displays the radial component of the electric field, E_r, as a function of the distance to the wire, $r - R$. This magnitude is evaluated at $f = 0.6$ THz for the four wires considered in the main panel.

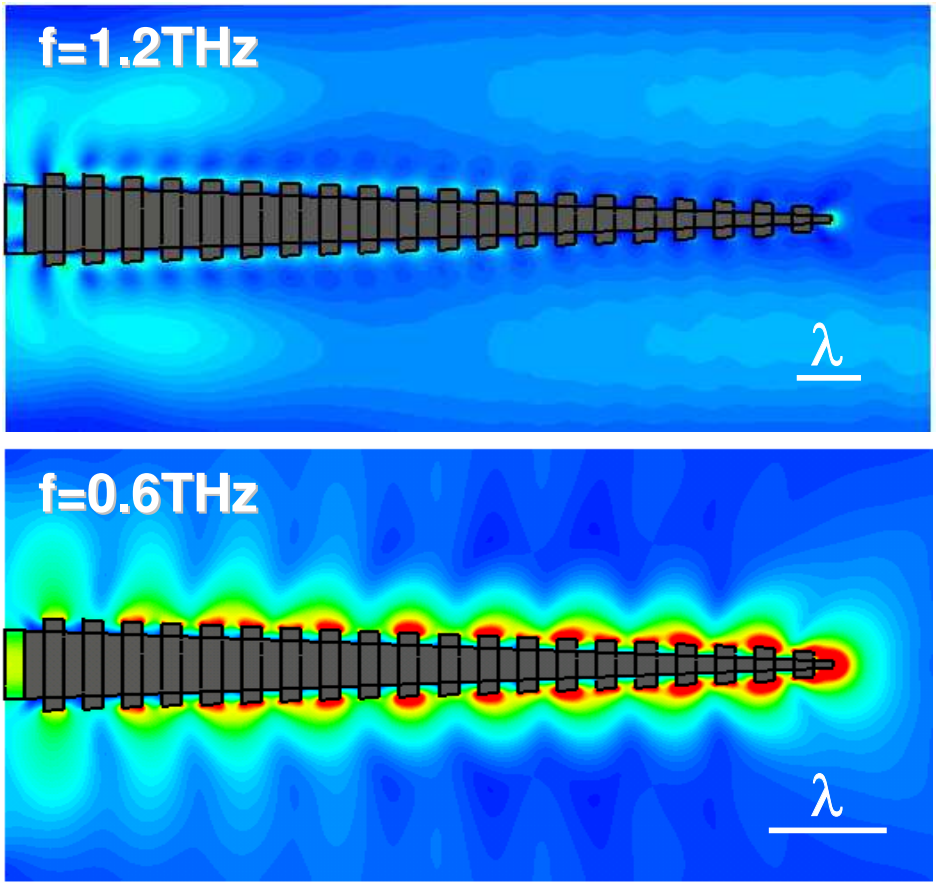

Figure 3.19.: Guiding and focusing of light through spoof SPPs propagating along a PEC cone of length 2 mm corrugated by a ring array in which the radius is gradually reduced from $R = 140\,\mu$m to $R = 40\,\mu$m. As expected from the dispersion relation of Fig. 3.17, spoof SPPs are excited at $f = 0.6$ THz, while at $f = 1.2$ THz surface EM modes are not supported by the structure.

Therefore, it is expected that if we construct a finite metawire in which the depth of the grooves is fixed and the external radius is gradually reduced from $R = 140\,\mu$m to $R = 40\,\mu$m, EM radiation of frequency $f = 0.6$ THz will be focused at the end of the conical design. This focusing effect is demonstrated in Figure 3.19 which shows FIT simulations on a conical wire of length 2 mm containing 20 periods of the ring array of Fig. 3.18 for two different frequencies, $f = 0.6$ and $f = 1.2$ THz. As expected from the ME calculations for infinite wires, at $f = 0.6$ THz, EM radiation is guided along the wire and focused as it propagates through it. However, the electric field pattern for $f = 1.2$

THz shows how EM waves are scattered at the entrance of the wire due to the absence of spoof SPPs at that particular frequency.

3.3.4. Helically grooved wires: comparison with experiments

This section is devoted to show the comparison between our theoretical study on the spoof SPPs sustained by PEC metawires with the experimental outcomes obtained by the group of Prof. S. A. Maier and Dr. S. R. Andrews on the propagation of THz radiation bound to structured metallic wires. The experimental setup consists in a 150 mm long helically grooved wire. It is formed by tightly wrapping a steel wire (radius 200 μm) around a 200 μm radius core. The assembly is then nickel plated (see the upper panel of Fig. 3.20). For comparison, a bare copper wire of the same outer radius and length (600 μm and 150 mm, respectively) is also studied. Measurements are performed using time-domain THz spectroscopy. Radially polarized, broadband ($\sim$ 2 THz) THz beams are collimated to a diameter of order 6 mm and end-fire coupled to the wires. In order to discriminate the bound EM modes against unguided free space radiation, the wires are bent along the arc of a circle of radius 26 cm.

Panel (a) of Fig. 3.20 displays time-domain traces of the receiver current for the wires with smooth and helically grooved surfaces. It is clear that a single-cycle-like pulse, which can be associated with a Sommerfeld wave [1], propagates along the smooth wire. However, propagation on the helical wire exhibits significant dispersion together with beating due to the presence of bound modes with different frequencies. Panel (b) plots the amplitude spectra of the traces in panel (a) together with the spectrum of a second, nominally identical sample of the helical structure which shows the reproducibility of the data to small variations in optical alignment. Note that the vertical scale is the same for all three spectra. To a first approximation, the amplitude spectrum is proportional to the electric field of the guided modes at the end of the wire, convolved with the receiver response and the transfer function taking into account the radiation of the guided modes into free space and propagation to the receiver in the far field.

In panel (b) of Fig. 3.20, the frequency at the band edge, f_{BE}, of the three lowest spoof SPP modes supported by the experimental structure are indicated by vertical arrows. They are obtained by means of the theoretical calculations described below, and correspond to the peaks in the amplitude spectra at 0.305 ± 0.002 THz, 0.326 ± 0.002 THz, and 0.353 ± 0.003 THz. The height of the peaks depends on the orientation of the receiver antenna, which reflects the different azimuthal symmetry of the spoof SPP modes. We show below that the structure observed in the spectra at frequencies lower than 0.3 THz can be associated with the propagation of radiation along the wire at smaller wave vectors.

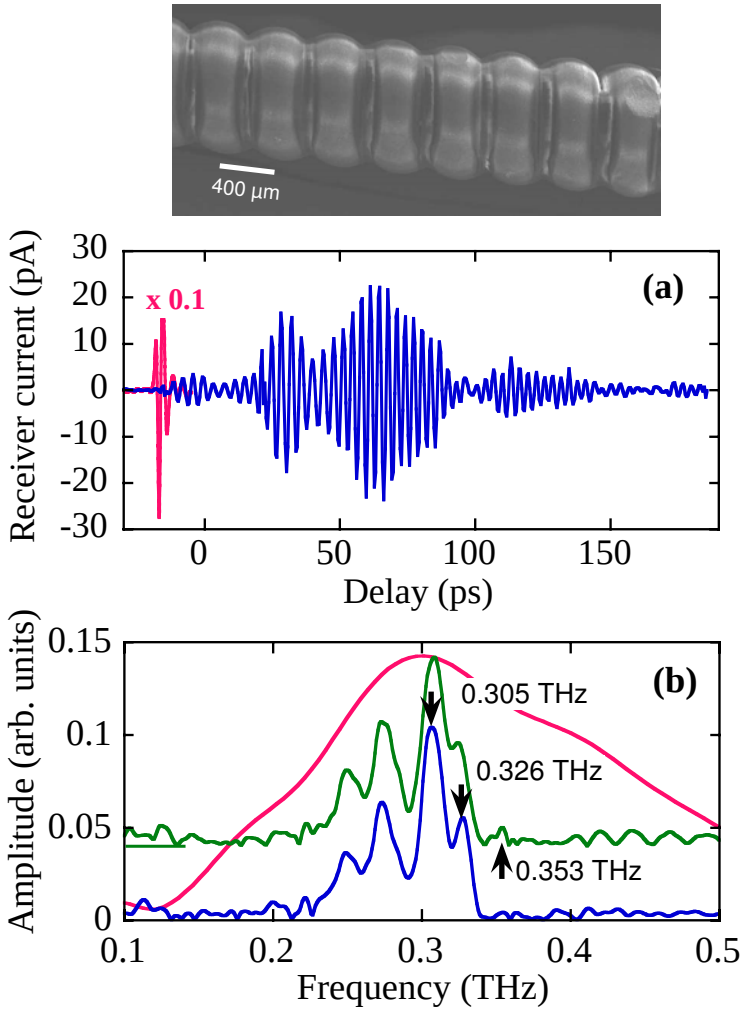

Figure 3.20.: Upper panel: Electron micrograph of the experimental helically grooved wire. Lower panels: (a) Receiver current as a function of time delay for the smooth wire (red line) and the grooved structure (blue line). (b) Amplitude spectra of the time domain data in (a) together with the spectrum of another, nominally identical helical sample (green curve, displaced for clarity). The arrows indicate the three azimuthal modes of the helical groove structure. The spectrum of the Sommerfeld wave (red curve) on the smooth wire extends to $\sim 1\,\mathrm{THz}$.

In Figure 3.21, the spoof SPP bands for an helical grooved PEC wire calculated using the FDTD method are displayed. In accordance with the experimental parameters, the helix pitch is $d = 400\,\mu\mathrm{m}$ and the wire radius, $R = 600\,\mu\mathrm{m}$. EM fields are evaluated inside a unit cell along the direction parallel to the wire axis (z-direction). Due to design limitations, the modelled groove has a triangular profile of width a and depth h (see lower inset). We find that $a = 200\,\mu\mathrm{m}$ and $h = 150\,\mu\mathrm{m}$ give a good match to the experi-

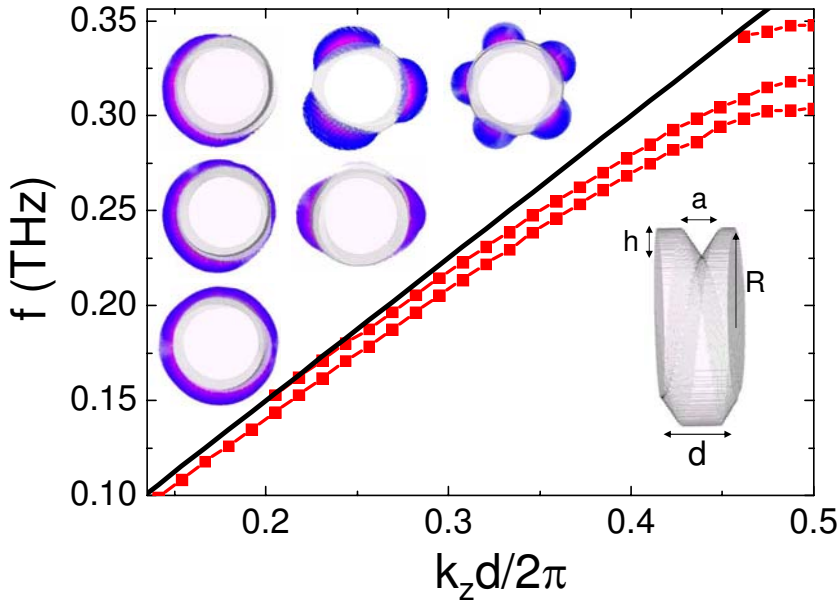

Figure 3.21.: Dispersion relation of the spoof SPP modes supported by a PEC wire of radius $R = 600\,\mu$m inscribed with a triangular cross-section helical groove of pitch $d = 400\,\mu$m. The groove has width $a = 200\,\mu$m and depth $h = 150\,\mu$m. The upper row of insets displays snapshots of the electric field at the three band edges, f_{BE}=0.305 THz (left), 0.320THz (center) and 0.349 THz (right). The next lower row correspond to the first mode at 0.280 THz (left) and the second mode at 0.180 THz (right). The pattern in the lowest row is for the first mode at 0.180 THz.

mental results for the f_{BE}'s. The main panel shows the dispersion relation for this set of geometrical parameters. The three theoretical f_{BE}'s obtained, 0.305 THz, 0.320 THz and 0.349 THz, are in excellent agreement with the spectral peaks found in the experiments.

The insets of Figure 3.21 render snapshots of the electric field amplitude, $|E|$, of the spoof SPPs supported by the metawire at various frequencies. Note that, as expected, the lack of azimuthal symmetry of the metallic structure leads to non-symmetrical $|E|$ distributions. The upper row displays the electric field amplitude at the three f_{BE}'s, increasing in frequency from left to right. The fields are confined within less than a wavelength of the wire surface. The field maps depicted in the lower two rows are evaluated at smaller k_z. The two left ones correspond to the first spoof SPP mode at 0.280 THz and 0.180 THz, and that on the right of the second row to the second spoof SPP at 0.180 THz. At f_{BE}, the modes exhibit an odd number of azimuthal nodes (1, 3 and 5) whereas with decreasing k_z, the number of nodes is gradually reduced by one and becomes even. Thus, the spoof

SPPs propagating along the helical structure at low k_z resemble the case of a ring array, where the number of nodes is even (see Sec. 3.3.2).

We analyze now why the spoof SPPs on helical grooved wires exhibit such a k_z dependent azimuthal symmetry. Any component of the EM fields bound to a helical structure [118] can be expanded in terms of diffracted waves as

$$F_m(r,\theta,z) = e^{ik_z z} e^{im\theta} \sum_n A_{n\,m-n}(r) e^{in(\frac{2\pi}{d}z-\theta)}, \tag{3.24}$$

where the modal amplitude $A_{n\,m-n}(r)$ contains the radial dependence of the n^{th}-diffracted wave. $F_m(r,\theta,z)$ is an eigenfunction of the helical translation operator, $S_{\phi\,\frac{d}{2\pi}\phi}$ [119], satisfying

$$S_{\phi\,\frac{d}{2\pi}\phi} F_m(r,\theta,z) = F_m\left(r,\theta+\phi,z+\frac{d}{2\pi}\phi\right) = e^{i(m+k_z\frac{d}{2\pi})\phi} F_m(r,\theta,z), \tag{3.25}$$

where index m controls the symmetry properties of the EM fields. We introduce the helical coordinate $\xi = z - \frac{d\theta}{2\pi}$ [120], which is parallel to the cylindrical coordinate z, but measured from the surface $z = \frac{d\theta}{2\pi}$. EM fields can be expressed in terms of ξ as

$$F_m(r,\theta,\xi) = f(r,\xi) e^{i(m+k_z\frac{d}{2\pi})\theta}. \tag{3.26}$$

It is now clear that this eigenfunction, evaluated along the helical surfaces (ξ = constant), evolves in time as $\cos[(m+k_z\frac{d}{2\pi})\theta - 2\pi f t]$, where f and t are the mode frequency and time, respectively. Thus, snapshots of the EM fields with $k_z = \pi/d$ show $2m+1$ nodes along one helix pitch, whereas for $k_z = 0$, they show only $2m$ nodes. This result allows us to label the spoof SPP modes in Figure 3.21 with the indices $m = 0$, $m = 1$ and $m = 2$.

We have also carried out FIT simulations on extended finite wires. As in the experiments, the helical structure is formed by wrapping a PEC wire of radius 200 μm around a straight cylindrical core of the same radius (see schematic picture of Fig. 3.22). The 9.6 cm long structure is illuminated in the near field with a radially polarized plane wave propagating parallel to the wire axis. Probes monitoring the longitudinal component of electric field, E_z, are located along the structure, close to the wire surface (615 μm away from its axis), at four different azimuthal positions ($\theta = 0$, $\frac{\pi}{2}$, π, and $\frac{3\pi}{2}$).

Figure 3.22 renders the amplitude of E_z versus frequency recorded by the probes located 1.5 cm away from the illuminated wire end. The simulation time (700 ps) is chosen so that reflection of the EM fields at the non-illuminated wire end is avoided. The spectrum resembles the experimental one, except for the structure in the tails below 0.3 THz. The black vertical arrows indicate the position of the three experimental peaks. These are in excellent agreement with the maxima in the electric field amplitude close to the wire surface in our FIT simulations, and in close correspondence with the f_{BE}'s obtained from

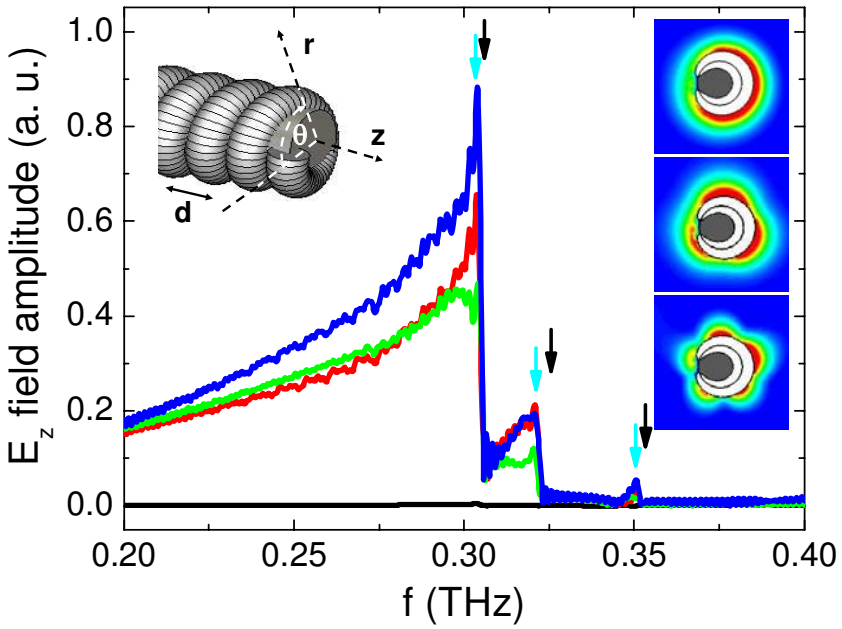

Figure 3.22.: FIT simulations of the propagation of surface EM modes on a 9.6 cm long wire. The metawire consists in a PEC wire of radius 200 μm tighly wound on a straight PEC wire of the same dimensions. The helix pitch is $d = 400\,\mu$m. Main panel shows the spectra of E_z at four points close to the structure surface ($r = 615\,\mu$m, $\theta = 0$, $\frac{\pi}{2}$, π, and $\frac{3\pi}{2}$) located 1.5 cm away from the illuminated wire end. Right insets show $|E_z|$ in a cross section at the three f_{BE}'s obtained from FDTD calculations (from top to bottom: 0.305 THz, 0.320THz and 0.349 THz). In the main panel, these frequencies are indicated by cyan arrows, whereas the corresponding frequencies in the experimental spectra are shown by black arrows.

FDTD calculations (vertical cyan arrows). In order to confirm that the three maxima in the FIT spectra correspond to the excitation of guided modes on the structure, we have also mapped the electric field amplitude in the plane containing the four field probes described above. The three right insets of Fig. 3.22 show the electric field amplitude at the frequencies indicated by vertical cyan arrows in the main panel. The field patterns are consistent with the FDTD results, which demonstrates that the FIT spectral maxima are associated with the resonant excitation of the $m = 0$, $m = 1$, and $m = 2$ spoof SPP modes.

The relative amplitudes of the spectral peaks reflects the efficiency with which the radially polarized incident beam is scattered into the spoof SPP modes and is similar to that observed experimentally. The modulation in amplitude below 0.3 THz observed in the experiments (see Fig. 3.20), does not appear in the long tail to lower frequencies in

the simulation shown in Fig. 3.22. In the experiments, spectral artifacts associated with reflections or finite delay range have been excluded. Therefore, we tentatively assign this structure to either variations in the pitch of the metawire or, more likely, to the frequency dependence of the coupling of the spoof SPPs to free space radiation, which is not explicitly modelled.

In this section, the propagation of spoof SPPs on corrugated wires has been studied theoretically and experimentally. In our theoretical analysis, different geometries have been considered, and a conical focusing scheme has been proposed. Finally, the guiding of THz radiation through spoof SPP modes on helical structures has been reported experimentally for the first time.

3.4. Corrugated channels and wedges

3.4.1. Spoof channel plasmon polaritons

Waveguides based on spoof SPPs supported by periodic groove and dimple arrays present a main drawback: the lack of lateral confinement of EM fields. As we showed in Section 3.2, spoof SPPs on these two structures spread infinitely along the in-plane coordinate perpendicular to the direction of propagation. In the case of dimple arrays, the lateral extension of the spoof SPPs can be reduced by varying the aperture dimensions [121], but subwavelength confinement of EM fields can not be achieved through this strategy.

In this section, we present a guiding scheme featuring subwavelength transverse confinement of EM fields at a planar surface. Our design, that consists of corrugated V-grooves milled on a PEC surface, borrows ideas from channel plasmon polaritons (CPPs) [26] and the concept of spoof SPPs. Moreover, we demonstrate that the combination of these two different physical mechanisms allows overcoming the limitations of SPPs-based waveguides at frequencies far below metallic plasma frequencies (see Sec. 3.2.1). Although our PEC model is scalable, in order to illustrate its functionality, we choose its geometrical parameters so that it works at frequencies laying in the THz range of the EM spectrum.

In the visible or telecom regimes, V-shaped grooves milled in metals support low loss, tightly confined CPPs [27, 29, 31]. The modal size of CPPs grows for increasing wavelength in such a way that, on PEC V-grooves, CPPs do not exist. As we have shown in the previous sections, the texturing of a metallic surface leads to the emergence of bound EM modes even in the PEC limit. Now, we test whether corrugated V-grooves milled on a flat PEC surface also sustain guided modes. For that, we analyze first the dependence of the EM modes propagating in the gap between two parallel groove arrays

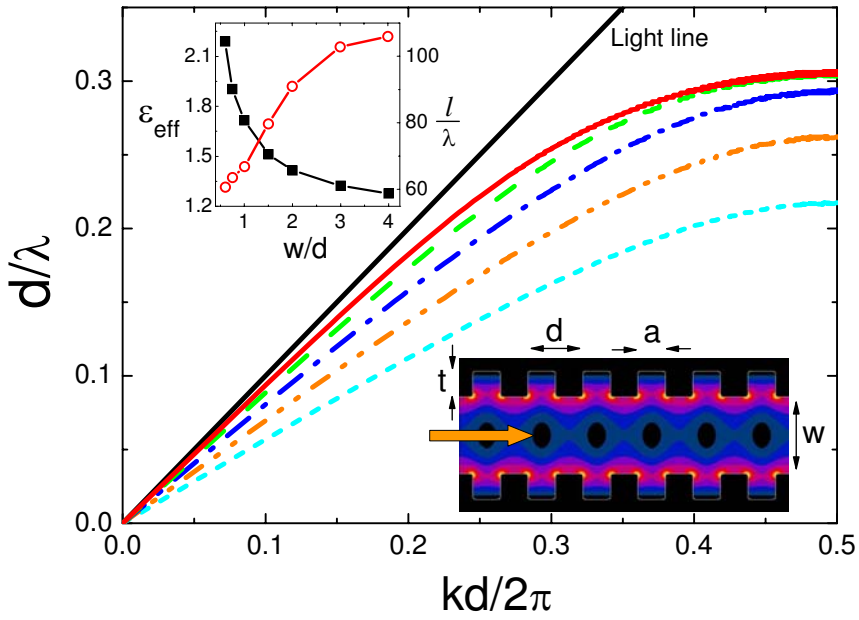

Figure 3.23.: Dispersion relation of the guided EM modes propagating between two corrugated PEC surfaces. Both surfaces are identical and consist of two groove arrays of period d. The grooves width, a, and depth, t, are equal to $0.5d$. Five different gap widths (w) are considered: $4d$ (red solid line), $2d$ (green dashed line), d (blue dotted dashed line), $0.5d$ (orange double dotted dashed line), and $0.25d$ (cyan dotted line). In the lower inset, the electric field amplitude at the band edge for the case $w = 1.5d$ is depicted. The upper inset renders ϵ_{eff} (black squares) and the propagation length (red circles) at $d/\lambda = 0.25$ obtained within the SIBC approximation for aluminum and $d = 200\,\mu$m.

(see lower inset of Fig. 3.23) on the gap width, w. Similar modes supported in the gap between two metallic surfaces textured with 2D hole arrays have been considered in the GHz regime [122]. Here we only consider EM modes associated with longitudinal electric fields having odd parity with respect to the gap center, as they have the same symmetry properties as the CPPs at optical frequencies [32]. Such modes can be described using our ME formalism (see Sec. 2.2). We denote the array period as d, and the grooves width and depth as a and t, respectively (see inset). Thus, in the single mode approximation (valid for $\lambda >> a$), the dispersion relation of these EM modes is given the condition

$$G - \epsilon = 0, \tag{3.27}$$

where $\epsilon = \cot(k_0 t)$ [see Eq. (2.40)] reflects the rebounds experienced by EM fields inside the grooves. The G term, which describes the coupling of EM fields coming from different

grooves, reads

$$G = i\sum_m \frac{k_0}{\sqrt{k_m^2 - k_0}}|\sigma_{m0}|^2 \tanh\left(\sqrt{k_m^2 - k_0}\frac{w}{2}\right), \tag{3.28}$$

where $k_m = k + m\frac{2\pi}{d}$, being k the mode parallel wave vector, and $\sigma_{m0} = \sqrt{\frac{a}{d}}\mathrm{sinc}(k_m\frac{a}{2})$ (see Appendix A). Note that G has the same form as for a single groove array [Eq. (2.42)] except for the term associated with the tangent function, which takes into account the anti-symmetric coupling of the EM fields bound to both PEC surfaces across the gap. In the limit $\lambda >> d$, we can neglect higher order diffraction order in G, having

$$\frac{\sqrt{k^2 - k_0^2}}{k_0}\coth\left(\sqrt{k^2 - k_0^2}\frac{w}{2}\right) = |\sigma_{00}|^2\tan(k_0 t). \tag{3.29}$$

Note that Eq. (3.29) resembles the dispersion relation of the anti-symmetric gap SPP modes supported in a dielectric slab sandwiched between two semi-infinite metals [116].

Figure 3.23 renders the dispersion relation of the gap modes travelling between two identical groove arrays. The bands have been calculated using Eq. (3.27), including a sufficiently large number of diffraction orders to achieve convergence. In all cases, the geometrical parameters of the grooves are $t = a = 0.5d$. Structures with five different gap widths have been analyzed, ranging from $w = 4d$ to $w = 0.25d$. Importantly, the dispersion bands are lowered as w is reduced. Thus, for a given frequency, k is larger for smaller w. This effect can be quantified by looking at the effective permittivity of the mode, ϵ_{eff}, defined as $\epsilon_{\mathrm{eff}} = k^2/k_0^2$. In the upper inset of Fig. 3.23, ϵ_{eff} of the gap modes evaluated at $d/\lambda = 0.25$ as a function of w is shown. For decreasing values of w, ϵ_{eff} increases very rapidly, reflecting a very large lateral confinement of the mode as the gap is reduced. In the lower inset, the electric field amplitude evaluated at the band edge for the case $w = 1.5d$ is depicted. The orange arrow indicates the direction of propagation.

In the upper inset of Fig. 3.23, the dependence of the modal propagation length, l, on the gap width is also shown (red circles). In order to take into account absorption losses in our model, we have exchanged PEC conditions by SIBCs in our ME equations, following the procedure presented in Section 2.2.5. Thus, the propagation length of the gap modes is given by the imaginary part of the parallel wave vector, $l = 1/[2\mathrm{Im}(k)]$. The propagation lengths in Fig. 3.23 are evaluated for aluminum at $d/\lambda = 0.25$ with $d = 200\,\mu$m (which corresponds to $f = 0.38\,$THz). The dielectric function of aluminum has been taken from [98]. From the evolution of l with w we can conclude that there is a trade-off between the propagation and confinement of the EM guided modes, as it is common in plasmonic structures.

The existence of EM guided modes in the gap between two corrugated PEC surfaces and the dependence of ϵ_{eff} with the gap width suggest that a corrugated V-groove milled

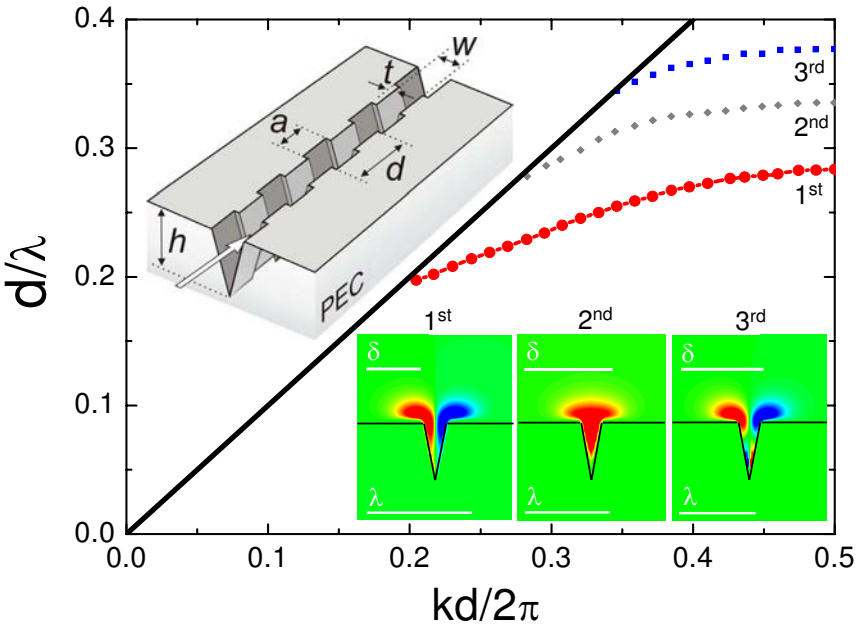

Figure 3.24.: FDTD dispersion relation of the first three spoof CPP modes supported by a corrugated V-channel milled on a PEC surface. An schematic picture of the structure is shown in the upper inset. Lower insets depict the amplitudes of the longitudinal component of the electric field evaluated at the band edge for the three modes. The wavelength, λ, and modal size, δ, for the three cases are represented.

on a PEC film (see upper inset of Fig. 3.24) supports the propagation of EM guided modes. These would be tightly confined in the transverse plane and localized at the bottom of the groove, where ϵ_{eff} is maximum. In order to verify this hypothesis, we have carried out FDTD calculations of the dispersion relation of the EM modes supported by corrugated V-grooves. The side of the FDTD mesh is $0.025d$, and the total number of mesh points, $360 \times 460 \times 40$. We assume that the metal behaves as a PEC, i.e., no absorption is present in the structure. The geometrical parameters are $a = t = 0.5d$, $w = 0.76d$, and $h = 5d$, corresponding to a groove angle of 20°. The bands associated with the first three EM guided modes (spoof CPPs) travelling along the corrugated channel are rendered in Fig. 3.24. As in the case of CPPs at optical frequencies [32], the fact that the corrugated V-channel has a finite height translates into the existence of a cut-off for these EM guided modes.

The longitudinal component of the electric field associated with the three spoof CPP modes is shown in the lower insets of Fig. 3.24. The fields are evaluated at the band edges of the three dispersion bands. Electric fields are plotted only inside the shallow part of

the corrugated V-channel, where EM fields are strongly localized. The first and third modes have odd parity, as the longitudinal electric fields have a different sign at both sides of the V-channel, vanishing at the middle plane. The lowest mode shows only two lobes, whereas the third one presents another plane, now parallel to the planar surface, in which the longitudinal electric field is also zero. The second EM guided mode has even parity with respect to the symmetry plane. In all three insets both λ and the modal size, δ, are represented. We have defined the modal size as the transverse separation between the locations where the electric field amplitude has fallen to one tenth of its maximum value, having $\delta = 0.52\lambda$, 1.02λ, and 1.06λ for the three spoof CPPs at the band edge.

Another interesting feature of the spoof CPPs modal shape is that, contrary to what the behavior of ϵ_{eff} predicts in Fig. 3.24, EM fields are not guided at the groove bottom but rather at the groove edges. This is due to their strong hybridization with wedge modes that run on the edges of the groove (see Sec. 3.4.2), much in the same way as it occurs in conventional CPPs [32]. It is also remarkable the small frequency overlap between the first and second spoof CPP bands, which facilitates the monomode operation of the corrugated V-groove as a THz waveguide.

Once we have demonstrated that spoof CPPs are supported by infinitely long corrugated V-grooves, it is worth analyzing how these EM modes behave in waveguides of finite length. For that, we have performed FIT simulations on finite corrugated V-channels. As in the previous FDTD calculations, PEC boundary conditions are considered. We have chosen the structure period $d = 200\,\mu$m, keeping the relation between the rest of the geometrical parameters and d as in Fig. 3.24. First, in order to cross-check the different numerical techniques, we analyze the case of a straight channel. The channel is 20 mm long and the structure is illuminated from one end with a 2D input port mode that resembles the spatial and vectorial dependencies of the lowest spoof CPP mode obtained from FDTD simulations.

Within FIT it is possible to calculate the EM transmission through the finite waveguide by integrating the longitudinal component of the Poynting vector in two perpendicular planes, located near the input and exit sides of the waveguide. Figure 3.25 displays this FIT transmission spectrum for the finite-length channel described above. Red dashed arrows indicate the cut-off and band edge frequencies predicted by the FDTD method (see Fig. 3.23) for the lowest spoof CPP mode supported by the structure. The agreement between the two distinct numerical techniques in the spectral location of the band edge is excellent. Regarding the cut-off frequency, FIT predicts a slightly higher location than that obtained with FDTD. Notice that, as the band approaches its cut-off frequency, the spoof CPP mode becomes less localized and both numerical calculations are less accurate due to the inherent finite size of the spatial simulation windows. The important point

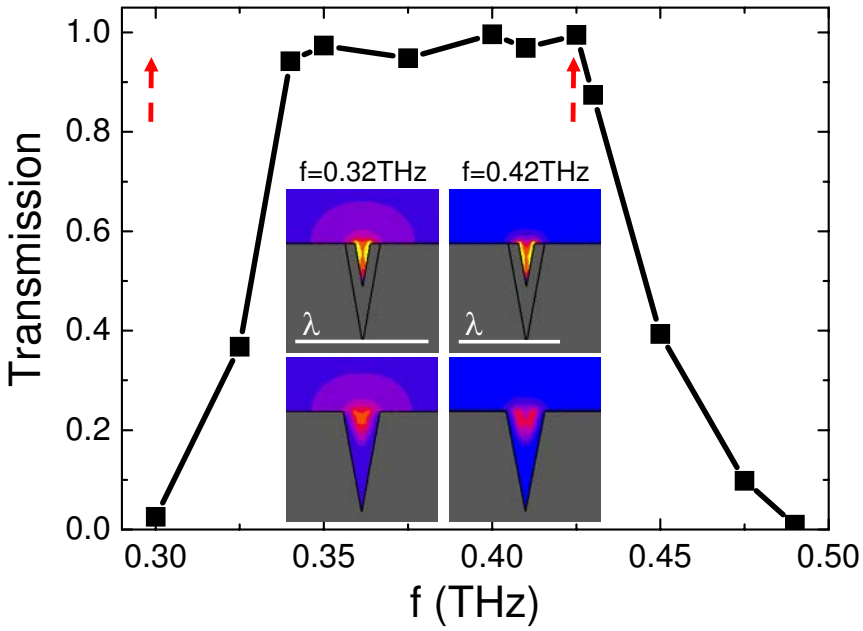

Figure 3.25.: FIT simulations of the transmission spectrum for the lower spoof CPP mode supported by a straight corrugated PEC V-channel of period $d = 200\,\mu$m and total length 20 mm. Red dashed arrows indicate the spectral position of the cutoff and band edge frequencies obtained from FDTD calculations. The left insets show the electric field amplitude at 0.32 THz, and the right ones, at 0.42 THz. Upper (lower) insets correspond to the plane located 9.1 mm (9.2 mm) away from the illuminated end of the structure.

is that the transmission approaches unity within the spectral region in which the lowest guided mode is supported.

The insets of Fig. 3.25 render the total electric field amplitudes at two different frequencies. Left panels are evaluated at 0.32 THz and the right ones at 0.42 THz. The upper insets depict the electric field in the plane located 9.1 mm away from the illuminated end of the structure and corresponds to the shallow part of the V-channel. The lower insets are displaced one half of the period, showing the deepest region in the groove. In accordance with the FDTD calculations, the electric field is strongly confined within the shallow channel. The insets also show clearly how the lateral confinement of the mode is much higher at 0.42 THz ($\delta = 0.42\,\text{mm} = 0.59\lambda$) than at 0.32 THz ($\delta = 1.37\,\text{mm} = 1.46\lambda$). Importantly, in contrast to other guiding schemes [123], the straight waveguide presented here features transverse subwavelength confinement of THz radiation.

In the previous calculations, we assumed ideal PEC boundary conditions and hence, the propagation length is infinite. We can estimate l in a real waveguide operating at THz

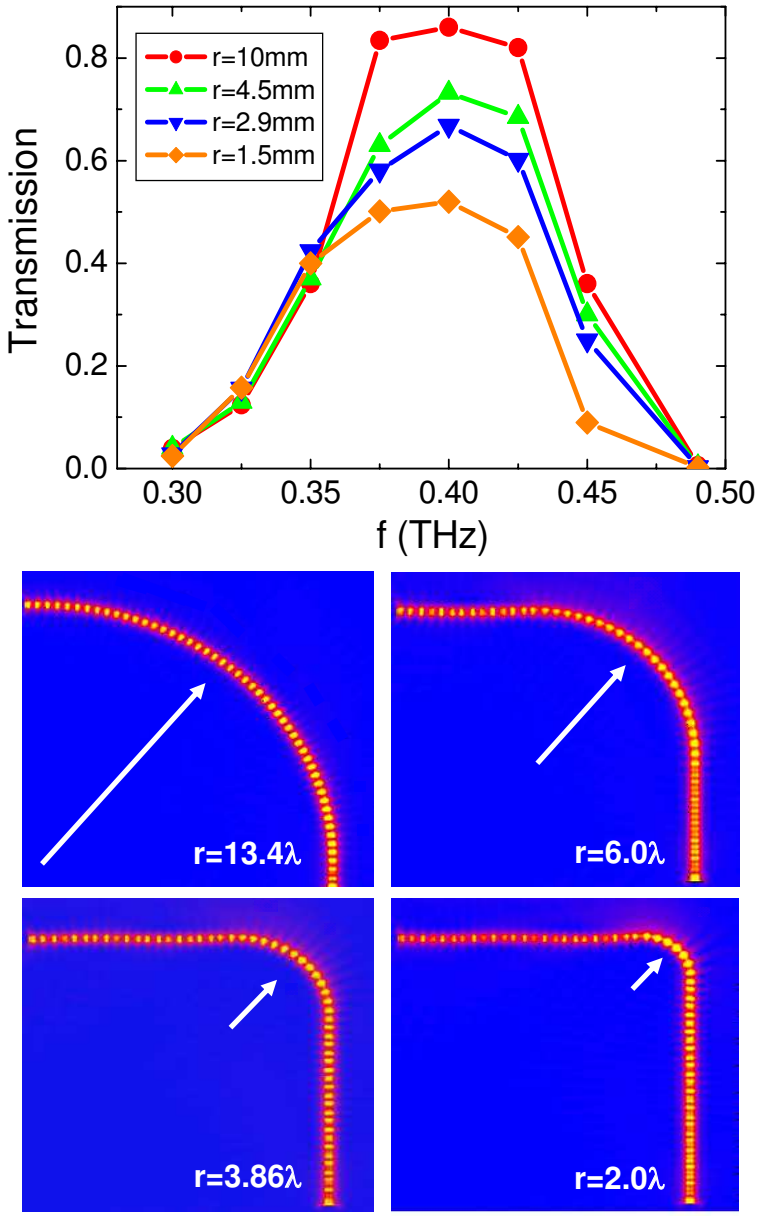

Figure 3.26.: FIT simulations of the spoof CPPs propagation through four 90° bend channels of different r. All structures are comprised by 100 periods. The upper panel renders the transmission spectrum for the four channels considered. The lower panels show the electric field amplitude at 0.40 THz evaluated at a height of 100 μm above the planar surface for the four structures analyzed.

frequencies from our ME calculations with SIBCs for the gap EM modes between two identical groove arrays. In the left inset of Fig. 3.23, l versus w is plotted at $f = 0.38$ THz, which corresponds to the center of the transmission plateau in Fig. 3.25. The propagation length for $w = 0.76d$, which coincides with the opening of the V-grooves under study, is of the order of 60λ. We have obtained similar estimations from FIT simulations in which the spoof CPPs propagation length is calculated by fitting the exponential decay of the electric field amplitude along straight corrugated aluminum V-channels. In these simulations, the Drude-like permittivity considered in [98] is used to model the dielectric response of the metal.

The possible use of spoof CPPs for routing THz radiation requires an study of the bending losses suffered by these modes. We have performed FIT simulations on corrugated bend V-grooves milled on PEC surfaces (in order to isolate bending losses from the absorption losses previously discussed). The results obtained for four different 90° bends with different radii of curvature, r, are shown in Fig. 3.26. In all cases, the structures contain up to 100 periods. The groove array period in the straight part of the channel is equal to 200 μm and is slightly adjusted in the bends in order to conform with the curved geometry. The transmittance spectra for the four structures analyzed are shown in the upper panel of Fig. 3.26. For the case of maximum r (10 mm), the transmission can be as large as 90%, but is reduced as r becomes smaller, being 50% in the case in which r is 1.5 mm (around two times the wavelength). These bending losses are much smaller than those reported for metallic wires at THz frequencies [124], as expected due to the subwavelength character of the spoof CPPs. In the four lower panels of Fig. 3.26, the electric field amplitude evaluated at 0.40 THz in a plane located 100 μm above the planar surface is depicted. It is clear how the bending losses in these structures stem from radiation into vacuum modes occurring just at the bend of the waveguide.

3.4.2. Spoof wedge plasmon polaritons

In the previous section, we have seen that spoof CPPs are not guided at the bottom of the channel, as ϵ_{eff} for gap modes seemed to indicate, but at its edges. We related such electric field distribution to the hybridization of spoof CPPs with the EM modes sustained by the edges of the corrugated channel. In this section, we study these geometrically induced EM modes and present a new guiding scheme for THz waves based on them.

The structure under study is depicted in Fig. 3.27: a PEC wedge milled with a periodic array of grooves. We can expect that, as in the case of PEC corrugated channels, the EM modes supported by such geometry resemble wedge plasmon polaritons (WPPs) [27, 28, 36] occurring at visible and telecom frequencies. The parameters defining the

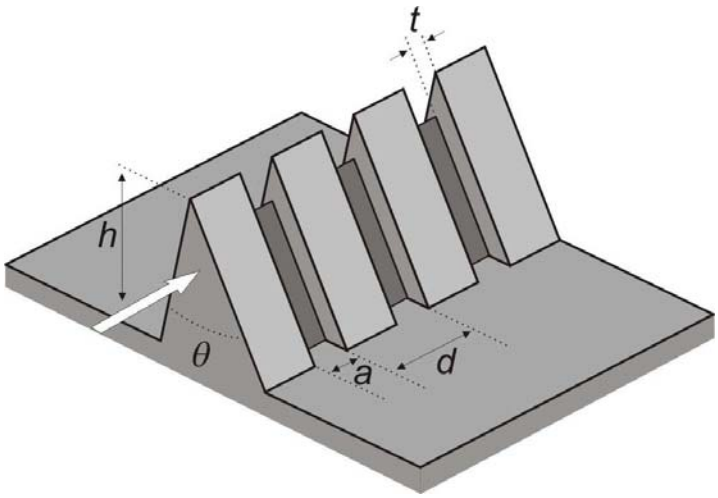

Figure 3.27.: Schematic picture of the proposed waveguiding scheme: a PEC wedge milled with a periodic array of grooves. The white arrow indicates the direction of propagation of the spoof WPPs supported by the structure.

wedge are the height, h, and angle, θ. The grooves milled on the wedge have depth t and width a, and the period of the corrugation is d. In our analysis we fix the groove width, $a = 0.5d$, and the wedge height, $h = 5d$.

Fig. 3.28 renders the two lowest bands of the spoof WPPs travelling along wedges with $\theta = 20°$. The wedges are textured with grooves of three different depths: $t = 0.75d$ (blue circles), $t = 0.5d$ (red squares), and $t = 0.75d$ (green diamonds). Dispersion bands are lowered as the groove depth is increased. Due to the finite height of the wedge, spoof WPP bands in Fig. 3.28 present a cut-off frequency, as also observed in conventional WPPs [36]. Insets (a) and (b) depict the longitudinal component of the electric field at the band edge for the two spoof WPP modes supported by the wedge with $t = 0.5d$ (red squares). The cross sections correspond to the deeper part of the corrugated wedge, where the EM fields are mainly localized. Inset (a), which renders the first spoof WPP mode, presents only one maximum within the transverse plane. However, the electric field associated to the second WPP, shown in inset (b), displays two lobes of different sign along the vertical direction, vanishing in the horizontal plane between them. Note that both EM modes have even parity with respect to the vertical symmetry plane. Although the longitudinal electric field in inset (a) is similar to that associated with WPPs sustained by real metals, the modal shape in inset (b) is not featured by conventional WPPs. Both dispersion relations and electric fields shown in Fig. 3.28 have been obtained from FDTD

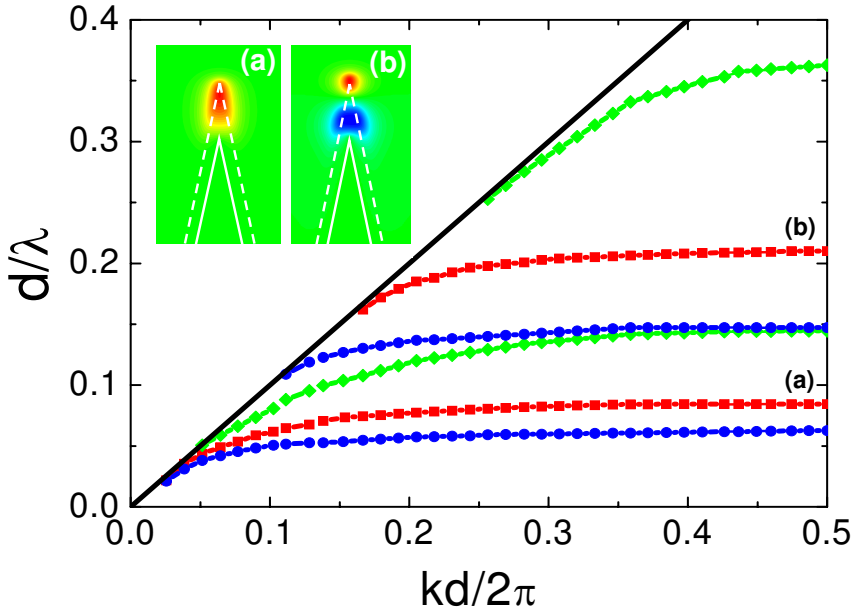

Figure 3.28.: Two lowest spoof WPP bands for wedges with three different depths: $t = 0.75d$ (blue circles), $t = 0.5d$ (red squares) and $t = 0.25d$ (green diamonds). The rest of the geometrical parameters are described in the text. Insets (a) and (b) show the longitudinal component of the electric field at the edge of the two bands for the case $t = 0.5d$.

calculations with a square mesh size of 5 μm.

Once we have demonstrated that periodically corrugated PEC wedges support spoof WPP modes whose dispersion relation can be controlled by the groove depth, we study the influence of the angle, θ, on the modal characteristics. In Figure 3.29, the fundamental WPP bands for wedges of different θ are shown (for all structures, a and d remain as in Fig. 3.28, and $t = 0.5d$). As θ increases, the bands shift to higher frequencies, tending to the limiting case of a flat ($\theta = 180°$) groove array (see Sec. 3.2.2), represented by a black dashed line. The insets of Fig. 3.29 render the electric field amplitude at the band edge for wedges with (a) $\theta = 20°$, and (b) $\theta = 60°$. In both cases, the half-wavelength ($\lambda/2$) is represented by vertical white bars. Following the convention used for spoof CPPs, the modal size for the 20° wedge is $\delta = 0.28\lambda$, whereas for $\theta = 60°$, it is equal to 0.78λ. These results demonstrate the subwavelenth transverse confinement featured by spoof WPPs.

To make our design work at THz frequencies, we set the corrugation period, d, to 200 μm. Although PEC boundary conditions are an excellent approximation in the THz regime, they do not take into account modal losses. Thus, we estimate the propagation length of spoof WPPs through FIT simulations in which the metal response is described

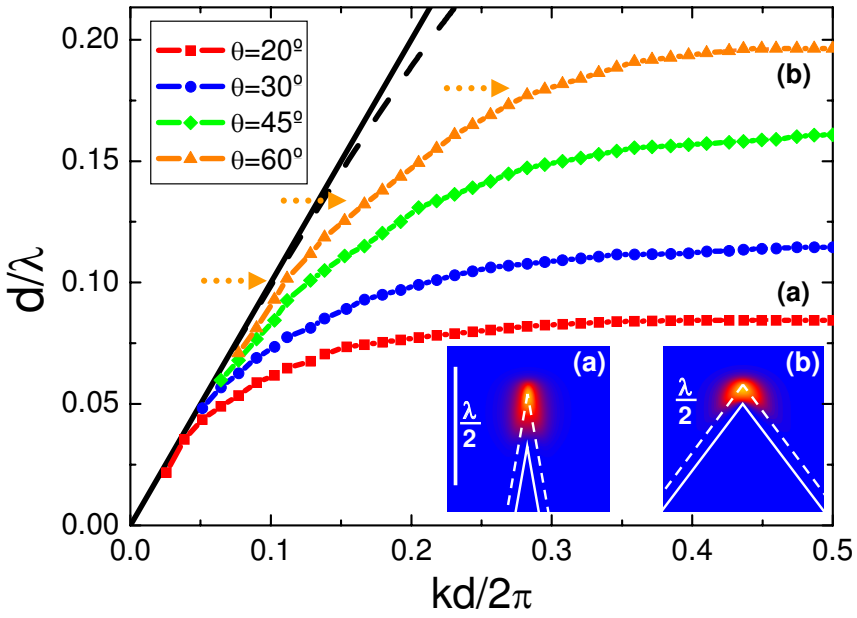

Figure 3.29.: Dispersion relation of the fundamental spoof WPP travelling along corrugated wedges for different θ. Dashed black line shows the dispersion band corresponding to the flat ($\theta = 180°$) case (groove array). The horizontal arrows indicate the frequencies for which the propagation length is estimated (see the text). Lower insets show the electric field amplitudes at the band edge for (a) $\theta = 20°$ and (b) $\theta = 60°$. In both insets, $\lambda/2$ is represented by white bars.

using a realistic dielectric function [98]. We consider a corrugated aluminum wedge with $\theta = 60°$ and a length of 40 mm (the remaining geometrical parameters being the same as in Fig. 3.29). As in the case of channels, the mode propagation length is obtained by fitting the exponential decay of the electric field amplitude along the wedge. To illustrate the dependence of l on the frequency, we choose three representative values indicated by orange dotted arrows in Fig. 3.29. Close to the light line, at $d/\lambda = 0.10$, which corresponds to $f = 0.16$ THz, we find $l = 120\,\text{mm} = 64\lambda$. At larger frequencies, the propagation length is reduced, being $l = 43.2\,\text{mm} = 29\lambda$ at $d/\lambda = 0.13$ ($f = 0.20$ THz). Finally, as we approach the flat part of the band, the propagation length decreases abruptly. Thus, at $d/\lambda = 0.18$ ($f = 0.27$ THz), we obtain $l = 1.56\,\text{mm} = 1.3\lambda$. It is remarkable that the values obtained for l/λ are comparable to those reported for WPPs in the telecom regime [36], where the physical origin of the field confinement is completely different. This correspondence of l/λ between conventional and spoof SPPs has been also observed in planar and wire geometries [125, 126].

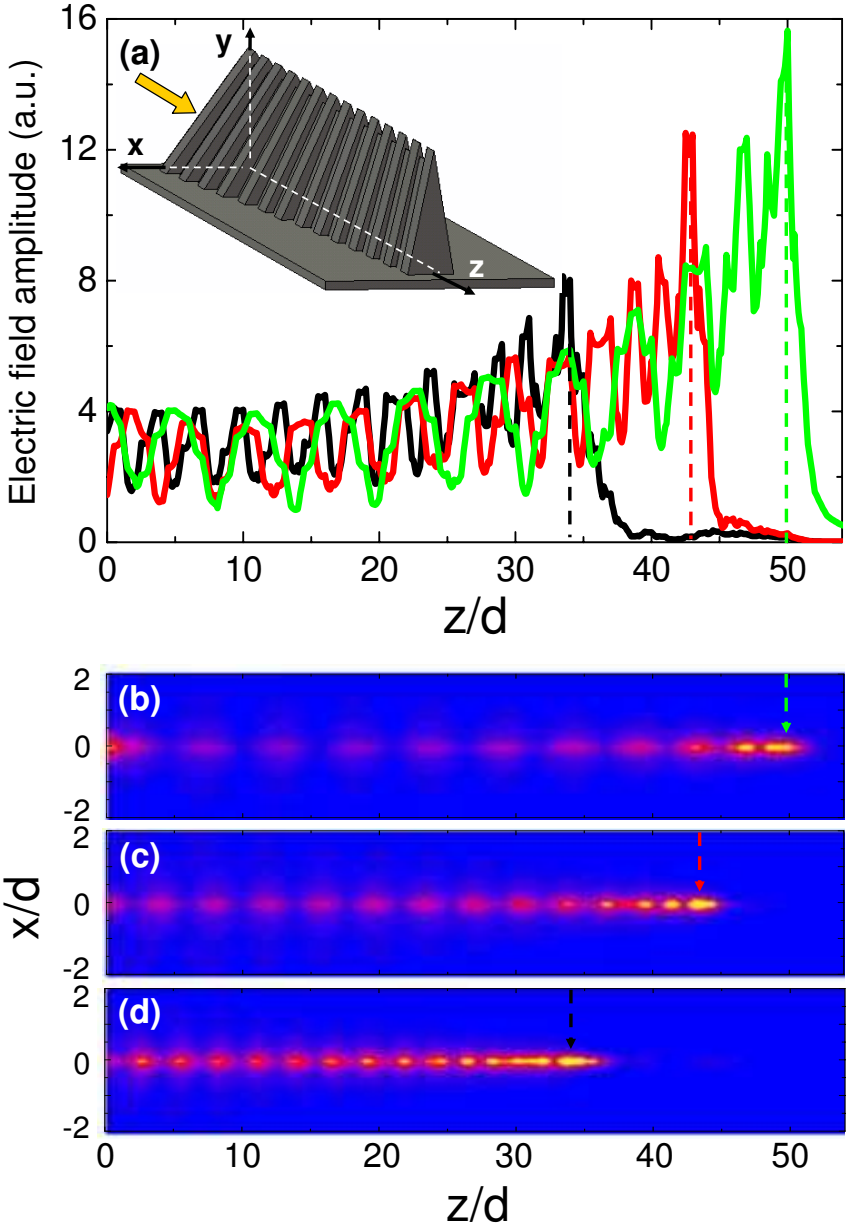

Figure 3.30.: (a) Left inset: Corrugated PEC wedge with θ varying smoothly along the z-direction from 60° to 20°. Main panel: Electric field amplitude versus z along the line located 100 μm above the structure apex. Three different frequencies are considered: 0.12 THz (green line), 0.16 THz (red line) and 0.20 THz (black line). Panels (b), (c), and (d) depict the electric field amplitude within the xz plane located 100 μm above the apex for these three frequencies. Dashed arrows indicate the position of the maxima of amplitude shown in panel (a).

Figure 3.29 provides us a hint on how THz waves can be focused and slowed down with the aid of spoof WPPs. The lowering of the dispersion bands for decreasing θ suggests that radiation of a given frequency propagating in a wedge which is sharpened along its length [see inset of Fig. 3.30] would be gradually concentrated within the transverse plane. Additionally, THz waves at frequencies above the band edge associated to a specific θ will never reach sections of the structure sharper than that angle, being slowed down as they approach it. In order to prevent backreflection and scattering of EM fields out of the structure, impedance mismatches along the wedge length can be minimized by performing the reduction in θ adiabatically.

The inset of Fig. 3.30 shows a diagram of the design proposed: a 10 mm long wedge with θ varying smoothly from 60° to 20° milled by 50 grooves disposed periodically with the same geometrical parameters as in Fig. 3.29. The guiding properties of the structure are studied by means of FIT simulations under PEC approximation. The wide end of the wedge is illuminated with a broadband pulse whose modal shape corresponds to that of spoof WPP modes supported by an infinitely long 60° wedge. Panel (a) of Fig. 3.30 renders the electric field amplitude, $|E|$, on a line parallel to the z-axis and 100 μm above the wedge apex. $|E|$ is evaluated at three different frequencies within the spectral range spanned by the dispersion bands shown in Fig. 3.29. Waves at $d/\lambda = 0.08$ ($f = 0.12$ THz) propagate until the sharpest end of the wedge, giving rise to a maximum in the electric field amplitude located at that position (green line). At higher frequencies, radiation is slowed down and stopped before reaching the wedge end. For $d/\lambda = 0.1$ ($f = 0.16$ THz), a peak in $|E|$ is developed at the 42^{nd} groove, for which $\theta = 26°$ (red line). At $d/lambda = 0.13$ (0.20 THz) EM fields explore an even shorter section of the wedge and $|E|$ presents a maximum at the 34^{th} groove, which correspond to $\theta = 32°$ (black line). Note that these results are in excellent agreement with the FDTD dispersion bands of Fig. 3.29.

Panels (b), (c), and (d) of Fig. 3.30 depict $|E|$ within the xy-plane located 100 μm above the wedge apex, for the three frequencies considered in panel (a). Vertical dashed arrows indicate the position of the maxima in panel (a). In these three contourplots, the reduction of the effective wavelength [$\lambda_{\text{eff}} = 2\pi/\text{Re}(k)$] experienced by the guided EM fields as they propagate along the structure can be observed. This fact points out that slowing down and stopping of THz waves is occurring along the wedge, at different locations depending on the frequency of the incoming radiation. Note that, as a difference with the scheme proposed in Ref. [127], the stopping mechanism presented here also leads to the transverse confinement of EM fields. Panels (b), (c) and (d) indicate that guided waves are not scattered out of the wedge as they travel in the z-direction. On the contrary, while propagating along the structure, EM fields are gradually concentrated, giving rise

to frequency selective focusing of THz waves.

3.5. Conclusions

In this chapter, we have studied the geometrically induced EM modes supported by different structures. We have introduced our work by reviewing the dispersion relation of conventional SPPs. Then, we have introduced spoof SPPs in planar geometries, both in single surfaces (groove and dimple arrays) and films (slit and holes). We have demonstrated that the characteristics of the EM modes bound to these structures are controlled by the width and depth of the perforations. Additionally, we have shown that our theoretical results are in excellent agreement with experimental measurements of the propagation and confinement of spoof SPPs on dimple arrays at THz frequencies.

Secondly, we have demonstrated that corrugated wires also sustain spoof SPP modes. We have motivated our study by describing the behavior of conventional SPPs on cylindrical surfaces in the limit of PEC metal. We have studied the geometrically induced EM modes bound to ring arrays, and proposed a scheme for achieving subwavelength focusing of EM fields based on these modes. We have also considered the case of helically grooved wires, where the comparison with experiments in the THz regime has been also shown.

Finally, we have presented two different guiding schemes for THz waves based on the spoof SPP concept. The designs consist of corrugated channels and wedges. We have demonstrated that subwavelength confinement of EM fields in the transverse plane is achieved in such structures due to the mode coupling in a similar way as it happens in channel and wedge plasmon polaritons in the visible and telecom ranges.

4. Role of order in the phenomenon of extraordinary transmission

4.1. Introduction

Since the discovery of the extraordinary optical transmission through periodic arrays of subwavelength holes [39], many theoretical and experimental works have been devoted to analyze the appearance of the phenomenon in different structures. Apart from hole arrangements [40, 44–46], resonant transmission has been reported in periodic arrays of slits [41–43, 128, 129], single apertures [130–134], and single apertures surrounded by corrugations [48–50]. Recently, several experimental works have been published reporting transmission resonances in quasiperiodic aperture arrays [135–140]. These papers suggest that the presence of long range order in the system is the fundamental ingredient to observe the phenomenon of extraordinary optical transmission.

In this chapter, we analyze the transmission properties of finite (periodic and quasiperiodic) slit arrays, and quasiperiodic hole arrangements. By means of our modal expansion formalism, we obtain the transmittance and the distribution of electromagnetic fields in such structures. In its reciprocal version, our theoretical framework enables us to link the electric field amplitudes at the film surfaces to the structure factor of the system. This provides us with a complete theoretical description of the connection between the structure order and transmission resonances. Moreover, we identify the leaky electromagnetic modes supported by perforated film as the key actors in the resonant transmission process.

Throughout this chapter, the metallic film will be treated as a perfect conductor, i.e., $\epsilon_M = -\infty$. This is a very good approximation in the microwave and terahertz regimes, where experiments on quasiperiodic apertures have been performed, and still has semiquantitative value at optical frequencies. Additionally, perfect conducting boundaries make all the lengths involved in the system scalable, which allows transferring our results to different ranges of the electromagnetic spectrum.

4.2. Finite and quasiperiodic slit arrays

4.2.1. Infinite array and single slit

We motivate the study of the transmission of light through finite arrays of subwavelength slits by first analyzing two interesting and limiting cases in which the ME continuity equations governing the electromagnetic (EM) fields behavior (2.46) have a very simple form: a single slit and an infinitely periodic array of identical slits, both systems illuminated by a normal incident p-polarized plane wave. In spite of being very different systems, in both cases we find that, by considering only the first waveguide mode inside the slit(s), the system of linear equations simplifies into just the same two equations

$$\begin{aligned} (G-\epsilon)E - G^V E' &= I, \\ (G-\epsilon)E' - G^V E &= 0. \end{aligned} \tag{4.1}$$

For both systems, the illumination term, $I = 2i\langle \text{slit}|k_0\rangle$, is proportional to the overlap between the incident plane wave and the slit(s) waveguide mode. The slit(s) waveguide mode is given by $\langle x|\text{slit}\rangle = 1/\sqrt{a}$, where a is the slit(s) width [see Eq. (2.37)]. The term $\epsilon = \cot(k_0 h)$ (where h is the film thickness) reflects the bouncing back and forth of the EM fields inside the aperture(s), and $G^V = 1/\sin(k_0 h)$ takes into account the coupling of the EM fields at different film sides through the slit(s). The only difference between the two systems resides in the expression for G in Eqs. (4.1), which describes the interaction of EM fields associated with slit waveguide modes through diffraction waves. For the single slit case, it reads

$$G = G_S = \int\int dx dx' \langle \text{slit}|x\rangle G(x,x')\langle x'|\text{slit}\rangle, \tag{4.2}$$

where the integrals on x and x' run over the width of the slit and $G(x,x')$ is given by Eq. (2.63). On the other hand, for the infinite case, the set of continuity equations is obtained from Eqs. (2.38). Thus, by considering only the fundamental slit waveguide mode, we can rewrite Eq. (2.42) as

$$G = G_\infty = i\sum_m Y_{k_m} |\langle k_m|\text{slit}\rangle|^2. \tag{4.3}$$

For normal incidence, $k_m = m\frac{2\pi}{d}$, where d denotes the array period, $Y_{k_m} = k_0/\sqrt{k_0^2 - k_m^2}$, and the wavefunction for the diffraction waves is $\langle x|k_m\rangle = e^{ik_m x}/\sqrt{d}$.

Several works have been published studying the transmission properties of perforated films [49] in which the single mode approximation that we are considering in our model is used. Note that for the case of 1D slits, irrespective of the ratio between a and λ, the first waveguide mode is always propagating. Since in the subwavelength regime ($\lambda >> a$), all

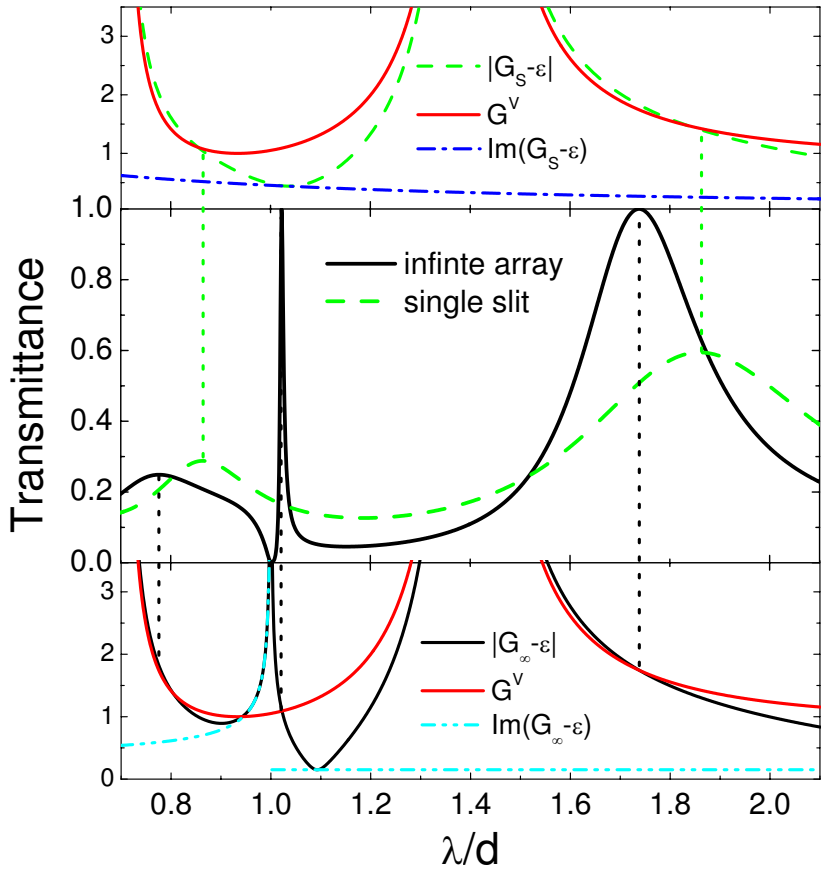

Figure 4.1.: Transmission spectra normalized to the light impinging the area corresponding to the array period, d, for a single slit and for an infinite periodic array of slits (for both structures, $h = 0.7d$ and $a = 0.15d$). Top: wavelength dependence of the relevant terms in Eq. (4.1) for the single slit. Bottom: the same but for the infinite array of slits.

higher modes are evanescent, it is a very good approximation to consider that only the first slit waveguide mode is excited by the incident plane wave.

The central panel of Figure 4.1 shows the comparison between the transmission spectra for a single slit and for an infinite array of slits. In both cases, the transmittance (defined as the ratio between the EM power exiting and impinging on the structure, see Section 2.2.1) is normalized to the EM flux incident on the area corresponding to the array period, d. For the normalization considered, the transmissivity of both structures can be calculated from the 1D version of Eqs. (2.33) and (2.34), having:

$$T = (G^V / Y_{k_0}) \mathrm{Im}(EE'^*). \tag{4.4}$$

In our model, we consider only perfect electric conducting (PEC) films. This means that all lengths in the structure are scalable and we can take d as the reference length. For the two structures analyzed in Fig. 4.1, the thickness of the film is chosen to be $h = 0.7d$ and the slits width, $a = 0.15d$.

In the wavelength range analyzed, the single slit spectrum presents two maxima which correspond to the first two slit cavity resonances, located near the Fabry-Perot condition $\sin(k_0 h) = 0$. The infinite array spectrum shows these two maxima too, but shifted to shorter wavelengths. However, slightly above the periodicity ($\lambda \gtrsim d$) this spectrum presents a strongly peaked feature which does not appear for the single slit. This maximum can be associated with the excitation of surface resonances at both sides of the film [43, 45]. It is accompanied by a sharp drop in the transmittance just at the periodicity, the well-known Wood-Rayleigh's anomaly [3, 4].

Although the phenomenology for a single slit and for an infinite array of slits is well known, the novelty of our approach is that it allows to understand the physics and mathematics behind the transmission resonances in both systems just by analyzing the terms appearing in Eqs. (4.1). The wavelength dependence of the different terms in these equations for a single slit and for an infinite array is shown in the top and bottom panels of Fig. 4.1, respectively. For example, the origin of the Wood-Rayleigh's anomaly, present only in the infinite array spectrum, stems from a divergence in G_∞ (see lower panel in Fig. 4.1) that appears just at the wavelength in which a diffraction order $(\pm 1, 0)$ becomes evanescent ($\lambda = d, k_z = 0$). This divergence makes the field intensity at the input and output sides of the slits vanishing, i.e. $|E| = |E'| = 0$ (see Eqs. (4.1)). As in typical resonant phenomena, the spectral locations of the EM resonances can be extracted by looking at the zeroes in the determinant of the matrix defining the associated set of linear equations [141, 142]. For both structures, the spectral locations of the transmission peaks coincide with cuts between G^V and $|G - \epsilon|$. Imposing $G^V = |G - \epsilon|$ in Eqs. (4.1) we find that, for wavelengths satisfying this condition, the electric field intensities at both sides of the slits are equal, i.e. $|E| = |E'|$. It is straightforward to demonstrate that this condition also leads to a resonant denominator in the expressions for the corresponding electric field amplitudes $\{E, E'\}$. Therefore, transmission maxima in both spectra rely on EM resonances with the same mathematics but with a different physical origin.

For a single slit, transmission maxima are due to the excitation of cavity resonances with the EM fields mainly concentrated inside the slits [130, 132]. For an infinite array, these slit cavity resonances still emerge in the transmission spectrum but their locations appear at shorter wavelengths. This shift is due to the EM coupling between the slits forming the infinite array. This interaction modifies in an effective way the reflectivity at the boundaries of the Fabry-Perot cavity, changing the spectral location of the corres-

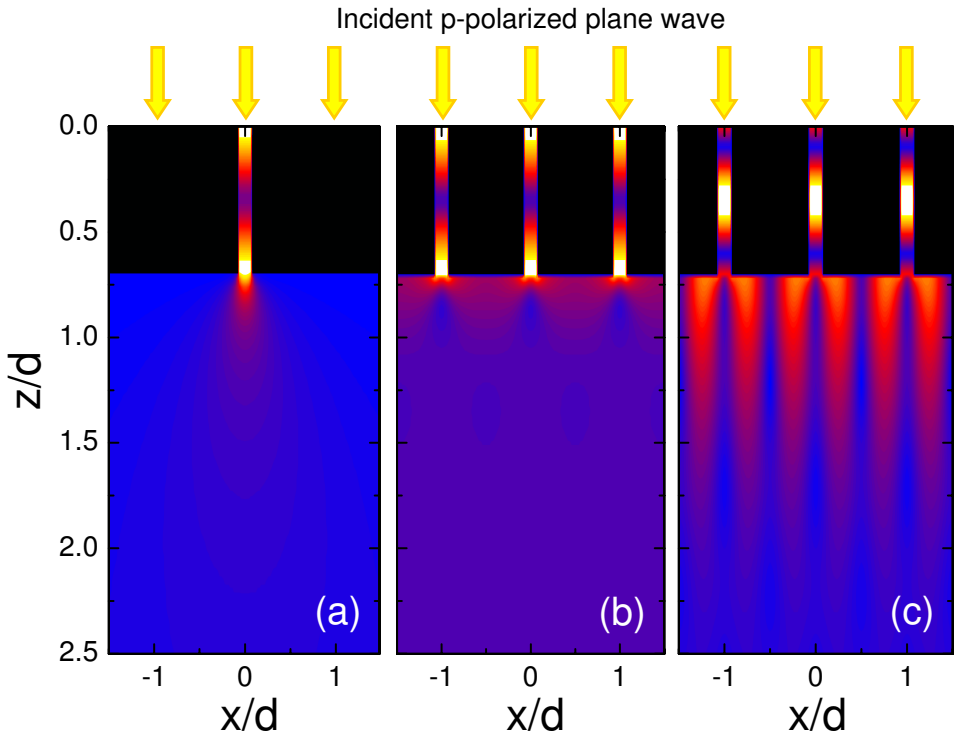

Figure 4.2.: Electric field amplitude, $|E|$, at the output side of the single slit and the periodic array of Fig. 4.1. Panel (a) shows $|E|$ for the single slit evaluated at $\lambda = 1.86d$. Panels (b) and (c) render the electric field pattern for the periodic array at $\lambda = 1.75d$ and $\lambda = 1.03d$, respectively.

ponding resonances [143]. Additionally, a new transmission peak appears close to the divergence of G_∞, which can be linked to surface resonances at the film sides [41, 42].

In order to check the validity of this physical picture in which transmission maxima are linked to slit cavity and surface EM resonances, we show in Figure 4.2 the amplitude of the electric field, $|E|$, at the exit side of the PEC film for both the single slit and the periodic array considered in Fig. 4.1. Panel (a) renders $|E|$ at the maximum at $\lambda = 1.86d$ in the single slit spectrum. Panels (b) and (c) correspond to the transmission maxima that the periodic array displays at $\lambda = 1.75d$ and $\lambda = 1.03d$, respectively. As expected, the electric field in panels (a) and (b) is mostly located inside the slits, which indicates that the transmission resonances in both systems have the same physical origin. However, in panel (c), $|E|$ shows a sequence of maxima in the x-direction which indicates that the resonance that governs the transmissivity of the system has a strong surface character.

Importantly, we can associate the transmission resonances appearing in perforated PEC films with the spoof SPP modes supported by such structures. As we showed in

Section 3.2.3, in the case of 1D apertures these geometrically induced EM modes have an hybrid nature, featuring characteristics of both surface and slit waveguide modes. Thus, whereas at the peak near the Fabry-Perot condition, the spoof SPPs are strongly influenced by the slit cavity resonance, close to the array period, it is the surface character of the spoof SPP modes which prevail.

4.2.2. Finite array of slits

Now, we apply our ME formalism to the study of the transmission properties of finite periodic arrays of N identical slits. As we showed in Section 2.2.2, the set of continuity equations for the system reads

$$\begin{aligned} (G_{\alpha\alpha} - \epsilon_\alpha)E_\alpha + \textstyle\sum_{\beta\neq\alpha} G_{\alpha\beta}E_\beta - G^V_\beta E'_\alpha = I_\alpha, \\ (G_\alpha - \epsilon_\alpha)E'_\alpha + \textstyle\sum_{\beta\neq\alpha} G_{\alpha\beta}E'_\beta - G^V_\alpha E_\alpha = 0, \end{aligned} \tag{4.5}$$

where index $\alpha = 1, 2, \ldots N$, labels the slit positions, $x_\alpha = \alpha d$. Note that the interpretation of the various terms appearing in Eqs. (4.5) is the same as in Eqs. (4.1). By solving the $2N \times 2N$ system of continuity equations, we obtain the set of unknown modal amplitudes $\{E_\alpha, E'_\alpha\}$. Thus, we can calculate the transmittance of the film and evaluate the EM fields at any point of the structure. The transmittance of a finite array of N slits normalized to the light impinging on the region corresponding to N times the array periodicity (Nd) reads

$$T(N) = \frac{1}{N}\sum_{\alpha=1}^{N} t_\alpha = \frac{G^V}{NY_{k_0}}\sum_{\alpha=1}^{N} \mathrm{Im}\left(E'_\alpha E^*_\alpha\right), \tag{4.6}$$

where $t_\alpha = (G^V/Y_{k_0})\mathrm{Im}(E'_\alpha E^*_\alpha)$ gives the transmission per slit forming the array (normalized to the array periodicity) i.e., the contribution of each slit to the total transmissivity of the structure.

Fig. 4.3 shows the transmission spectra of periodic arrays with increasing number of slits. The geometrical parameters of all the structures are $h = 0.7d$ and $a = 0.2d$. We have focused our analysis on the evolution of the surface and first slit cavity resonant peaks. The maximum at the cavity resonance ($\lambda = 1.75d$), which already appears in the single slit spectrum, is almost completely formed for an array containing only 2 slits. This fast development relies on the localized nature of the EM modes involved in the scattering process. However, at the surface resonance peak ($\lambda = 1.03d$), the coupling between the incident light and the spoof SPPs depends strongly on the corrugation of the structure and light coming from several slits is involved in the transmission process. It can be seen in Fig. 4.3 that this peak evolves, not only in height but also in linewidth, gradually

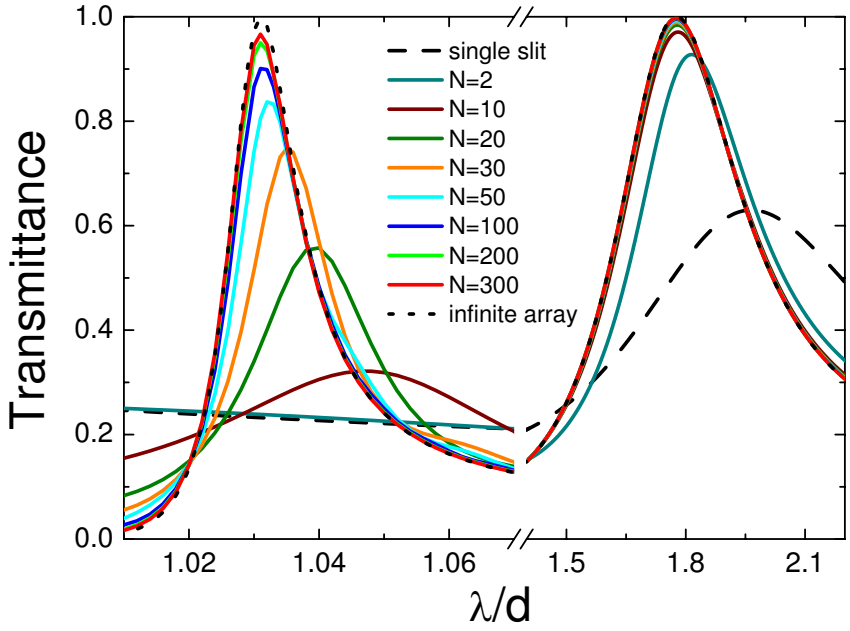

Figure 4.3.: Evolution of the resonant peaks in the transmission spectra of finite arrays of slits as the number of slits is increased. The transmittance is normalized to the EM flux impinging on N times the array period. For all the structures, $h = 0.7d$ and $a = 0.2d$.

as the size of the array increases. This fact reinforces our interpretation of the surface resonance as an spoof SPP mode emerging from the collective interaction among slits.

In order to study the effect on the transmittance of the interaction among EM fields coming from different slits, we have plotted in Fig. 4.4, the normalized to period transmission per slit (t_α) for finite arrays of slits evaluated at the surface resonance. We have taken the same geometrical parameters as in Fig. 4.3. For small arrays ($N \leq 100$), the transmittance is maximum at the center of the array. However, for large enough arrays, we can distinguish between two kind of slit contributions to the total transmittance of the structure. The transmission per slit pattern is composed by a flat central region, whose width grows as the array size is increased, and two edge regions, each of them involving N_E slits, which is almost independent of the array size, N. The transmittance through the central $(N - 2N_E)$ slits is, except some small oscillations, uniform and equal to the value for the infinite case ($T_\infty = 1$ for the normalization considered). However, for the N_E slits close to each array edge, t_α falls from 1 to 0.5 as we approach the array ends. It can be seen in Fig. 4.4 that, for the structure considered in our calculation, $N_E \simeq 20$.

The transmission per slit distribution depicted in Fig. 4.4 is reflected in the electric field

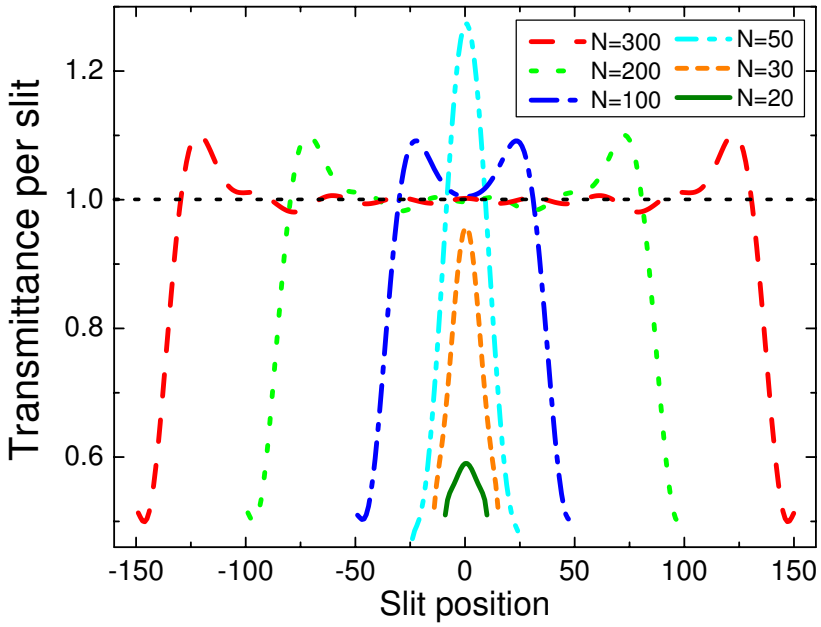

Figure 4.4.: Normalized to period transmission per slit evaluated at the surface resonance for arrays of different sizes with $h = 0.7d$ and $a = 0.2d$. Dotted black line corresponds to the uniform transmission pattern for an infinite array of slits.

distribution close to the metallic film. Figure 4.5 renders the electric field amplitude, $|E|$, for the periodic array of 30 slits considered in Fig. 4.4. $|E|$ is evaluated at $\lambda = 1.04d$, which corresponds to the location of the surface resonance peak in the transmission spectrum (see Fig. 4.3). The high transmissivity of the central slits is accompanied by a strong field enhancement originated by the excitation of spoof SPPs in the central region of the structure. As in infinite arrays (see Fig. 4.2), the propagation of these leaky EM modes along the system gives rise to the sequence of maxima in $|E|$ at the film surfaces. We can relate the distance between two consecutive maxima to the spoof SPPs half-wavelength which, as expected, is slightly larger than $d/2$.

Taking advantage of the scalable pattern of t_α, we can obtain an approximated expression for the peak height at the surface resonance as a function of the number of slits (for large enough arrays). The transmittance through an array containing N slits can be written as the sum of contributions corresponding the different regions found in Fig 4.4. For the $(N - 2N_E)$ central slits, the total transmittance is $(N - 2N_E)T_\infty = N - 2N_E$. For the $2N_E$ edge slits, it results in a good approximation to take the average value $2[(1 + 0.5)N_E/2]T_\infty = 3N_E/2$. The transmittance of the array normalized to the EM flux

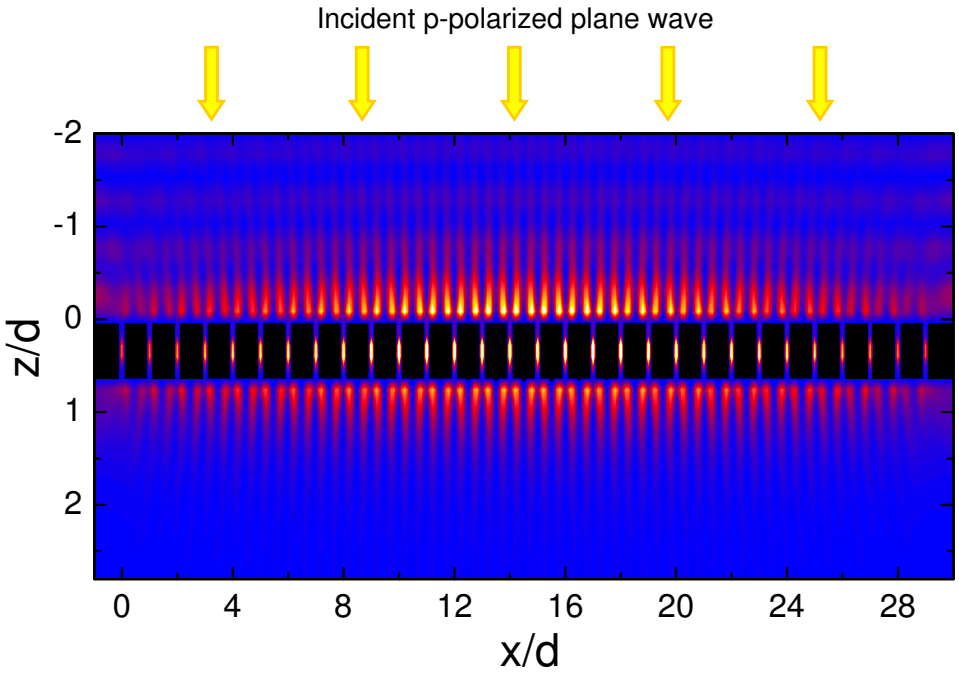

Figure 4.5.: Amplitude of the transverse component of the electric field evaluated at the surface resonance for a periodic array of 30 slits.

incident on the area corresponding to N times the array periodicity is then given by

$$T_{\max}(N) = \frac{1}{N}\left(N - 2N_E + \frac{3N_E}{2}\right) = 1 - \frac{N_E}{2N}. \tag{4.7}$$

Figure 4.6 plots the evolution with N of the height of the transmission peak at the surface resonance for arrays of slits of different widths perforated in a perfect conducting film of thickness $h = 0.7d$. Dots correspond to values obtained from the exact calculation using Eq. (4.6) . For all the structures, peak growth has a similar behavior. For small arrays, the transmittance depends linearly with N, but for larger ones, it grows much more slowly, going as the inverse of the number of slits, as predicted by Eq. (4.7). This change in tendency does not occur abruptly at a fixed array size, but in a range whose position and width depend strongly on the width of the slits. The narrower the slits, the wider this range is. We can relate this two tendencies with the t_α distribution depicted in Fig. 4.4. For small arrays ($N < 2N_E$), the peak height grows linearly, while t_α is peaked around the array center. However, for arrays with $N > 2N_E$, the peak goes as the inverse of the slit number and a flat plateau appears in the transmission per slit pattern. This picture is reinforced by comparing the case analyzed in Fig. 4.4 ($a = 0.20d$), where the flat plateau is formed for $50 < N < 100$. The change in tendency for orange up triangles

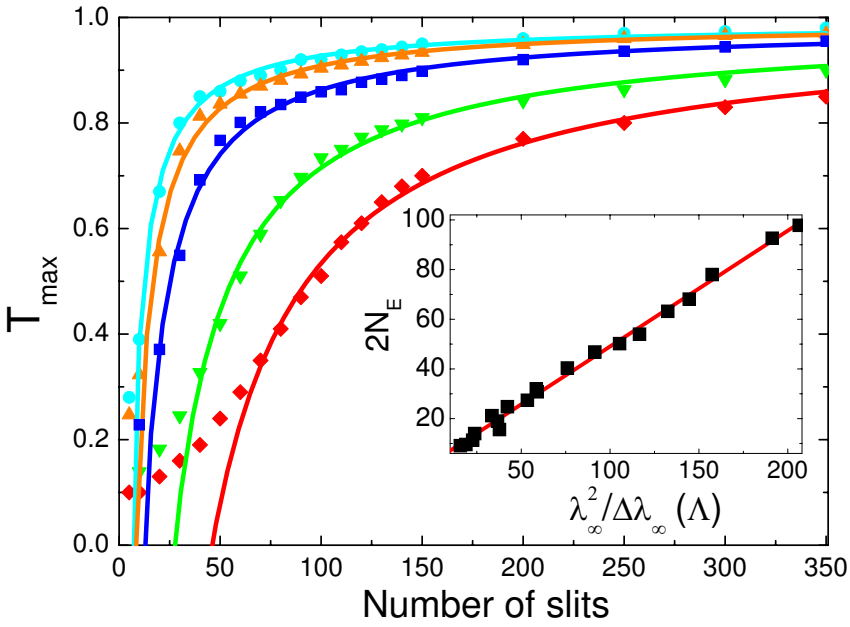

Figure 4.6.: Transmittance at the surface resonance calculated from Eq. (4.6) for different slits width: $a = 0.24d$ (cyan circles), $a = 0.20d$ (orange up triangles), $a = 0.15d$ (blue squares), $a = 0.10d$ (green down triangles), and $a = 0.08d$ (red diamonds). For all structures $h = 0.7d$ Solid lines: Fitting curves given by Eq. (4.7) for $N > N_E$. Inset: Linear relation between $2N_E$ and $\lambda_\infty^2/\Delta\lambda_\infty$ for structures with $0.08\lambda \leq a \leq 0.24d$ and $0.6d \leq h \leq 0.8d$.

in Fig. 4.6, which corresponds to the same structure, occurs for $N \sim 70$. Solid lines in Fig. 4.6 correspond to curves of the form of Eq. (4.7) fitted to exact calculated values for arrays with $N > 2N_E$. N_E values obtained from the fitting parameters are in very good agreement with the corresponding transmission per slit patterns at resonance. For instance, from Fig. 4.4, we have $N_E \simeq 20$ for $a = 0.20d$, and from the fitting curve, we obtain $N_E = 16$.

In the following, we demonstrate that the phenomenological parameter $2N_E$ is closely related to the spatial extension of the surface EM mode responsible of the enhanced transmission. This spatial extension can be extracted from the corresponding transmission spectrum for the infinite array. The linewidth of the resonant peak is related to the time, $\Delta\tau$, that EM fields spend during the resonant process before being re-emitted from the structure. If we assume that the EM fields associated with the resonant mode travel at the speed of light, c, the spatial extension of the mode would be $c\Delta\tau = (\lambda_\infty^2/\Delta\lambda_\infty)$, with λ_∞ being the peak position and $\Delta\lambda_\infty$ the linewidth at half maximum of the peak. In the inset of Figure 4.6, we represent $2N_E$ versus $(\lambda_\infty^2/\Delta\lambda_\infty)$ (in units of d) for the four cases

analyzed in the main panel and for other ones in which the thickness of the metallic film is also varied. This figure clearly demonstrates that there is a linear relation between the two magnitudes, with a proportionality factor being close to 0.4. Although the linewidth of the resonant peak appearing close to the period of the array is a complex function of the geometrical parameters of the structure (a, d and h) and the resonant wavelength, Fig. 4.6 demonstrates that the main controlling factor is the ratio between the width of the slits and the period of the array, a/d.

All these results have been obtained assuming that the perforated metal behaves as a perfect conductor. As stated in chapter 2, our results have quantitative value for metals at microwave or THz frequencies. At optical frequencies, it is expected that absorption in the metal would play an important role in the evolution of the transmission spectra as a function of the number of slits. Absorption introduces another lifetime into the problem, the time taken by the photon to get absorbed. Associated with this lifetime we can introduce a new length scale, L_{abs}, roughly defined as the product of the photon lifetime and the light velocity. If L_{abs} is smaller than $N_E d$, the number of slits needed to obtain the transmittance of the infinite array will be mainly controlled by absorption in the metal. In the opposite case, transmission resonances can be built up before the photons are absorbed and hence the values of N_E calculated within the perfect conductor approach still hold.

4.2.3. Fibonacci array of slits

In this section, we analyze the transmission characteristics of slits disposed following a Fibonacci sequence. This is probably the earliest and best known deterministic aperiodic system. In its simplest version, it can be generated from two basic elements $\{a, b\}$ by iteratively applying the substitution rules:

$$a \rightarrow ab, b \rightarrow a, \tag{4.8}$$

Thus, we can construct Fibonacci chains of increasing number of elements, having:

$$a \Rightarrow ab \Rightarrow aba \Rightarrow abaab \Rightarrow abaababa \Rightarrow \ldots \tag{4.9}$$

Each sequence S_j in (4.9) can be obtained from the two preceding ones by applying the recursion relation $S_j = S_{j-1} \cap S_{j-2}$, where symbol $\cap$ means composition. Sequences of a and b elements obtained through this iterating process do not have a well defined regularity, but they present several interesting properties due to their quasiperiodic character.

Figure 4.7 depicts a Fibonacci array of slits. The distance between consecutive slits in this arrangement follows a Fibonacci sequence of two basic lengths, d_1 and d_2. The

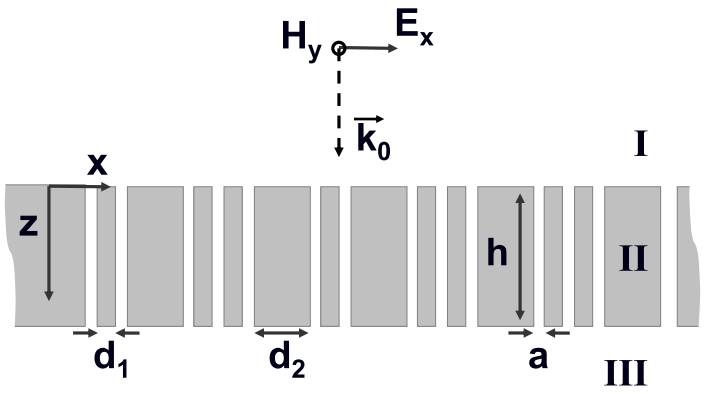

Figure 4.7.: Schematic cross section of the structure analyzed in the text, a perfect conducting film of thickness h drilled with an array of slits a. Slits are disposed following a Fibonacci sequence generated from two basic distances d_1 and d_2 (see text for definition).

position of the slits in a Fibonacci array [144] is given by

$$x_\alpha = d_1 \mathrm{int}\left(\frac{\alpha}{\tau}\right) + d_2\left[\alpha - 1 - \mathrm{int}\left(\frac{\alpha}{\tau}\right)\right], \tag{4.10}$$

where $\alpha = 1, 2, \ldots, N$, being N the number of slits in the array. The constant $\tau = (1+\sqrt{5})/2$ is the golden ratio and int() denotes the integer part function.

In panel (a) of Fig. 4.8, the modulus of the structure factor, $S(k) = \sum_\alpha e^{ikx_\alpha}$, for a Fibonacci array of 200 slits is depicted. The two basic lengths defining the array are $d_1 = 0.68d$ and $d_2 = 1.55d$, where d is the mean distance between slits. Panel (b) renders the structure factor for a periodic array of 200 slits of period d. It vanishes for all k's which are far from the multiples of $2\pi/d$, and is narrowly peaked around each of these multiples. At wave vectors close to the peaks, all summands in $S(k)$ are in phase, and $|S|_{\max} = N = 200$. The structure factor for the Fibonacci array also presents several peaked features. The formation of these maxima relies on the appearance of a limited degree of coherence among summands in $S(k)$ which makes $|S|_{\max} < 200 = N$ (for $k \neq 0$). These peaks are clear fingerprints of the presence of long range order in the system. For comparison, in panel (c) we have plotted the structure factor of a random array of 200 slits of the same size. Except at $k = 0$, it does not show any peaked feature, which demonstrates the absence of order in the slits distribution.

In Fig. 4.9, transmission spectra of a PEC film of thickness $h = 0.68d$ perforated with a Fibonacci (black solid line), a periodic (red dashed line) and a random (blue dotted line) arrays of 200 slits of width $a = 0.17d$ are shown. Transmittances are normalized to the transmissivity of 200 independent slits. The transmission of a single slit, T_0, taken as

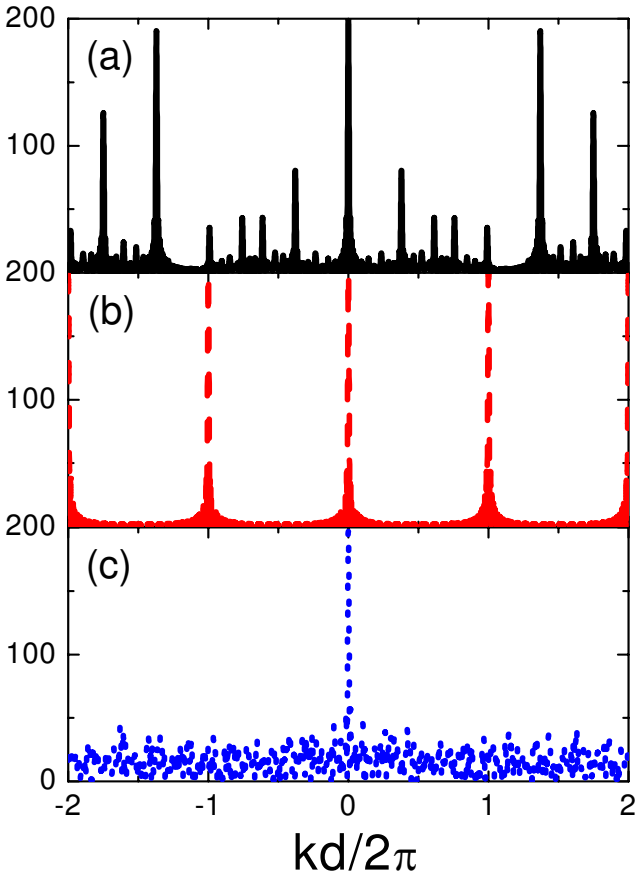

Figure 4.8.: Absolute value of the structure factor corresponding to: (a) a Fibonacci array of 200 slits with $d_1 = 0.68d$ and $d_2 = 1.55d$ (where d is the mean distance between the slits), (b) a periodic array of 200 slits of period d, and (c) a random array of 200 slits of the same dimensions.

reference for normalization, is plotted in the inset of the figure. Within the wavelength range considered in our analysis, T_0 shows two maxima corresponding to the two first slit cavity resonances ($\lambda = 0.86d$ and $\lambda = 1.87d$). The Fibonacci and periodic array spectra display these maxima too, but slightly shifted to shorter wavelengths. This fact leads to the appearance of two low maxima ($T_{\max} \lesssim 2$) in the corresponding normalized spectra (see Fig. 4.9). For the random array, $T = NT_0$. The absence of order in the array makes the interference of radiation coming from different slits destructive and the spectrum of the structure is governed by the single slit transmission.

Transmission versus wavelength for periodic and Fibonacci arrangements display higher and narrower peaks that are not present in the single slit spectrum. As we showed in Sec.

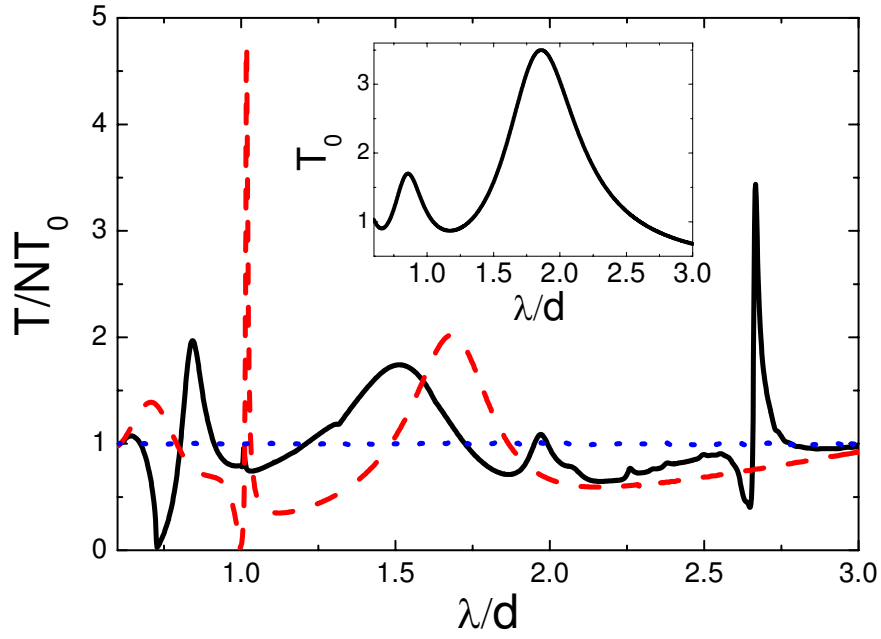

Figure 4.9.: Transmission spectra of the Fibonacci (black solid line), periodic (red dashed line) and random (blue dotted line) arrays of 200 slits considered in the text. The slits width is $a = 0.17d$ and the film thickness, $h = 0.68d$. Transmittances are normalized to the transmissivity of 200 independent slits. Inset: Transmission spectrum of a single slit of the same dimensions.

4.2.2, the narrow peak that periodic structures present at wavelengths close to the array period is linked to the excitation of spoof SPPs at the system interfaces. The question that arises now is whether the origin of the very similar resonant features observed in the Fibonacci spectrum is the same.

In the coupling process between the incident light and the surface modes supported by an infinitely periodic array of slits, Bragg momentum matching conditions must be satisfied [39]. This fact relates the position of the resonant features in the transmission spectrum with the structure factor of the aperture array, $S_\infty(k) = \sum_{\alpha=-\infty}^{\infty} e^{ik\alpha d} = \frac{2\pi}{d}\sum_l \delta(k - b_l)$ (where $\delta(x)$ denotes the Dirac's delta function). This function defines a set of resonant parallel wave vectors which turn to be equal to the reciprocal lattice vectors, $b_l = l\frac{2\pi}{d}$. Wave vectors $b_{\pm 1} = \pm 2\pi/d$ provide the lowest incident energy and momentum needed for the coupling. As a result, a very efficient transmission channel is opened in the system, which leads to a transmittance peak at a wavelength slightly larger than the array period, d. Note that, just at $\lambda = d$, the system presents the transmission dip associated with the Wood-Rayleigh's anomaly. For finite periodic arrays, discrete resonant

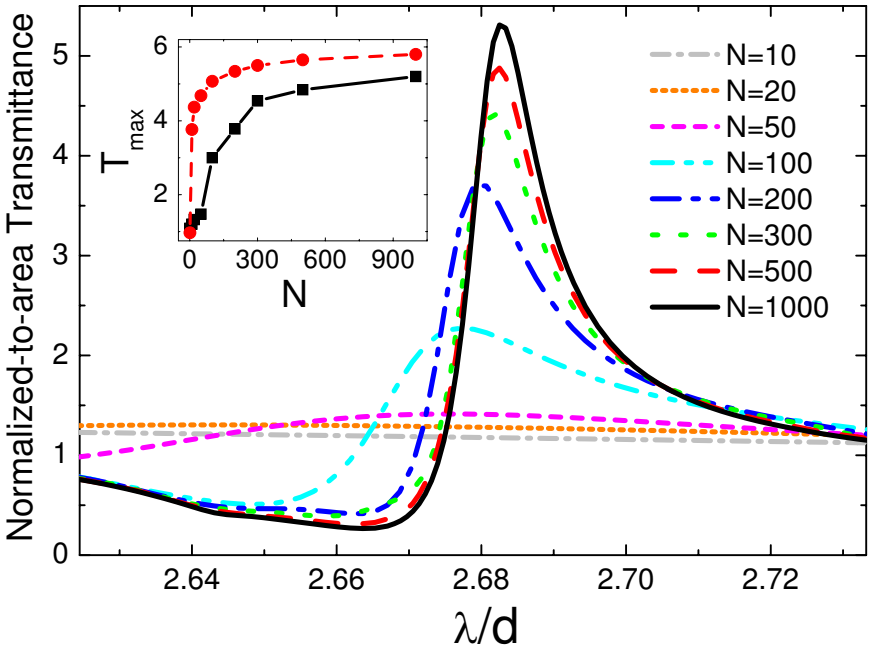

Figure 4.10.: Evolution of the transmission peak in a Fibonacci array as the number of slits is increased. The transmittance is normalized to the EM flux impinging on the slits area. The geometrical parameters considered are the same as in Fig. 4.9. Inset: Transmission peak height as a function of the number of slits for a Fibonacci (black squares) and periodic (red dots) arrays.

k's are not well defined, but the close correspondence between the location of the first maximum in the structure factor ($\lambda = d$) and the surface resonance transmission peak that the system presents at $\lambda = 1.02d$ remains.

The connection between the spectral location of transmission peaks and resonant features in the structure factor seems to hold also for the Fibonacci array considered in Fig. 4.9. Its structure factor shows a first maximum at $kd/2\pi = 0.375$ ($\lambda = 2.66d$). The highest peak in its transmission spectrum occurs at $\lambda = 2.68d$ (see Fig. 4.9). Moreover, the transmission dip also has its own quasiperiodic counterpart in a narrow drop ($\lambda = 2.66d$), whose position coincides with the maximum in $S(k)$. All these similarities seem to point out that surface resonances also play a crucial role in the transmission properties of Fibonacci structures. The fact that transmission features are less pronounced in the quasiperiodic structure can be interpreted as a consequence of the less efficient coupling between the incident light and the spoof SPPs due to the absence of a well defined regularity in the system.

In Figure 4.10 we study the evolution of the transmission maximum with the number

of slits present in a Fibonacci arrangement. The gradual increase of the transmission peak height observed is compatible with the fact that the origin of the resonance stems from the excitation spoof SPPs in the film sides. As the number of slits is increased, the structure factor becomes more and more peaked around the resonant wave vectors, resulting in a more efficient excitation of the spoof SPP modes and, consequently, in a higher transmissivity. This behavior is similar to that shown in Fig. 4.3. In the inset of Fig. 4.10, peak heights for Fibonacci (black squares) and periodic (red dots) arrays with constant mean distance between slits are plotted as a function of the number of slits. We can observe that the tendency is very similar in both cases, being the transmittance always lower for the quasiperiodic system.

From our analysis it seems clear that the structure factor plays a fundamental role in the transmission properties of slit arrangements. Thus, it is convenient to consider the k-space version of our ME formalism, in which $S(k)$ appears explicitly. As we stated in Section 2.2.3, the set of equations which control the $k = 0$ Fourier component of the parallel electric field amplitude at the film sides, $E_0(0)$ and $E_0'(0)$, has the form

$$\begin{aligned}(\Sigma_0 - \epsilon_0)E_0(0) - G_0^V E_0'(0) &= I,\\ (\Sigma_0 - \epsilon_0)E_0'(0) - G_0^V E_0(0) &= 0.\end{aligned} \tag{4.11}$$

where, ϵ_0 and G_0^V remain the same as in real space equations (4.1). The term Σ_0 is given by

$$\Sigma_0 = \frac{1}{E^{(\prime)}(0)} \int_{-\infty}^{\infty} dk\, G_{00;k} S(-k) E^{(\prime)}(k). \tag{4.12}$$

It represents the scattering process that couples $E^{(\prime)}(0)$ to the continuum $E^{(\prime)}(k)$, the momentum difference being provided by the apertures through the structure factor $S(-k)$. Note that we have checked that Σ_0 acquires the same values calculated from the modal amplitudes at the input and output sides of the film. The amplitude of the scattering process depends on $G_{00;k}$, which is given by

$$G_{00;k} = \frac{1}{2\pi} Y_{\gamma=2}(k) \langle k|\text{slit}\rangle = \frac{ia}{2\pi} \frac{k_0}{\sqrt{k_0^2 - k^2}} \text{sinc}^2(ka/2), \tag{4.13}$$

where simple expressions for the admittance, $Y_{\gamma=2}(k)$, and the overlapping integral, $\langle k|slit\rangle$, are given in Sec. 2.2.2 and Appendix A, respectively. Note that $G_{00;k}$ diverges whenever a p-polarized diffraction wave goes glancing ($k = k_0$). This indicates the important role that surface modes play in the formation of transmission resonances, as they govern the amplitude of the scattering processes between the incoming light and the structure. In Section 2.2.3, we showed that the zero-order diffracted beam ($k = 0$) governs the transmissivity of aperture arrays for wavelengths much larger than the mean

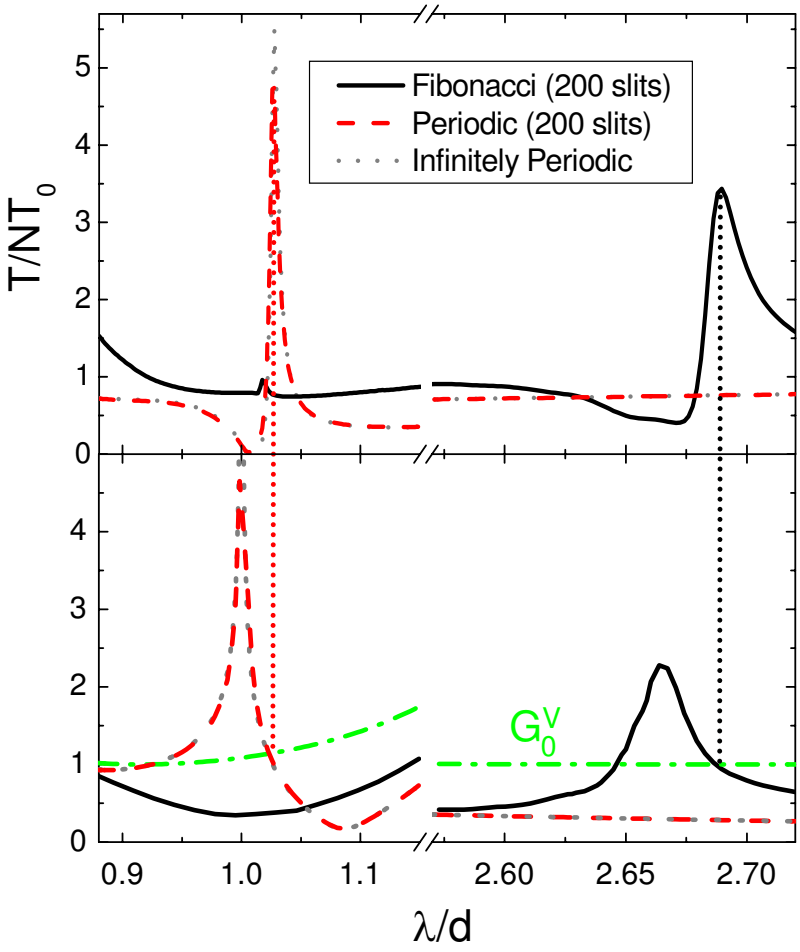

Figure 4.11.: Upper panel: Transmission peaks for the Fibonacci and periodic arrays of 200 slits considered in the text. The transmissivity of an infinitely periodic array with the same geometry is also shown. Lower panel: Relevant terms in Eqs. (4.11) for these three systems. Vertical dotted lines indicate the coincidence between the location of the transmission peaks and the cuts between $|\Sigma_0 - \epsilon_0|$ and G_0^V for each system.

distance between apertures. Thus, we can expect that the system of equations (4.11) describe the physical and mathematical foundation of the transmission resonances observed in finitely periodic and Fibonacci slit arrays.

Let us consider first the case of an infinitely periodic array. As we showed in Sec. 2.2.3, Σ_0 for this structure is equal to the G_∞ term [see Eq. (4.1)] which appears in the real-space version of the ME formalism. Therefore, the phenomenology that we described in Section 4.2.1 relating transmission resonant features to the behavior of the different terms in Eqs. 4.1 is also valid for Eqs. 4.11. In Fig. 4.11, we have plotted in grey dotted

line the transmission spectrum (upper panel) and the dependence on λ of the relevant terms in Eqs. 4.11 (lower panel) for an infinite array of slits with $a = 0.17d$ and $h = 0.68d$. We can see that the divergence of $|\Sigma_0 - \epsilon_0|$, which makes $E_0(0) = E_0'(0) = 0$, coincides with the location of the Wood-Rayleigh's anomaly. Moreover, at a wavelength slightly larger, the condition $|\Sigma_0 - \epsilon_0| = G_0^V$ is satisfied. This gives rise to the surface resonance transmission peak in the spectrum, which is accompanied by an enhancement of $E_0(0)$ and $E_0'(0)$.

The arguments presented above can be extended to finite systems. These are also described by Eqs. (4.11), where now Σ_0 must be numerically evaluated from the expression (4.12). The lower panel of Fig. 4.11 renders $|\Sigma_0 - \epsilon_0|$ for the finitely periodic (red dotted line), and Fibonacci (black solid line) arrays of 200 slits considered in Fig. 4.9. Although Σ_0 does not diverge for any of them, both arrangements show a dip in transmittance when $|\Sigma_0 - \epsilon_0|$ is maximum. Moreover, for both structures, the condition $|\Sigma_0 - \epsilon_0| = G_0^V$ still coincides with the locations of the transmission peaks. This correspondence, indicated by vertical dotted lines in Fig. 4.11, allows us to link the appearance of transmission peaks with the excitation of spoof SPP modes in both systems.

Our theoretical results on the transmission properties of finite slit arrays are in very good agreement with experimental works recently published studying the role of order and finite size effects in such structures [145, 146].

4.3. Quasiperiodic hole arrays

Finite size effects in the transmission of light through periodic hole arrays have been extensively studied both theoretically and experimentally [147–149]. Here we focus on analyzing the transmission properties of quasiperiodic hole arrangements disposed following Penrose lattices as those studied experimentally in [136–138]. Penrose tiles are composed of two different types of rhombuses with equal edges, d, but different angles, 36° and 72°. It can be demonstrated [150] that these two basic elements can be matched to pave all the 2D plane. Although periodicity is absent in the resulting lattice, it presents long range order with ten-fold spatial symmetry. Figure 4.12 renders a schematic picture of such Penrose tiling. The two types of rhombuses comprising the lattice has been colored in order to make them clearly distinguishable.

We choose the holes parameters to be the same as in the experiments in Ref. [138]. Thus, the hole radius is $a = 0.2$ mm, the thickness of the metallic film, $h = 0.075$ mm, and the rhombuses edge, $d = 1$ mm. For these geometrical parameters, the transmission resonances of the structure are located in the THz range of the EM spectrum where, as we

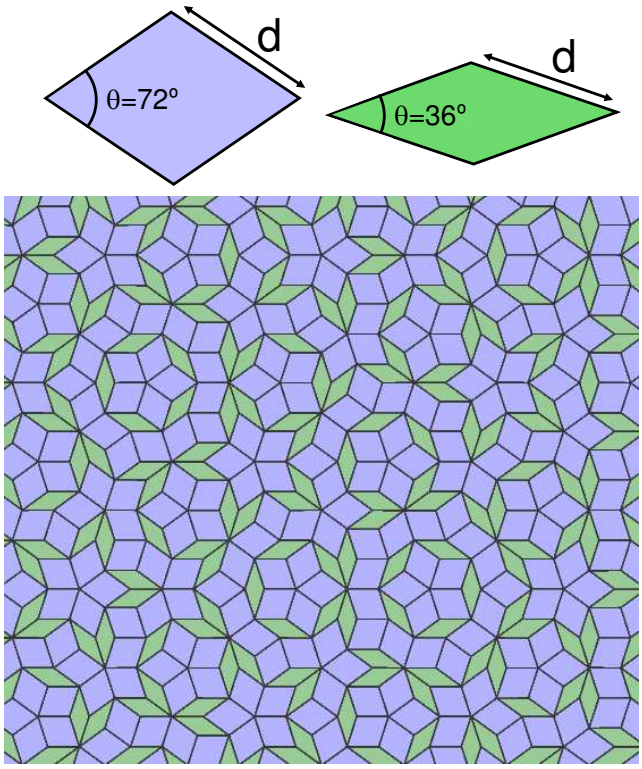

Figure 4.12.: Schematic picture of the Penrose tiling considered in the text. The two basic rhombuses comprising the quasiperiodic lattice are also depicted.

stated in Sec. 2.2.5, PEC boundary conditions are an excellent approximation. The upper panels in Fig. 4.13 depict the three different types of hole arrangements considered. Left, center and right panels correspond to a periodic square lattice, a Penrose lattice and a random distribution of circular holes, respectively. In all three cases, the film thickness, the number of holes ($N = 1506$), their radius, and the size of the external diameter are the same. In this way, the density of holes and the area occupied by them are equal in the three structures, enabling a direct comparison between them. The coordinates in the Penrose lattice were generated by the Dual Generalized Method [151, 152]. The periodic structure is a circular portion of a square lattice of period $P = 0.89$mm. In the disordered case, N holes are randomly distributed but without allowing any interhole distance to be smaller than the minimum one found in the quasiperiodic case.

The scattering properties and EM field distributions for these three systems can be calculated within our real space ME framework [93]. The set of continuity equations for 2D arrangements has the same form as Eqs. (4.5), where index α runs over hole positions and

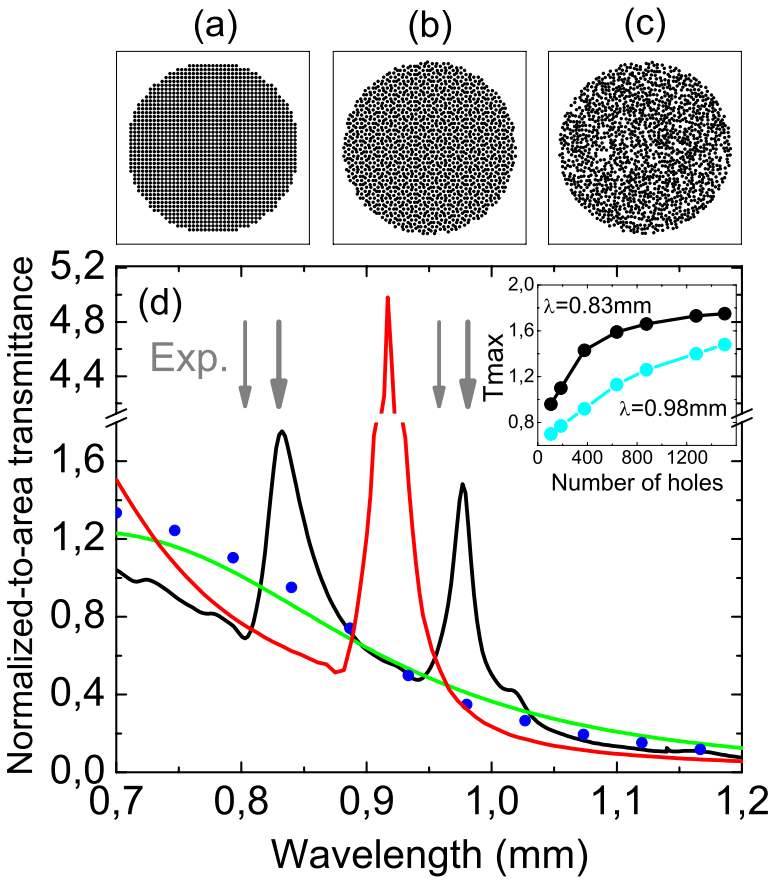

Figure 4.13.: (a-c) Structures under study. Square (left), Penrose (center) and random hole arrangements (right). (d) Normalized-to-area transmittance, T, spectra for: single hole (green line), square array (red line), Penrose lattice (black line) and a random configuration (blue dots). Gray arrows mark the locations of the dips (thin lines) and peaks (thick lines) of the experimental transmittance spectrum reported in Ref. [138]. Inset in panel (d) shows the dependence with N for T at resonant peaks for the quasiperiodic array, $\lambda = 0.83$ mm (black dots) and $\lambda = 0.98$ mm (cyan dots).

waveguide modes inside each aperture. By solving it, we get the electric field amplitudes at the input (E_α) and output (E'_α) sides of the holes. The transmittance of the structure is then obtained through Eq. (4.6). Panel (d) of Fig. 4.13 depicts the normal incidence transmission spectra computed for the three structures, along with the transmittance associated with a single hole (green line). In all cases, the transmittance is normalized to the flux of light impinging on the area occupied by the holes. In the spectral range considered, the single hole transmittance is a smooth decreasing function of the wavelength. In the ordered case (red line), the transmission spectrum is also smooth, except

close to the resonant peak appearing at $\lambda = 0.92$ mm, where the normalized-to-area transmittance, T, is about 5. This is the canonical peak associated with the extraordinary optical transmission (EOT) phenomenon, which occurs at a resonant wavelength slightly larger that the array period.

As in the experiments, resonant transmission also appears when holes are arranged in a Penrose lattice (black curve in Fig. 4.13). In this case, maximum transmission values of about 1.5 are obtained at two resonant wavelengths, $\lambda = 0.83$ mm and $\lambda = 0.98$ mm. The agreement between theory and experiment in the spectral locations of these transmission peaks is excellent. On the other hand, blue dots in Fig. 4.13 demonstrate that transmission peaks do not appear for any distribution of holes: the transmission spectrum for the random array does not show any resonant feature. This is just a representative example of disordered arrays. We have generated several random configurations finding always a non-resonant behavior.

As we showed in Section 2.2.3, when dealing with a finite collection of apertures, from a numerical point of view, it is more convenient to work with the system of linear equations in real space (4.5). However, the dependence of transmission properties of aperture arrangements on the lattice structure can be made more apparent by working with the reciprocal space version of our ME formalism. Physical insight is gained by analyzing the k-space continuity equations for $\mathbf{k} = \mathbf{k}_i = \mathbf{0}$. As in 1D structures, we consider only the fundamental waveguide mode inside the circular holes, which is a linear combination of the TE_{11} modes shown in Appendix B. The resulting set of continuity equations can be written in the same form as Eqs. (4.11), but the different terms in the equations now read

$$I = 2i\langle \text{hole}|\mathbf{k}_i, \sigma_i\rangle, \tag{4.14}$$

$$\epsilon_0 = -i\frac{\sqrt{k_0^2 - v^2}}{k_0}\frac{1+e^{2ivh}}{1-e^{2ivh}}, \tag{4.15}$$

$$G_0^V = -2i\frac{\sqrt{k_0^2 - v^2}}{k_0}\frac{e^{ivh}}{1-e^{2ivh}}, \tag{4.16}$$

where $v = \sqrt{k_0^2 - (\gamma'_{11}/a)^2}$, and γ'_{11} is the first zero of the derivative of the Bessel function of first order. Analytical expressions for the overlap between the incident plane wave and the hole waveguide mode, $\langle \mathbf{k}_i, \sigma_i|\text{hole}\rangle$, are provided in Appendix B. The Σ_0 function is given by

$$\Sigma_0 = \frac{1}{E_0^{(\prime)}(\mathbf{0})}\int d\mathbf{k} G_{00;\mathbf{k}} S(-\mathbf{k}) E^{(\prime)}(\mathbf{k}), \tag{4.17}$$

with $G_{00;\mathbf{k}} = \frac{i}{4\pi^2}\sum_\sigma Y_{\mathbf{k}\sigma}|\langle \mathbf{k}, \sigma|\text{hole}\rangle|^2$.

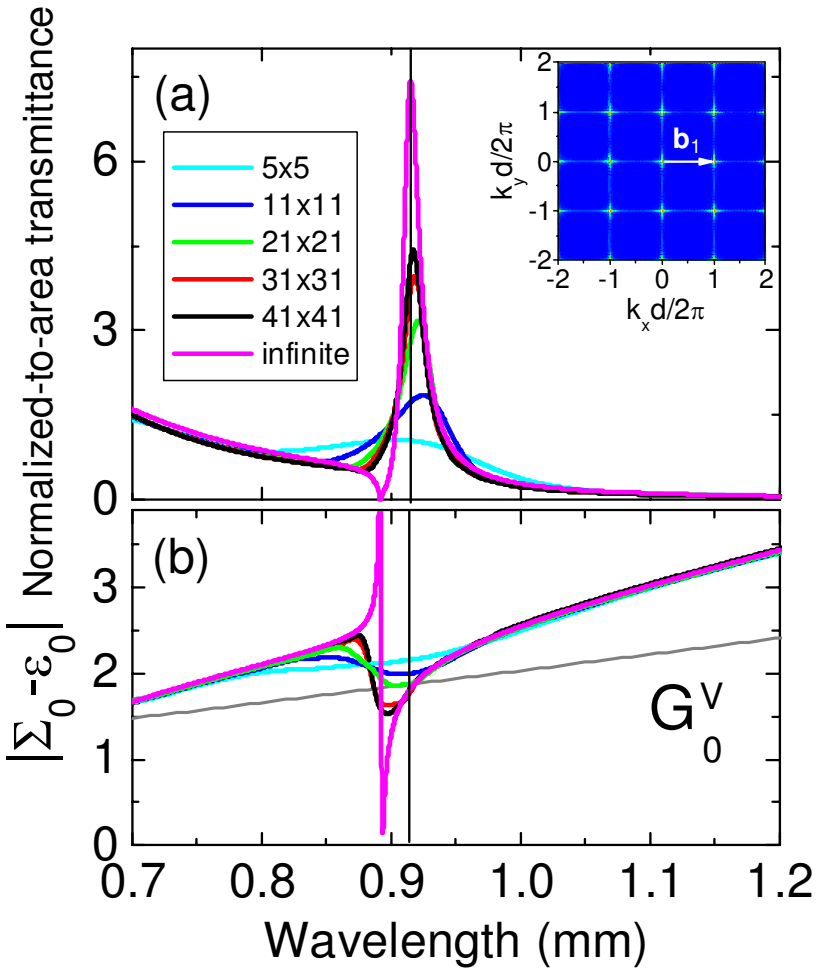

Figure 4.14.: (a) Normalized-to-area transmittance versus wavelength for an infinite periodic array (magenta line) and several finite square arrays. The geometrical parameters are: $a = 0.2$mm, $h = 0.075$mm and $P = 0.89$mm. Inset shows the structure factor for the 41x41 case. (b) $|\Sigma_0 - \epsilon_0|$ and G_0^V (gray line) versus wavelength for the cases depicted in (a).

In Figure 4.14, T (panel a) and $|\Sigma_0 - \epsilon_0|$ (panel b) versus wavelength are depicted for an infinite periodic array (magenta line). The geometrical parameters of this array are the same as the periodic one analyzed in Fig. 4.13. As in 1D structures, Σ_0 for infinitely periodic arrays coincides with the G function appearing in the real space version of the formalism. It diverges at $\lambda = P = 0.89$ mm (as a consequence of the divergence of $G_{00;\mathbf{k}}$ at this λ), both $E_0(\mathbf{0})$ and $E_0'(\mathbf{0})$ are zero, which leads to null transmission. Again, we have the Wood-Rayleigh's anomaly or anti-resonance as quoted in Ref. [138]. Moreover, at a wavelength slightly larger, $|\Sigma_0 - \epsilon_0| = G_0^V$, which leads to a resonant enhancement of

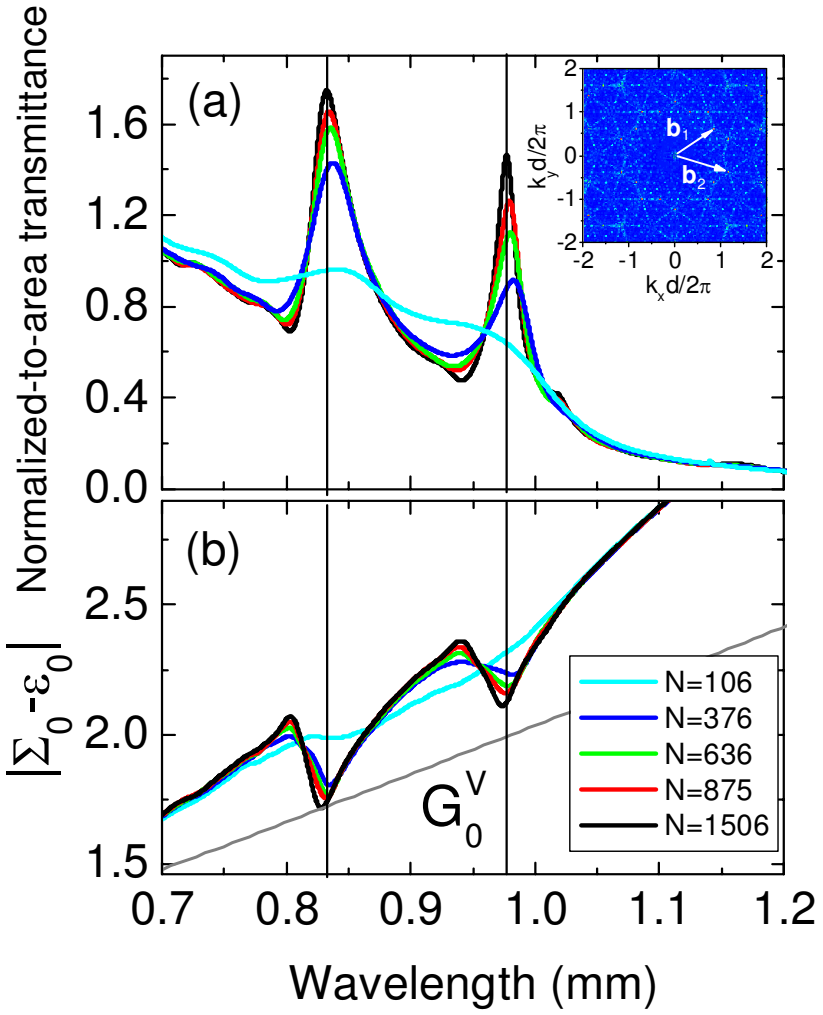

Figure 4.15.: (a) Normalized-to-area transmittance versus wavelength for several quasiperiodic arrays with different number of holes, N. The geometrical parameters are: $a = 0.2$mm, $h = 0.075$mm and $d = 1$mm. Inset shows the structure factor for the $N = 1506$ case. (b) Both $|\Sigma_0 - \epsilon_0|$ and G_0^V (gray line) versus wavelength for the cases depicted in (a).

the electric field amplitudes at the interfaces of the system, and consequently, T presents a maximum. As in 1D apertures, the field enhancement at the film sides can be assigned to the excitation of leaky spoof SPPs in the perforated film.

As in 1D slit arrays, the discussion presented above can be also applied to the case of finite arrays (both periodic and quasiperiodic). In principle, continuity equations (2.66) should be solved for a continuum of states $\mathbf{k}$ for finite hole arrangements. However, as in 1D structures, we use the approximation of considering only $E_0(\mathbf{0})$ and $E_0'(\mathbf{0})$, neglect-

ing the Fourier components of modal amplitudes with $\mathbf{k} \neq \mathbf{0}$. This allows us to relate transmission resonances with the k-space continuity equations under the single mode approximation (4.11). The results of our approach applied to square periodic arrays (going from 5×5 to 41×41 holes) are shown in Figure 4.14. Again, in finite systems Σ_0 presents no divergences, but there is still a resonant feature appearing close to $\lambda = P$. The first consequence is that transmission dips do not reach zero transmittance in finite arrays. Moreover, the cut between $|\Sigma_0 - \epsilon_0|$ and G_0^V marks the location of the transmission peak for large arrays (41×41 and 31×31). However, for smaller arrays, there is no cut, and the transmission peak appears at the wavelength in which the difference between $|\Sigma_0 - \epsilon_0|$ and G_0^V is minimal.

The scheme described above is also valid for quasiperiodic arrays. In panel (b) of Figure 4.15, the evolution of $|\Sigma_0 - \epsilon_0|$ versus wavelength is studied for Penrose lattices with increasing number of holes (ranging from $N = 106$ to $N = 1506$, the case analyzed in Fig. 4.13). $|\Sigma_0 - \epsilon_0|$ present maxima at wavelengths corresponding to the two main wave vectors of the structure factor (see inset of the upper panel of Fig. 4.15): $\mathbf{b}_1$ ($\lambda_1 = 0.8$ mm) and $\mathbf{b}_2$ ($\lambda_2 = 0.94$ mm). Consequently, T shows two minima at these two wavelengths. At slightly larger wavelengths, the difference between $|\Sigma_0 - \epsilon_0|$ and G_0^V is minimal and two transmission peaks appear in the spectrum. Therefore, these resonant transmission peaks stem from the excitation of surface EM modes at the film sides, much in the same way as in periodic arrays [39, 45]. Notice that, however, in the quasiperiodic case, there is no minimum wave vector for diffraction (i.e. the structure factor is non-zero for wave vectors with modula smaller than $|\mathbf{b}_1|$, see inset of the upper panel of Fig. 4.15). This results in diffraction onto additional propagating modes in vacuum (other than the zero-order mode), which leads to both smaller resonant peaks and less pronounced Wood-Rayleigh's anomalies than those emerging in the periodic case.

Finally, it is worth analyzing the spatial distribution of light emerging from the quasiperiodic array. Figure 4.16 renders the transmission-per-hole in a Penrose lattice of $N = 1506$ holes at the two resonant wavelengths ($\lambda = 0.83$ mm and $\lambda = 0.98$ mm in panels (b) and (c), respectively). For comparison, panel (a) shows the corresponding distribution for the ordered array at resonance ($\lambda = 0.92$ mm). In all three cases, the incident electric field is pointing along the x-direction. In the ordered case, due to finite size effects, the maximum transmission is located at the center of the structure [148]. In quasiperiodic arrangements, the transmission-per-hole distribution presents a completely different pattern: it is far from being uniform, showing the appearance of some holes with high transmission (hot spots), which are highlighted in the insets of panels (b) and (c). Interestingly, in the Penrose lattice, for a given resonant wavelength, hot spots show similar local environment. However, the existence of hot spots does not imply that resonant

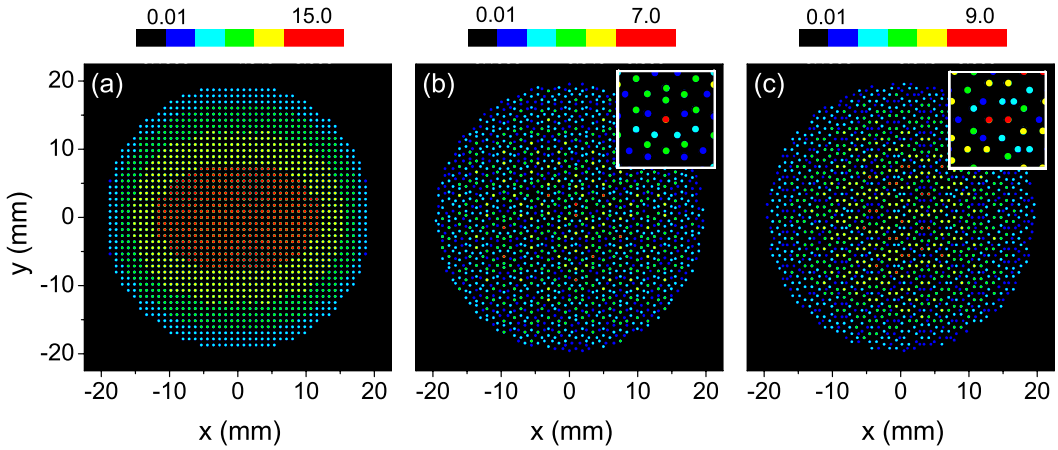

Figure 4.16.: Transmission per hole (normalized to the single hole transmission) displayed in a color scale for (a) ordered case evaluated at $\lambda = 0.92$mm, (b) Penrose lattice at $\lambda = 0.83$mm and (c) Penrose lattice at $\lambda = 0.98$mm. The geometrical parameters are given the same as in Fig. 4.13.

transmission in quasiperiodic systems is dominated by very localized resonant configurations of holes. We have observed that the hot spots show an increase of transmittance as a function of number of neighbors included in the lattice. This point is reinforced by the fact that the resonant peaks observed in the transmission spectra of finite Penrose lattices do not saturate for small N values (see inset of panel (d) of Fig. 4.13). Both these results are consistent with the interpretation based on extended leaky spoof SPPs described above.

4.4. Conclusions

In this chapter, we have analyzed the resonant transmission of light through finite arrangements of apertures perforated in perfect conducting films. We have studied three different structures: periodic and quasiperiodic (Fibonacci) arrays of slits, and quasiperiodic (Penrose) arrays of holes. We have shown that the resonant features occurring in the transmission spectra of these systems can be explained in terms of the spoof surface plasmon polaritons supported by the film. Additionally, we have related the excitation of these electromagnetic modes with the structure factor of the aperture arrangement. This allows us to explain the appearance of the phenomenon of extraordinary transmission in general conditions. Finally, we have shown that our theoretical results are in excellent agreement with experiments recently performed on quasiperiodic systems.

5. Resonant transmission and beaming of cold atoms assisted by surface matter waves

5.1. Introduction

In the last years, several papers have been published reporting enhanced transmission and beaming of light in photonic crystals [74–76]. These works have demonstrated that resonant transmission and beaming effects are general electromagnetic phenomena that do not occur only in metallic structures. This discovery has allowed achieving a more profound understanding of both phenomena and has opened the way for their transfer to other undulatory entities such as cold atoms (matter waves) or sound (acoustic waves).

In this chapter, we describe in detail the appearance of resonant transmission and beaming of non-interacting cold atoms in various geometries. We show that the resonant excitation of surface matter waves, the analog of surface plasmon polaritons in the electromagnetic case, on both sides of a perforated impenetrable film allows the formation of efficient transmission channels that assist cold atoms to pass through apertures much smaller than their de Broglie wavelength (λ_{dB}). As a difference with surface plasmon polaritons, which propagate on bare vacuum-metal interfaces, surface matter waves require an attractive potential close to a solid surface in order to be supported. We consider a very simple model of surface matter waves based on square well potentials which nevertheless contains all the physical mechanisms that are behind the phenomena.

The issue of a feasible experimental implementation of these ideas is also addressed. We present a possible experimental scenario for the 1D case (array of slits). We show that a realistic attractive potential supporting surface matter waves can be realized by combining the intrinsic van der Waals interaction between a neutral atom and a dielectric surface, and an external repulsive optical potential created by a blue-detuned laser field propagating along an array of dielectric fibers.

5.2. Surface matter waves

Surface Matter Waves (SMWs) are solutions of the Schrödinger equation confined in the direction normal to a vacuum-solid interface and propagating along it. Unlike Maxwell equations, which admit confined waves at bare metal-dielectric interfaces, Schrödinger equation requires an attractive potential close to the material surface for the existence of such waves. The simplest potential supporting SMWs is depicted in Figure 5.1: a semi-infinite square well along the z-direction (normal to the material surface), translationally invariant in the surface plane. The energies of the bound states ($E_n < 0$) associated with this potential well are given by the transcendental equation [153]

$$\tan\left(\sqrt{\frac{2m}{\hbar^2}\left(E_n - V_0\right)}\, h\right) = -\sqrt{\frac{V_0 - E_n}{E_n}}, \tag{5.1}$$

where $V_0 < 0$ is the potential depth, h its width, and m the mass of the non-interacting atoms forming the SMW.

In what follows, we consider a potential well supporting one single bound state of energy E_0. The dispersion relation of the associated SMWs is

$$E(k) = E_0 + \frac{(\hbar k)^2}{2m}, \tag{5.2}$$

where E and $\hbar k$ are the energy and in-plane momentum of the SMW, respectively. In Fig. 5.1, a cross-cut of the potential function along the z-direction is shown. Blue solid line corresponds to the bound state energy E_0, whereas red dashed line renders its wavefunction. The associated SMWs propagate parallel to the impenetrable surface (modelled by an infinite potential barrier) and decay in the z-direction outside the potential well.

Due to energy and momentum conservation principles, SMWs can not be excited by plane matter waves impinging on the above described structure. As we showed in chapter 4, the periodic corrugation of a flat metallic surface allows the coupling of incident radiation with surface plasmon polaritons (SPPs). The analogous process involving matter waves is shown schematically in Fig. 5.1: incident cold atoms of energy E_{in} (green line) are transferred to SMWs after receiving the scattering momentum $\hbar k$ supplied by the structure corrugation. This coupling between plane matter waves and SMWs will later allow the appearance of the resonant transmission phenomenon through perforated films.

With this motivation, first we calculate the dispersion relation of the SMWs supported by a corrugated structure, namely a groove array of period Λ surrounded by a square potential well of depth $V_0 < 0$ and thickness h. The grooves width and depth are w and t, respectively. The structure is shown in the inset of Fig. 5.1. We develop a formalism based

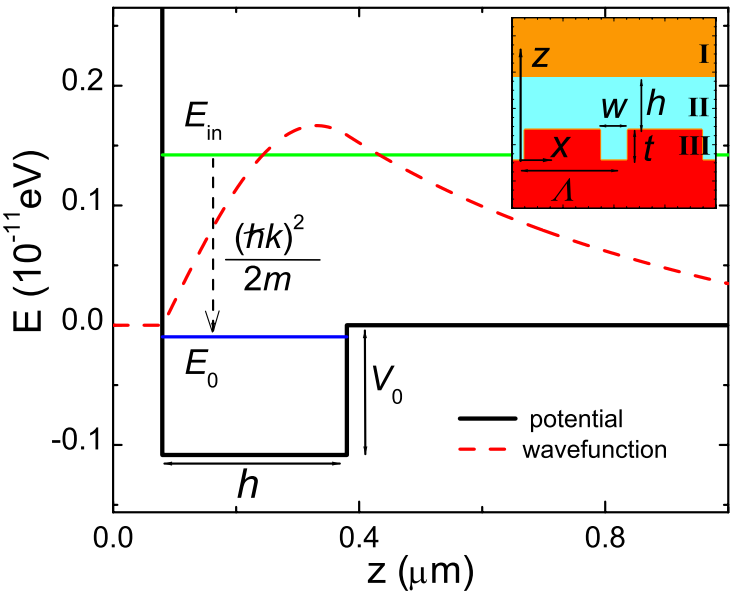

Figure 5.1.: Cross-cut along the z-direction of the potential function supporting SMWs (black line). The potential well has only one bound state of energy E_0 (blue line). The corresponding wavefunction (red dashed line) is confined in the z-direction. The indicated transition (dashed arrow) from a collision state E_{in} (green line) to the SMWs associated to E_0 is only possible once the surface is modulated. Inset: 2D potential landscape resulting from the corrugation of the material surface. Colors code the potential as follows: Orange (region I) $\rightarrow$ $V = 0$, blue (region II) $\rightarrow$ $V = V_0 < 0$, and red (region III) $\rightarrow$ $V = +\infty$. For the parameters considered in our calculations ($h = 0.30\,\mu$m and $V_0 = -1.06 \times 10^{-11}$ eV), $E_0 = -0.095 \times 10^{-11}$ eV.

on the modal expansion of the matter wavefunction (Ψ) within the different regions forming the structure. The ideas behind this approach are very similar to those presented in chapter 2 for the case of electromagnetic (EM) waves. Taking advantage of the periodic character of the system, we can apply Bloch's theorem and solve Schrödinger equation only inside the unit cell of length Λ along the x-direction (see Fig. 5.1). In region I (see inset of Fig. 5.1), Ψ is written as a sum over diffracted waves as

$$|\Psi_{\text{I}}\rangle \quad = \sum_n \rho_n |k_n\rangle e^{ik_z^{(n)} z}, \tag{5.3}$$

where ρ_n are unknown complex coefficients, and $k_n = k_x + n\frac{2\pi}{\Lambda}$ and $k_z^{(n)} = \sqrt{k_0^2 - k_n^2}$ are the wave vector components of the Bloch wave $|k_n\rangle$ along x and z-directions, respectively. The SMW modal wave vector is k_x, and k_0 is the wave vector modulus in vacuum. Note that $k_0 = \sqrt{2mE}/\hbar = 2\pi/\lambda_{\text{dB}}$, where E is the SMW energy and λ_{dB}, the de Broglie

wavelength. Finally, the wavefunction in real space for the n^{th} diffracted Bloch wave is $\langle x|k_n\rangle = \frac{e^{ik_n x}}{\sqrt{\Lambda}}$.

In region II, the wavefunction is expanded again in terms of Bloch waves as

$$|\Psi_{\text{II}}\rangle = \sum_n \left(A_n e^{iq_z^{(n)} z} + B_n e^{-iq_z^{(n)} z}\right)|k_n\rangle, \tag{5.4}$$

where A_n and B_n are the unknown expansion coefficients and $q_z^{(n)} = \sqrt{\xi k_0^2 - k_n^2}$, with $\xi = 1 + \frac{|V_0|}{E}$, is the wave vector component along the z-direction.

In our analysis, we consider groove widths much smaller than λ_{dB} and $\lambda_{\text{dB}}/\sqrt{\xi}$ (the de Broglie wavelength inside the grooves). In Section 2.2.1, we showed that taking only the lowest waveguide mode in the expansion of EM fields inside the apertures is a very good approximation in the subwavelength regime. We can extend this statement to the modal expansion of Ψ inside the grooves. The first waveguide mode inside the groove governs the SMW behavior, as it is the least evanescent wave along the z-direction (note that here resides an important difference with the EM case for p-polarization, where the fundamental slit waveguide mode is always propagating). Thus, in region III we have

$$|\Psi_{\text{III}}\rangle = C\sin(\beta z)|\psi_{\text{WM}}\rangle, \tag{5.5}$$

where C is unknown. Note that as $\lambda_{\text{dB}}/\sqrt{\xi} << w$, the wave vector $\beta = \sqrt{\xi k_0^2 - (\pi/w)^2}$ is imaginary and $\sin(\beta z)$ can be replaced by $i\sinh(|\beta|z)$ in Eq. (5.5). The wavefunction in real space for the first groove waveguide mode is $\langle x|\psi_{\text{WM}}\rangle = \sqrt{\frac{2}{w}}\sin[\frac{\pi}{w}(x + w/2)]$ inside the groove ($|x| \leq w/2$), and $\langle x|\psi_{\text{WM}}\rangle = 0$, otherwise. We have chosen $z = 0$ at the groove bottom so that $\langle x|\Psi_{\text{III}}\rangle$=0 at that position.

In order to obtain the set of modal expansion coefficients {ρ_n, A_n, B_n, and C}, we impose continuity conditions on Ψ and its z-derivative at the interfaces of the system ($z = t$ and $z = t + h$). The wavefunction and its derivative must be continuous in all space, except at the infinite potential barriers modelling the impenetrable surface, where $\partial_z\Psi$ presents a discontinuity [153]. Thus, in order to remove their dependence on the x-coordinate, we project the matching equations at $z = t + h$ onto Bloch waves. Similarly, equations at $z = t$ associated to Ψ ($\partial_z\Psi$) are projected onto $|k_n\rangle$ ($|\psi_{\text{WM}}\rangle$). Defining the quantity $\psi = C\sin(\beta t)$, which corresponds to the amplitude of the matter wavefunction at the openings of the grooves, we obtain a single continuity equation of the form

$$(G - \epsilon)\psi = 0. \tag{5.6}$$

Note that Eq. (5.6) has the same form as Eq. (2.73) which provides the dispersion relation of the bound EM modes supported by groove and dimple arrays.

The term $\epsilon = \beta/[k_0\tan(\beta t)]$ contains the effect of the penetration of matter waves inside the grooves. Note that it has exactly the same form as in the case of s-polarized light

[see Eq. (2.40)]. Its physical meaning can be clarified by comparison with the case of wide grooves, where β is a real number, and thus propagating modes are supported inside each groove. In such case, the zeros of the denominator in ϵ correspond to resonances within the grooves due to bouncing of the groove mode at the bottom and opening of the indentation. For the chosen subwavelength grooves, β is imaginary and no propagating modes nor resonances exist, but the interpretation of ϵ is analog. The G term reflects the coupling of the matter wavefunction at different grooves through diffracted waves. It is given by

$$G = \sum_{n=-\infty}^{\infty} \frac{iq_z^{(n)}}{k_0} f(k_n, h) |\langle k_n | \psi_{\mathrm{WM}} \rangle|^2, \tag{5.7}$$

where the function $f(k_n, h)$ has the form

$$f(k_n, h) = \frac{k_z^{(n)} \cos(q_z^{(n)} h) - iq_z^{(n)} \sin(q_z^{(n)} h)}{q_z^{(n)} \cos(q_z^{(n)} h) - ik_z^{(n)} \sin(q_z^{(n)} h)}. \tag{5.8}$$

We have found that the G term describing the SMWs supported by a groove array is very similar to the case of s-polarized light when only the first waveguide mode is considered inside the apertures [see Eq. (2.42)]. The only difference resides in the function $f(k_n, h)$, which takes into account the presence of the attractive potential at the material surface.

For $k_n = 0$, the denominator in $f(k_n, h)$ vanishes for energies satisfying Eq. (5.1). This fact indicates the close link between the bound states supported by the potential well surrounding the modulated surface and resonances in the G term, which governs the coupling between different grooves. The dispersion relation of the SMWs propagating along the structure is obtained by imposing the condition $|G - \epsilon| = 0$, leading to non-zero solutions of Eq. (5.6). This condition can be rewritten as

$$\cot(\beta t) = \sum_{n=-\infty}^{\infty} \frac{iq_z^{(n)}}{\beta} f(k_n, h) |\langle k_n | \psi_{\mathrm{WM}} \rangle|^2. \tag{5.9}$$

In Figure 5.2, $|G - \epsilon|$ for an array period of $\Lambda = 0.80\,\mu$m is plotted. The groove dimensions are $w = t = 0.16\,\mu$m. The attractive potential depth is $V_0 = -1.06 \times 10^{-11}$ eV and its width $h = 0.30\,\mu$m. As explained above, this set of parameters is tuned to observe resonant transmission for the 1D case. Black regions correspond to $|G - \epsilon|$ values close to zero, showing the dispersion relation of the SMWs supported by the structure. In our calculations, we have considered that the SMWs are composed of cold ^{87}Rb atoms ($m = 1.45 \times 10^{-25}$ kg). Kinetic energy versus momentum for free ^{87}Rb atoms is depicted in dashed green line. Note that SMWs are strictly guided modes only below this line. The solutions of k_x of Eq. (5.6) have an additional imaginary part. This means that above this line SMWs are leaky, radiating while they propagate along the structure.

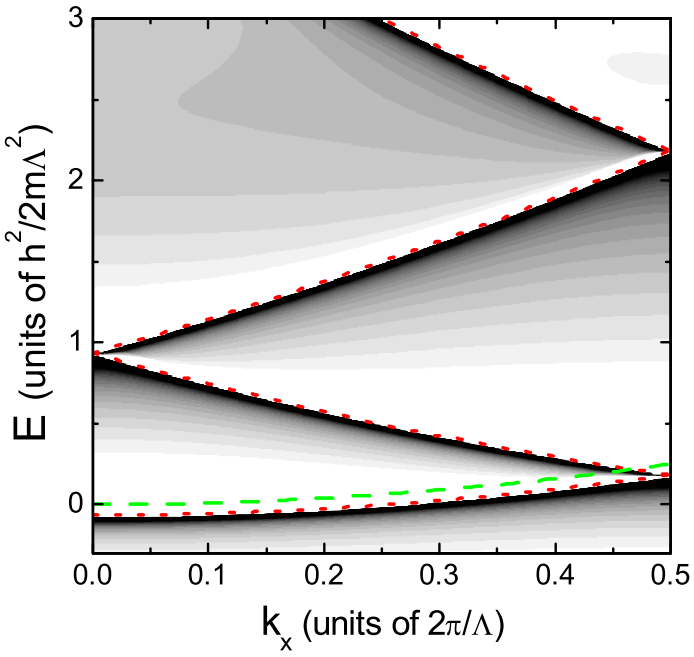

Figure 5.2.: Dispersion relation of the SMWs supported by the groove array depicted in the inset of Fig. 5.1. The array period is $\Lambda = 0.80\,\mu$m and the groove dimensions, $w = t = 0.16\,\mu$m. The potential well depth and thickness are $V_0 = -1.06 \times 10^{-11}$ eV and $h = 0.30\,\mu$m, respectively. The SMWs are composed by cold ^{87}Rb atoms ($m = 1.45 \times 10^{-25}$ kg). Red dotted lines correspond to the approximated bands obtained from Eq. (5.2). Green dashed line renders E versus k_x for free ^{87}Rb atoms.

An approximate expression for the dispersion relation of SMWs on corrugated surfaces can be extracted from Eq. (5.2) by simply applying Bloch's theorem to the parallel momentum component $k = k_x$. This leads to different bands of energy $E_n(k_x) = E_0 + (\hbar^2/2m)(k_x + n\frac{2\pi}{\Lambda})^2$ shown in red dotted line in Fig. 5.2. For the potential well considered in our calculations, $E_0 = -0.095 \times 10^{-11}$eV is much lower than the kinetic energy close to the $n = 1$ band edge, $h^2/2m\Lambda^2 = 1.48 \times 10^{-11}$ eV. As we can see in Figure 5.2, this approximated expression is in very good agreement with the exact SMWs dispersion relation.

In our design of SMWs we have found several similarities with the case of s-polarized light. As in the case of matter waves, bare metallic surfaces do not support s-polarized bound modes. A dielectric slab close to the metal surface is required for the formation of such bound modes. In fact, our model of SMWs on groove arrays can be mapped

into a dielectric-coated textured perfect electric conducting (PEC) surface in which the dielectric function of the coating is given by $\xi = 1 + |V_0|/E$. Recently, the appearance of extraordinary optical transmission (EOT) for *s*-polarization assisted by these modes has been demonstrated theoretically and experimentally [154, 155].

5.3. Resonant Transmission through slit arrays

Once we have designed SMWs with properties similar to those of SPPs, we study the appearance of resonant transmission for cold atoms. We go further with our simple model and consider a material slab perforated with a periodic array of narrow slits and surrounded by a square potential well (see right inset of Fig. 5.3). Such structure supports SMWs at both sides of the slab which, as in the EM analog, will play a crucial role in the resonant transmission process (see chapter 4). The close correspondence between SMWs and the surface EM modes supported by coated metals introduced in the previous section leads to several similarities between resonant transmission in slit arrays for cold atoms and *s*-polarized light.

We extend the modal expansion framework presented in the previous section to the study of the transmission of a plane matter wave impinging from the top ($z < 0$) on the perforated film. We follow the same strategy as in the case of EM fields, described in detail in chapter 2. The right inset of Fig. 5.3 shows the division of the system into 5 different regions along the z-direction. The wavefunction in region I can be written as the incident plane wave with parallel momentum $k_i = \sqrt{2mE}/\hbar \sin\theta = 2\pi \sin\theta/\lambda_{dB}$ (where θ is the incidence angle) plus a sum over reflected Bloch waves, $|k_n\rangle$, with $k_n = k_i + n\frac{2\pi}{\Lambda}$

$$|\Psi_I\rangle \quad = |k_i\rangle e^{ik_z^{(i)}z} + \sum_{n=-\infty}^{\infty} \rho_n |k_n\rangle e^{-ik_z^{(n)}z}. \tag{5.10}$$

Note that the exponential function describing the dependence of the reflected waves on z has now a negative sign which did not appear in Eq. (5.3). This is due to the fact that the orientation of the z-axis with respect to the input side of the film is the opposite to that considered in groove arrays.

Inside the attractive potential well surrounding the material slab (regions II and IV), Ψ is written as a linear combination of Bloch waves of the same form as Eq. (5.4). In region V, the transmitted matter wave can be expressed as a sum of diffracted Bloch waves of the form

$$|\Psi_V\rangle = \sum_{n=-\infty}^{\infty} t_n |k_n\rangle e^{ik_z^{(n)}z}. \tag{5.11}$$

For subwavelength slits ($w << \lambda_{dB}, \lambda_{dB}/\sqrt{\xi}$) the behavior of the matter waves inside region III is accurately described by considering only the first slit waveguide mode $|\psi_{WM}\rangle$

in the wavefunction expansion:

$$|\Psi_{\mathrm{III}}\rangle \;\; = \left(Ce^{i\beta z} + De^{-i\beta z}\right)|\psi_{\mathrm{WM}}\rangle. \tag{5.12}$$

Imposing continuity conditions on the wavefunction and its z-derivative at the structure interfaces, we end up with a set of two linear equations in the amplitudes of the matter wavefunction at the entrance, $\psi = C + D$, and exit, $\psi' = -(Ce^{i\beta t} + De^{-i\beta t})$, of the slits:

$$\begin{aligned} (G-\epsilon)\psi - G^V\psi' &= I, \\ (G-\epsilon)\psi' - G^V\psi &= 0. \end{aligned} \tag{5.13}$$

As in the EM version of our formalism, extending the physical picture that we have linked to Eq. (5.6), the upper (lower) equation in system (5.13) can be associated with the matter waves at the input (output) film surface. Thus, the inhomogeneous term $I = (2\sqrt{2}i/\pi)\xi/[\xi\cos(\xi k_0 h) - i\sin(\xi k_0 h)]$, which is present only in the upper equation, provides the overlap between the incident matter plane wave and the slits waveguide mode $|\psi_{\mathrm{WM}}\rangle$. The term $G^V = \beta/[k_0\sin(\beta t)]$ describes the coupling of Ψ at both sides of the film through the slits, whereas ϵ remains the same as in the previous section. Finally, G, which describes the coupling of the matter wavefunction at different slits openings, is given by Eq. (5.7). Note that, again, the physical interpretation of the various terms in Eqs. (5.13) is the same as in their EM analog.

Solving Eqs. (5.13), amplitudes ψ and ψ' are obtained. The matter wavefunction in each point of the space and also the transmissivity (T) of the structure can be then calculated. Within our formalism, the last one is given by

$$T = \frac{\int_\Lambda j_z^t(x)dx}{\int_\Lambda j_z^i(x)dx} = G^V \mathrm{Im}[\psi^*\psi'], \tag{5.14}$$

where $j_z^{t(i)}(\mathbf{r}) = (\hbar/m)\mathrm{Im}\{\Psi^{t(i)}(\mathbf{r})^*\partial_z\Psi^{t(i)}(\mathbf{r})\}$ is the z-component of the probability density current associated to the transmitted (incident) matter waves.

Figure 5.3 renders, in logarithmic scale, the transmittance of cold ^{87}Rb atoms impinging at normal incidence on a film of thickness $t = 0.16\,\mu$m perforated with a periodic array of slits of width $w = 0.22\,\mu$m. The potential depth is $V_0 = -1.06\times10^{-11}$ eV and its width $h = 0.3\,\mu$m. Three different array periods are considered: $\Lambda = 0.80\,\mu$m (black solid line), $\Lambda = 0.78\,\mu$m (red dashed line) and $\Lambda = 0.82\,\mu$m (green dotted line). Spectra are normalized to the current flux impinging on the array period. Close to Λ, all the structures display a sharp dip in transmittance ($T = 0$ within the numerical precision of our calculations) followed by two adjacent narrow 100% transmission peaks. Note that these two peaks can not be distinguished in Fig. 5.3 due to the wide spectral region displayed. In

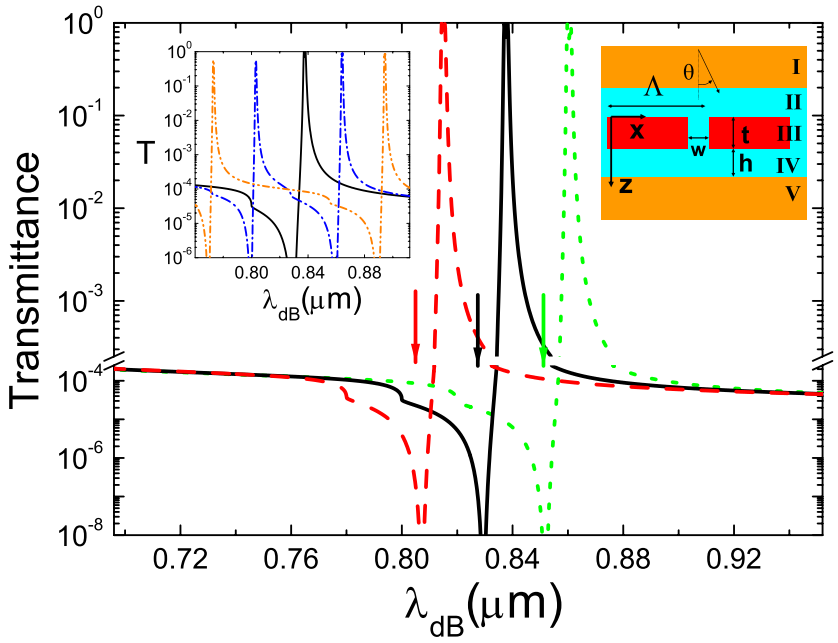

Figure 5.3.: Cold ^{87}Rb atoms transmission spectrum through a film of thickness $t = 0.16\,\mu$m perforated with a periodic array of slits of width $w = 0.22\,\mu$m. Three different array periods are considered: $\Lambda = 0.80\,\mu$m (black solid line), $\Lambda = 0.78\,\mu$m (red dashed line) and $\Lambda = 0.82\,\mu$m (green dotted line). Vertical arrows indicate the values of λ_{dB}^{SMW} obtained from Eq. (5.15) for each case. Left inset renders T versus λ_{dB} for $\Lambda = 0.80\,\mu$m and three different incidence angles: $\theta = 0°$ (black solid line), $\theta = 2°$ (blue dash-dotted line) and $\theta = 4°$ (orange dash-double-dotted line). Right inset: 2D display of the perforated material film ($h = 0.30\,\mu$m and $V_0 = -1.06 \times 10^{-11}$ eV). Colors code the potential as in Fig. 5.1.

the EM analog, these are the main fingerprints of the presence of EOT. Their appearance in Fig. 5.3 indicates that the resonant transmission phenomenon for cold atoms occurs in our model structures.

We showed in chapter 4 that the physical origin of EOT relies on the resonant excitation of surface EM modes supported by metallic films. In order to confirm that SMWs are the key actors in the formation of the analogous phenomenon for matter waves, we compare the spectral position of the transmission resonances with the approximate predictions obtained from the dispersion relation of SMWs on uncorrugated interfaces (5.2). Since the coupling between the incident atom beam and SMWs is mainly governed by first order processes ($n = \pm 1$), at normal incidence the parallel momentum of the SMWs propagating along the film surface is $|k_{\pm}| = 2\pi/\Lambda$. Thus, the corresponding de Broglie

wavelength is given by

$$\lambda_{\mathrm{dB}}^{\mathrm{SMW}} = \frac{\Lambda}{\sqrt{1+(2mE_0/h^2)\Lambda^2}} \simeq \Lambda\Big(1+\frac{2m|E_0|\Lambda^2}{h^2}\Big), \tag{5.15}$$

where we have taken into account that, for the parameters we are considering $|E_0| << h^2/2m\Lambda^2$. For the three arrays of Figure 5.3, $\lambda_{\mathrm{dB}}^{\mathrm{SMW}}$ (indicated by vertical short arrows) coincides with the position of the sharp dip in transmission spectra. In the EOT phenomenon, this close correspondence between the position of the Wood-Rayleigh's anomaly and the frequency of the SPPs supported by the uncorrugated metal surface has been also observed [143]. In the previous section, we showed that the exact SMWs dispersion relation (5.9) leads to lower energies than predicted from this approximation. This fact, together with the interaction through the slits of the SMWs at both sides of the film shifts the spectral location of the transmission peaks to larger λ_{dB}.

Although the dispersion relation of the SMWs supported by the film predicts the position of the resonant peaks in the transmission spectra, it does not contain any information about the peaks shape. In order to understand the asymmetric profile of the transmission maxima in Fig. 5.3, a more complex interpretation based on a Fano-type picture [156] is required. Such scheme, which has been successfully applied to the analysis of EOT [157], distinguishes between two different contributions to the transmission process: a resonant contribution due to the excitation of surface waves on the film sides and a non-resonant contribution due to the direct scattering of the incident radiation through the apertures. The interference between these two channels induces the observed asymmetry in the transmission maxima. According to this picture, the Wood-Rayleigh's anomaly can be associated to the destructive interference between these two channels.

In the left inset of Fig. 5.3, T versus λ_{dB} for an array of period $\Lambda = 0.80\,\mu$m and three different incidence angles (θ) is shown. For non-normal incidence, $\theta = 2^\circ$ (blue dash-dotted line) and $\theta = 4^\circ$ (orange dash-double-dotted line), T displays the characteristic resonant features twice, located at larger and lower λ_{dB} than at normal incidence (black solid line). This splitting of the resonances with the angle of incidence can be understood again in terms of SMWs on uncorrugated interfaces. For $\theta \neq 0$, the incident atom beam excites SMWs with two different parallel momenta $|k_\pm| = 2\pi|\sin\theta/\lambda_{\mathrm{dB}} \pm 1/\Lambda|$. This leads to the formation of two transmission channels with different resonant energies $E(k_\pm)$. For small θ, a simple expression for the λ_{dB} associated to these SMWs can be obtained

$$\lambda_{\mathrm{dB}}^{\mathrm{SMW}\pm}(\theta) = \lambda_{\mathrm{dB}}^{\mathrm{SMW}}\Big(1 \pm \frac{\theta}{\sqrt{1+(2mE_0/h^2)\Lambda^2}}\Big), \tag{5.16}$$

where $\lambda_{\mathrm{dB}}^{\mathrm{SMW}}$ is given by Eq. (5.15). This result is in very good agreement with the spectra

depicted in the left inset of Fig. 5.3. As predicted, for small angles the transmission peaks deviate linearly with θ from the normal incidence position.

5.4. Resonant Transmission through hole arrays

The next step in our study is to transfer the resonant transmission phenomenon from 1D structures (slit arrays) to 2D ones (hole arrays), for which EOT was firstly reported [39]. As in the 1D case, 2D SMWs are supported by a square potential well surrounding the material film drilled with the hole arrangement. The structure is displayed in the inset of Fig. 5.4, SMWs propagate along the film surface (xy plane) and decay in z-direction for increasing distances from the film.

We study the scattering of cold atoms by rectangular arrays of holes (see the inset of Fig. 5.4) by means of an extension of the formalism applied to 1D structures. The system is divided into the 5 regions shown in Fig. 5.3. We expand the matter wavefunction within each region in terms of the corresponding eigenmodes of the Schrödinger equation (Bloch waves and waveguide modes). For 2D periodic arrays, Bloch's theorem labels the parallel momentum associated to the discrete diffraction orders with two indexes (n and m)

$$\mathbf{k}_{nm} = \mathbf{k}_{\mathrm{i}} + n\frac{2\pi}{\Lambda_x}\hat{\mathbf{x}} + m\frac{2\pi}{\Lambda_y}\hat{\mathbf{y}}, \tag{5.17}$$

where the incident parallel momentum $\mathbf{k}_{\mathrm{i}} = \sqrt{2mE}/\hbar(\sin\theta\sin\phi\hat{\mathbf{x}} + \sin\theta\cos\phi\hat{\mathbf{y}})$ is characterized by the polar (θ) and azimuthal (ϕ) angles, and Λ_x and Λ_y are the array periods in the x and y directions, respectively. Bloch waves, $|\mathbf{k}_{nm}\rangle$, form the eigenmode basis onto which the matter wavefunction is expanded outside the film (regions I, II, IV and V). The associated wavefunctions in real space are $\langle\mathbf{r}|\mathbf{k}_{nm}\rangle = e^{i\mathbf{k}_{nm}\mathbf{r}}/\sqrt{\Lambda_x\Lambda_y}$, where $\mathbf{r} = x\hat{\mathbf{x}} + y\hat{\mathbf{y}}$.

We focus our analysis on two different aperture shapes: rectangular holes (characterized by the hole sides w_x and w_y) and circular holes (characterized by the hole radius r_{c}). In both cases, the hole dimensions are much smaller than the de Broglie wavelength, i.e., $w_x, w_y, r_{\mathrm{c}} << \lambda_{\mathrm{dB}}/\sqrt{\xi}$. Thus, as for 1D slits, it is a good approximation to consider only the first hole waveguide mode $|\psi^{\mathrm{2D}}_{\mathrm{WM}}\rangle$ in the description of Ψ inside the slab, having

$$|\Psi_{\mathrm{III}}\rangle = \left(Ce^{i\beta_{\mathrm{2D}}z} + De^{-i\beta_{\mathrm{2D}}z}\right)|\psi^{\mathrm{2D}}_{\mathrm{WM}}\rangle, \tag{5.18}$$

where, for rectangular holes, the waveguide mode is given by

$$\begin{aligned}\langle\mathbf{r}|\psi^{\mathrm{2D}}_{\mathrm{WM}}\rangle &= \langle x|\psi_{\mathrm{WM}}\rangle\langle y|\psi_{\mathrm{WM}}\rangle = \\ &= \frac{2}{\sqrt{w_x w_y}}\sin\left[\frac{\pi}{w_x}\left(x + \frac{w_x}{2}\right)\right]\sin\left[\frac{\pi}{w_y}\left(y + \frac{w_y}{2}\right)\right]\end{aligned} \tag{5.19}$$

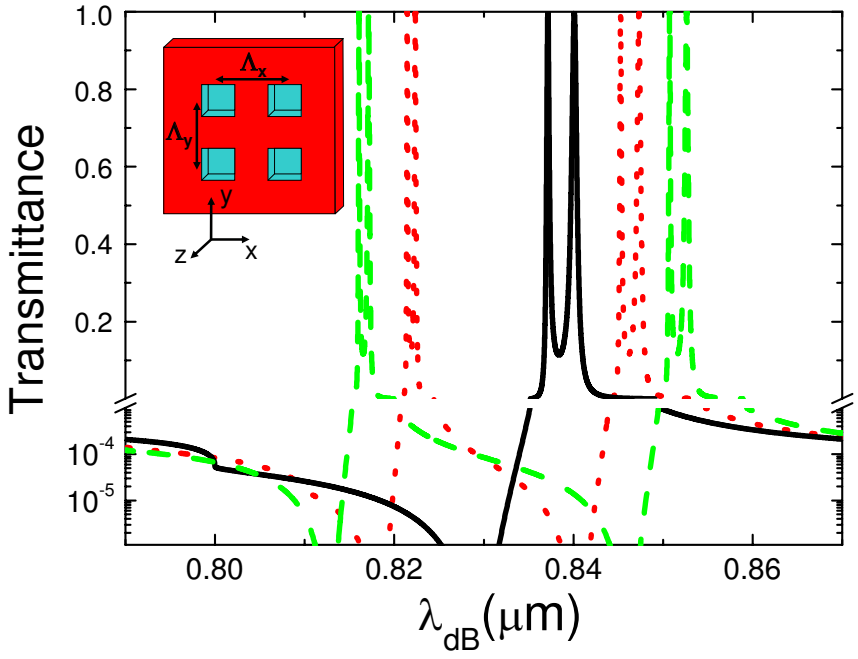

Figure 5.4.: Transmittance of cold ^{87}Rb atoms through a film of thickness $t = 0.16\,\mu$m drilled with a periodic array of square holes of side $w = 0.28\,\mu$m as a function of $\lambda_{\rm dB}$. Three different structures are considered. Black solid line: Square array with $\Lambda_x = \Lambda_y = 0.800\,\mu$m. Red dotted line: Rectangular array with $\Lambda_x = 0.790\,\mu$m and $\Lambda_y = 0.810\,\mu$m. Green dashed line: $\Lambda_x = 0.785\,\mu$m and $\Lambda_y = 0.815\,\mu$m. Inset: Schematic view of the structure.

inside the hole and $\langle \mathbf{r}|\psi^{\rm 2D}_{\rm WM}\rangle = 0$, otherwise. The z-component of the wave vector is $\beta_{\rm 2D} = \sqrt{\xi k_0^2 - (\pi/w_x)^2 - (\pi/w_y)^2}$.

For circular holes, the wavefuntion for the fundamental waveguide mode is

$$\langle \mathbf{r}|\psi^{2D}_{WM}\rangle = \frac{1}{\sqrt{\pi r_{\rm c}^2 [J_1(\gamma_{01})]^2}} J_0\Big(\frac{\gamma_{01}}{r_{\rm c}} r\Big), \tag{5.20}$$

where J_0 and J_1 are the zero and first order Bessel functions of the first kind, respectively, and $\gamma_{01} \approx 2.4048$ is the first zero of $J_0(r)$. The wave vector along the z-direction is $\beta_{\rm 2D} = \sqrt{\xi k_0^2 - (\gamma_{01}/r_{\rm c})^2}$. Note that the fundamental waveguide mode of the hole depends only on the radial coordinate $r = \sqrt{x^2 + y^2}$. For $r > r_{\rm c}$, we have $\langle \mathbf{r}|\psi^{2D}_{WM}\rangle = 0$

The continuity equations obtained from the modal expansion procedure for 2D hole arrays keep the same form as for 1D slit arrays [Eqs. (5.13)], where again the unknowns, ψ and ψ', are equal, except for a phase factor, to the wavefunction amplitudes at the hole openings. The definition and the physical interpretation of the different terms for the case of 1D apertures still hold for holes, with the only difference that wave vector β must

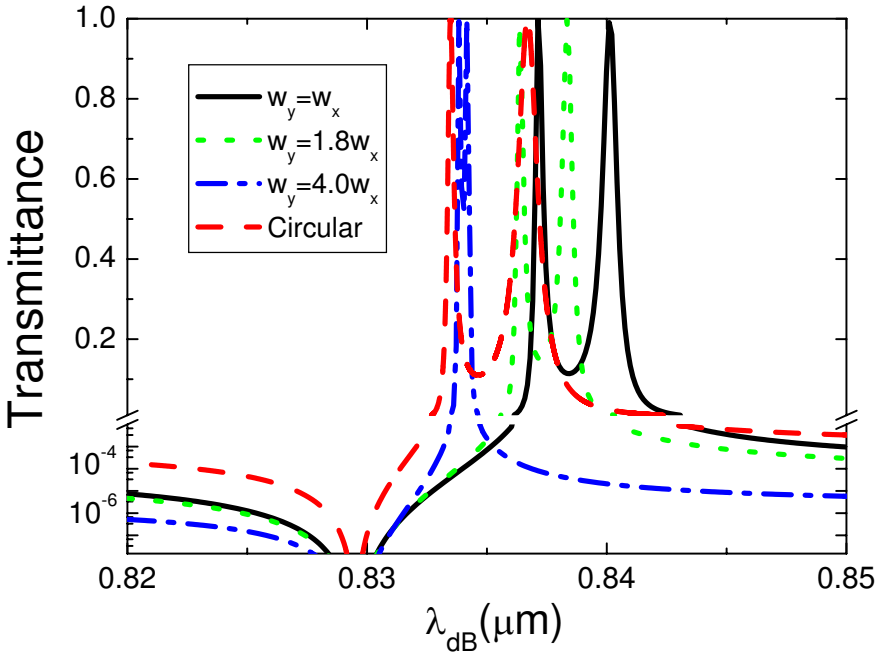

Figure 5.5.: Cold ^{87}Rb atoms transmission through square arrays ($\Lambda_x = \Lambda_y = 0.800\,\mu$m) of holes of area equal to $7.84 \times 10^{-2}\mu$m^2. Four different hole shapes are considered (see main text). The rest of the parameters defining the structure are the same as in Fig. 5.4.

be replaced by its 2D counterpart β_{2D}. $G = G_{2D}$ is the only term within Eqs. (5.13) which varies substantially from its 1D version. It includes now a double sum over diffraction orders,

$$G_{2D} = \sum_{n,m=-\infty}^{\infty} \frac{iq_z^{(nm)}}{k_0} f(\mathbf{k}_{nm}, h) |\langle \mathbf{k}_{nm} | \psi_{\mathrm{WM}}^{2D} \rangle|^2, \tag{5.21}$$

where $f(\mathbf{k}_{nm}, h)$ is given by Eq. (5.8) substituting $k_z^{(n)}$ and $q_z^{(n)}$ by $k_z^{(nm)} = \sqrt{k_0^2 - |\mathbf{k}_{nm}|^2}$ and $q_z^{(nm)} = \sqrt{\xi k_0^2 - |\mathbf{k}_{nm}|^2}$, respectively. Once the set of matching equations is solved, T can be evaluated from Eq. (5.14), where now the total probability current fluxes are integrated inside the 2D unit cell of area $\Lambda_x \times \Lambda_y$.

Figure 5.4 shows the transmittance of cold ^{87}Rb atoms at normal incidence through a material slab of thickness $t = 0.16\,\mu$m. Three different periodic arrays of square holes are considered. In all three cases $w_x = w_y = 0.28\,\mu$m. Black line corresponds to a square array of period $\Lambda_x = \Lambda_y = 0.80\,\mu$m. It shows the characteristic twin maxima accompanied by a sharp dip close to the period already analyzed for 1D structures. In contrast to Fig. 5.3, in Fig. 5.4 the two resonant peaks are clearly distinguishable since the wavelength

range displayed is much narrower. As in the 1D case, both resonant maxima are linked to the excitation of SMWs at both film surfaces. However, since the coupling of the SMWs through the apertures (both slits and holes) is evanescent (β and β_{2D} are imaginary for the geometrical parameters considered), two different configurations of the matter wave-function arises [158]. The two possible profiles of Ψ correspond to the symmetric and antisymmetric superposition of the isolated SMWs through the apertures. It is discussed below how the symmetric (antisymmetric) profile with respect to the middle of the film is higher (lower) in energy, leading to a resonant peak at a shorter (larger) λ_{dB} in the transmission spectrum. In EOT, double peaked features only occur in the transmission spectrum of 2D hole arrangements. In slit arrays, the fact that the lowest slit waveguide mode is always propagating translates into that only one single peak appears in the transmission spectrum.

The transmittance versus λ_{dB} for two rectangular arrays of periods $\Lambda_x = 0.790\,\mu$m, $\Lambda_y = 0.810\,\mu$m (red dotted line), and $\Lambda_x = 0.785\,\mu$m, $\Lambda_y = 0.815\,\mu$m (green dashed line) is also plotted in Figure 5.4. Although both arrays are almost square, the transmission spectra are very different from the square one. Rectangular arrays present the usual resonant features twice. This splitting can be understood again turning back to Eq. (5.2). In 1D arrays under non-normal incidence, non-zero $\mathbf{k}_i$ allows the excitation of SMWs with two different wave vectors $\mathbf{k}_\pm$, leading to different resonant energies $E(\mathbf{k}_\pm)$. In 2D rectangular hole arrays, it is the fact that $\Lambda_x \neq \Lambda_y$ what makes the resonant energies associated to SMWs propagating along x and y-direction different, i.e., $E(\mathbf{k}_{10}) \neq E(\mathbf{k}_{01})$. As expected, transmission resonances for both rectangular arrays in Fig. 5.4 are located close to Λ_x and Λ_y. This splitting of the transmission resonances in rectangular hole arrays does not occur in the EM case, where the incident light excites only surface EM modes travelling along the direction defined by the electric field component parallel to the metallic film. Thus, the polarization of the incident light defines a preferred direction at the film surface and only transmission resonances associated to the structure periodicity along that direction appear in the spectra [93].

In order to study the dependence of the transmission properties of hole arrays on the hole shape, the transmission spectra for square arrays of period $\Lambda_x = \Lambda_y = 0.800\,\mu$m and four different hole geometries are shown in Figure 5.5. The geometrical parameters of the perforated film are the same as in Fig. 5.4. The hole area is fixed to $7.84 \times 10^{-3}\,\mu\text{m}^2$. Black solid line renders the transmittance for square holes of side $w_x = w_y = 0.28\,\mu$m. Green dotted and red dashed dotted lines correspond to rectangular arrays of side $w_x = 0.21\,\mu$m and $w_y = 0.37\,\mu$m, and $w_x = 0.14\,\mu$m and $w_y = 0.56\,\mu$m, respectively. The transmission for circular holes of radius $r_c = 0.16\,\mu$m is plotted in red dashed line. The profile of the transmission maxima for the four structures is very similar, whereas

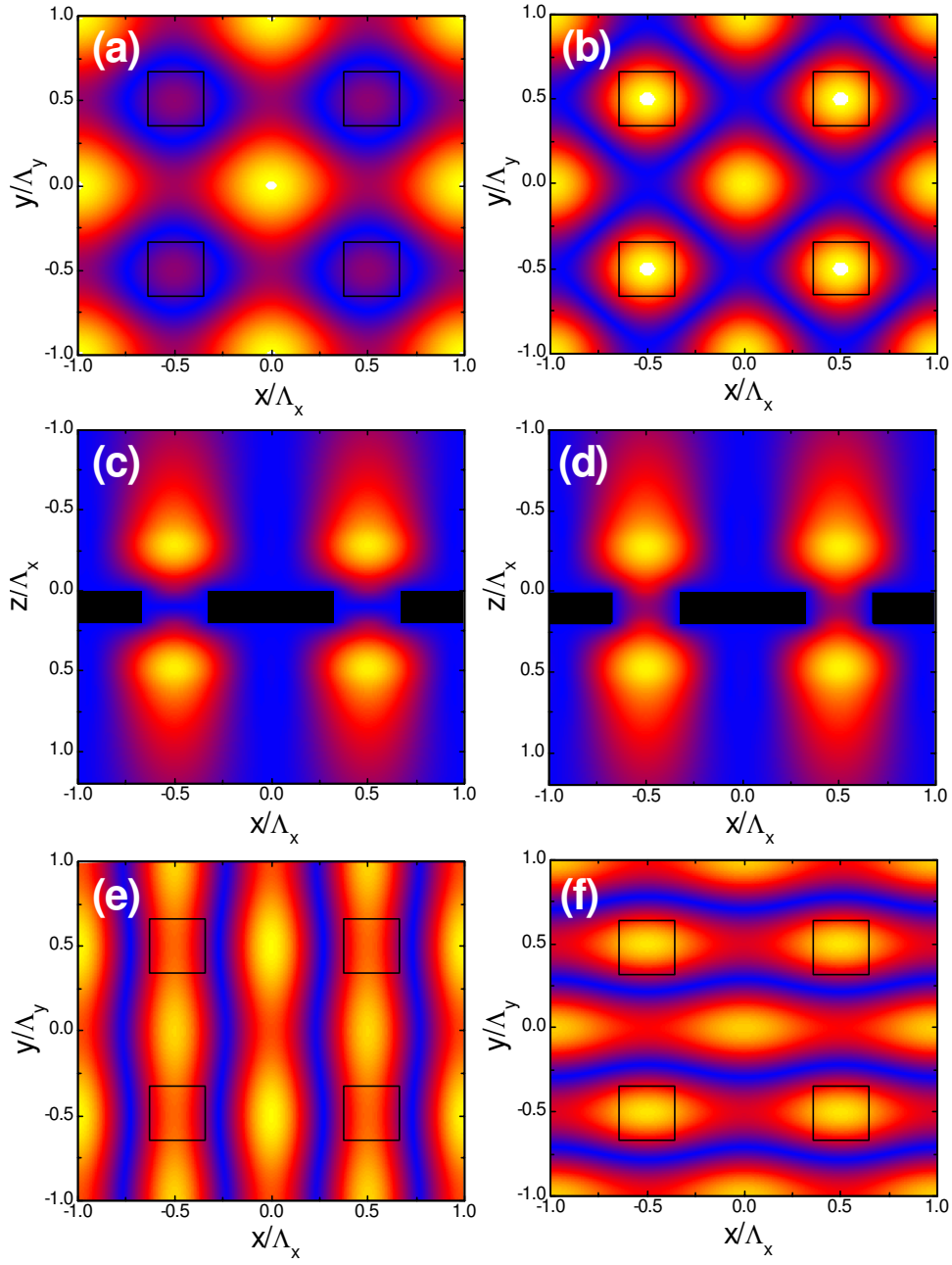

Figure 5.6.: Modulus of the matter wavefunction passing through periodic hole arrays at resonance. Panels (a) and (b): at the output surface of the square array considered in Fig. 5.4 for $\lambda_{\rm dB} = 0.829\,\mu$m and $\lambda_{\rm dB} = 0.837\,\mu$m, respectively. Panels (c) and (d): cross-cut in xz-plane for $\lambda_{\rm dB} = 0.837\,\mu$m and $\lambda_{\rm dB} = 0.840\,\mu$m. Panels (e) and (f): $|\Psi|$ at the output surface for the rectangular array in green in Fig. 5.4 evaluated at $\lambda_{\rm dB} = 0.816\,\mu$m and $\lambda_{\rm dB} = 0.850\mu$m. $|\Psi|$ increases from blue to yellow. Black squares indicate hole positions.

their width and position change. Thus, although the width of the peaks for square and circular holes is the same, the spectral position is shifted to shorter λ_{dB} in the circular case. This blue shift of the transmission resonances also occurs for rectangular holes, accompanied by a reduction of the peaks width. The ratio between hole sides control this effect: for larger w_y/w_x, the transmission peaks approach the periodicity while they become narrower.

In Figure 5.6, the wavefunction modulus, $|\Psi|$ passing through the hole arrays of Fig. 5.4 is depicted. Upper panels show $|\Psi|$ in the output side ($z = 0.36\,\mu$m) of the square array of Fig. 5.4. Panel (a) corresponds to the transmission dip at $\lambda_{dB} = 0.829\,\mu$m and panel (b) to the peak at $\lambda_{dB} = 0.837\,\mu$m. As expected from Eq. (5.14), the wavefunction modulus at holes exit presents a minimum (maximum) at the resonant dip (peak) in the spectrum. However, in both cases it displays a maximum in the center of the square formed by four neighbor holes in the array. These maxima do not appear in the EM case [159] due to the asymmetry of the electric field induced by the incident polarization. Panels (c) and (d) show a cross-cut of the matter wavefunction inside the xz-plane for the same structure. They correspond to the resonant transmission peaks at $\lambda_{dB} = 0.837\,\mu$m and $\lambda_{dB} = 0.840\,\mu$m, respectively. They show clearly that the maximum at higher (lower) λ_{dB} is linked to a symmetric (antisymmetric) profile of Ψ with respect to the middle plane of the perforated film. As a result, the modulus of the wavefunction inside the holes vanishes at $z = \frac{t}{2}$ in panel (c), whereas $|\Psi|$ presents a minimum different from zero inside the holes in panel (d).

Finally, lower panels in Fig. 5.6 render the matter wavefunction at resonance in the output surface of the rectangular hole array in green in Fig. 5.6. Panel (e) is evaluated at $\lambda_{dB} = 0.816\,\mu$m and panel (f), at $\lambda_{dB} = 0.850\,\mu$m. These two panels demonstrate that the resonant transmission process for $\lambda_{dB} \simeq \Lambda_x$ is controlled by SMWs propagating along x-direction, whereas for $\lambda_{dB} \simeq \Lambda_y$, SMWs travelling in the y-direction assist it.

5.5. Resonant transmission and beaming through single apertures

In this section, we study the phenomenon of resonant transmission and beaming through single apertures for matter waves. It is well known that SPPs constitute a route to mold the flow of light [48]. The question here is whether SMWs can be tailored in a similar way to SPPs in order to control the diffraction of matter waves exiting from a single aperture. We consider a simple 1D structure composed by a central slit flanked by an array of grooves symmetrically disposed at both sides (left and right) of the aperture in

both faces (input and output) of the film.

We modify our theoretical formalism to deal with finite structures. We consider an artificial supercell of length L containing the structure shown in the right inset of Fig. 5.7: a material slab of thickness t perforated with a single slit of width w surrounded by $4 \times N$ grooves of width w_g and depth t_g. As $\lambda_{dB} >> w, w_g$, the wavefunction inside the film is accurately described by considering only the first waveguide mode inside each indentation. If we label the indentations with index α, the wavefunction inside the film can be written as

$$|\Psi_{III}\rangle = \sum_{\alpha=-N}^{N} \phi_\alpha(z)|\psi_{WM}^\alpha\rangle, \tag{5.22}$$

where the function $\phi_\alpha(z)$ contains the dependence on z of Ψ inside indentation α. We label the central slit with $\alpha = 0$. The associated waveguide mode in real space is $\langle x|\psi_{WM}^0\rangle = \sqrt{2/w}\sin[\pi/w(x + w/2)]$ for $|x| < w/2$, and vanishes otherwise. As we saw in Section 5.3, the dependence on z is given by $\phi_0(z) = C_0 e^{i\beta z} + D_0 e^{-i\beta z}$, with $\beta = \sqrt{\xi k_0^2 - (\pi/w)^2}$.

The waveguide mode supported by groove α ($\alpha \neq 0$) can be expressed as $\langle x|\psi_{WM}^\alpha\rangle = \sqrt{2/w_g}\sin[\pi/w_g(x - x_\alpha + w_g/2)]$ if $|x - x_\alpha| < w_g/2$ (where x_α is the grove position) and $\langle x|\psi_{WM}^\alpha\rangle = 0$, otherwise. The fact that the grooves are arranged periodically allows us to write $x_\alpha = \alpha\Lambda$, where Λ is the array period. For grooves milled in the input side of the structure ($0 < z \leq t_g$), we have $\phi_\alpha(z) = C_\alpha \sin\beta_g(z - t_g)$, whereas for grooves in the output side ($t - t_g < z \leq t$), $\phi_\alpha(z) = D_\alpha \sin\beta_g(z - t + t_g)$. In both cases, the z-component of the wave vector inside the grooves is $\beta_g = \sqrt{\xi k_0^2 - (\pi/w_g)^2}$.

Similarly as we did in Section 2.2.2, we take into account the finite size of the structure by making the supercell length L tending to infinite ($L \to \infty$). As a result, discrete diffraction orders can not be defined and the matter wavefunction must be expanded in terms of a continuum of diffraced waves. As for periodic structures, we define the quantities ψ_α (ψ'_α), which give the amplitude of Ψ at the openings of the indentations perforated in the input (output) surface of the film. At the central slit, we have $\psi_0 = C_0 + D_0$ and $\psi'_0 = -(C_0 e^{i\beta t} + D_0 e^{-i\beta t})$, whereas for $\alpha \neq 0$, $\psi_\alpha = -C_\alpha \sin(\beta_g t_g)$ and $\psi'_\alpha = -D_\alpha \sin(\beta_g t_g)$. Imposing continuity of the wavefunction at the interfaces of the structure, we obtain a set of $(4N + 2)$ equations in the unknowns $\{\psi_\alpha, \psi'_\alpha\}$ of the form:

$$\begin{aligned} (G_{\alpha\alpha} - \epsilon_\alpha)\psi_\alpha + \textstyle\sum_{\gamma\neq\alpha} G_{\alpha\gamma}\psi_\gamma - G^V\psi'_0\delta_{\alpha 0} = I_\alpha, \\ (G_{\alpha\alpha} - \epsilon_\alpha)\psi'_\alpha + \textstyle\sum_{\gamma\neq\alpha} G_{\alpha\gamma}\psi'_\gamma - G^V\psi_0\delta_{\alpha 0} = 0. \end{aligned} \tag{5.23}$$

The role played by the various terms in Eqs. (5.23) remains the same as in Eqs. (5.13). The upper $(2N + 1)$ equations control the flow of the matter waves at the input surface of the film, where $I_\alpha = (2\sqrt{2}i/\pi)\xi/[\xi\cos(\xi k_0 h) - i\sin(\xi k_0 h)]$ reflects the overlap between

the normal incident plane wave and the waveguide mode supported by indentation α. Note that, under normal incidence, I_α does not depend on the position of the groove α. The term ϵ_α describes the penetration of the matter waves inside the indentations. For $\alpha = 0$, it has the form $\epsilon_0 = \beta/[k_0 \tan(\beta t)]$ whereas for $\alpha \neq 0$, $\epsilon_\alpha = \beta_g/[k_0 \tan(\beta_g t_g)]$. The term $G^V = \beta/[k_0 \sin(\beta t)]$ takes into account the overlap of Ψ at both sides of the film through the slit. It is only present in the equations associated to ψ_0 and ψ_0'. Finally, $G_{\alpha\gamma} = \langle \psi^\alpha_{\mathrm{WM}} | \hat{G} | \psi^\gamma_{\mathrm{WM}} \rangle$ describes the coupling of the matter waves coming from indentations α and γ through the SMWs travelling along the film surfaces. The representation of the propagator $\hat{G}$ in real space is

$$G(x, x') = \frac{1}{2\pi} \int_{-\infty}^{\infty} dk_x \frac{iq_z}{k_0} f(k_x, h) e^{ik_x(x-x')}, \tag{5.24}$$

where the wave vector along the z-direction is $k_z = \sqrt{k_0^2 - k_x^2}$ in vacuum, and $q_z = \sqrt{\xi k_0^2 - k_x^2}$ inside the potential well surrounding the film. The function $f(k_x, h)$ is given by

$$f(k_x, h) = \frac{k_z \cos(q_z h) - iq_z \sin(q_z h)}{q_z \cos(q_z h) - ik_z \sin(q_z h)}. \tag{5.25}$$

Note that, as in periodic structures, the propagator (5.24) has the same form as $G_s(x, x')$, defined in Eq. (2.59), except for the function $f(k_x, h)$.

The quantities $\{\psi_\alpha, \psi_\alpha'\}$ are found by solving the Eqs. (5.23), and once they are known, the matter wavefunction in all the space can be constructed. The transmissivity of the structure is then given by the ratio between the transmitted and incident probability density current fluxes through the slit. This ratio can be expressed as a function of the matter wave amplitudes at the slit openings as $T = G^V \mathrm{Im}[\psi_0^* \psi_0']$. As a difference with the previous sections, the incident wave is now normalized to the slit width w and T corresponds to the normalized-to-area transmittance.

Figure 5.7 represents T versus λ_{dB} for normal incidence of the atoms. The red dashed line corresponds to the single slit case ($w = 0.3\,\mu$m and $t = 0.16\,\mu$m). As $\lambda_{\mathrm{dB}} >> w$, $T < 1$ and the transmission spectrum shows an exponentially decaying behavior as λ_{dB} increases. When grooves ($w_g = 0.22\,\mu$m and $t_g = 0.065\,\mu$m) are milled surrounding the slit on both surfaces of the film, T develops a resonant peak close to the periodicity of the groove array $\Lambda = 0.8\,\mu$m. As the number of grooves increases from $N = 5$ (blue dashed dotted line) to $N = 15$ (green dashed double dotted line), the transmission peak becomes higher and spectrally narrower. This is a clear fingerprint of the excitation of SMWs running along the film surfaces. For higher N, the coupling between the incident plane matter wave and the SMWs becomes more efficient, leading to a better defined resonant

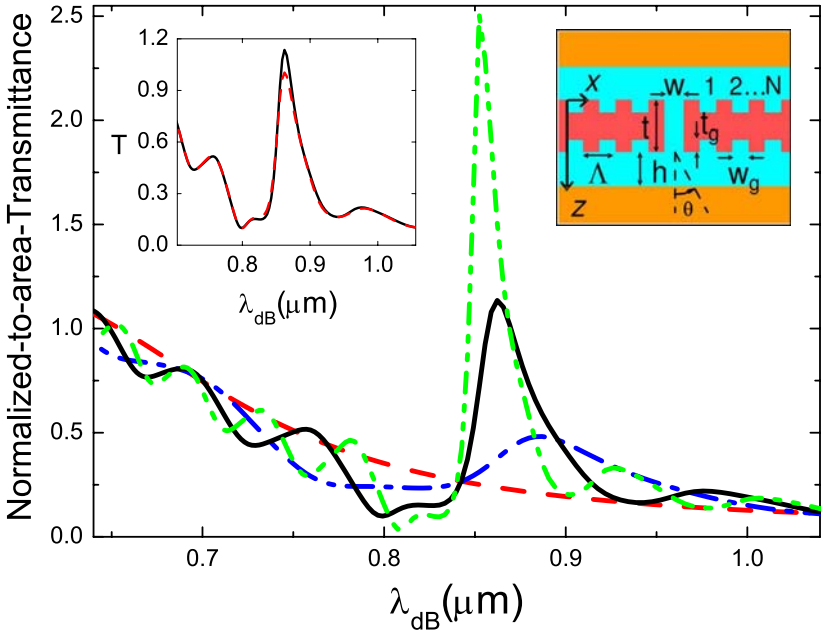

Figure 5.7.: Normalized-to-area transmittance for four different structures. Dashed red line: single slit. Blue dashed-dotted line: single slit flanked by $N = 5$ grooves located at each side (right and left) of the central slit at both the input and output surfaces. Black solid line and green dash-double-dotted lines: same as before but with $N = 10$ and $N = 15$, respectively. Left inset renders T versus λ_{dB} for $N = 10$ grooves milled at the two surfaces (black solid line) or only at the input surface (red dashed line). Right inset: Structure supercell containing the central slit surrounded by $4N$ grooves.

transmission peak. In the left inset of Fig. 5.7, the comparison between the transmission spectrum for a single slit surrounded by $N = 10$ grooves in both the input and output sides of the film (solid black line) and the same slit surrounded by $N = 10$ grooves only in the input side (red dashed line) is shown. It is clear that the total transmission is mainly controlled by the corrugation placed at the input surface of the structure. Let us stress that all the phenomenology described in Fig. 5.7 is similar to that reported for EOT in a single slit surrounded by corrugations [50].

In order to study the shape of the beam emerging from the structure, we calculate the transmitted matter wavefunction (Ψ_t) in the vacuum region below the structure ($z > t + h$, see right inset of Fig. 5.7). It can be written as a superposition of plane waves of the form

$$\Psi_t(x,z) = \int_{-\infty}^{\infty} dk_x t(k_x) e^{ik_z z} e^{ik_x x}, \tag{5.26}$$

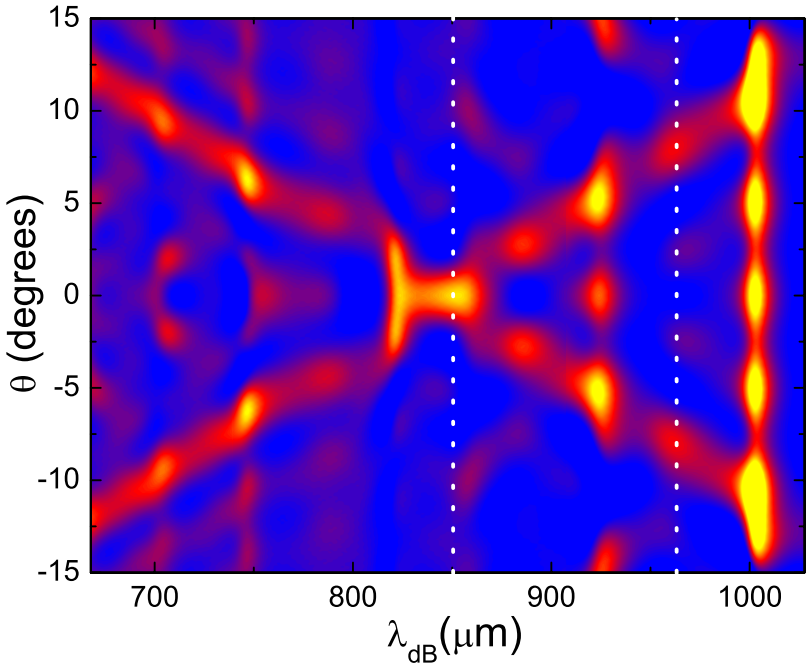

Figure 5.8.: Radial probability density current j_r^t emerging from a single slit as a function of the exiting angle θ and the de Broglie wavelength λ_{dB}. The slit ($w = 0.22\,\mu$m) is flanked by $N = 15$ grooves of width $w_g = 0.30\,\mu$m and depth $t_g = 0.065\,\mu$m disposed periodically ($\Lambda = 0.80\,\mu$m) at both surfaces of a film of height $t = 0.16\,\mu$m. White dashed lines indicate the λ_{dB} values considered in Fig. 5.9.

where the transmission coefficient $t(k_x)$ depends on the amplitudes ψ'_α as

$$t(k_x) = \frac{q_z e^{-ik_z(t+h)}}{[q_z \cos(q_z h) - ik_z \sin(q_z h)]} \sum_{\alpha=-N}^{N} \left[\frac{\cos(k_x w_\alpha/2) e^{-ik_x x_\alpha}}{w_\alpha[(\pi/w_\alpha)^2 - k_x^2]}\right] \psi'_\alpha. \tag{5.27}$$

Once Ψ_t is obtained, the radial probability density current $j_r^t = (\hbar/m)\mathrm{Im}\{\Psi^{t*}\partial_r\Psi^t\}$ can be calculated. Figure 5.8 renders j_r^t in the far field ($r = 150\Lambda$) as a function of the exiting angle θ and λ_{dB} for the structure with $N = 15$ grooves perforated on both film surfaces. At $\lambda_{\mathrm{dB}} = 0.85\,\mu$m, j_r^t shows a maximum around $\theta = 0$ which leads to a collimated beam emerging from the single slit in forward direction. This λ_{dB} coincides with the position of the transmission peak in the spectrum (green dashed double dotted line in Fig. 5.7). This fact indicates that, as in the EM case [49], the resonant transmission and beaming phenomena have the same physical origin: the excitation of SMWs propagating along the film surfaces. We have also studied j_r^t for films corrugated only in the input surface. The angular patterns of j_r^t obtained display the uniform behavior characteristic of a wave

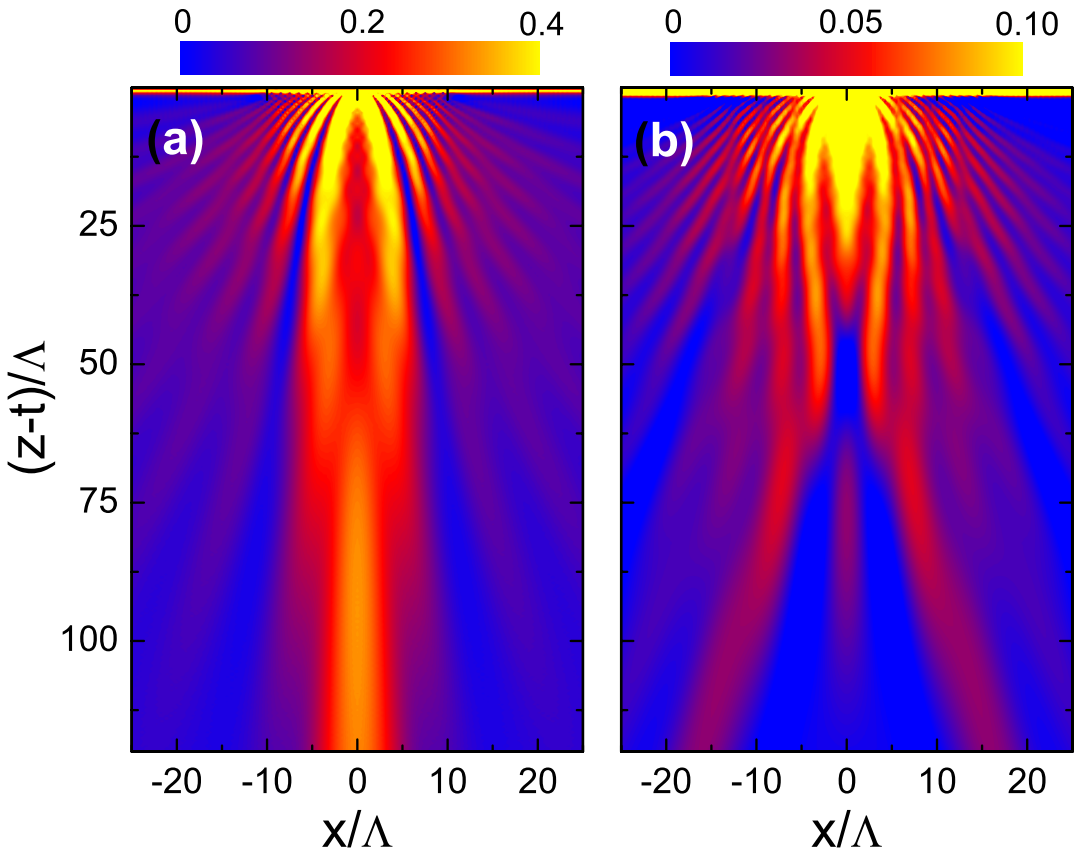

Figure 5.9.: Amplitude of the matter wavefunction emerging from the structure considered in Fig. 5.8 at two different wavelengths: (a) at resonance ($\lambda_{\mathrm{dB}} = 0.85\,\mu$m) and (b) out of resonance ($\lambda_{\mathrm{dB}} = 0.96\,\mu$m). Note that the color scale is different in each panel.

emerging from a single aperture much smaller that the wavelength. From this result, we can conclude that the corrugation of the output surface of the film governs the shape of the atom beam exiting from the central slit. Figure 5.9 renders the amplitude of the matter wavefunction emerging from a single slit flanked by $N = 15$ grooves evaluated at two different de Broglie wavelengths (indicated by white dashed lines in Fig. 5.8). Wavefunction in panel (a) is associated to the peak ($T = 2.5$) in transmission spectrum at $\lambda_{\mathrm{dB}} = 0.85\,\mu$m (see Fig. 5.7). At resonance, the scattering of the SMWs with the grooves perforated in the output surface of the film leads to a coherent reemission of matter waves. The interference of these matter waves with those stemming from the central slit gives rise to a very collimated beam along the z-direction. Panel (b) is evaluated out of resonance ($\lambda_{\mathrm{dB}} = 0.96\,\mu$m). The transmissivity of the structure is $T = 0.25$, much lower than in panel (a). As expected from Fig. 5.8, two different beams emerge from the

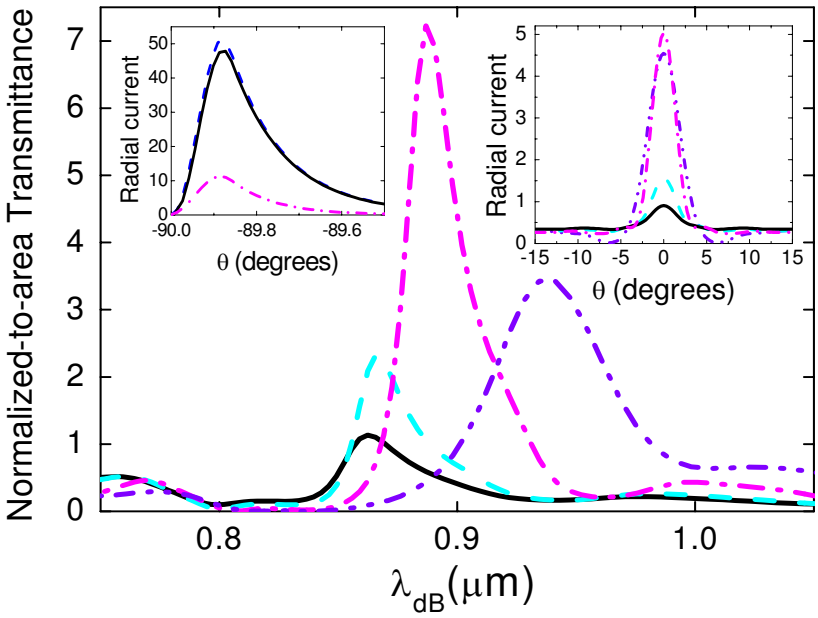

Figure 5.10.: Normalized-to-area transmission spectrum for a single slit flanked by $N = 10$ grooves. Structures with four different potential depths inside the grooves, V_g, are considered: $V_g = V_0$ (black solid line), $V_g = 9.5V_0$ (cyan dashed line), $V_g = 17V_0$ (pink dashed double dotted line), and $V_g = 19V_0$ (violet dashed dotted line). Right inset displays the dependence of the far field ($r = 150\Lambda$) transmitted radial current, j_r^t, in the vicinity of $\theta = 0°$ for these four systems. Left inset renders j_r^t versus θ approaching 90° for three cases. Blue dashed line: single slit. Black solid line: $N = 10$ and $V_g = V_0$. Pink dashed dotted line: $N = 10$ and $V_g = 17V_0$.

structure, travelling with an angle $\theta \approx \pm 8$. The matter wave reemission by the surface corrugation is now much less efficient than at resonance. This fact allows us to see clearly the SMWs travelling away from the central slit along the film surface at $z = t$.

We can add a new degree of freedom to our model by making the attractive potential inside the grooves, V_g, different from the potential well surrounding the material slab, V_0. Thus, the z-component of the wave vector associated with the groove waveguide modes is now $\beta_g = \sqrt{\xi_g k_0^2 - (\pi/w_g)^2}$, with $\xi_g = 1 + \frac{|V_g|}{E}$. Figure 5.10 renders the transmission spectrum for a single slit surrounded by $N = 10$ grooves with the same geometrical parameters as in Fig. 5.7. It shows how the transmissivity of the structure evolves as V_g is increased from $V_g = V_0$ (black solid line) up to $V_g = 19V_0$ (violet dashed dotted line). There is an optimum value, $V_g = 17V_0$ (pink dashed double dotted line) for which the transmittance is maximum, which results in an additional enhancement of 7 in T with

respect to the structure with $V_g = V_0$. For the geometrical parameters considered, Ψ is propagating along the z-direction inside the grooves. The transmission peak for the case $V_g = 17V_0$ is located very close to the Fabry-Perot resonant condition $\sin(\beta_g t_g) = 0$. This fact enables us to link the transmission enhancement to the excitation of cavity resonances inside the grooves, as in the EM analog of the system [50].

The insets of Fig. 5.10 demonstrates that the tuning of the potential inside the grooves also allows reducing the angular width of the beam of cold atoms exiting from the structure. In the right inset, we plot the radial probability current in the far field evaluated at resonance for the four cases considered in the main panel of the figure. Clearly, the transmission enhancement is accompanied by a narrowing of the matter beam. Thus, whereas for $V_g = V_0$ the beam width is 6°, for the optimum case, $V_g = 17V_0$, it can be as small as 2°. Additionally, the left panel depicts the behavior of j_r^t in the vicinity of $\theta = 90°$ for these two structures. This quantity provides an estimation of the amplitude of the leaky SMW after its passage through the groove array. For comparison, we have also plotted the single slit case (blue dashed line). We can see that the amplitude of the SMW has been reduced, being the decay even more dramatic for $V_g = 17V_0$. The decrease of the amplitude of the leaky SMW reflects that part of it has been radiated, leading to the enhancement in the transmission and collimation effect mentioned above.

5.6. Feasible implementation for the case of slit arrays

Once we have demonstrated that the phenomenon of resonant transmission is possible for matter waves, let us now discuss a feasible implementation of the 1D slit array analyzed in Section 5.3. The fundamental ingredient is the existence of a potential well close to the material interface. In principle, one could take advantage of the atom-surface potential present in front of a dielectric surface as a result of the long-range van der Waals (vdW) attraction and the very short-range repulsion between the electronic cloud of the atom and that of the surface. Although this potential supports surface states [160], it suffers from two important drawbacks. First, the energies involved are very different from the ones we are interested in (cold atoms at temperatures of μK have energies of the order of 10^{-11} eV whereas typical values in vdW potentials are of the order of 10^{-3} eV). And second, the centers of mass of these bound states are very close to the surface so that strong electronic interaction between the incident atom and the surface atoms is expected. In principle, this should be avoided in order to maintain the coherence of the atom wave and to minimize atom heating during the transmission process. In addition, if it was possible to externally tune the potential, one could implement an atom switch

by opening or closing the transmission channel.

For these reasons external forces have to be exerted on the cold atom to obtain a potential well with a depth of about 10^{-10} eV at a distance away from the surface of the order of 1 μm. Such potential can be built by adding to the inherent attractive vdW force a repulsive dipolar interaction due to a laser field [161, 162]. The frequency of the laser field is blue-detuned slightly above the frequency of a given optical transition of the atom so that its polarizability becomes negative, resulting in an effective repulsive potential. The sum of the optical repulsive potential plus the vdW attraction gives rise to a potential barrier keeping the atoms sufficiently far away from the surface (a so-called evanescent atomic mirror [163, 164]), and to a potential well that may support bound states at an appropriate distance away from the surface. Similar ideas have been used to guide cold atoms along optical fibers [165, 166]. In addition, periodicity is also needed to couple the incident plane matter wave to the SMW. A structure fulfilling all these requirements is an array of parallel cylindrical optical fibers carrying a blue-detuned optical mode propagating along them. This is the structure we propose to experimentally test the phenomenon of extraordinary transmission of matter waves through very narrow slits.

The phenomenon occurs in a certain parameter range, and we have chosen the following realistic values in our numerical simulations. The optical fibers have radius $R = 0.20\,\mu$m, dielectric constant $\epsilon = 13$, and the array period is $\Lambda = 0.80\,\mu$m. We take again ^{87}Rb cold atoms and will be considering the atomic transition D_2 ($5^2S_{1/2} \rightarrow 5^2P_{3/2}$) at $\omega_0 = 2\pi \times 384\,$THz. The laser frequency is chosen in such a way that the detuning is $\delta = \omega - \omega_0 = 2\pi \times 6\,$THz. The repulsive optical potential at the position $\mathbf{r}$ outside the fiber is given by [167]

$$V_{\text{opt}}(\mathbf{r}) = \frac{\hbar\delta}{2}\frac{\Gamma^2}{\Gamma^2 + 4\delta^2}\frac{I(\mathbf{r})}{I_{\text{sat}}}, \tag{5.28}$$

where $\Gamma = 2\pi \times 6\,$MHz is the linewidth of the considered transition, $I_{\text{sat}} = 2.5\,\text{mW/cm}^2$, and $I(\mathbf{r})$ is the intensity profile of the laser guided mode. The chosen detuning is sufficiently small so that a two-level atom approximation is valid, but large enough so that recoil heating is low. The vdW attractive potential is obtained by means of a simple calculation assuming pairwise interaction between the atom and the points inside the fiber (retardation is not taken into account). This leads to the following approximation

$$V_{\text{vdW}}(\mathbf{r}) = \frac{1-\epsilon}{1+\epsilon}\frac{\pi C_3}{r^3}\sum_{n=1}^{\infty}\frac{1}{n}\left(\frac{(2n+1)!!}{2^n(n-1)!}\right)^2\left(\frac{R}{r}\right)^{2n}, \tag{5.29}$$

where r is the distance to the fiber axis and the parameter C_3 is $7.78 \times 10^{-12}\,\text{eV}\mu\text{m}^3$ (C_3 is known for vdW interaction with a flat metal interface [168]). Note that r and

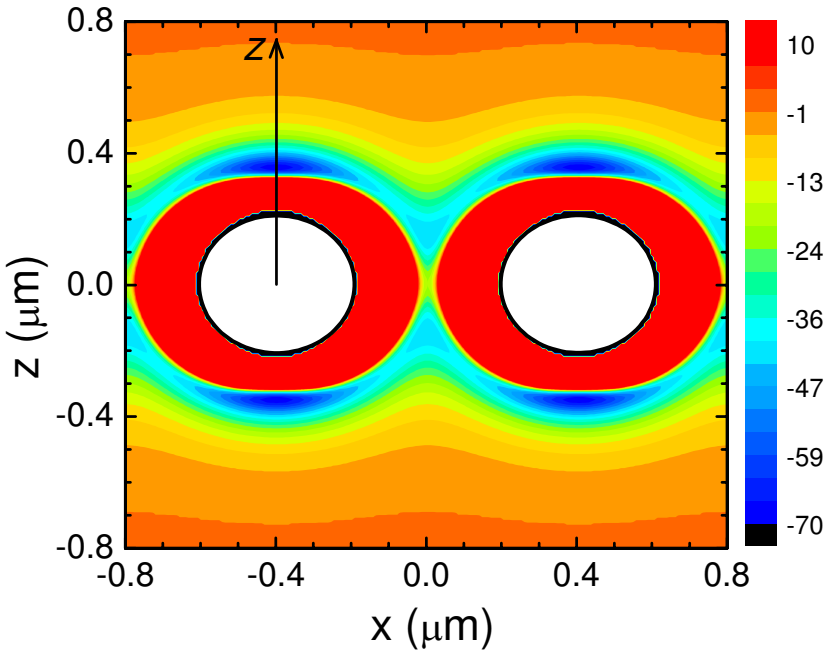

Figure 5.11.: 2D total potential for ^{87}Rb cold atoms impinging on a array of cylindrical dielectric fibers carrying a blue-detuned optical guided mode. The white circles represent the fibers' cross section. Color scale codes potential energies in units of 10^{-11} eV. Blue and green regions correspond to an attractive potential well. The effective slit width is of the order of $0.05\,\mu$m.

R are expressed in μm. The total potential is $V(\mathbf{r}) = V_{\text{opt}}(\mathbf{r}) + V_{\text{vdW}}(\mathbf{r})$. The chosen parameters guarantee that the requirements about potential well depth and position mentioned above can be fulfilled.

Figure 5.11 plots the total potential for the case when the optical power carried by the laser mode running along one fiber is $P_0 = 20.7\,$mW. As desired, the overall picture of this potential resembles our basic model [compare inset of Fig. 5.3]. White regions in Fig. 5.11 correspond to the locations of the fibers. In the immediate vicinity of the fibers' surfaces vdW attraction dominates (black narrow ring adjacent to the fiber), but for distances to the fiber center between $0.21\,\mu$m and $0.32\,\mu$m the total potential is repulsive (red doughnut-shaped region around the fiber). This potential barrier is much higher than the incident energy so that tunnelling to the inner attractive ring adjacent to the surface fiber is negligible. Due to the evanescent character of the optical field outside the fiber, vdW attraction again dominates for distances larger than $0.40\,\mu$m. In the inter-

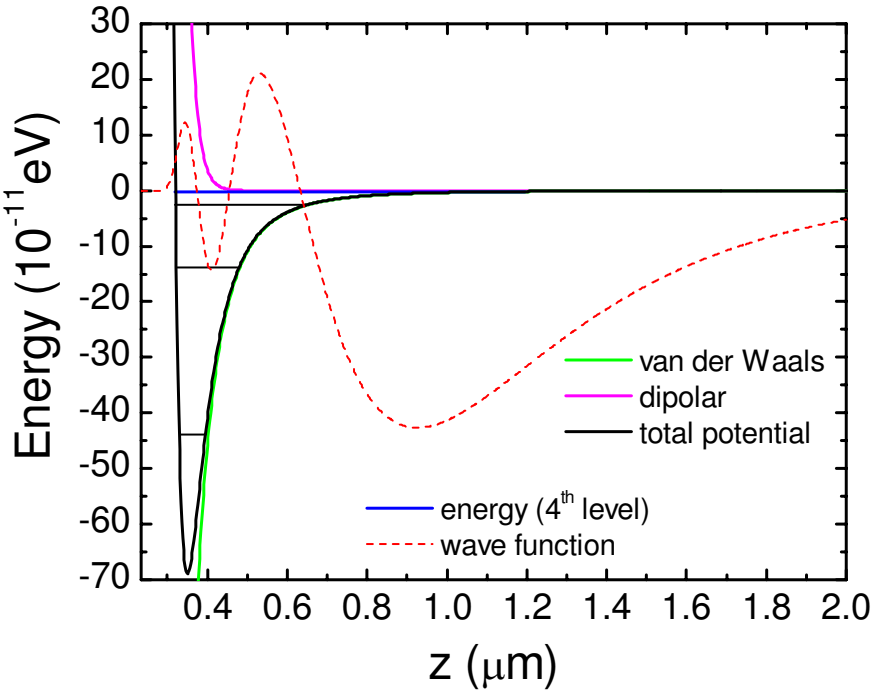

Figure 5.12.: Black line renders a crosscut along vertical z line of potential shown in Fig. 5.11. Green and magenta lines: van der Waals and dipolar contribution to the total potential, respectively. The energy of the fourth level of this 1D potential is represented by the blue line, and the red dashed line shows the corresponding wavefunction.

mediate region, a potential well develops (blue and green colored areas). Importantly, the potential between the fibers is strongly repulsive, leaving out an extremely narrow effective slit (width $\approx 0.05\,\mu$m) for the transmission of atoms through the structure. Figure 5.12 displays a one-dimensional (1D) crosscut of the potential along the z-direction through the center of one fiber. This potential well has four bound states, found by solving the 1D Schrödinger equation using the Numerov's method [169]. The energy of the uppermost level is $E_4 = -0.155 \times 10^{-11}$ eV (blue line). This bound state is the candidate to assist in the transmission of Rb atoms with de Broglie wavelengths of the order of the array periodicity.

Figure 5.13 renders the transmission spectra of normally incident Rb atoms for different values of the laser field power P, taking P_0 as a reference. The results have been obtained through converged transfer matrix calculations (see Sec. 2.3). We have taken advantage of the correspondence between Schrödinger equation and Maxwell equations described at the end of Section 5.2. We have mapped the potential landscape, $V(\mathbf{r})$, into

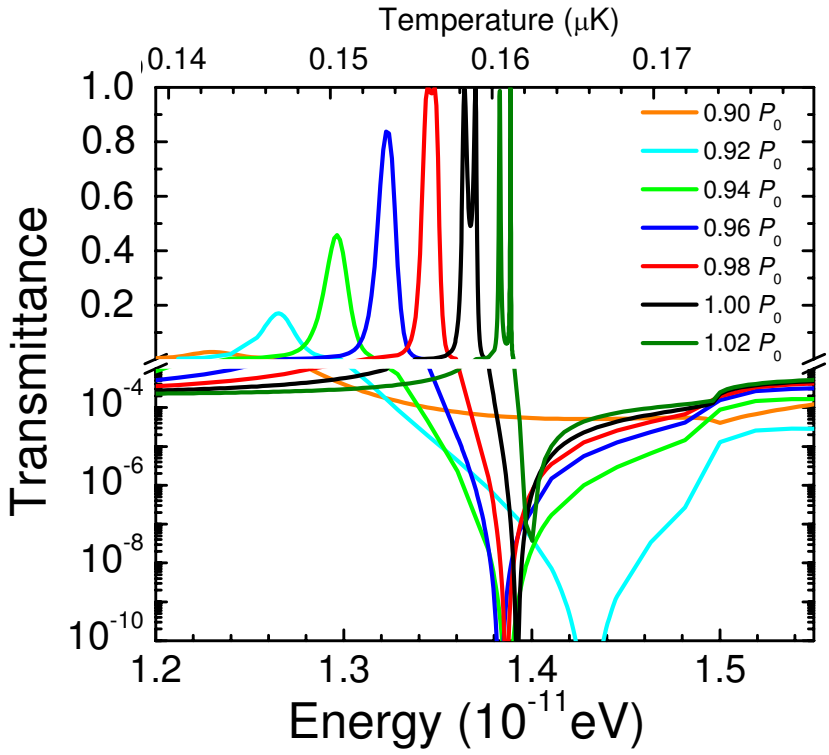

Figure 5.13.: Transmittance of cold ^{87}Rb atoms orthogonally incident on the structure shown in Fig. 5.12, as a function of the incident energy. The various lines correspond to different optical powers P carried by the fibers. Thus, P controls the switch functionality of the structure.

a dielectric function of the form

$$\epsilon(\mathbf{r}) = 1 - \frac{V(\mathbf{r})}{E}, \tag{5.30}$$

where E denotes the kinetic energy of the incoming Rb atoms.

Let us first analyze the transmission corresponding to $P = P_0$ (black line in Fig. 5.13). The spectrum shows two very close maxima reaching 100% transmission and a zero for slightly larger energy. We can safely conclude that the phenomenon of resonant extraordinary transmission of matter waves is present in the designed structure. This conclusion is reinforced by looking at the pattern of the wavefunction modulus [Fig. 5.14], associated to the left peak at about 1.364×10^{-11} eV. Here, it can be distinctly seen that SMWs above and below the structure are excited, building up an even mode. These SMWs have maxima at a distance away from the fiber axis of $0.90\,\mu$m, in good agreement with the maximum's location of the fourth eigenmode in the 1D potential [Fig. 5.12, dashed curve].

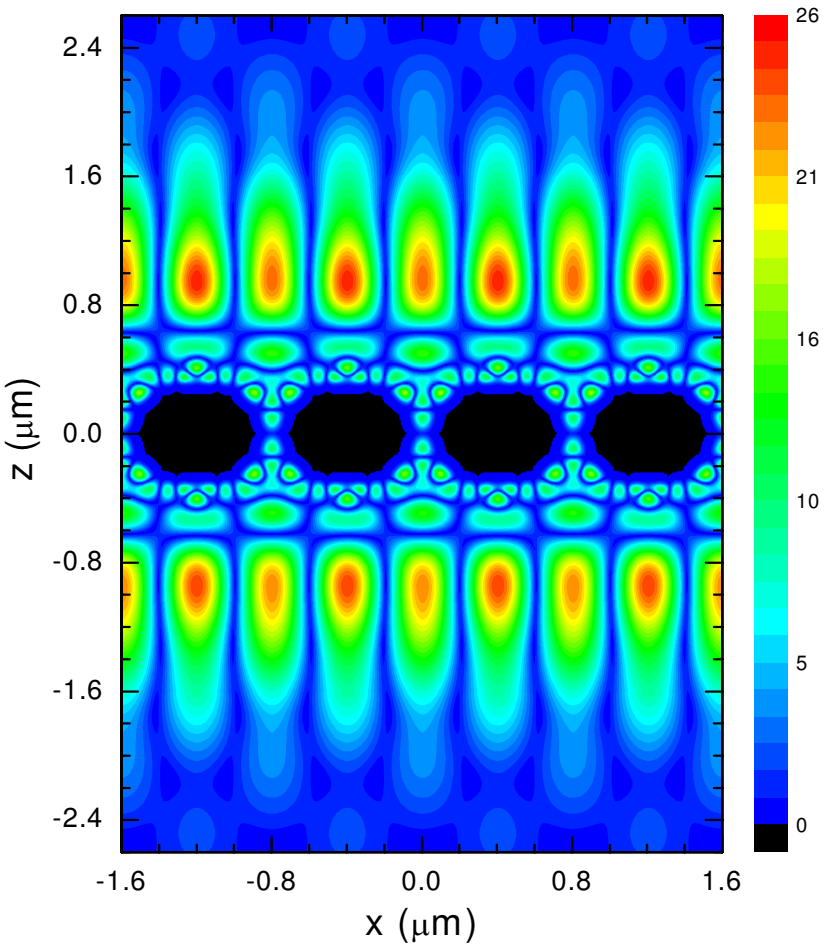

Figure 5.14.: Modulus of the matter wavefunction for the left peak of the curve corresponding to $P = P_0$ in Fig. 5.13. The scale is normalized to the incident amplitude. The plot corresponds to 100% transmission.

If the power P of the laser field is now changed, the total potential and the corresponding transmission spectrum are modified. We have found that transmittance is extremely sensitive to the laser power. This feature opens up the possibility of using the structure as an atomic switch. When the power P is reduced by just a 10%, the transmission peak almost vanishes [Fig. 5.13, orange curve]. Notice that, as P is being lowered, two physical magnitudes change: first, the energy of the eigenmode involved in the transmission process sinks to lower energies, explaining the shift to lower energies of the transmission peak found in Fig. 5.13. Secondly, the channels between the fibers broaden so that the coupling between the SMWs at both interfaces becomes less resonant provoking a re-

duction in the height of the peaks. On the other hand, when P is increased the channel between the fibers is effectively shut. The two peaks become narrower and closer to each other and, in the limit, they merge together with the zero and disappear

5.7. Conclusions

In this chapter, we have studied the formation of surface matter waves in vacuum-solid interfaces, with properties similar to surface plasmon polaritons. In contrast to the electromagnetic case, the Schrödinger equation requires an attractive potential surrounding the material surface in order to support such bounded solutions. By means of a simple model based on square wells, we have studied the appearance of the resonant transmission phenomenon of matter waves through periodic arrays of apertures. We have shown how the scalar character of the matter wavefunction leads to important differences with the electromagnetic case, where polarization effects play a relevant role.

Surface matter waves can also lead to an enhancement of matter waves transmission through a single aperture flanked by a periodic array of indentations. We have studied how a collimated beam emerging from the aperture can be obtained by tailoring the corrugation at the output side of the film.

Finally, we have proposed a feasible implementation for the case of one-dimensional apertures. We have described how a realistic attractive potential can be constructed by combining the attractive van der Waals interaction and a repulsive optical potential created by a blue-detuned laser field.

The work presented here, together with several others recently published analyzing the transfer of the extraordinary transmission phenomenon to acoustic waves (sound) [79–83], demonstrates that both resonant transmission and beaming phenomena are very general undulatory processes based on the excitation of surface waves on perforated films. It is also remarkable that other electromagnetic phenomena such as optical cloaking [170–172] have been also exported to matter [173, 174] and acoustical [175] waves.

6. General conclusions

English

Throughout this thesis, we have studied the electromagnetic phenomena occurring in metal structures which support localized surface modes. We have developed a theoretical formalism based on the modal expansion technique which enables us to analyze these complex systems within a quasi-analytical approach. In our models, the dielectric response of metals is treated within the perfect conductor approximation, which yields accurate results in the microwave and terahertz regimes. In order to go beyond this approximation, we have also performed numerical simulations to estimate the effect of the field penetration into metals in these frequency ranges.

The first step in our research has consisted in a thorough analysis of the geometrically induced electromagnetic modes, also termed spoof surface plasmon polaritons, supported by different metal structures. Two different planar geometries are studied: textured surfaces and perforated films. We have demonstrated that spoof plasmon polaritons in two-dimensional apertures (dimples and holes) are surface waves localized at the structure interfaces. However, in the one-dimensional case (grooves and slits), these modes have a hybrid nature, being strongly influenced by the cavity resonances occurring inside the apertures. We have found that the modal characteristics in all these structures are controlled by the width and depth of the perforations, which allows us to consider these systems as plasmonic metamaterials. The predictive value of our theoretical results has been demonstrated through the comparison with recent experiments realized in the terahertz regime.

The appearance of spoof surface plasmon polaritons in cylindrical structures has been also considered. We have shown that wires milled with a periodic array of rings support bound modes whose properties are dictated by the geometry of the corrugation. Taking advantage of the geometrical origin of these modes, we have designed a conical scheme achieving subwavelength focusing of terahertz radiation. As in planar structures, our theoretical predictions are corroborated by experimental studies on the propagation of terahertz waves along helically grooved wires.

Based on our studies on spoof surface plasmon polaritons in simple geometries, we

have developed two routing schemes for terahertz waves consisting of corrugated channels and wedges. The electromagnetic modes supported by such designs mimic channel and wedge plasmon polaritons at optical frequencies. We have demonstrated that these guided modes allow the subwavelength confinement of electromagnetic fields in the transverse plane and show long propagation lengths and low bending losses.

The scattering properties of perforated metallic films can be also treated within our theoretical framework. This has enabled us to analyze the role of order in the extraordinary optical transmission. We have studied three different finite structures: periodic and quasiperiodic (Fibonacci) arrays of slits, and quasiperiodic (Penrose) arrays of holes. Considering the reciprocal-space version of our formalism, we have been able to link the resonant features in the spectra of these systems with their structure factor. We have shown that long-range order is the only requirement for the appearance of the phenomenon. Moreover, we have explained the formation of transmission resonances in terms of leaky electromagnetic modes supported by the structures. Again, our theoretical results are in good agreement with experiments performed on quasiperiodic hole arrays.

We have also studied the transfer of extraordinary transmission and beaming phenomena to non-interacting cold atoms. By means of a model consisting of square wells, we have shown that, as in the electromagnetic case, the presence of surface modes is the key ingredient in both phenomena. Our model has enabled us to demonstrate that resonant transmission of matter waves appears in periodic arrays of one and two dimensional apertures, and that enhanced transmission and associated beaming effects emerge in single apertures surrounded by corrugations. Finally, we have proposed a feasible implementation of our ideas in which realistic attractive potentials are constructed by combining the intrinsic van der Waals interaction with an external optical potential.

Español

A lo largo de esta tesis hemos estudiado los fenómenos electromagnéticos que ocurren en estructuras metálicas que soportan modos localizados de superficie. Para ello, hemos empleado un formalismo basado en la expansión modal de los campos electromagnéticos, lo que nos ha permitido analizar estos complejos sistemas con un enfoque cuasi-analítico. En nuestros modelos, hemos tratado la respuesta dieléctrica de los metales dentro de la aproximación de metal perfecto, que proporciona resultados precisos en los regímenes de microondas y terahercios. Hemos superado esta aproximación realizando simulaciones numéricas para estimar el efecto de la penetración de los campos electromagnéticos dentro del metal a estas frecuencias.

El primer paso en nuestra investigación ha consistido en un analisis exhaustivo de los modos electromagnéticos de origen geométrico, también llamados polaritones plasmónicos spoof, en diferentes estructuras. Hemos estudiado dos geometrías planas diferentes: superficies corrugadas y láminas perforadas. Hemos demostrado que los polaritones plasmónicos spoof en aperturas bidimensionales son ondas de superficie localizadas en las interfaces de la estructura. Sin embargo, en el caso unidimensional estos modos tienen una naturaleza híbrida ya que están fuertemente influenciados por las resonancias de cavidad dentro de las aperturas. En ambos casos, las características de los modos están controladas por la anchura y profundidad de las perforaciones, lo que nos ha permitido considerar estas estructuras como metamateriales plasmónicos. El valor predictivo de nuestro trabajo teórico ha quedado demostrado por su excelente acuerdo con experimentos realizados recientemente en el régimen de terahercios.

Hemos tratado también la aparición de polaritones plasmónicos spoof en estructuras cilíndricas. Demostramos que un conjunto periódico de anillos en la superficie de un cable metálico soporta estos modos confinados y que sus propiedades están controladas por la geometría de los anillos. Aprovechando el origen geométrico de estos modos electromagnéticos, hemos diseñado una estructura cónica que permite focalizar radiación de terahercios en regiones menores que su longitud de onda. Como en el caso de geometrías planas, nuestras predicciones teóricas han sido corroboradas por estudios experimentales analizando la propagación de ondas de terahercios en cables perforados con un surco helicoidal.

Basándonos en nuestro estudio de polaritones plasmónicos spoof en geometrías sencillas, hemos desarrollado dos diseños para el guiado de radiación de terahercios que consisten en canales y cuñas metálicas corrugadas. Los modos electromagnéticos soportados por estas estructuras son similares a los polaritones plasmónicos de canal y de cuña en el rango óptico. Demostramos también que estos modos guiados permiten el confi-

namiento de campos electromagnéticos en regiones menores que su longitud de onda y que muestran grandes longitudes de propagación y pequeñas pérdidas en estructuras curvas.

Las propiedades de scatering de láminas metálicas perforadas pueden ser también estudiadas dentro del marco teórico que hemos desarrollado. Esto nos ha permitido analizar el papel que juega el orden en el fenómeno de transmisión extraordinaria. Hemos estudiado tres estructuras finitas diferentes: conjuntos periódicos y cuasi-periódicos (Fibonacci) de ranuras y conjuntos cuasi-periódicos (Penrose) de agujeros. A través de la versión en el espacio recíproco de nuestro formalismo, hemos podido vincular las características resonantes en el espectro de transmisión de estos sistemas con su factor de estructura. Hemos demostrado que la presencia de orden a largo alcance es el único requisito que debe cumplir la estructura para la aparición del fenómeno. Esto nos ha permitido relacionar el aumento de transmisión con los modos electromagnéticos radiativos soportados por las láminas. Una vez más, nuestros resultados teóricos concuerdan con experimentos realizados en terahercios sobre conjuntos cuasi-periódicos de agujeros.

Hemos estudiado también la transferencia de los fenómenos de transmisión extraordinaria y colimación a átomos fríos no interactuantes. A través de un modelo de potenciales cuadrados, hemos demostrado que, como en el caso electromagnético, la presencia de modos de superficie es el ingrediente principal en ambos fenómenos. Nuestro modelo nos ha permitido mostrar que la transmisión resonante de ondas de materia ocurre en conjuntos periódicos de agujeros de una y dos dimensiones, y que en el caso de una apertura rodeada de corrugaciones, el aumento en la transmisión está acompañado de efectos de colimación. Finalmente, hemos propuesto una posible implementación física de nuestras ideas en la que los potenciales atractivos realistas surgen de la combinación de la interacción intrínseca Wan der Waals y un potencial óptico externo.

A. Overlapping integrals between Bloch waves and rectangular hole and slit waveguide modes

In this appendix, we provide analytical formulae for the overlapping integrals between Bloch waves and rectangular hole and slit waveguide modes appearing in our ME formalism under PEC approximation. We present general expressions for both periodic hole (2D) and slit (1D) arrangements.

For 1D slit arrays, the overlapping integrals are defined as

$$\sigma_{ml}^{\gamma} = \langle k_m, \gamma | q_l, \gamma \rangle = \int dx \langle k_m, \gamma | x \rangle \langle x | q_l, \gamma \rangle. \tag{A-1}$$

For TE modes, these overlaps have the form

$$\begin{aligned} \sigma_{ml}^{\gamma=1} &= \sqrt{\frac{2}{ad}} \int_{-\frac{a}{2}}^{\frac{a}{2}} dx\, e^{-ik_m x} \sin \frac{l\pi}{a}\left(x + \frac{a}{2}\right) = \\ &= \sqrt{\frac{2}{ad}} \frac{l\pi/a}{k_m^2 - \left(\frac{l\pi}{a}\right)^2} \left[(-1)^l e^{-ik_m \frac{a}{2}} - e^{ik_m \frac{a}{2}}\right]. \end{aligned} \tag{A-2}$$

For TM modes, they read

$$\begin{aligned} \sigma_{ml}^{\gamma=2} &= \sqrt{\frac{2-\delta_{l0}}{ad}} \int_{-\frac{a}{2}}^{\frac{a}{2}} dx\, e^{-ik_m x} \cos \frac{l\pi}{a}\left(x + \frac{a}{2}\right) = \\ &= \sqrt{\frac{2-\delta_{l0}}{ad}} \frac{ik_m}{k_m^2 - \left(\frac{l\pi}{a}\right)^2} \left[(-1)^l e^{-ik_m \frac{a}{2}} - e^{ik_m \frac{a}{2}}\right]. \end{aligned} \tag{A-3}$$

Overlapping integrals for 2D hole arrangements are defined as

$$S_{mn\sigma}^{ls\gamma} = \langle \mathbf{k}_{mn}, \sigma | \mathbf{q}_{ls}, \gamma \rangle = \int_{-\frac{a_x}{2}}^{\frac{a_x}{2}} dx \int_{-\frac{a_y}{2}}^{\frac{a_y}{2}} dy \langle \mathbf{k}_{mn}, \sigma | \mathbf{r} \rangle \langle \mathbf{r} | \mathbf{q}_{ls}, \gamma \rangle. \tag{A-4}$$

Analytical expressions for these overlaps can be written in terms of their 1D counterparts,

having

$$S_{ls\gamma=1}^{mn\sigma=1} = \frac{-1}{|\mathbf{k}_{mn}||\mathbf{q}_{ls}|}\left[k_y^{(n)}\left(\frac{s\pi}{a_y}\right)\sigma_{ml}^{\gamma=2}\sigma_{ns}^{\gamma=1} + k_x^{(m)}\left(\frac{l\pi}{a_x}\right)\sigma_{ml}^{\gamma=1}\sigma_{ns}^{\gamma=2}\right], \quad \text{(A-5)}$$

$$S_{ls\gamma=2}^{mn\sigma=1} = \frac{-1}{|\mathbf{k}_{mn}||\mathbf{q}_{ls}|}\left[k_y^{(n)}\left(\frac{l\pi}{a_x}\right)\sigma_{ml}^{\gamma=2}\sigma_{ns}^{\gamma=1} - k_x^{(m)}\left(\frac{s\pi}{a_y}\right)\sigma_{ml}^{\gamma=1}\sigma_{ns}^{\gamma=2}\right], \quad \text{(A-6)}$$

$$S_{ls\gamma=1}^{mn\sigma=2} = \frac{1}{|\mathbf{k}_{mn}||\mathbf{q}_{ls}|}\left[k_x^{(m)}\left(\frac{s\pi}{a_y}\right)\sigma_{ml}^{\gamma=2}\sigma_{ns}^{\gamma=1} - k_y^{(n)}\left(\frac{l\pi}{a_x}\right)\sigma_{ml}^{\gamma=1}\sigma_{ns}^{\gamma=2}\right], \quad \text{(A-7)}$$

$$S_{ls\gamma=2}^{mn\sigma=2} = \frac{1}{|\mathbf{k}_{mn}||\mathbf{q}_{ls}|}\left[k_x^{(m)}\left(\frac{l\pi}{a_x}\right)\sigma_{ml}^{\gamma=2}\sigma_{ns}^{\gamma=1} + k_y^{(n)}\left(\frac{s\pi}{a_y}\right)\sigma_{ml}^{\gamma=1}\sigma_{ns}^{\gamma=2}\right], \quad \text{(A-8)}$$

where σ_{ml}^{γ} (σ_{ns}^{γ}) denotes the 1D overlapping integral for polarization γ, evaluated at $a = a_x$, $d = d_x$ and $k_m = k_x^{(m)}$ ($a = a_y$, $d = d_y$ and $k_n = k_y^{(n)}$).

B. Circular hole waveguide modes and overlapping integrals

This appendix is devoted to present the general expressions for the waveguide modes sustained by circular holes. Additionally, analytical formulae for the overlapping integrals between these modes and Bloch's waves are presented. Whereas waveguide modes of rectangular holes are labelled with three indexes, in the case of circular apertures, four indexes are required. Index γ labels the mode polarization, having $\gamma = 1$ ($\gamma = 2$) for TE (TM) modes. Indexes l and s, together with the fourth index, t, characterize the transverse wave vector associated with the waveguide mode. Index t also indicates the mode orientation. It distinguishes those modes having a zero azimuthal component of the electric field along the aperture diameter defined by $\theta = 0, \pi$ (horizontal modes), from those having a zero radial component of the electric field along the same diameter (vertical modes).

The dependence of the circular hole waveguide modes, $|ls, t, \gamma\rangle$, on the spatial coordinates (r, θ) is given by [38, 95]:

- for horizontal TE modes

$$\langle \mathbf{r}|ls, t = 1, \gamma = 1\rangle = g_{ls}\left[\frac{la}{\gamma'_{ls}r}\mathrm{J}_l\left(\frac{\gamma'_{ls}r}{a}\right)\cos(l\theta)\mathbf{u}_r - \mathrm{J}'_l\left(\frac{\gamma'_{ls}r}{a}\right)\sin(l\theta)\mathbf{u}_\theta\right], \quad \text{(B-1)}$$

- for horizontal TM modes

$$\langle \mathbf{r}|ls, t = 1, \gamma = 2\rangle = h_{ls}\left[\mathrm{J}'_l\left(\frac{\gamma_{ls}r}{a}\right)\cos(l\theta)\mathbf{u}_r - \frac{la}{\gamma_{ls}r}\mathrm{J}_l\left(\frac{\gamma_{ls}r}{a}\right)\sin(l\theta)\mathbf{u}_\theta\right], \quad \text{(B-2)}$$

- for vertical TE modes

$$\langle \mathbf{r}|ls, t = 2, \gamma = 1\rangle = g_{ls}\left[\frac{la}{\gamma'_{ls}r}\mathrm{J}_l\left(\frac{\gamma'_{ls}r}{a}\right)\sin(l\theta)\mathbf{u}_r + \mathrm{J}'_l\left(\frac{\gamma'_{ls}r}{a}\right)\cos(l\theta)\mathbf{u}_\theta\right], \quad \text{(B-3)}$$

- for vertical TM modes

$$\langle \mathbf{r}|ls, t = 2, \gamma = 2\rangle = h_{ls}\left[\mathrm{J}'_l\left(\frac{\gamma_{ls}r}{a}\right)\sin(l\theta)\mathbf{u}_r + \frac{la}{\gamma_{ls}r}\mathrm{J}_l\left(\frac{\gamma_{ls}r}{a}\right)\cos(l\theta)\mathbf{u}_\theta\right], \quad \text{(B-4)}$$

where a is the aperture radius, and $\mathbf{u}_r$ and $\mathbf{u}_\theta$ are the radial and azimuthal unit vectors, respectively. J_l is the Bessel function of l^{th} order and J_l', its derivative. The constants γ_{ls} and γ'_{ls} are the s^{th}-zero of J_l and J_l', respectively [96]. The longitudinal wave vector associated with $|ls,t,\gamma\rangle$ is $q_z^{lst=1} = \sqrt{k_0^2 - (\gamma'_{ls}/a)^2}$ (for horizontal modes) and $q_z^{lst=2} = \sqrt{k_0^2 - (\gamma_{ls}/a)^2}$ (for vertical modes).

Note that in Eqs. (B-1)-(B-4) we have introduced the normalization factors

$$g_{ls} = \sqrt{\frac{2-\delta_{l0}}{\pi}} \frac{\gamma'_{ls}}{a\,\mathrm{J}_l(\gamma'_{ls})\sqrt{\gamma'^2_{ls} - l^2}}, \tag{B-5}$$

$$h_{ls} = \sqrt{\frac{2-\delta_{l0}}{\pi}} \frac{1}{a\,\mathrm{J}_{l-1}(\gamma_{ls})}, \tag{B-6}$$

so that the waveguide modes fulfill the orthonormality relation

$$\langle l's',t',\gamma'|ls,t,\gamma\rangle = \int d\mathbf{r}\langle l's',t',\gamma'|\mathbf{r}\rangle\langle\mathbf{r}|ls,t,\gamma\rangle = \delta_{ll'}\delta_{ss'}\delta_{tt'}\delta_{\gamma\gamma'}. \tag{B-7}$$

The overlapping integrals between circular waveguide modes and Bloch's waves are defined as

$$S_{mn\sigma}^{lst\gamma} = \langle\mathbf{k}_{mn},\sigma|ls,t,\gamma\rangle = \int d\mathbf{r}\langle\mathbf{k}_{mn},\sigma|\mathbf{r}\rangle\langle\mathbf{r}|ls,t,\gamma\rangle. \tag{B-8}$$

Analytical expressions for these integrals are as follows [176]

$$S_{mn\sigma=1}^{ls,t=1,\gamma=1} = \sqrt{\frac{2-\delta_{l0}}{\pi}} \frac{(-i)^{l-1}\,k_0 a\,\cos(l\theta_{mn})\,J_l'(|\mathbf{k}_{mn}|a)}{\sqrt{\gamma'^2_{ls} - l^2}\,[1-(|\mathbf{k}_{mn}|a/\gamma'_{ls})^2]}, \tag{B-9}$$

$$S_{mn\sigma=1}^{ls,t=2,\gamma=1} = -\tan(l\theta_{mn})\,S_{mn\sigma=1}^{ls,t=1,\gamma=1}, \tag{B-10}$$

$$S_{mn\sigma=2}^{ls,t=1,\gamma=1} = \sqrt{\frac{2-\delta_{l0}}{\pi}} \frac{(-i)^{l-1}\,lk_0\,\sin(l\theta_{mn})\,J_l(|\mathbf{k}_{mn}|a)}{|\mathbf{k}_{mn}|\sqrt{\gamma'^2_{ls} - l^2}}, \tag{B-11}$$

$$S_{mn\sigma=2}^{ls,t=2,\gamma=1} = \cot(l\theta_{mn})\,S_{mn\sigma=2}^{ls,t=1,\gamma=1}, \tag{B-12}$$

$$S_{mn\sigma=1}^{ls,t,\gamma=2} = 0, \tag{B-13}$$

$$S_{mn\sigma=2}^{ls,t=1,\gamma=2} = \sqrt{\frac{2-\delta_{l0}}{\pi}} \frac{(-i)^{l-1}\,k_0|\mathbf{k}_{mn}|\,\cos(l\theta_{mn})\,J_l(|\mathbf{k}_{mn}|a)}{|\mathbf{k}_{mn}|^2 - (\gamma_{ls}/a)^2}, \tag{B-14}$$

$$S_{mn\sigma=2}^{ls,t=2,\gamma=2} = \tan(l\theta_{mn})\,S_{mn\sigma=2}^{ls,t=1,\gamma=2}, \tag{B-15}$$

where angle θ_{mn} satisfies $\tan(\theta_{mn}) = k_y^{(n)}/k_x^{(m)}$.

List of publications

Publications related to this thesis

- E. Moreno, A. I. Fernández-Domínguez, J. Ignacio Cirac, F. J. García-Vidal, and L. Martín-Moreno, *Resonant transmission of cold atoms through subwavelength apertures*, Physical Review Letters **95**, 170406 (2005).

- A. I. Fernández-Domínguez, E. Moreno, L. Martín-Moreno, and F. J. García-Vidal, *Beaming matter waves from a subwavelength aperture*, Physical Review A **74**, 21601(R) (2006).

- A. I. Fernández-Domínguez, F. J. García-Vidal, and L. Martín-Moreno, *Resonant transmission of light through a finite array of slits*, Physical Review B **76**, 235430 (2007).

- J. Bravo-Abad, A. I. Fernández-Domínguez, F. J. García-Vidal, and L. Martín-Moreno, *Theory of extraordinary transmission of light through quasiperiodic arrays of subwavelength holes*, Physical Review Letters **99**, 203905 (2007).

- C. R. Williams, S. R. Andrews, S. A. Maier, A. I. Fernández-Domínguez, L. Martín-Moreno, and F. J. García-Vidal, *Highly confined guiding of terahertz surface-plasmon polaritons on structured metal surfaces*, Nature Photonics **2**, 175 (2008).

- A. I. Fernández-Domínguez, I. Hernández-Carrasco, L. Martín-Moreno, and F. J. García-Vidal, *Transmission resonances through a Fibonacci array of subwavelength slits*, Electromagnetics **28**, 186 (2008).

- A. I. Fernández-Domínguez, D. Martín-Cano, E. Moreno, L. Martín-Moreno, and F. J. García-Vidal, *Resonant transmission and beaming of cold atoms assisted by surface matter waves*, Physical Review A **78**, 023614 (2008).

- A. I. Fernández-Domínguez, S. R. Andrews, L. Martín-Moreno, F. J. García-Vidal, and S. A. Maier, *Spoof surface plasmon polariton modes propagating along periodically corrugated wires*, IEEE Journal of Selected Topics in Quantum Electronics, **14**, 1515 (2008).

- A. I. Fernández-Domínguez, C. R. Williams, F. J. García-Vidal, L. Martín-Moreno, S. R. Andrews, and S. A. Maier, *Terahertz Surface Plasmon Polaritons on a helically grooved wire*, Applied Physics Letters, **93**, 141109 (2008).
- A. I. Fernández-Domínguez, E. Moreno, L. Martín-Moreno, and F. J. García-Vidal, *Guiding terahertz waves along subwavelength channels*, submitted 2008.
- A. I. Fernández-Domínguez, E. Moreno, L. Martín-Moreno, and F. J. García-Vidal, *Terahertz wedge plasmon polaritons*, submitted 2009.

Other publications

- J. Christensen, A. I. Fernández-Domínguez, F. de Leon-Pérez, L. Martín-Moreno, and F. J. García-Vidal, *Collimation of sound assisted by acoustic surface waves*, Nature Physics **3**, 851 (2007).
- E. S. Lee, D. H. Kang, A. I. Fernández-Domínguez, F. J. García-Vidal, L. Martín-Moreno, D. S. Kim and T.-I. Jeon, *Bragg reflection of terahertz waves in plasmonic crystals*, submitted 2009.

Bibliography

[1] A. Sommerfeld. *Ann. Phys. und Chemie*, 303:233, 1899. (cited on pages 1, 59, and 87)

[2] J. Zenneck. *Ann. Phys.*, 23:846, 1907. (cited on pages 1, 59, and 73)

[3] R. W. Wood. *Proc. Phys. Soc. London*, 18:269, 1902. (cited on pages 1 and 110)

[4] Lord Rayleigh. *Proc. Roy. Soc. London*, A79:399, 1907. (cited on pages 1 and 110)

[5] U. Fano. *J. Opt. Soc. Am.*, 31:213, 1941. (cited on p. 1)

[6] R. H. Ritchie. *Phys. Rev.*, 106:874, 1957. (cited on pages 1 and 41)

[7] R. H. Ritchie, E. T. Arakawa, J. J. Cowan, and R. N. Hamm. *Phys. Rev. Lett.*, 21:1530, 1968. (cited on pages 1 and 60)

[8] E. Kretschmann and H. Raether. *Z. Naturforschung*, 23A:2135, 1968. (cited on p. 1)

[9] H. Raether. *Surface plasmons on smooth and rough surfaces and on gratings*. Springer Verlag, New York, 1988. (cited on pages 1, 2, and 60)

[10] J. D. Jackson. *Classical electrodynamics*. John Wiley & Sons, New York, 3rd edition, 1999. (cited on pages 3, 17, 40, and 78)

[11] T. M. Ebbesen, C. Genet, and S. I. Bozhevolnyi. *Physics Today*, 61:44, 2008. (cited on p. 3)

[12] W. L. Barnes, A. Dereux, and T. M. Ebbesen. *Nature*, 424:824, 2003. (cited on pages 3 and 6)

[13] S. A. Maier. *Plasmonics: Fundamentals and applications*. Springer, New York, 2007. (cited on p. 3)

[14] E. Ozbay. *Science*, 311:189, 2006. (cited on pages 4 and 6)

[15] H. Ditlbacher, J. R. Krenn, G. Schider, A. Leitner, and F. R. Aussenegg. *Appl. Phys. Lett.*, 81:1762, 2002. (cited on p. 4)

[16] J.-C. Weeber, J. R. Krenn, A. Dereux, B. Lamprecht, Y. Lacroute, and J. P. Goudonnet. *Phys. Rev. B*, 64:045411, 2001. (cited on p. 5)

[17] S. C. Kitson, W. L. Barnes, and J. R. Sambles. *Phys. Rev. Lett.*, 77:2670, 1996. (cited on p. 5)

[18] S. I. Bozhevolnyi, J. Erland, K. Leosson, P. M. W. Skovgaard, and J. M. Hvam. *Phys. Rev. Lett.*, 86:3008, 2001. (cited on p. 5)

[19] D. Sarid. *Phys. Rev. Lett.*, 47:1927, 1981. (cited on p. 5)

[20] P. Berini. *Phys. Rev. B*, 61:10484, 2000. (cited on p. 5)

[21] P. Berini. *Phys. Rev. B*, 63:125417, 2001. (cited on p. 5)

[22] J. R. Krenn and J. C. Weeber. *Phylos. Trans. R. Soc. London Ser. A*, 362:739, 2004. (cited on p. 5)

[23] J. R. Krenn, A. Dereux, J. C. Weeber, E. Bourillot, Y. Lacroute, J. P. Goudonnet, G. Schider, W. Gotschy, A. Leitner, F. R: Aussenegg, and C. Girard. *Phys. Rev. Lett.*, 82:2590, 1999. (cited on p. 5)

[24] S. A. Maier, P. G. Kik, H. A. Atwater, S. Meltzer, E. Harel, B. E. Koel, and A. A. G. Requicha. *Nature Materials*, 2:229, 2003. (cited on p. 5)

[25] J. Q. Lu and A. A. Maradudin. *Phys. Rev. B*, 42:11159, 1990. (cited on p. 5)

[26] I. V. Novikov and A. A. Maradudin. *Phys. Rev. B*, 66:035403, 2002. (cited on pages 5 and 92)

[27] D. F. P. Pile and D. K. Gramotnev. *Opt. Lett.*, 29:1069, 2004. (cited on pages 5, 92, and 99)

[28] D. F. P. Pile and D. K. Gramotnev. *Opt. Lett.*, 30:1186, 2005. (cited on pages 5 and 99)

[29] S. I. Bozhevolnyi, V. S. Volkov, E. Devaux, and T. W. Ebbesen. *Phys. Rev. Lett.*, 95:046802, 2005. (cited on pages 5 and 92)

[30] V. S. Volkov, S. I. Bozhevolnyi, E. Devaux, and T. W. Ebbesen. *Appl. Phys. Lett.*, 89:143108, 2006. (cited on p. 5)

[31] S. I. Bozhevolnyi, V. S. Volkov, E. Devaux, J.-Y. Laluet, and T. W. Ebbesen. *Nature*, 440:508, 2006. (cited on pages 5, 6, 59, and 92)

[32] E. Moreno, F. J. García-Vidal, S. G. Rodrigo, L. Martín-Moreno, and S. I. Bozhevolnyi. *Opt. Lett.*, 31:3447, 2006. (cited on pages 5, 93, 95, and 96)

[33] L. Dobrzynski and A. A. Maradudin. *Phys. Rev. B*, 6:3810, 1972. (cited on p. 5)

[34] D. F. P. Pile, T. Ogawa, D. K. Gramotnev, T. Okamoto, M. Haraguchi, M. Fukui, and S. Matsuo. *Appl. Phys. Lett.*, 87:061106, 2005. (cited on p. 5)

[35] N. Yan and M. Qiu. *J. Opt. Soc. Am. B*, 24:2333, 2007. (cited on p. 5)

[36] E. Moreno, S. G. Rodrigo, S. I. Bozhevolnyi, L. Martín-Moreno, and F. J. García-Vidal. *Phys. Rev. Lett.*, 100:023901, 2008. (cited on pages 5, 6, 59, 99, 100, and 102)

[37] H. Bethe. *Phys. Rev.*, 66:163, 1944. (cited on p. 6)

[38] A. Roberts. *J. Opt. Soc. Am. A*, 4:1970, 1987. (cited on pages 7 and 169)

[39] T. W. Ebbesen, H. J. Lezec, H. F. Ghaemi, T. Thio, and P. A. Wolff. *Nature*, 391:667, 1998. (cited on pages 7, 26, 28, 107, 120, 130, and 143)

[40] A. Krishnan, T. Thio, T. J. Kim, H. J. Lezec, T. W. Ebbesen, P. A. Wolff, J. Pendry, L. Martín-Moreno, and F. J. García-Vidal. *Opt. Commun.*, 200:1, 2001. (cited on pages 8 and 107)

[41] U. Schröter and D. Heitmann. *Phys. Rev. B*, 58:15419, 1998. (cited on pages 8, 107, and 111)

[42] M. M. J. Treacy. *Appl. Phys. Lett.*, 75:606, 1999. (cited on pages 8, 107, and 111)

[43] J. A. Porto, F. J. García-Vidal, and J. B. Pendry. *Phys. Rev. Lett.*, 83:2845, 1999. (cited on pages 8, 16, 107, and 110)

[44] E. Popov, M. Nevière, S. Enoch, and R. Reinisch. *Phys. Rev. B*, 62:16100, 2000. (cited on pages 8 and 107)

[45] L. Martín-Moreno, F. J. García-Vidal, H. J. Lezec, K. M. Pellerin, T. Thio, J. B. Pendry, and T. W. Ebbesen. *Phys. Rev. Lett.*, 86:1114, 2001. (cited on pages 8, 59, 107, 110, and 130)

[46] L. Salomon, F. D. Grillot, A. V. Zayats, and F. de Fornel. *Phys. Rev. Lett.*, 86:1110, 2001. (cited on pages 8 and 107)

[47] C. Genet and T. W. Ebbesen. *Nature*, 445:39, 2007. (cited on p. 8)

[48] H. J. Lezec, A. Degiron, E. Deveux, R. A. Linke, L. Martín-Moreno, F. J. García-Vidal, and T. W. Ebbesen. *Science*, 297:820, 2002. (cited on pages 8, 107, and 148)

[49] L. Martín-Moreno, F. J. García-Vidal, H. J. Lezec, A. Degiron, and T. W. Ebbesen. *Phys. Rev. Lett.*, 90:167401, 2003. (cited on pages 8, 16, 107, 108, and 152)

[50] F. J. García-Vidal, H. J. Lezec, T. W. Ebbesen, and L. Martín-Moreno. *Phys. Rev. Lett.*, 90:213901, 2003. (cited on pages 8, 16, 107, 151, and 155)

[51] D. Qu, D. Grischkowsky, and W. Zhang. *Opt. Lett.*, 29:896, 2004. (cited on p. 9)

[52] Y. H. Ye and J. Y. Zhang. *Appl. Phys. Lett.*, 84:2977, 2004. (cited on p. 9)

[53] H. Cao and A. Nahata. *Opt. Express*, 12:1004, 2004. (cited on p. 9)

[54] F. Yang and J. R. Sambles. *Phys. Rev. Lett.*, 89:063901, 2002. (cited on p. 9)

[55] M. Beruete, M. Sorolla, I. Campillo, J. S. Dolado, L. Mart/'in-Moreno, J. Bravo-Abad, and F. J. García-Vidal. *Opt. Lett.*, 29:2500, 2004. (cited on p. 9)

[56] J. B. Pendry, L. Martín-Moreno, and F. J. García-Vidal. *Science*, 305:847, 2004. (cited on pages 9, 16, and 59)

[57] F. J. García-Vidal, L. Martín-Moreno, and J. B. Pendry. *J. Opt. A: Pure Appl. Opt.*, 7:S97, 2005. (cited on pages 9, 10, and 59)

[58] G. Gobau. *J. Appl. Phys.*, 21:1119, 1950. (cited on pages 10 and 59)

[59] R. Ulrich and M. Tacke. *Appl. Phys. Lett.*, 22:251, 1973. (cited on pages 10 and 59)

[60] D. L. Mills and A. A. Maradudin. *Phys. Rev. B*, 39:1569, 1989. (cited on pages 10 and 59)

[61] F. J. García de Abajo and J. J. Saenz. *Phys. Rev. Lett.*, 95:233901, 2005. (cited on pages 10, 36, and 59)

[62] E. Hendry, A. P. Hibbins, and J. R. Sambles. *Phys. Rev. B*, 78:235426, 2008. (cited on pages 10 and 59)

[63] S. A. Maier, S. R. Andrews, L. Martín-Moreno, and F. J. García-Vidal. *Phys. Rev. Lett.*, 97:176805, 2006. (cited on pages 10, 59, 79, and 85)

[64] A. P. Hibbins, B. R. Evans, and J. R. Sambles. *Science*, 308:670, 2005. (cited on pages 10 and 59)

[65] A. P. Hibbins, M. J. Lockyear, I. R. Hooper, and J. R. Sambles. *Phys. Rev. Lett.*, 96:073904, 2006. (cited on pages 10 and 59)

[66] C. R. Williams, S. R. Andrews, S. A. Maier, A. I. Fernández-Domínguez, L. Martín-Moreno, and F. J. García-Vidal. *Nature Photonics*, 2:175, 2008. (cited on p. 10)

[67] B. F. Ferguson and X.-C. Zhang. *Nature Materials*, 1:26, 2002. (cited on p. 11)

[68] A. Tredicucci R. Köhler, F. Beltram, H. E. Beere, E. H. Linfield, A. G. Davies, D. A. Ritchie, R. C. Iotti, and F. Rossi. *Nature*, 417:156, 2002. (cited on p. 11)

[69] S. Komiyama, O. Astaflev, T. Kutsuwa, and H. A. Hirai. *Nature*, 403:405, 2000. (cited on p. 11)

[70] J. Zhang and D. Grischkowsky. *Opt. Lett.*, 29:1617, 2004. (cited on p. 11)

[71] S. P Mickan, A. Menikh, H. Liu, C. A. Mannella, R. MacColl, D. Abbott, J. Munch, and X.-C. Zhang. *Phys. Med. Biol.*, 47:3789, 2002. (cited on p. 11)

[72] M. Nagel, P. Haring Bolivar, M. Brucherseifer, H. Kurz, A. Bosserhoff, , and R. Büttner. *Appl. Phys. Lett.*, 80:154, 2002. (cited on p. 11)

[73] J. F. Federici, B. Schulkin, F. Huang, D. Gary, R. Barat, F. Oliveira, and D. Zimdars. *Semicond. Sci. Technol.*, 20:S266, 2005. (cited on p. 11)

[74] E. Moreno, F. J. García-Vidal, and L. Martín-Moreno. *Phys. Rev. B*, 69:121402(R), 2004. (cited on pages 11 and 133)

[75] P. Kramper, M. Agio, C. M. Soukoulis, A. Birner, F. Müller, R. B. Wehrspohn, U. Gösele, and V. Sandoghdar. *Phys. Rev. Lett.*, 92:113903, 2004. (cited on pages 11 and 133)

[76] I. Bulu, H. Caglayan, and E. Ozbay. *Opt. Lett.*, 30:3078, 2005. (cited on pages 11 and 133)

[77] E. Moreno, A. I. Fernández-Domínguez, J. I. Dirac, F. J. García-Vidal, and L. Martín-Moreno. *Phys. Rev. Lett.*, 95:170406, 2005. (cited on p. 11)

[78] P. Darancet, V. Olevano, and D. Mayou. *Phys. Rev. Lett.*, 102:136803, 2009. (cited on p. 11)

[79] M.-H. Lu, X.-K. Liu, L. Feng, J. Li, C.-P. Huang, Y.-F. Chen, Y.-Y. Zhu, S.-N. Zhu, and N.-B. Ming. *Phys. Rev. Lett.*, 99:174301, 2007. (cited on pages 11 and 161)

[80] B. Hou, J. Mei, M. Ke, W. Wen, Z. Liu, J. Shi, and P. Sheng. *Phys. Rev. B*, 76:054303, 2007. (cited on pages 11 and 161)

[81] J. Christensen, A. I. Fernández-Domínguez, F. de Leon-Pérez, L. Martín-Moreno, and F. J. García-Vidal. *Nature Physics*, 3:851, 2007. (cited on pages 11 and 161)

[82] J. Christensen, L. Martín-Moreno, and F. J. García-Vidal. *Phys. Rev. Lett.*, 101:014301, 2008. (cited on pages 11 and 161)

[83] H. Estrada, P. Candelas, A. Uris, F. Belmar, F. J. G. de Abajo, and F. Meseguer. *Phys. Rev. Lett.*, 101:084302, 2008. (cited on pages 11 and 161)

[84] B. A. Munk. *Frequency selective surfaces: Theory and design*. Wiley, New York, 2000. (cited on p. 15)

[85] P. Sheng, R. S. Stepleman, and P. N. Sanda. *Phys. Rev. B.*, 26:2907, 1982. (cited on p. 15)

[86] T. López-Ríos and A. Wirgin. *Solid State Commun.*, 52:197, 1984. (cited on p. 15)

[87] A. Wirgin and A. A. Maradudin. *Prog. Surf. Sci.*, 22:1, 1986. (cited on p. 15)

[88] M. Fleischmann, P. J. Hendra, and A. J. McQuillan. *Chem. Phys. Lett.*, 26:163, 1974. (cited on p. 15)

[89] A. Mary, S. G. Rodrigo, F. J. García-Vidal, and L. Martín-Moreno. *Phys. Rev. Lett.*, 101:103902, 2008. (cited on p. 16)

[90] J. A. Stratton. *Electromagnetic theory*. McGraw-Hill, New York, 1941. (cited on pages 16, 21, and 78)

[91] M. A. Leontovich. *Investigation of propagation of radiowaves, part II*. USSR Acad. Sci., Moscow, 1948. (cited on pages 17 and 40)

[92] T. B. A. Senior. *Appl. Sci. Res. B*, 8:418, 1960. (cited on pages 17 and 41)

[93] J. Bravo-Abad, F. J. García-Vidal, and L. Martín-Moreno. *Phys. Rev. Lett.*, 93:227401, 2004. (cited on pages 28, 125, and 146)

[94] J. Bravo-Abad, L. Martín-Moreno, and F. J. García-Vidal. *IEEE J. Sel. Top. Quantum Electron.*, 12:1221, 2006. (cited on p. 28)

[95] J. Bravo-Abad. *Transmisión resonante de luz a través de láminas metálicas nanoestructuradas*. PhD Thesis, 2006. (cited on pages 28 and 169)

[96] G. B. Arfken and H. J. Weber. *Mathematical methods for physicists*. Harcourt Academic Press, London, 5th edition, 2001. (cited on pages 31, 32, 77, 78, and 170)

[97] N. W. Ashcroft and N. D. Mermin. *Solid state physics*. Thomson Learning, London, 1976. (cited on pages 32 and 53)

[98] M. A. Ordal, L. L. Long, R. J. Bell, S. E. Bell, R. R. Bell, R. W. Alexander Jr., and C. A. Ward. *Appl. Opt.*, 22:1099, 1983. (cited on pages 41, 77, 94, 99, and 102)

[99] E. D. Palik. *Handbook of optical constants of solids*. Academic Press Handbook series, New York, 1985. (cited on p. 41)

[100] A. D. Rakić, A. B. Djurišić, J. M. Elazar, and M. L. Majewski. *Appl. Opt.*, 37:5271, 1998. (cited on pages 41, 43, and 48)

[101] S. Yuferev, L. Proekt, and N. Ida. *IEEE Trans. Magn.*, 37:3465, 2001. (cited on p. 41)

[102] R. Gordon and A. G. Brolo. *Opt. Express*, 13:1933, 2005. (cited on p. 42)

[103] E. Yablonovitch, T. J. Gmitter, and K. M. Leung. *Phys. Rev. Lett.*, 67:2295, 1991. (cited on p. 43)

[104] E. Yablonovitch, T. J. Gmitter, R. D. Meade, A. M. Rappe, K. D. Brommer, and J. D. Joannopoulos. *Phys. Rev. Lett.*, 67:3380, 1991. (cited on p. 43)

[105] J. B. Pendry and A. MacKinnon. *Phys. Rev. Lett.*, 69:2772, 1992. (cited on pages 44 and 46)

[106] J. B. Pendry. *J. Mod. Opt.*, 41:209, 1994. (cited on p. 47)

[107] J. B. Pendry. *Low energy electron diffraction*. Academic, London, 1974. (cited on p. 47)

[108] K. S. Yee. *IEEE Trans. Antennas Propagat.*, 14:302, 1966. (cited on pages 49, 50, and 53)

[109] A. Taflove. *IEEE Trans. Electromagn. Compat.*, 22:191, 1980. (cited on p. 49)

[110] A. Taflove and S. C. Hagness. *Computational electrodynamics: The finite-difference-time-domain method*. Artech House, Boston, 3rd edition, 2005. (cited on p. 49)

[111] D. F. Kelley and R. J. Luebbers. *IEEE Trans. Antennas Propagat.*, 44:792, 1996. (cited on p. 53)

[112] T. Weiland. *Electron. Commun.*, 31:116, 1977. (cited on p. 53)

[113] T. Weiland. *Int. J. Numer. Model. Electron. Networks Devices Fields (AEÜ)*, 3:295, 1996. (cited on p. 54)

[114] R. Marklein. *Numerical methods for the modeling of acoustic, electromagnetic, elastic and piezoelectric wave propagation problems in the time domain based on the finite integration technique*. Shaker Verlag, Aachen, 1997. (cited on p. 54)

[115] M. Clemens and T. Weiland. *J. Electromagn. Waves Appl.*, 15:79, 2001. (cited on pages 54 and 57)

[116] E. N. Economou. *Phys. Rev.*, 182:539, 1969. (cited on pages 70 and 94)

[117] T.-I. Jeon and D. Grischkowsky. *Appl. Phys. Lett.*, 88:061113, 2006. (cited on p. 73)

[118] P. J. Crepeau. *Proc. IEEE*, 52:33, 1964. (cited on p. 90)

[119] J. B. Knorr and P. R. McIsaac. *IEEE Trans. Microw. Theory Tech.*, 19:854, 1971. (cited on p. 90)

[120] R. A. Waldron. *Q. J. Mech. Appl. Math.*, 11:438, 1958. (cited on p. 90)

[121] S. A. Maier and S. R. Andrews. *Appl. Phys. Lett.*, 88:251120, 2006. (cited on p. 92)

[122] A. P. Hibbins, M. J. Lockyear, and J. R. Sambles. *Phys. Rev. B*, 76:165431, 2007. (cited on p. 93)

[123] W. Zhu, A. Agrawal, and A. Nahata. *Opt. Express*, 16:6216, 2008. (cited on p. 97)

[124] K. Wang and D. M. Mittleman. *Nature*, 432:376, 2004. (cited on p. 99)

[125] L. Shen, X. Chen, and T.-J. Yang. *Opt. Express*, 16:3326, 2008. (cited on p. 102)

[126] L. Shen, X. Chen, Y. Zhong, and K. Agarwal. *Phys. Rev. B*, 77:075408, 2008. (cited on p. 102)

[127] Q. Gan, Z. Fu, Y. J. Ding, and F. J. Bartoli. *Phys. Rev. Lett.*, 100:256803, 2008. (cited on p. 104)

[128] H. E. Went, A. P. Hibbins, J. R. Sambles, C. R. Lawrence, and A. P. Crick. *Appl. Phys. Lett.*, 77:2789, 2001. (cited on p. 107)

[129] S. Collin, F. Pardo, R. Teissier, and J. L. Pelouard. *Phys. Rev. B*, 63:033107, 2001. (cited on p. 107)

[130] Y. Takakura. *Phys. Rev. Lett.*, 86:5601, 2001. (cited on pages 107 and 110)

[131] F. J. G. de Abajo. *Optics Express*, 10:1475, 2002. (cited on p. 107)

[132] H. F. Schouten, T. D. Visser, D. Lenstra, and H. Blok. *Phys. Rev. E*, 67:036608, 2003. (cited on pages 107 and 110)

[133] F. J. García-Vidal, E. Moreno, J. A. Porto, and L. Martín-Moreno. *Phys. Rev. Lett.*, 95:103901, 2005. (cited on p. 107)

[134] P. Lalanne, J. P. Hugonin, and J. C. Rodier. *Phys. Rev. Lett.*, 95:263902, 2005. (cited on p. 107)

[135] M. Sun, J. Tien, Z.-Y. Li, B.-Y. Cheng, D.-Z. Zhang, and A.-Z. Jin andH. F. Yang. *Chin. Phys. Lett.*, 23:486, 2006. (cited on p. 107)

[136] F. Przybilla, C. Genet, and T. W. Ebbesen. *App. Phys. Lett.*, 89:121115, 2006. (cited on pages 107 and 124)

[137] N. Papasimakis, V. A. Fedotov, A. S. Schwanecke, N. I. Zheludev, and F. J. García de Abajo. *App. Phys. Lett.*, 91:081503, 2007. (cited on pages 107 and 124)

[138] M. Matsui, A. Agrawal, A. Nahata, and Z. V. Vardeny. *Nature*, 446:517, 2007. (cited on pages 107, 124, 126, and 128)

[139] C. Rockstuhl, F. Lederer, T. Zentgraf, and H. Giessen. *App. Phys. Lett.*, 91:151109, 2007. (cited on p. 107)

[140] A. Agrawal, T. Matsui, Z. V. Vardeny, and A. Nahata. *Opt. Express*, 16:6267, 2008. (cited on p. 107)

[141] A. A. Maradudin, A. V. Shchegrov, and T. A. Leskova. *Opt. Commun.*, 135:352, 1997. (cited on p. 110)

[142] R. A. Depine and D. C. Skigin. *Phys. Rev. E*, 61:4479, 2000. (cited on p. 110)

[143] Q. Cao and P. Lalanne. *Phys. Rev. Lett.*, 88:057403, 2002. (cited on pages 111 and 142)

[144] V. Galdi, G. Castaldi, V. Pierro, I. M. Pinto, and L. B. Felsen. *IEEE Trans. Antenna Propagat.*, 53:2044, 2005. (cited on p. 118)

[145] J. Li, S. Liu, C. Huang, T. Li, Q. Wang, and Y. Zhu. *J. Opt. A: Pure Appl. Opt.*, 10:075202, 2008. (cited on p. 124)

[146] Y. Pang, C. Genet, and T. W. Ebbesen. *Opt. Commun.*, 280:10, 2007. (cited on p. 124)

[147] F. Miyamaru and M. Hangyo. *Appl. Phys. Lett.*, 84:2742, 2004. (cited on p. 124)

[148] J. Bravo-Abad, A. Degiron, F. Przybilla, C. Genet, F.J. García-Vidal, L. Martín-Moreno, and T.W. Ebbesen. *Nature Physics*, 2:120, 2006. (cited on pages 124 and 130)

[149] F. Przybilla, A. Degiron, C. Genet, T.W. Ebbesen, F. de León-Pérez, J. Bravo-Abad, F. J. García-Vidal, and L. Martín-Moreno. *Opt. Express*, 16:9571, 2008. (cited on p. 124)

[150] K. Ingersent and P. J. Steinhardt. *Phys. Rev. Lett.*, 64:2034, 1990. (cited on p. 124)

[151] D. Levine and P. J. Steinhardt. *Phys. Rev. B*, 34:596, 1986. (cited on p. 125)

[152] D. A. Rabson, N. D. Mermin, D. S. Rokhsar, and D. C. Wright. *Rev. Mod. Phys.*, 63:699, 1991. (cited on p. 125)

[153] B. H. Bransden and C. J. Joachim. *Quantum mechanics*. Pearson Education Ltd., Essex, 2000. (cited on pages 134 and 136)

[154] A. Christ, S. G. Tikhodeev, N. A. Gippius, J. Kuhl, and H. Giessen. *Phys. Rev. Lett.*, 91:183901, 2003. (cited on p. 139)

[155] E. Moreno, L. Martín-Moreno, and F. J. García-Vidal. *J. Opt. A: Pure Appl. Opt.*, 8:S94, 2006. (cited on p. 139)

[156] U. Fano. *Phys. Rev.*, 124:1866, 1961. (cited on p. 142)

[157] C. Genet, M. P. van Exter, and J. P. Woerdman. *Opt. Commun.*, 225:331, 2003. (cited on p. 142)

[158] L. Martín-Moreno and F. J. García-Vidal. *Opt. Express*, 12:3619, 2004. (cited on p. 146)

[159] J. Bravo-Abad, L. Martín-Moreno, F. J. García-Vidal, E. Hendry, and J. Gómez-Rivas. *Phys. Rev. B*, 76:241102(R), 2007. (cited on p. 148)

[160] E. G. Lima, M. Chevrollier, O. Di Lorenzo, P. C. Segundo, and M. Oriá. *Phys. Rev. A*, 62:013410, 2000. (cited on p. 155)

[161] J. P. Gordon and A. Ashkin. *Phys. Rev. A*, 21:1606, 1980. (cited on p. 156)

[162] V. I. Balykin, V. S. Letokhov, Y. B. Ovchinnikov, and A. I. Sidorov. *Phys. Rev. Lett.*, 60:2137, 1988. (cited on p. 156)

[163] R. J. Cook and R. K. Hill. *Opt. Commun.*, 43:258, 1982. (cited on p. 156)

[164] A. Landragin, J.-Y. Courtois, G. Labeyrie, N. Vansteenkiste, C. I. Westbrook, and A. Aspect. *Phys. Rev. Lett.*, 77:1464, 1996. (cited on p. 156)

[165] S. Marksteiner, C. M. Savage, P. Zoller, and S. L. Rolston. *Phys. Rev. A*, 50:2680, 1994. (cited on p. 156)

[166] F. L. Kien, V. I. Balykin, and K. Hakuta. *Phys. Rev. A*, 70:063403, 2004. (cited on p. 156)

[167] V. I. Balykin, V. G. Minogin, and V. S. Letokhov. *Rep. Prog. Phys.*, 63:1429, 2000. (cited on p. 156)

[168] M. Marinescu, A. Dalgarno, and J. F. Babb. *Phys. Rev. A*, 55:1530, 1997. (cited on p. 156)

[169] B. V. Numerov. *Astronomische Nachrichten*, 230:359, 1927. (cited on p. 158)

[170] U. Leonhardt. *Science*, 312:1777, 2006. (cited on p. 161)

[171] J. B. Pendry, D. Schurig, and D. R. Smith. *Science*, 312:1780, 2006. (cited on p. 161)

[172] D. Schurig, J. J. Mock, B. J. Justice, S. A. Cummer, J. B. Pendry, A. F. Starr, and D. R. Smith. *Science*, 314:977, 2006. (cited on p. 161)

[173] S. Zhang, D. A. Genov, C. Sun, and X. Zhang. *Phys. Rev. Lett.*, 100:123002, 2008. (cited on p. 161)

[174] A. Greenleaf, Y. Kurylev, M. Lassas, and G. Uhlmann. *Phys. Rev. Lett.*, 101:220404, 2008. (cited on p. 161)

[175] S. A. Cummer, B.-I. Popa, D. Schurig, D. R. Smith, J. B. Pendry, M. Rahm, and A. Starr. *Phys. Rev. Lett.*, 100:024301, 2008. (cited on p. 161)

[176] N. Amitay and V. Galindo. *IEEE Trans. Microw. Theory Tech.*, 16:265, 1968. (cited on p. 170)